UNIVERSITY OF OXFORD

Department of Engineering Science

QUANTITATIVE STUDIES OF THE NANOSCALE MECHANICAL PROPERTIES OF METAL-ORGANIC FRAMEWORK MATERIALS

ZHIXIN ZENG

Balliol College

July 2018

A dissertation submitted for the degree of Doctor of Philosophy

PREFACE

This dissertation is submitted for the degree of Doctor of Philosophy in the University of Oxford, U.K. The research described in this dissertation was carried out by the author in the period October 2014 to July 2018, under the supervision of Prof. Jin-Chong Tan, in the Department of Engineering Science at the University of Oxford.

To the best of my knowledge, the work described in this dissertation is original, except where due reference has been made to the work of others, and the work done in collaboration with others has not been included, except where noted. No part of this dissertation, or any similar to it, has been, or is currently being submitted for any degree at this, or any other university. This dissertation is less than 61,000 words in length.

Zhixin Zeng
Oxford
July, 2018

ABSTRACT

The nanoscale mechanical properties of metal-organic framework (MOF) materials including the elasticity (Young's modulus), plasticity (hardness, yield stress, ultimate strength, and work hardening coefficient), adhesion property (adhesive force and energy), and failure mechanisms (failure modes, corresponding threshold forces and failure strengths) have been studied in the range of sub-nm to ~100s nm in depth. MOF materials are a topical class of porous crystalline solids that are constructed from the self-assembly of metal clusters and organic linkers, to yield tuneable framework structures with a vast range of physical and chemical properties. Herein, three model MOF systems are of particular interest: the nanocrystals and micron-sized crystals of ZIF-8, two-dimensional nanosheets of CuBDC, and submillimetre-sized crystals of HKUST-1. The three MOF materials were prudently selected because they represent three distinctive structures in terms of the response to stress.

In this work, depth-sensing nanoindentation techniques, particularly the 'conventional' instrumented indentation technique (force sensitivity ~ 50 nN) and the atomic force microscopy (AFM)-based nanoindentation (force sensitivity < 0.05 nN), have been intensively employed and adapted to enable the accurate characterisation of the fine-scale mechanical behaviour of MOF materials. By leveraging the force and displacement sensitivities of the AFM instrument, the AFM-based nanoindentation method has been rationally established and improved by extending its application to study MOF mechanics at the nanoscale. This is a challenging field that has not yet been rigorously addressed by means of detailed experiments. Amongst the depth-sensing techniques, the AFM-based nanoindentation measurements are usually criticised for their instability and low reproducibility. Herein, the major factors that could interfere with the measurement precision have been systematically investigated. The research has led to the development of comprehensive approaches for AFM instrumental controls to achieve reliable force-displacement data and improved contact models for nanoindentation data analysis.

Quantification of the nanoscale mechanical properties sheds light on the complicated deformation behaviour of the porous MOF structures. AFM nanoindentation data obtained at the nanometre length scale reveal new structure-property information about the surface energy, incipient plasticity, and fracture mechanisms underpinning the inorganic-organic building blocks of MOF systems. Accurate materials data about mechanical performance and durability will be fundamental towards the development of functional devices and practical applications.

ACKNOWLEDGEMENTS

Firstly, I would like to express my sincere gratitude to my supervisor Prof. Jin-Chong Tan for the tremendous support provided during my DPhil study and for his patience, motivation, and erudition. At every stage of my research and thesis writing, his valuable guidance was not only very helpful during my DPhil period, but also greatly nurturing of my research ability for my future career development. I could never have imagined having a better supervisor and mentor for my DPhil study.

Besides my supervisor, I would like to thank my college (Balliol College), especially the officers Revd Canon Bruce Kinsey and Dr. Stacey McGowen, as well as the University for their generous supports. I am thankful to my college advisor, Prof. Dominic O'Brien, who gave me lots of help with the college grants for attending scientific conferences.

I acknowledge the provision of advanced materials characterisation facilities by the Research Complex at Harwell (RCaH), Rutherford Appleton Laboratory, and Diamond Light Source in the Harwell Science & Innovation Campus. I also need to thank Dr. Kalin Dragnevski and Marzena Tkaczyk for the help with the research instruments in the LIMA laboratory.

I am also grateful to Prof. John Huber for kindly allowing access to the AFM instrument and Prof. Steve Roberts for kindly allowing access to the MTS XP NanoIndenter.

I would also like to thank all my colleagues who are also my friends and companions in the Multifunctional Materials & Composites (MMC) Laboratory: (in chronological order of joining the group) Matthew, Mahdi, Abhijeet, Kirill, Yueting, Irina, Luke, Arun, Barbara.

Last but not the least, I would like to send my deepest gratitude to my parents and my sister, for their unconditional supports throughout my life. This thesis is dedicated to my family with love, without them none of this would have been accomplished.

TABLE OF CONTENTS

NOMENCLATURE

List of Symbols

Latin Symbols	Description
A	True contact area
A_{adhesion}	Projected area where the adhesion takes effect
$A_{\text{projected}}$	Projected contact area
Al	Aluminium
a	Hertz contact radius
C	Total compliance
C_{f}	Compliance of the load frame
c	Radius of the total stressed area in the DMT model
d	The counter-acting deformation imposed from a specific crystallographic orientation to the other crystal facets (for anisotropic materials)
E	Young's modulus
E_{indenter}	Young's modulus of an indenter
E_{eff}	Effective modulus, also known as reduced modulus
f	Frequency
G	Energy release rate
H	Hardness
h	Indentation depth or potential-related separation between two planar surfaces
h_{cell}	Characteristic (unit cell) length
$H_{\text{threshold}}$	Threshold depth at failure
h_{f}	Final depth after complete unloading
h_{max}	Maximum indentation depth
h_{unit}	Unit threshold depth
h_0	Initial separation between the two surfaces
$\dot{h}$	Displacement rate
$\overline{h}$	Normalised displacement

I	Indentation modulus
K	Bulk modulus
k	Spring constant or the coefficient of the Hollomon's equation
l	Side length of a crystal
m	Side length of an indenter (in the numerical simulation)
n	Effective height of an indenter (in the numerical simulation) or work hardening coefficient
nm	Nanometer
nN	Nano-newton
P	Loading force in a force-displacement curve
P_{ad}	Adhesive force
$P_{threshold}$	Threshold force leading to failure modes
$P_{interaction}$	Interaction force between adjacent nanosheets
P_{f}	Failure force
$P_{friction}$	Friction
$\overline{P}_{higher\text{-}bound}$	Normalised force at the higher bound of the linear regime in the adhesion map
$\overline{P}_{lower\text{-}bound}$	Normalised force at the lower bound of the linear regime in the adhesion map
P_{max}	Maximum loading force
$P_{pull\text{-}off}$	Pull-off force
$P_{surrounding}$	Force from the surrounding materials of nanosheets
P_{trans}	Transition pressure
P_{unit}	Unit threshold force
P'_{nx}	Resolved indentation forces in the plane of nanosheet surface
P-h	Force-displacement curve
$\overline{P}$-$\overline{h}$	Normalised force-displacement curve in the numerical simulation
$\dot{P}$	Loading rate
$\overline{P}$	Normalised force
p	Local pressure
pN	Pico-newton

R or r	AFM tip apex radius
$R_{contact}$	Radius of the projected contact area
R_{eff}	Effective radius of the two spheres in contact
S	Contact stiffness
S_{def}	Calibration of deflection sensitivity
S_x	Distance of the scratch in the instrumented scratch experiment
s	Displacement from the deepest point of an indenter or the height of a pile-up
s'	Slope of the linear regime in the adhesion map
T	Temperature
T_g	Glass transition temperature
T_m	Melting temperature
T_t	Transition temperature
T^*	Temperature constant
t	Thickness
V	Scan rate of the cantilever probe
V_a	Indenter approaching velocity
W	Tungsten
W_{ad}	Energy of adhesion (work of adhesion times contact area)
W_e	Elastic recovery
W_{el}	Elastic work
W_{pl}	Plastic work
Z_0	Separation in equilibrium between the indenter and the sample surface

Greek Symbols	**Descriptions**
α	Displacement from indentation experiment
α_{off}	Displacement at the most negative adhesion (*viz.* pull-off force) between the indenter and the sample surface
α_{zero}	Displacement at the point where the resultant force reaches zero
$\Delta\alpha$	Displacement between α_{off} and α_{zero}
β	Dimensionless correction factor
γ	Work of adhesion, also known as thermodynamic work of adhesion
$\gamma_{indenter}$	Surface energy of an indenter
$\gamma_{interfacial}$	Interfacial energy
γ_s	Surface energy
γ_{sample}	Surface energy of a sample
Δ	Cantilever deflection
ε	Length parameter representing the range of interaction
ε_p	Plastic strain
$\dot{\varepsilon}$	Unloading strain rate
$\dot{\varepsilon}_0$	Reference strain rate in the Johnson-Cook hardening model
$\bar{\varepsilon}^{pl}$	Equivalent plastic strain
η	Degree of work hardening
θ	Half of the included angle of an indenter
λ	Elasticity parameter
μ	Tabor's parameter
μm	Micrometer
μN	Micron-newton
ν	Poisson's ratio
$\nu_{indenter}$	Poisson's ratio of an indenter
σ	Stress
σ_f	Failure strength
σ_{sd}	Surface detachment stress
σ_{sf}	Engineering stress resulting in splitting fracture

σ_{unit}	Unit threshold stress at failure
σ_y	Yield stress
σ_0	Constant adhesive stress
σ^0	Static yield stress in the Johnson-Cook hardening model
Ω	Domain in the plane of the sample surface

List of Abbreviations

Acronyms	**Description**
ABAQUS	A software suite for finite-element analysis
AFM	Atomic force microscope
AgQRE	Silver wire as a quasi-reference electrode
AM-FM	Amplitude modulated-frequency modulated
Au	Gold
BECC	Bottom effect cone correction method
BET	Brunauer–Emmett–Teller surface area
B3LYP	Becke, three-parameter, Lee-Yang-Parr
BDC	1,4-Benzenedicarboxylate organic ligand
BTC	1,3,5-Benzentricarboxylate organic ligand
CFD	Computational fluid dynamic
CHDA	Trans-cyclohexane-1,4-dicarboxylate
COF	Covalent organic framework material
COS	Carpick-Ogletree-Salmeron model
CSD	Cambridge structural database
CSM	Continuous stiffness measurement
Cu	Copper
CuBDC	A type of metal-organic framework: CuBDC MOF (copper 1,4-benzenedicarboxylate)
DFT	Density functional theory
DMA	Dynamic mechanical analysis

DMF	*N*,*N*-dimethylformamide
DMT	Derjaguin-Muller-Toporov contact model
ECM	Extracellular matrices
FE	Finite-element modelling/method
FPOP	Triazine-based fluorinated organic polymer
HDPE	High density polyethylene
HKUST-1	A type of metal-organic framework: CuBTC MOF (copper 1,3,5-benzentricarboxylate)
IIT	Instrumented indentation techniques
INA	Isonicotinate
ISE	Indentation size effect
IST	Instrumented scratch technique
JKR	Johnson-Kendall-Roberts contact model
LDPE	Low density polyethylene
LiF	Lithium fluoride
LJ	Lennard-Jones potential
MD	Maugis-Dugdale model or molecular dynamics
MIL-53 (Al)	A type of metal-organic framework: aluminium terephthalate
MnDMS	A 2-D nonporous inorganic-organic framework: (manganese 2,2-dimethylsuccinate)
MOF	Metal-organic framework material
MON	Metal-organic nanosheet
MTS	MTS Nanoindenter® XP (a type of instrumented indenter)
mIM	2-Methylimidazolate organic ligand
NiO	Nickel(II) oxide
OP	Oliver and Pharr Model
PAA	Polyacrylic acid
PC	Polycarbonate
PCM	Pericelluar matrices
PDMS	Polydimethylsiloxane

P-h	Force-displacement (also known as load-deformation) data from an indentation experiment
pH	Potential of hydrogen
PMMA	Poly(methyl methacrylate)
PnBMA	Poly(n-butyl methacrylate)
PS	Polystyrene
PT	Piétrement and Troyon model
Pt	Platinum
PVA	Polyvinyl alcohol
PVC	Polyvinyl chloride
PXRD	Powder x-ray diffraction
QNM	Quantitative nanomechanical mapping
SEM	Scanning electron microscopy
Si	Silicon
SPM	Scanning probe microscopy
SSP	Successive search procedure
STP	Standard temperature and pressure
TEM	Transmission electron microscopy
TGA	Thermogravimetric analysis
TTS	Time-temperature superposition
UHMWPE	Ultrahigh molecular weight polyethylene
VSR	Virtual state relaxation method
WLF	Williams-Landell-Ferry
YAS-GNP	Hybrid coating of Y_2O_3-Al_2O_3-SiO_2 glass and graphene nanoplatelets
ZIFs	A subclass of metal-organic framework: zeolitic imidazolate frameworks
ZIF-8	A type of metal-organic framework: ZIF-8 MOF (zinc 2-methylimidazolate)
1-D	One-dimensional
2-D	Two-dimensional
3-D	Three-dimensional

Chapter 1: Introduction

*In this chapter, the motivation of the research, the structure of the thesis, the materials of interest, the methodology used and developed, as well as the main achievements are outlined for the convenience of readers to grasp the structure and key features of this thesis. In **Chapter 2** and **Chapter 3**, two comprehensive literature review chapters cover the status quo of the intriguing nanomaterials, namely the metal-organic frameworks (MOFs), summarising the prime characteristics. This is followed by an overview of the experimental techniques used to date to characterise the mechanical behaviour of MOFs. **Chapter 4** gives a detailed explanation of the experimental, analytical, and numerical approaches employed in my research. **Chapter 5** presents the AFM-based nanoindentation technique to characterise the nanoscale elasticity, plasticity and adhesion strength of the prototypical ZIF-8 nano- and micron-sized crystals. As a model material, ZIF-8 exhibits relatively low elastic anisotropy. Subsequently, an extended mechanical property investigation on the nanoscale failure modes of ZIF-8 is presented in **Chapter 6**. Further development of the established nanoindentation techniques have been made to quantify the fine-scale mechanical properties of two more complex MOF systems, which behave markedly different at the nanoscale, they are: the CuBDC nanosheets in **Chapter 7** and the auxetic HKUST-1 crystals in **Chapter 8**. The ultimate objective of the research is to develop reliable mechanical characterisation techniques along with the establishment of novel analysis tools to study the structure-property correlations of contemporary porous materials.*

1.1 Motivations

Further to the traditional applications of nanoporous materials, such as gas separations and storage, metal-organic frameworks (MOFs) as a type of hybrid organic-inorganic materials have potential applications in catalysis, energy production and transfer, photoluminescence, drug delivery, and electronics. The versatility of MOFs is evidenced from the myriad of framework architectures as depicted in Figure 1.1, which are constructed by connecting inorganic building units (e.g. transition metal cations) with multidentate organic linkers by strong bonds (i.e. coordination bonds) and synthesised *via* a broad range of processing routes.[1] One of the remarkable characteristics of MOFs is the exceedingly high inner surface area, which is normally in the range of 1,000 to 10,000 m^2/g.[2] This is complemented by a vast range of physical and chemical properties that can be rationally designed and tuned to afford technological applications.

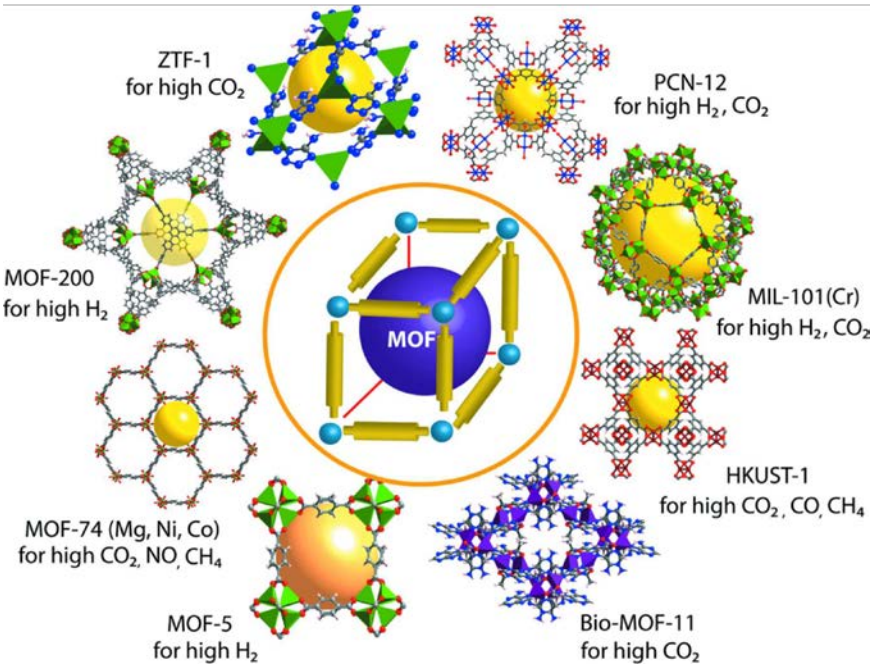

Figure 1.1 Schematic illustration of eight examples of MOF structures with excellent gas storage capacity. Reprinted from Ref. [3] with permission. Copyright (2014) International Union of Crystallography.

Although the study of MOFs has been ongoing for more than 20 years, the evolution of innovative MOF architectures and the discovery of novel applications are steadily increasing in the literature.[4] As summarised in Figure 1.2, MOF-derived nanostructures have been representing the cutting-edge of nanomaterials science in the last decade.

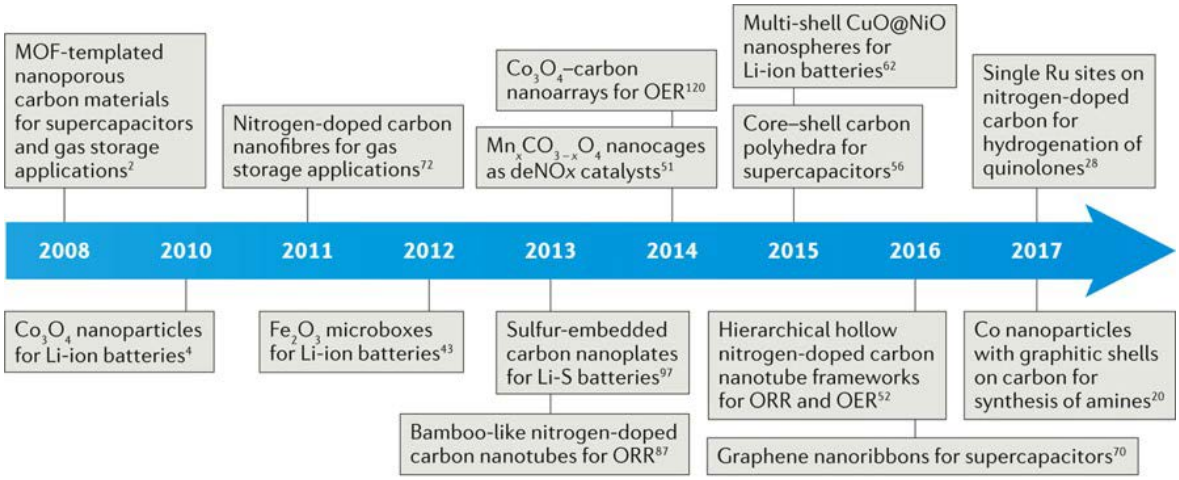

Figure 1.2 Timeline of representative innovations of MOF-derived nanostructures. Reprinted with permission from Ref. [4]. Copyright (2017) Springer Nature.

1.2 Research Objectives

In spite of the breakthroughs from the standpoint of chemistry, the structural stability and the detailed nanomechanical characteristics of MOFs are substantially less well understood, not to mention the decisive effect of mechanical properties on the long-term durability and functional performance of these porous nanomaterials. A good example is their application in hydrogen storage, the capacity of which is directly associated with the active surface area at 77 K and 10-90 bar.[5-6] The persistent inner surface area is determined by the nanomechanical property of the framework such as the stiffness and hardness of the open framework, which will dictate whether the accessible porosity can last under a certain level of pressure or indeed to survive multicyclic adsorption and release processes.

Since MOFs are crystalline materials, the position of the constituent components is well-organised, thus the correlation between structure and property can be quantified at very high accuracy using established techniques such as X-ray and neutron diffraction. On the contrary, the nanomechanical characterisation tools available today to probe the mechanical behaviour of MOFs are less developed. In order to investigate their mechanical resilience and structural robustness, in this thesis, I have dedicated the work to study the different nanomechanical properties of MOFs, encompassing the elasticity, plasticity, anisotropy, adhesion strength, and to unravel the underpinning mechanisms behind nanoscale failure modes and fracture phenomena.

1.3 Structure of the Thesis

As summarised in the flow chart in Figure 1.3, my research focuses on the quantification of the nanomechanical properties of porous MOF materials for the purpose of identifying their functionality and applicability under specific loading conditions. The mechanical characterisation experiments were mainly performed using depth-sensing techniques, especially the atomic force microscopy (AFM)-based nanoindentation due to its unparalleled force and spatial detection sensitivities. Although the major interest lies in material behaviour at the nanoscale, complementary experiments have also been performed to investigate the microscale mechanical properties. The goal was to correlate the nanoscale and the larger scale properties since the latter is pertinent to the practical uses of MOFs.

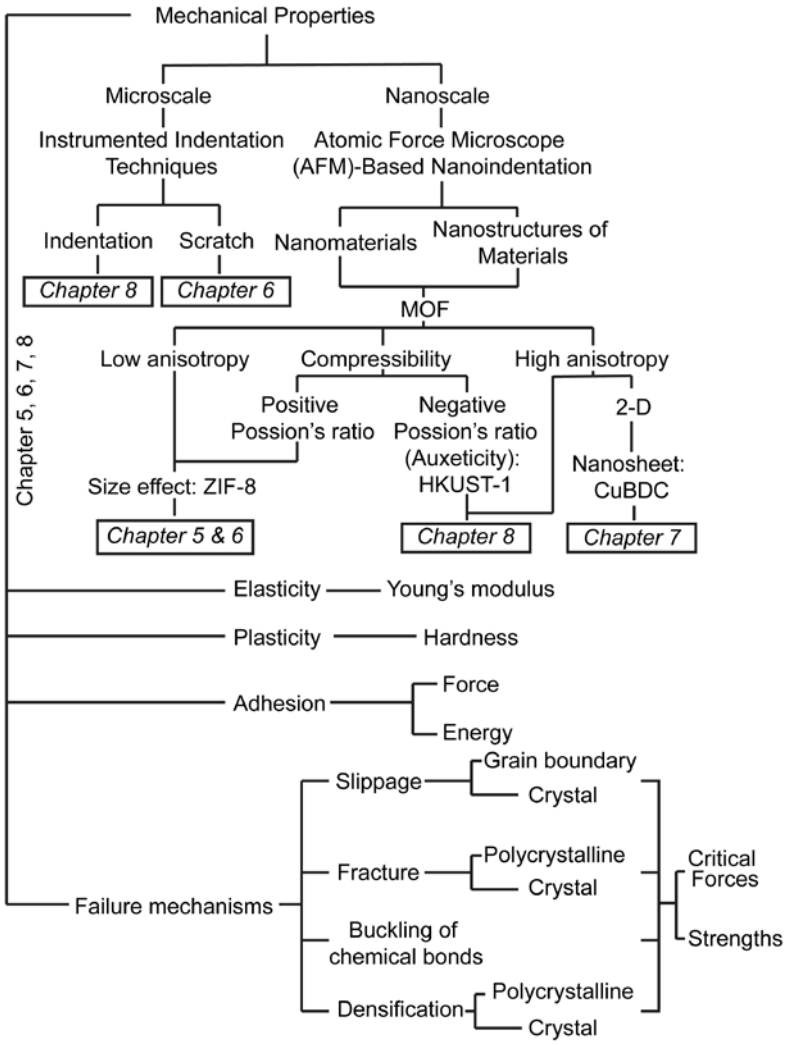

Figure 1.3 A flow chart outlines the structure of research contents in the thesis

In the two literature review chapters (Chapter 2 and Chapter 3), there are five subsections for each that provide an inclusive summary of relevant research works in the field. Chapter 2 starts with the introduction of MOFs in terms of the history of research, their structures, applications, advantages/limitations, and the need for accurate quantification of their nanomechanical properties. The second subsection briefly explains the three MOF systems studied in my thesis. The third subsection summarises the relevant experimental and computational approaches in the field of MOF mechanics. The fourth subsection introduces the limited available research on the failure modes of MOFs. Finally, the previous studies related to 2-D MOF materials are discussed.

Chapter 3 begins with the explanation of a typical atomic force microscope (AFM) apparatus in terms of its basic operating principles and technical specifications. The main advantages of AFM are then summarised, followed by five representative example applications. The most frequently measured properties by AFM nanoindentation are described, encompassing elasticity and plasticity, specifically, elastic modulus and hardness. The subsequent subsection emphasises the key factors to be considered during indentation experiment for accurate determination of mechanical properties. To conclude this chapter, the applicability of the contact models commonly used in the literature are elucidated.

In the materials and methods chapter (Chapter 4), the following experimental methods are presented: syntheses of the three MOF materials studied in the thesis (ZIF-8 micron- and nano-sized crystals, CuBDC nanosheets, and HKUST-1 submillimetre-sized crystals), the topography characterisation techniques including the AFM imaging (including the geometrical characterisation of the cube-corner indenter tip used in the AFM-based nanoindentation), electron microscopy imaging, and optical imaging, followed by the X-ray diffraction technique to confirm the crystalline structure. Subsequently, details are given on the configurations of the mechanical quantification experiments by employing the

instrumented indentation technique (IIT), instrumented scratch technique (IST) and AFM-based nanoindentation approach. Chapter 4 concludes with a concise overview of the contact models implemented in the thesis, namely: the adhesion model based on Sneddon method (Chapter 5), Oliver and Pharr (OP) method (Chapter 5, 7, 8), unloading strain rate principle to remedy the OP method (Chapter 5, 7, 8), Lennard-Jones potential (Chapter 8), Derjaguin's approximation (Chapter 8), Carpick-Ogletree-Salmeron (COS) and Piétrement-Troyon (PT) methods (Chapter 8), as well as the numerical simulation method (Chapter 8). Thereafter, the finite-element (FE) method employed in Chapter 7 and Chapter 8 was briefly introduced. In the end, the programming languages implemented in the thesis to process the huge amount of data from experiments and theoretical calculations are concisely explained.

Chapter 5 is the first results chapter wherein the AFM-based nanoindentation technique (at shallow indentation depth of ~10s nm) is established for quantifying the nanomechanical properties of ZIF-8 crystals (E_{max} ~ 3.8 GPa and E_{min} ~ 2.8 GPa).[7] The ZIF-8 samples studied are in two forms: polycrystalline thin-film coatings composed of nanocrystals and the standalone micron-sized crystals. Through the AFM technique development, the Young's modulus (E ~ 3–4 GPa) and hardness (H ~ 500 MPa) of these ZIF-8 crystals have been measured with excellent accuracy. Herein, an adhesion model on the basis of the Sneddon method has been enhanced to calculate the adhesion energy (γ ~0.42–3.31 J/m^2), and to minimise the unwanted effect of adhesive force on the measurement of E.

Chapter 6 is the second results chapter wherein the application of the AFM-based nanoindentation technique is extended to probe the interfacial and fracture strengths of both polycrystalline thin-film coatings and individual crystals of ZIF-8. For the thin-film coatings made from nanocrystals of ZIF-8, the failure modes proposed are: shear-induced grain

boundary slippage (interfacial strength up to 3.5 GPa), polycrystalline fracture (strength up to 1 GPa), cumulative material compaction, and continuous buckling of chemical bonds. Four similar failure modes for the individual ZIF-8 micron-sized crystals are proposed. But instead of revealing the interparticle behaviour, the failure modes of a single crystal induced by the indenter tip reveal plausible deformation patterns of the metal-linker-metal linkages in the ZIF-8 framework. It is worth noting that upon sample failure, the indentation could be significantly deeper than the one without failures (Chapter 5) thus resulting in an erroneously low value of Young's modulus and hardness.

Chapter 7 is the third results chapter wherein the AFM-based nanoindentation is applied to explore nanomechanical behaviour of 2-D MOF nanosheets, termed CuBDC. Building upon the established techniques demonstrated in the last two results chapters, the Young's modulus (E ~23 GPa) and hardness (H ~2 GPa) of CuBDC have been measured in the through-thickness direction. Furthermore, an iteration approach has been developed to deduce the yield stress (σ_y ~448 MPa), with which, the ultimate strength (σ_u ~674 MPa) of CuBDC was estimated. In the course of analysing the plastic deformation and failure mechanisms, a finite-element (FE) model was formulated to help interpret data from the AFM nanoindentation experiment. The nature of the interlayer interactions and displacements between adjacent monolayers was then studied, where the failure modes of stacks of CuBDC nanosheets (thickness t ~ 2–400 nm, bound together by van de Waals forces) have been characterised. This was possible using the AFM probe because small forces can be sensed by the AFM instrument rather than the IIT. It was found that the failure modes of CuBDC nanosheets include: slippage of monolayers, interlayer fracture, and delamination of nanosheets. The threshold indentation forces and corresponding depths leading to these failure modes have been quantified as: 42.6 nN (6.47 Å), 70.4 nN (6.35 Å), and 56.0 nN (5.80 Å), respectively.

Chapter 8 is the fourth results chapter, in which there is an in-depth investigation on the applicability of the AFM-based nanoindentation technique to measure the highly anisotropic crystal of HKUST-1. It was previously predicted by density functional theory (DFT) that HKUST-1 may exhibit a negative Poisson's ratio (*viz.* auxeticity) along the [110] crystallographic axis.[8] The size of the HKUST-1 crystals tested here was of the order of 100s μm. These relatively large crystals were necessary to allow IIT measurements at microscales, and the results of which were compared to the AFM nanoindentation at the nanoscale. The effect of crystal anisotropy was characterised using a combination of experimental, analytical and numerical methods, and found to be in good agreement with the DFT calculations. Similar to the above three results chapters, I have identified distinctive failure modes of HKUST-1: slippage along the aligned porosity, framework fracture, porous framework densification, buckling and recovery of bonds. The corresponding failure strengths of the failure modes have been determined, and found to be relatively higher than that of the 2-D structures in Chapter 7. Finally, the work also led to the demonstration of the novel "nanoscale tensile test" approach developed in the chapter as a means of investigating the adhesion properties of relatively soft matter at the nanoscale.

In Chapter 9, the significance of the nanoscale mechanical studies on MOFs as well as the characterised mechanical properties of the three MOF systems are summarised. Subsequently, the foreseeable future work is included. It is envisaged that the nanomechanical characterisation techniques and data analysis tools developed in this thesis will be useful for the study of other families of nanomaterials and hybrid systems.

Chapter 2: MOFs and Studies on Their Mechanical Properties

Amongst a variety of nanomaterials, metal-organic frameworks (MOFs) have continuously attracted intense attention of researchers due to their crystalline porous architecture and strongly correlated structure-property relations found at the nanoscale. This chapter begins with a general overview of the main structural features of MOF materials, before focusing on the recent reports pertaining to the characterisation of their mechanical properties, especially the Young's modulus, hardness and failure modes. This review chapter has been divided into five sections: (a) history of the discovery and typical structures of MOFs; (b) chemical structures of the three MOF systems investigated in this thesis; (c) complementary techniques reported for quantifying the mechanical properties of MOFs; (d) identification of the failure modes of MOFs; and (e) investigation of 2-D MOF structures.

2.1 Metal-Organic Framework (MOF) Materials

MOFs are crystalline hybrid (inorganic-organic) compounds, constructed from the self-assembly of metal clusters and organic linkers to yield porous framework structures exhibiting tuneable physical and chemical properties.[9-10] Ever since the term metal-organic framework (MOF) was proposed in 1995,[11] the exploration and advance towards real life applications have gone through a rapid development in the field.[2] To date, there are more than 69,000 MOF structures stored in the Cambridge Structural Database (CSD) and more than 6,000 new MOFs are published per year.[12] While MOF materials may no longer be considered as a new class of nanomaterials, the novelty has never diminished because the newly designed and synthesised MOF structures have continued to attract a great deal of attention from the scientific and technological communities.[4]

Several topical families of MOF materials are currently under intense study, encompassing zeolitic imidazolate frameworks (ZIFs),[13] zirconium-based UiOs[14] and MIL-140s,[15] a vast variety of carboxylate-based MOFs[16] (e.g. MILs,[17] HKUST-1,[8] and MOF-74s[18]) and isoreticular frameworks (IRMOFs).[19] There is considerable interest in the development of high-performance MOFs targeting gas separations and storage applications,

catalysis,[20-26] and with more recent emphasis shifting towards technological device applications for optoelectronics, low-*k* dielectrics, chemical sensors, energy converters, photoluminescence, guest (e.g. drug molecule) delivery, and electronics.[27-34]

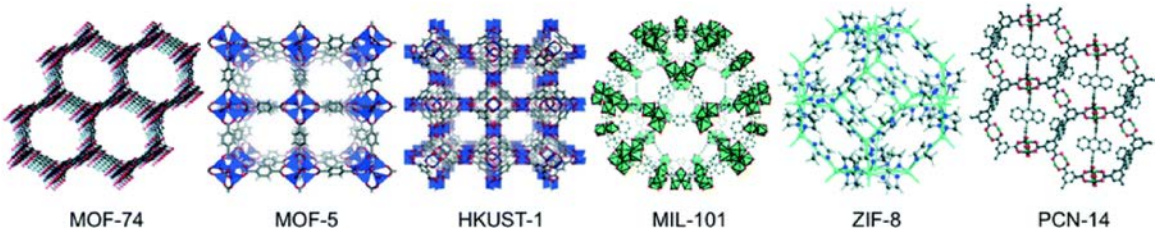

Figure 2.1 Crystallographic structures of six topical MOFs. Reproduced from Ref. [6] with permission from The Royal Society of Chemistry.

Several representative MOF structures are presented in Figure 2.1. Notably, MOFs exhibit a vast range of structural and chemical variability since their crystalline nanoporous structures are constructed by connecting different combinations of organic and inorganic building blocks *via* coordination bonds (bond energy shown in Figure 2.2). There is huge possibility to tune the geometry, pore size and surface area, physicochemical properties, and to yield host-guest composite systems by encapsulating functional guest molecules.[4, 35-36] The inorganic building blocks that are generally transition metal cations or clusters differentiate MOFs from the covalent organic frameworks (COFs), which are also a class of porous polymeric materials but usually with lower crystallinity. A myriad of organic building blocks, also known as organic ligands or linkers, can be selectively adopted to construct MOFs and a number of examples are presented in Figure 2.3.

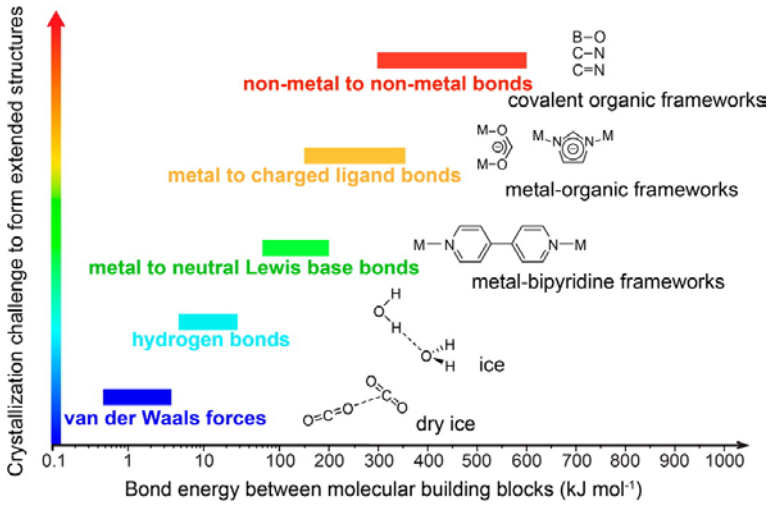

Figure 2.2 Energy levels of different bonds between the molecular building blocks. Reprinted with permission from Ref. [37]. Copyright (2016) American Chemical Society.

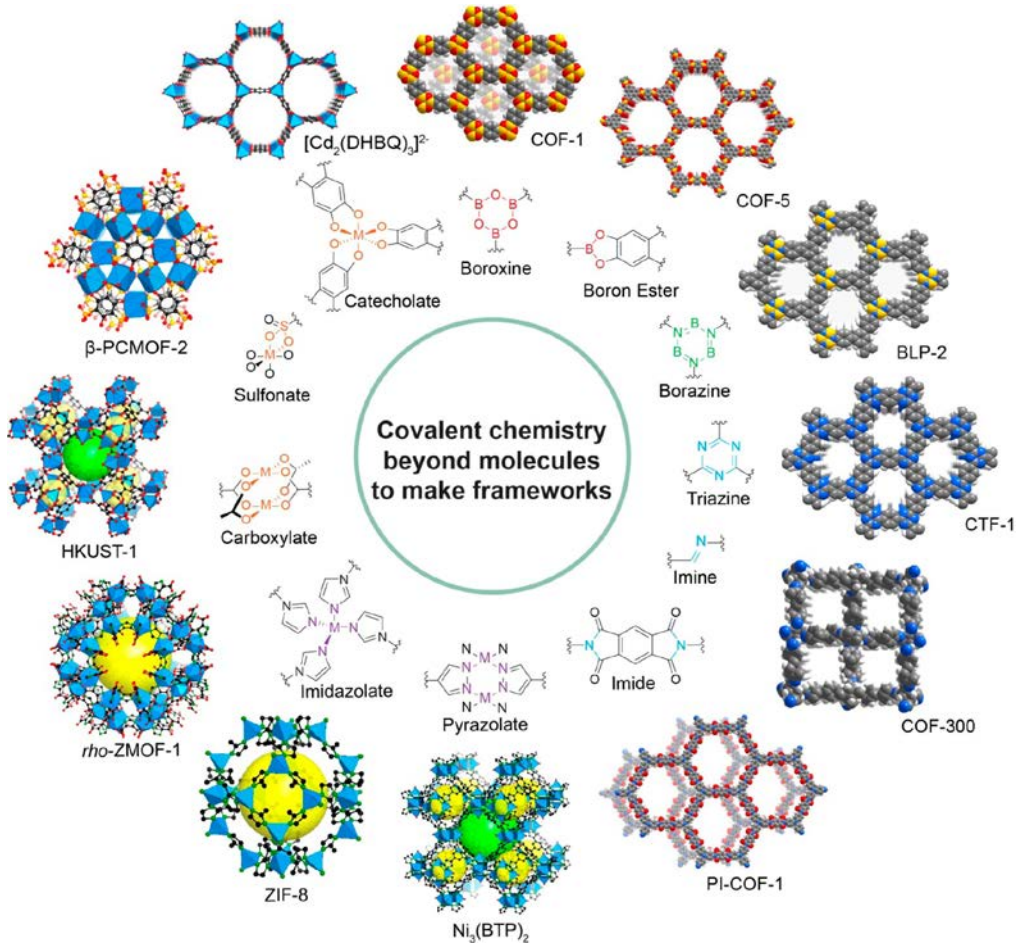

Figure 2.3 Inner ring: the coordination environment of the metal cations and the organic functional groups. Outer ring: MOFs and COFs constructed. Reprinted with permission from Ref. [37]. Copyright (2016) American Chemical Society.

In contrast to the major developments witnessed in the chemistry and functional properties of MOFs, the study of the nanoscale mechanical behaviour of MOFs is relatively scarce. Understanding the mechanical properties and structural durability of MOFs is central to the scale up and implementation of MOFs for real world applications.[35, 38-39] For this reason, in this research I concentrate on the development of novel nanoindentation methodologies (Chapter 4) that will allow accurate quantification of the mechanical behaviour of MOF materials at the nanoscale.

2.2 The Three MOF Materials Studied in the Thesis

2.2.1 Zeolitic Imidazolate Framework-8 (ZIF-8) Crystals

ZIF-8 [Zn(2-methylimidazolate)$_2$] is composed of tetrahedrally-coordinated zinc cations (ZnN_4) linked by 2-methylimidazolate ligands, as depicted in Figure 2.4. ZIF-8 crystallises in the cubic space group $I\bar{4}3m$. It has porous sodalite framework architecture, which is topologically isomorphic with (inorganic) zeolites. ZIF-8 possesses a high surface area of ~1630 m^2/g [Brunauer–Emmett–Teller (BET) model] and the corresponding pore volume could be as large as ~0.636 cm^3/g.[40] ZIF-8 exhibits a small degree of elastic anisotropy and has an exceedingly low shear modulus of ~1 GPa compared with zeolites whose shear moduli are normally ranging from ~15 GPa to ~50 GPa,[41] even though the value as low as 3.7 GPa was reported in Ref.[42].[7] It is an excellent candidate material with good water stability due to its hydrophobicity,[43] it may also serve as the scaffolding cages for hosting functional guest molecules by encapsulation to yield unconventional properties.[44]

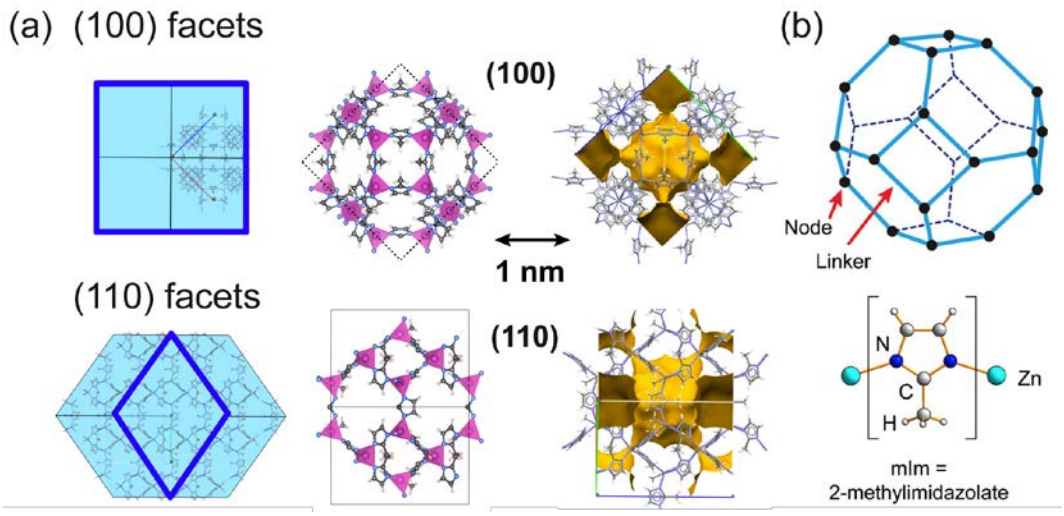

Figure 2.4 (a) Porous crystalline framework architecture of ZIF-8, where the purple tetrahedron represents the ZnN_4 coordination environment connected by the 2-methylimidazolate (mIm) organic ligands; (right) the yellow surfaces designate the solvent accessible volume (porosity) in a cubic unit cell of ZIF-8 viewed down the [100]- and [110]-axes, respectively. Note that the solvent accessible volume is volume occupied by a number of spherical probes, i.e. the union of atom balls whose radii are 1.2 Å. (b) (top) The sodalite structure of ZIF-8, in which the ZnN_4 is situated at the nodes and the mIm ligands is represented by the bars. (b) is reprinted with permission from Ref. [45]. Copyright (2010) National Academy of Science.

I have tested ZIF-8 crystals of two different sizes: nanoscale (<500 nm) and microscale (~2 μm). The synthesis methods are described in §4.1.1. As an important step of the synthesis, size control of ZIF-8 crystals relies on the change of the relative reactants molar ratios, mixing procedures, reaction conditions, and reaction duration. Figure 2.5 illustrates the morphology evolution of a ZIF-8 crystal with respect to the reaction time.[46] More comprehensive synthesis methods of ZIF-8 crystals together with the X-ray diffraction pattern of the micron-sized ZIF-8 crystals can be found in Ref. [47].

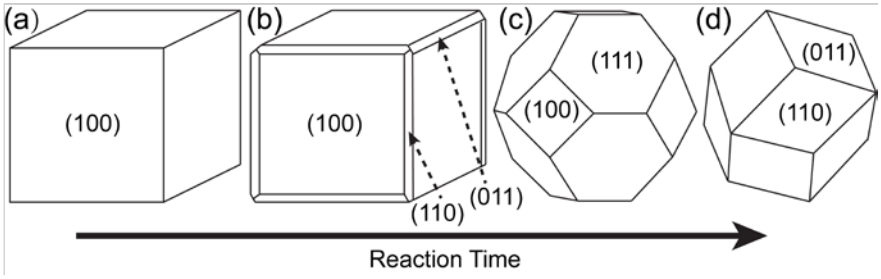

Figure 2.5 Schematic illustration of the typical morphology evolution of a ZIF-8 crystal versus reaction time. Adapted from Ref. [46].

2.2.2 Copper 1,4-Benzenedicarboxylate (CuBDC) Lamellae

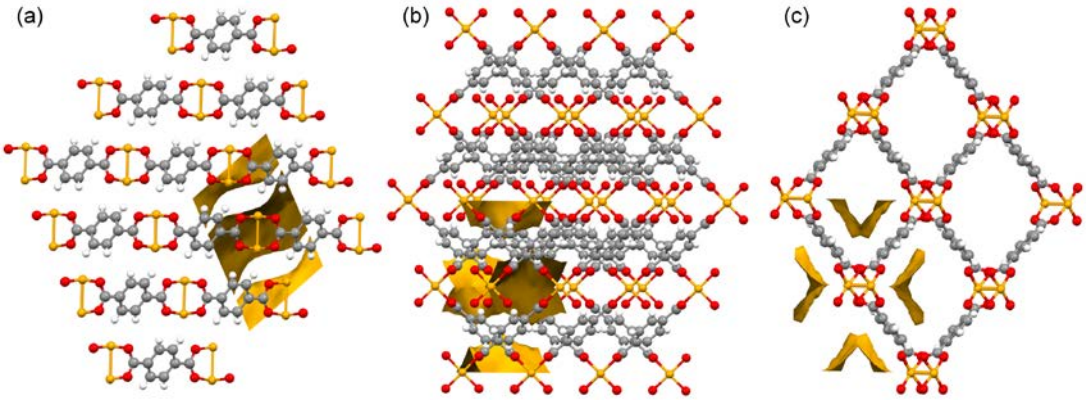

Figure 2.6 Crystalline framework structure of CuBDC, where the yellow atom represents the copper centres coordinated by the terephthalate organic ligands; the yellow surfaces designate the solvent accessible volume (porosity). The crystallographic structure (a) viewed down the [010]-axis, thus showing the stacking direction; (b) viewed down along the $[\bar{2}01]$-axis; (c) viewed down the pore channel, respectively.

CuBDC (BDC = 1,4-benzenedicarboxylate) is constructed by connecting the square-pyramidal copper centre formed by the square-planar Cu(II) dimers with the 1,4-benzenedicarboxylate ligands.[48] CuBDC crystallises in the monoclinic space group *C*2/*m*. It has a 2-D layered crystalline structure, wherein the components stack along the $(\bar{2}01)$ crystallographic orientation.[49] The layered architecture suggests the promise of using such a material to selectively adsorb and separate gaseous molecules. For instance, the composite mixed-matrix membrane formed by integrating the CuBDC nanosheet with the polyimide matrix exhibits superior performance in separating CO_2 from its mixture with methane.[49] The synthesis route of the CuBDC nanosheets is described in §4.1.2.

2.2.3 Copper Benzene-1,3,5-tricarboxylate (CuBTC) Crystals or HKUST-1

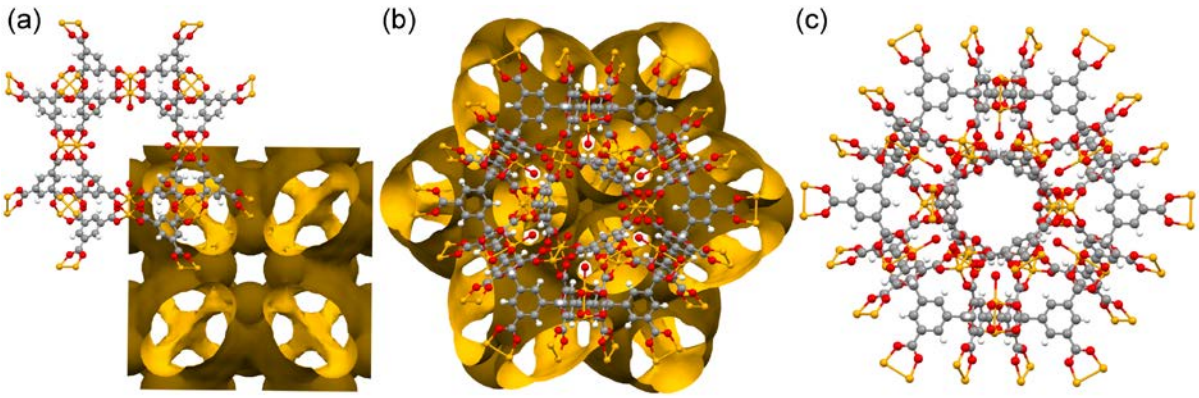

Figure 2.7 Porous crystalline framework architecture of CuBTC, where the yellow atom represents the copper paddlewheel cluster interconnected with the benzene-1,3,5-tricarboxylate organic ligands; the yellow surfaces designate the solvent accessible volume (porosity). The crystallographic structure viewed down the (a) [100]-axis and (b-c) [111]-axis, respectively.

$Cu_3(BTC)_2$ (BTC = 1,3,5-benzentricarboxylate), also known as HKUST-1, comprises square Cu(II) paddlewheel clusters coordinated with BTC linkers.[50] CuBTC crystallises in the cubic space group $Fm\bar{3}m$. The reported surface area of HKUST-1 ranges from 1500 to 2100 m^2/g (BET model). According to the calculation from the *ab initio* density functional theory (DFT), the HKUST-1 crystal is predicted to exhibit negative Poisson's ratio (auxeticity) associated with its elastic anisotropy,[8] while experiments have already confirmed that it has a negative thermal expansion.[51] Regarding its auxetic behaviour, DFT reveals that HKUST-1 may show a negative Poisson's ratio ($\nu = -0.3$) along the [110]-axis. There are a multitude of applications of HKUST-1, such as preferential adsorption useful for the separations of gas molecules,[52-54] storage of energy molecules,[55] electronics[56] and so forth.

Through adding modulators such as nitric acid[57] and acetic acid[58], the deprotonation of the organic ligand H_3BTC can be inhibited, and thus allowing the growth of large HKUST-1 crystals (~1.5 mm can be achieved). A good example is the micron-sized

HKUST-1 crystals synthesised using a microwave-assist method.[59] In this method, the monocarboxylic acid, i.e. lauric acid, acting as the modulator to perturb the coordination between the Cu(II) cations and 1,3,5-benzentricarboxylate organic ligands so as to attain the directional growth habit.[59] The following Figure 2.8 displays the SEM images of the crystals derived from this method.

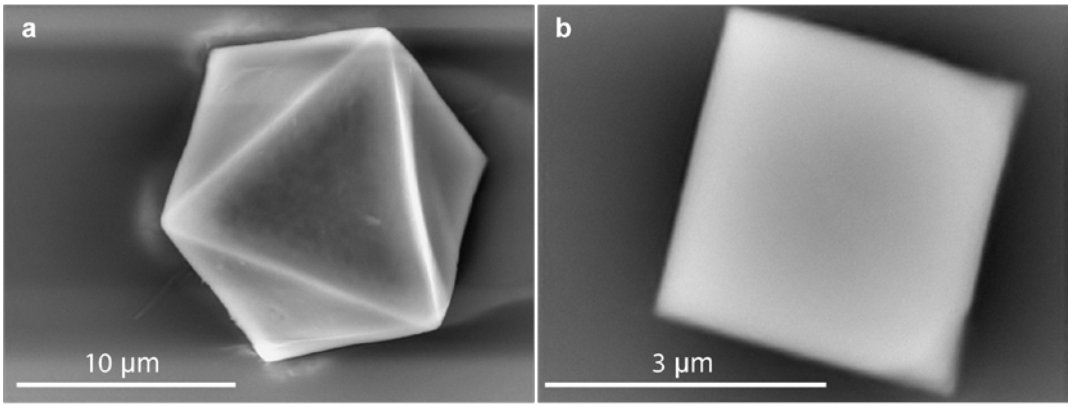

Figure 2.8 SEM images (collected in this work) using the Hitachi TM3030Plus tabletop microscope. Top view of the HKUST-1 crystals normal to the (a) {111}-oriented facet and (b) {100}-oriented facet. It is clear that the (100) and (111) crystallographic orientations can be confirmed by using the software Mercury CSD to predict the crystal morphology.[60] Note that these are the smaller version of the HKUST-1 crystals that were not studied in the thesis.

However, in this thesis, instead of using lauric acid, the glacial acetic acid (the synthesis approach introduced in §4.1.3) was chosen. The synthesis method was proposed by Tovar *et al.*, who characterised the crystal morphology and single-crystal X-ray diffraction pattern as shown in Figure 2.9.[58] The reason for using acetic acid is that the synthesised submillimetre-sized HKUST-1 crystals are larger, in fact about two orders of magnitude greater than the ones in Figure 2.8. Submillimetre-sized HKUST-1 crystals are preferred in this study, with the view of minimising the influence of the confinement from the cured epoxy resin used to mount the crystals for the nanoindentation experiments (§8.2)

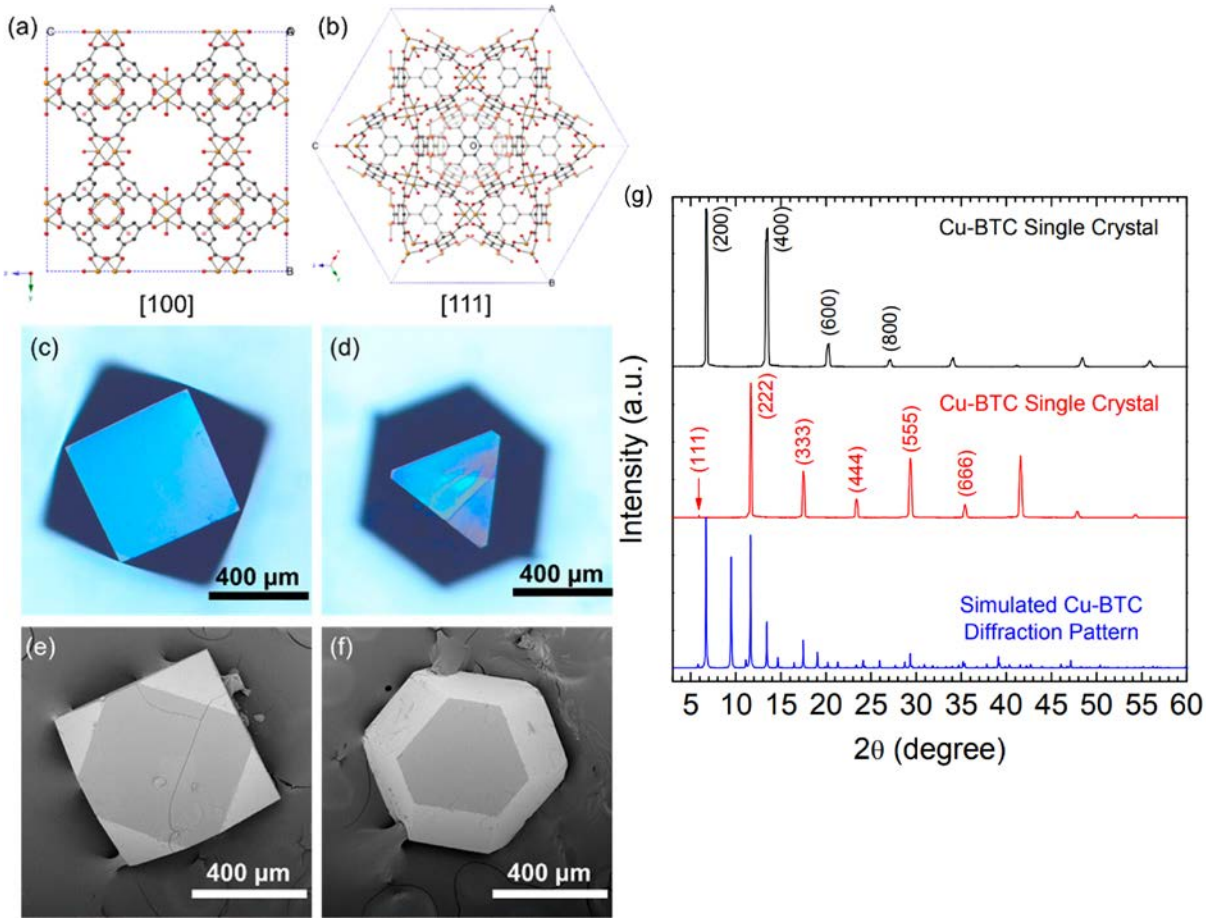

Figure 2.9 Crystal morphologies of HKUST-1 along the (a) [100]- and (b) [111]-axes. Cu (yellow), O (red), C (black), and H (not shown). Optical images of HKUST-1 along the (c) [100]- and (d) [111]-axes. SEM images of HKUST-1 along the (c) [100]- and (d) [111]-axes. (g) X-ray diffraction pattern of a single crystal of HKUST-1 (100) plane (black) and (111) plane (red). The simulated diffraction pattern is shown in blue. Reprinted from Ref. [58] with permission. Copyright (2016) American Chemical Society.

2.3 Characterisation of the Elastic-Plastic Properties of MOFs

There are many challenges surrounding the translation of basic research from the laboratory to the industry to achieve commercial applications.[61] Accurate characterization of the mechanical properties of emergent functional materials, such as metal-organic frameworks (MOFs), therefore is central towards the engineering of practical applications.[6, 38, 62]

Design, fabrication and deployment of the foregoing applications will depend on the availability of comprehensive mechanical properties information, plus a detailed understanding of the underpinning MOF mechanics which remains lacking in the literature.[38, 63] There is, however, a growing body of work adopting theoretical methodologies, such as density functional theory (DFT) to compute the full set of elastic constants of an ideal MOF crystal,[64-67] and by implementation of group theory,[68] to enable systematic studies of the structural flexibility of MOFs. Likewise, molecular dynamics (MD)[69-70] and density functional theory (DFT)[71] calculations have been used to interrogate the possible mechanisms that could be accommodating (irreversible) plastic deformation beyond the elastic regime.

On the contrary, experimental methods for studying the mechanical properties of MOF crystals are far less established. To measure the Young's modulus (E) and hardness (H) properties, the MOF and crystal engineering community thus far has relied on the instrumented nanoindentation technique (for example, see Refs. [45, 72-75]), which requires access to a "large" single crystal of at least ~100 μm across.[76] Unfortunately, this is typically not feasible *via* most MOF synthesis routes,[77] where sub-micron sized crystals of the order of ~100 nm or polycrystalline powders are commonplace; such fine crystalline samples are not appropriate for conventional nanoindentation studies. For situations where only sub-micron crystals are achievable, nanoindentation experiments have been attempted on μm-thick polycrystalline MOF films and coatings,[78-79] but these results are less quantitative because the indentation measurements are affected by the bulk substrate underneath (causing E and H values to artificially rise with indentation depth, see for example Ref. [80]). Nanoscratch experiments have also been demonstrated for the characterization of the adhesion behaviour of polycrystalline MOF films, again the data obtained so far are semi-quantitative.[81-82]

The objective for characterising the mechanical properties of MOFs is to understand their behaviours under specific loading conditions in terms of their different structural designs, chemical topology, unit building cells, and packing schemes. On this basis, Tan and Cheetham[38] have proposed a mechanical properties selection chart (Figure 2.10) showing how the elastic modulus and hardness of porous MOFs and dense hybrid crystals are compared with the conventional engineering materials – metals, ceramics, and polymers. The mechanical study of MOFs requires sufficient awareness of the localised properties since MOFs possess small pores ranging from 4 Å to 48 Å.[83-84] Accurate characterisation of the local mechanical response will therefore necessitate the application of a combination of experimental tools and theoretical methodologies presented in the section below.

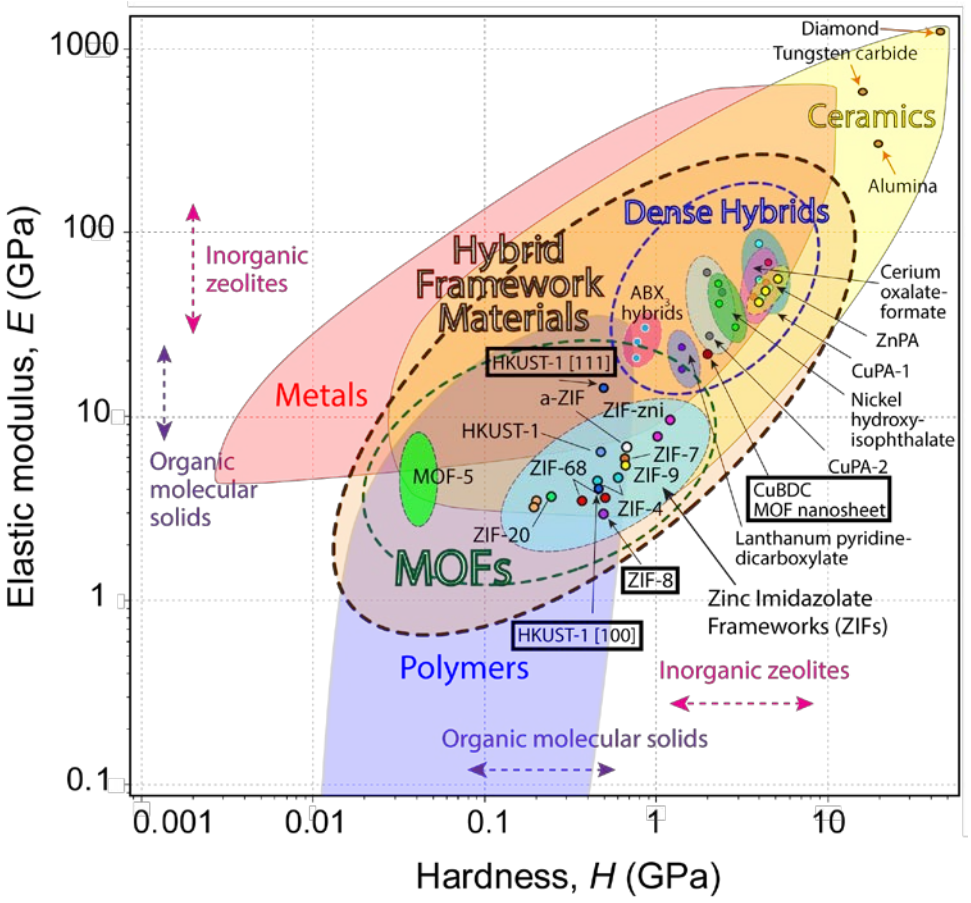

Figure 2.10 Materials property map of the elastic modulus as a function of hardness for the comparison of nanoporous MOFs with the dense hybrids, polymers, metals, and ceramics. The three MOF systems studied in the thesis are labelled. Adapted from Ref. [38] with permission from The Royal Society of Chemistry.

2.3.1 Experimental Approaches to Probe Fine-Scale Mechanical Behaviour

2.3.1.1 Depth-Sensing Nanoindentation Techniques

Depth-sensing techniques such as indentation are still the chief approach to characterise the mechanical properties of a small volume of material and of a thin structure. By far, the majority of important investigations on MOFs were achieved by employing instrumented indentation techniques (IIT). The commercial IIT instruments include the MTS Nanoindenter® (Agilent),[45] G200 Nanoindenter® (Agilent),[85] TriboIndenter® (Hysitron),[86-87] and Knoxville nanoindenter.[88]

Amongst these IIT techniques, single-crystal nanoindentation has been demonstrated as an effective technique to probe the mechanical properties including the elastic and plastic anisotropy of submillimetre-sized MOFs.[89] Through applying a directional compressive strain, the stiffness of the chemical structure along different orientations can be measured. For instance, Tan *et al.* successfully characterised the anisotropic mechanical properties of a series of hybrid inorganic-organic framework materials.[90] These hybrid frameworks are usually less porous and thus denser than MOFs. Moreover, Tan and co-workers quantitatively studied the elastic anisotropy of a 2-D inorganic-organic framework MnDMS [Mn 2,2-dimethylsuccinate] nanosheet stacks (i.e. bulk MnDMS crystals before being exfoliated into thin nanosheets) by conducting the single-crystal nanoindentation to 1 μm penetration depth.[91] Unlike the CuBDC MOF nanosheet (in Chapter 7), the MnDMS is a dense hybrid framework. The nanoindentation tests were conducted on three different crystallographic orientations (see Figure 2.11), i.e. the {001}-, {010}-, and {100}-oriented facets, and showing appreciable differences of the directional Young's moduli: 9.4 ± 0.3, 20.9 ± 0.2, and 13.6 ± 0.2 (in GPa), respectively. In addition, a systematic study of seven zeolitic imidazolate frameworks (ZIFs) has been reported by Tan *et al.* where the ZIFs crystals (diameter ~ 100 μm) were indented down to 1 μm depth. The Young's moduli and

hardness of these ZIFs that represent five different network topologies have been shown to be correlated to the framework density and porosity.[45]

Apart from the IIT techniques, the multifrequency atomic force microscopy under the amplitude modulated-frequency modulated (AM-FM) mode has also been adopted to measure the Young's moduli of MOF nanoparticles. The AM mode is applied for topographic imaging whereas the FM mode can be used to derive the sample mechanical properties. For instance, this technique has been used to measure the elastic moduli of HKUST-1 coatings[92] and of UiO-66(Zr) powder nanocrystals[93]. Nevertheless, the measurement of Young's modulus is usually not accurate enough.

Besides, the use of the PeakForce^{TM} quantitative nanomechanical mapping (QNM) technique can also be employed for measuring the elastic modulus and adhesion strength of materials as evaluated by Young *et al.* for a range of polymers[94] and by Smolyakov *et al.* on the textured chitin-silica hybrid films[95]. The manufacturer of the instrument claims that this technique can measure Young's moduli in the range of ~1 MPa to >20 GPa. However, given that the derivation of Young's modulus and adhesion strength adopted by this technique is based on the DMT model (§3.5.4), thus the scope of application of the DMT model also restricts the applicability of the PeakForce^{TM} technique. For example, the DMT model is normally suitable for the study of stiff samples with low but long-range adhesive forces. Additionally, there are also difficulties when the elastic modulus of the sample is significantly different from the calibration one.[94]

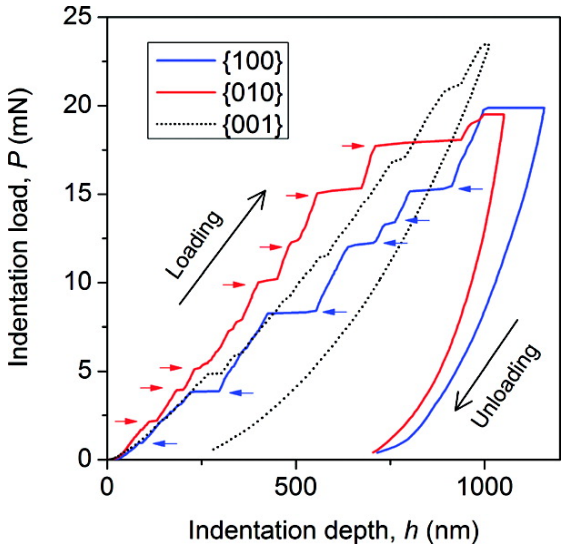

Figure 2.11 Representative force-displacement (*P*-*h*) curves from the instrumented nanoindentation experiment of single orthorhombic crystals of MnDMS along the three principal directions. The pop-in phenomena are indicated. Reprint from Ref. [91] with permission. Copyright (2012) American Chemical Society.

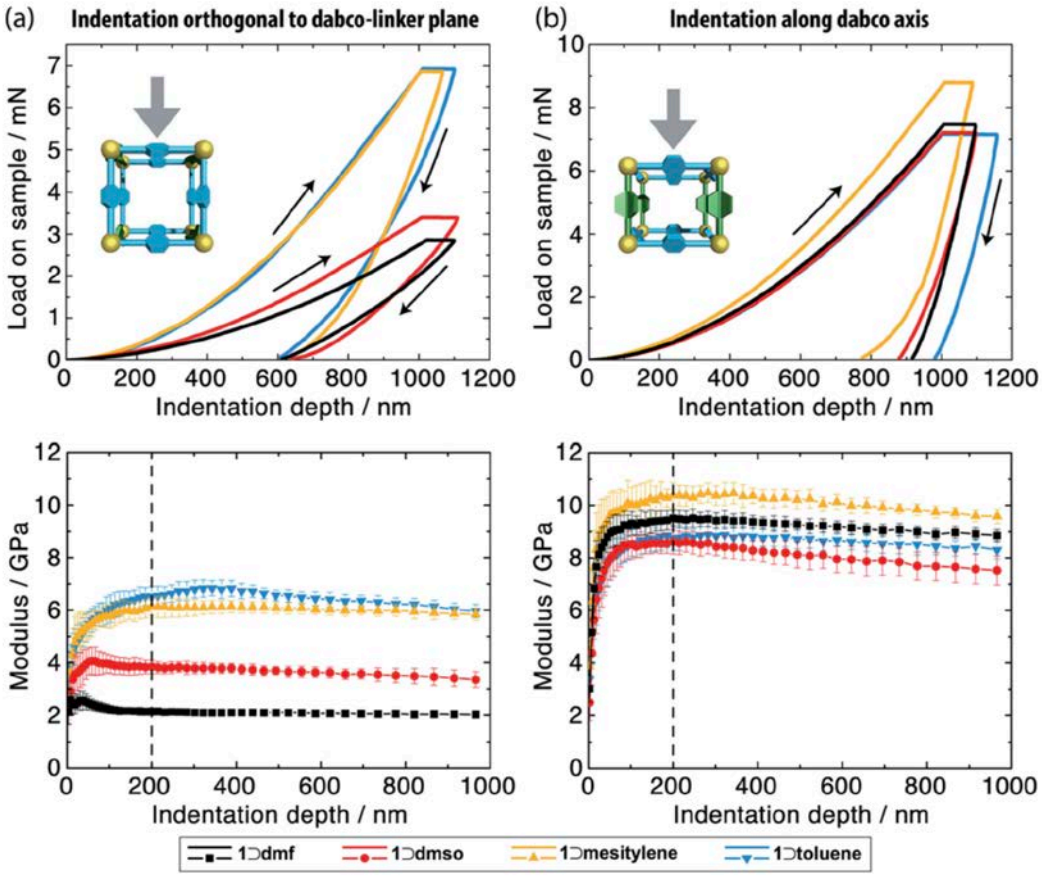

Figure 2.12 Representative force-displacement (*P*-*h*) curves and the measured elastic modulus as a function of the indentation depth of the $[Zn_2(NO_2\text{-bdc})_2(dabco)]_n$ (denoted as the number 1 in the figure) hosting four different types of molecules. (a) Indentation

perpendicular to the plane of the dabco linkers on the {110}-oriented facet for 1□DMF and 1□DMSO or on the {100}-oriented facet for 1□ mesitylene and 1□toluene. (b) Indentation parallel to the dabco axis on the {001}-oriented facet. Reprinted from Ref. [73] with permission. Copyright (2014) Royal Society of Chemistry.

As a matter of fact, the porous MOF structures are flexible, and thus their mechanical properties are normally dependent on the encapsulated molecules. By using the single-crystal nanoindentation technique, Henke and co-workers found the substantial elastic moduli variances of the soft and porous $[Zn_2(NO_2\text{-bdc})_2(dabco)]_n$, a type of MOF, containing four different guest molecules: DMF, DMSO, mesitylene, and toluene.[73] The effect of mechanical anisotropy with guest encapsulation was investigated by conducting the indentation experiments along the different crystallographic orientations, as shown in Figure 2.12.

Replacing the inorganic nodes or clusters of MOFs would also result in considerable changes of the mechanical properties. A good example is the single-crystal nanoindentation experiment performed by Tan and co-workers on $[(CH_3)_2NH_2]M(HCOO)_3$ ($M = Mn^{2+}$, Co^{2+}, Ni^{2+}, Zn^{2+}) wherein the visible difference of the resulting force-displacement (*P*-*h*) curves were observed.[96] Likewise, other types of bonds between the constituents of MOF structure could also cause significant alteration of its mechanical properties. For instance, the indentation experiment conducted by Li *et al.* revealed a large degree of Young's moduli rising due to the existence of the strong hydrogen bonding, suggesting the scope for mechanical tunability by exploiting host-guest interactions.[97]

Additionally, by implementing cyclic indentations of the same region of a material, as demonstrated in Ref. [98], the magnitude of energy dissipated in the form of plastic deformation can be measured, based on which the relative toughness between two porous organic polymers (FPOP-100 and FPOP-101) can be determined.

Apart from the indentation approach that applies normal force to the sample surface, some of the IIT instruments such as the MTS Nanoindenter® XP, are capable of exerting lateral and tangential forces which are inclined to detach a portion of the materials from the substrate and crush the other part of the materials into a compacted layer underneath. This is also known as instrumented scratch technique (IST), by using which Buchan *et al.* have identified film-to-substrate adhesion for the $Cu_3(BTC)_2$ (commonly known as HKUST-1) thin film coatings.[82] Another example described by Van de Voorde *et al.* concerns the adhesion strength of three different electrochemical Cu-MOF coatings: $Cu_3(BTC)_2$, Cu(CHDA), and $Cu(INA)_2$.[79] The example scratches on the $Cu(INA)_2$ coatings produced using a Berkovich tip are depicted in Figure 2.13.

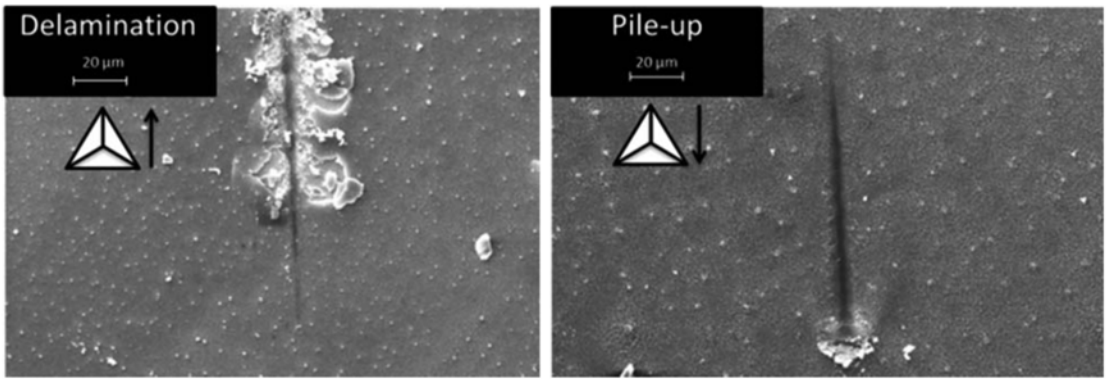

Figure 2.13 SEM images of the scratch tracks on the $Cu(INA)_2$ coating generated by (left) the edge-forward (ploughing) and (right) the face-forward (pushing) scratch modes. Reprinted from Ref. [79] with permission. Copyright (2013) The Royal Society of Chemistry.

The advantage of these instrumented techniques is their excellent stability in applying indentation force and standard ability to perform thermal drift so as to minimise the time-dependent effects such as creep. However, the configuration limits their applications to the micron-Newton (μN) level in terms of the peak force, in other words, the instrumented techniques hardly apply loads lower than hundreds of μN even if they claimed

to have nm-level displacement sensitivities.[99-102] In contrast to IIT, the AFM instruments are capable of sensing forces as low as a few pico-Newtons (pN), thereby providing a significantly higher force sensitivity (< 0.05 nN, *viz.* at least 1000 times lower) and indenter displacement sensitivity (≲0.05 nm). Thus weaker forces, such as the van der Waals force, capillary force, hydrophobic and hydrophilic forces can be detected *via* AFM. This enables the AFM to be applied to probe considerably more localised properties (e.g. exploration of the inhomogeneity of materials)[103-107] and for studying relatively softer matter such as biological entities and hydrogels (Young's moduli in the range from 100 Pa to tens of kPa).[108] There are reports where the stiffness measured using the AFM-based nanoindentation and IIT is in a good agreement even for soft viscoelastic materials.[109] The outstanding challenge is to obtain a good agreement between the different indentation techniques, when applied across the length scales covering a broad range of materials.

2.3.1.2 Brillouin Light-Scattering Technique

For many years, the Brillouin scattering technique has been used to characterise the independent elastic coefficients (C_{ij}'s) of minerals[110-111] and inorganic zeolites[112-113]. More recently, this non-destructive approach was applied to measure the elasticity of MOF single crystals, specifically that of ZIF-8.[7] Through Brillouin scattering, the lateral and transverse velocities of the acoustic wave travelling along specific crystallographic directions can be measured directly. The elastic tensor C_{ij} of the sample can then be determined according to the velocity of phonons *via* the Christoffel equation.[114-115] For instance, Tan *et al.* have established the complete elastic constants of a ZIF-8 crystal (Table 2.1), from which the directional Young's moduli, Poisson's ratios, and shear moduli can be derived. Their results reveal that the Young's moduli (E) of ZIF-8 is moderately anisotropic (Figure 2.14), for example the moduli on three main crystallographic facets are: $E_{[100]}$ ~3.77 GPa, $E_{[110]}$ ~2.98 GPa, and $E_{[111]}$ ~2.78 GPa, which are in close agreement with the results from

the IIT experiments.[7] Subsequently, the pressure dependence of ZIF-8 has been reported using high pressure Brillouin scattering,[116] which shows flexibility and dynamics of ZIF-8 under external pressure. More specifically, it was evidenced that the elastic constant C_{11} of the guest-containing (i.e. the pressure transmitting mediums) ZIF-8 increased by ~183% when a pressure of only 1.47 GPa was applied.

Table 2.1 Elastic properties of single crystal of ZIF-8 measured by Brillouin scattering in comparison with the values from the single-crystal nanoindentation experiments and theoretical predictions based on perfect crystal of ZIF-8. Reprinted from Ref. [7] with permission. Copyright (2012) Physical Review Letters.

Elastic properties		Experimental data (295 K)		*Ab initio* calculations
		Brillouin scattering	Nanoindentation	B3LYP (0 K)
Stiffness coefficient, C_{ij} (GPa)	C_{11}	9.5226 ± 0.0066		11.038
	C_{12}	6.8649 ± 0.0144	···	8.325
	C_{44}	0.9667 ± 0.0044		0.943
Compliance coefficient, S_{ij} (GPa^{-1})	S_{11}	0.2652		0.2578
	S_{12}	−0.1111	···	−0.1108
	S_{44}	1.0345		1.0605
Acoustic wave velocities, V($km\,s^{-1}$)	Longitudinal (maximum and minimum)	3.17 & 3.08	···	3.41 & 3.32
	Transverse (maximum and minimum)	1.18 & 1.01		1.19 & 1.00
Young's modulus, E (GPa)	$E_{max} = E\{100\}$	3.77 ± 0.01	3.29 ± 0.11	3.879
	$E\{110\}$	2.98 ± 0.01	3.07 ± 0.07	2.953
	$E_{min} = E\{111\}$	2.78 ± 0.01	2.87 ± 0.09	2.736
Shear modulus, G (GPa)	$G_{max} = 1/2(C_{11} - C_{12})$	1.329 ± 0.005	···	1.36
	$G_{min} = C_{44}$	0.967 ± 0.005		0.94
Poisson's ratio, ν	$\nu_{max} = \nu\langle 110, 1\bar{1}0\rangle$	0.54	···	0.57
	$\nu_{min} = \nu\langle 110, 001\rangle$	0.33		0.33
Anisotropy measure	Zener, A (= 1 if isotropic)	0.73	···	0.70
	E_{max}/E_{min}	1.35	1.22	1.42

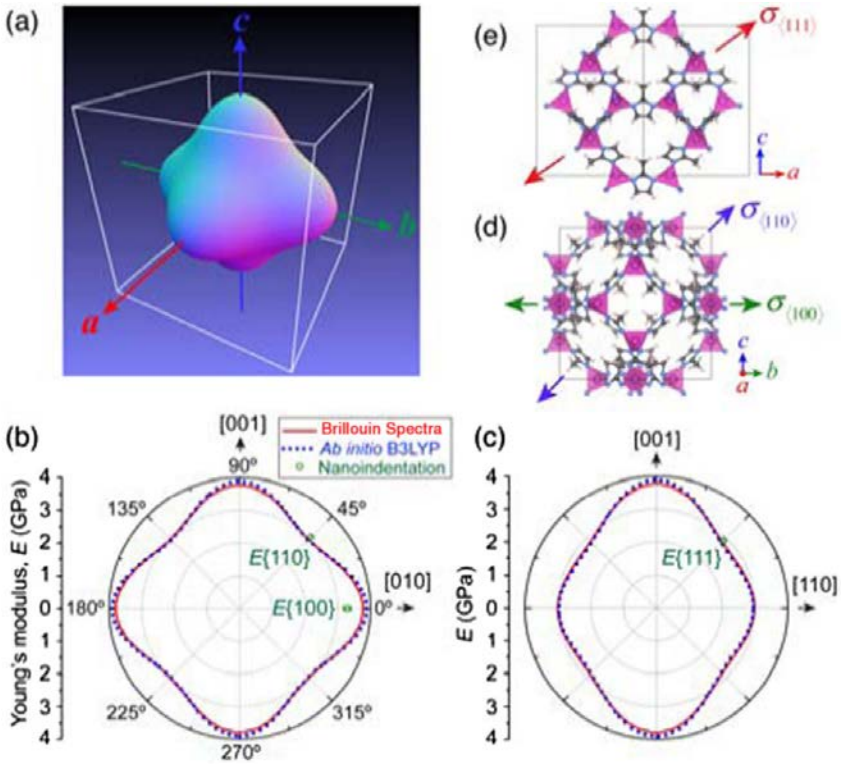

Figure 2.14 Representation surfaces of Young's modulus (E). (a) 3-D surface according to C_{ij}'s measured by the Brillouin scattering experiments. (b-c) Projection of the polar plots on the (100) and (1$\bar{1}$0) planes, respectively. (d-e) Normal stresses (σ) corresponding to the maximum, the intermediate, and the minimum stiffnesses. Reprinted from Ref. [7] with permission. Copyright (2012) Physical Review Letters.

2.3.2 Computational Approaches

2.3.2.1 Density-Functional Theory (DFT)

Density-functional theory is an *ab initio* computational method to perform quantum mechanical modelling to calculate atomistic forces and energy of periodic systems. DFT codes such as CRYSTAL[117] and CASTEP[118] can be used to compute the elastic constants (C_{ij}'s) of materials at 0 K, from which the Young's modulus, shear modulus, linear compressibility and Poisson's ratio can be derived.[119] Now there is an increasing body of work where DFT calculation has been used to investigate the mechanical properties of MOF structures. For instance, Mattesini *et al.*[120] used the local density approximation (LDA) exchange-correlation functional and Tan *et al.*[67] employed the PBE functional[121] to calculate

the single-crystal elastic constants of MOF-5 and two ZIFs (-4, -zni), respectively. Moreover, Bahr *et al.*[72] and Kuc *et al.*[122] utilised the generalised gradient approximation (GGA) functional and the DFT-based tight-binding method to compute the mechanical properties of isoreticular MOFs. Amongst the different derivations of the exchange-correlation functionals, B3LYP is one of the most popular hybrid functionals that is widely adopted for elasticity calculations. For example, DFT with B3LYP has been applied to predict the structure-property relations of many MOF systems, recent studies include MIL-140(A-D),[15] HKUST-1,[8] and ZIFs.[64] In addition, Ortiz *et al.* adopted the B3LYP hybrid exchange-correlation functional[123] and then discovered the highly anisotropic elastic behaviour of five flexible MOFs who exhibited as high as 400 : 1 ratio of anisotropy and extremely large negative linear compressibility.[66] This observation is different from the nonflexible MOFs such as ZIF-8. Moreover, by using the DFT calculations and first-principles molecular dynamics (introduced in the following section §2.3.2.2), the dynamical MOF linker disorder that could have noteworthy impact on the mechanical properties can be characterised. For instance, the diazo-linker of UiO-abdc with local site disorder stabilises the framework against compression leading to a large elastic modulus comparing with UiO-67.[124]

Closely related to the study described in Chapter 8, the DFT predictions of the mechanical properties of HKUST-1 has been reported by Ryder *et al.* using the B3LYP functional.[8] Implications of the predicted C_{ij}'s (C_{11}, C_{12}, C_{44}) are the cubic symmetry and elastic anisotropy as presented in Table 2.2. According to the DFT calculations, HKUST-1 exhibits obvious elastic anisotropy (Figure 2.15) and auxeticity (Figure 2.16). Because there is a lack of experiments to corroborate these theoretical findings, the nanoindentation experiments have been performed to confirm the theoretical results from DFT (see Chapter 8).

Table 2.2 Mechanical properties of HKUST-1 from the DFT calculations. Reprinted from Ref. [8] with permission. Copyright (2016) Royal Society of Chemistry

Elastic property		B3LYP	B3LYP-D
Young's modulus, E (GPa)	E_{max}	15.15	14.81
	E_{min}	2.96	3.05
	$A_E = E_{max}/E_{min}$	5.12	4.86
Shear modulus, G (GPa)	G_{max}	5.40	5.27
	G_{min}	1.00	1.03
	$A_G = G_{max}/G_{min}$	5.40	5.12
Linear compressibility, β (TPa^{-1})	β	12.63	12.74
Poisson's ratio, ν	ν_{max}	1.21	1.19
	ν_{min}	−0.31	−0.28
Zener anisotropy, A		5.41	5.11
Acoustic velocities(km s^{-1})	max	6.18	6.14
	min	5.62	5.59

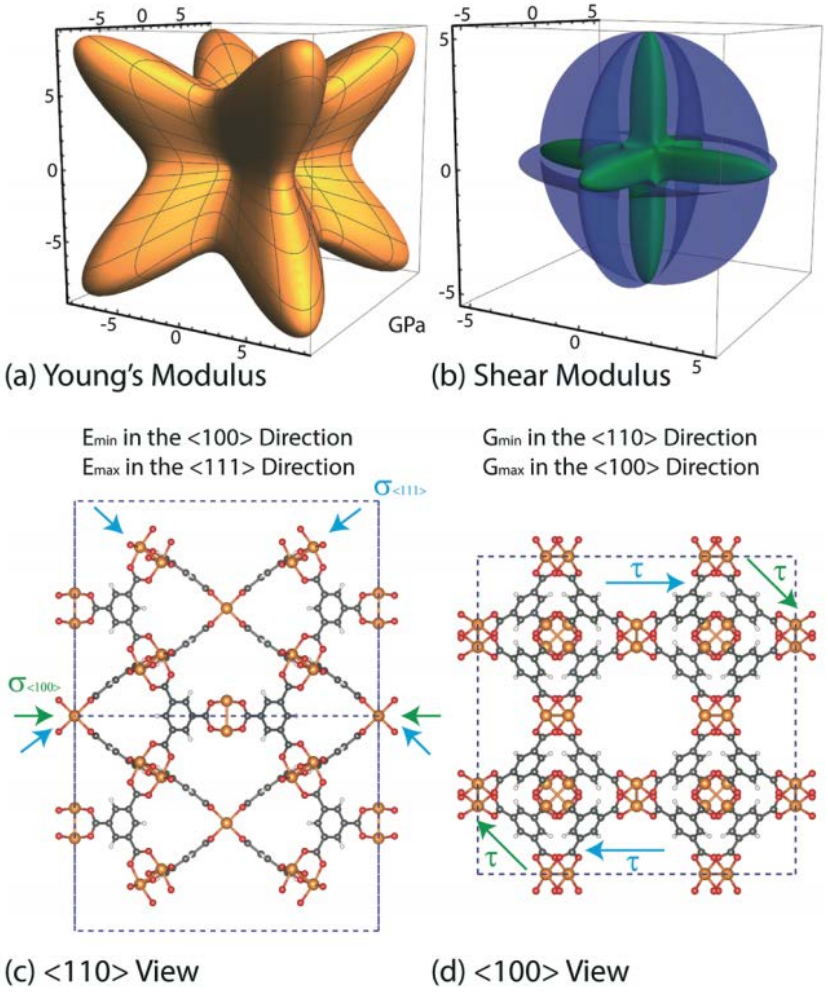

Figure 2.15 (a) Representation surface of Young's modulus (E) in 3-D spherical coordinates. (b) Representation surface of Shear modulus (G). (c) View down the [100]- and [111]-axes, E_{min} and E_{max} are identified, respectively. (d) G_{min} along the [110]-axis and G_{max}

along the [100]-axis are also marked, respectively. Reprinted from Ref. [8] with permission. Copyright (2016) Royal Society of Chemistry

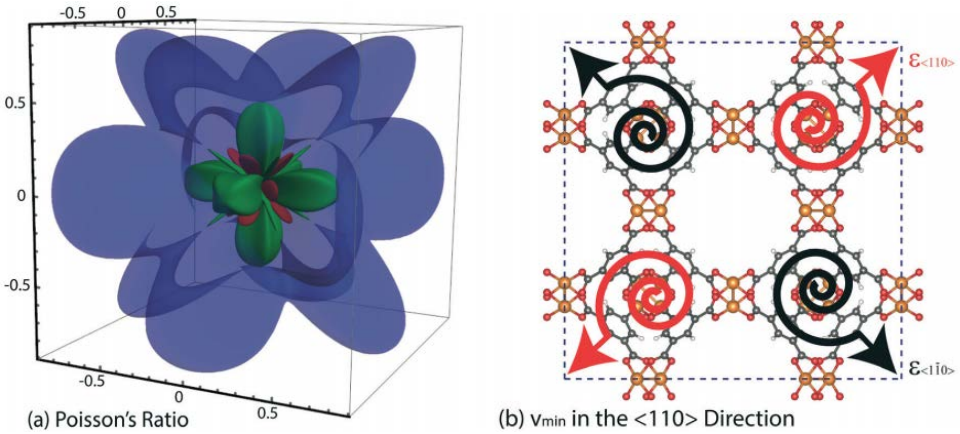

Figure 2.16 (a) Representation surface of Poisson's ratio (*v*). The blue region denotes the maximum, and green region signifies the positive Poisson's ratios, respectively. While the red region represents the negative minimum Poisson's ratio. (b) A deduced mechanism correlated to the cluster rotational dynamics could reason the auxeticity of HKUST-1. Reprinted from Ref. [8] with permission. Copyright (2016) Royal Society of Chemistry

2.3.2.2 Molecular Dynamics (MD) Simulation

Molecular dynamics (MD) simulation is an alternative method to investigate the mechanical properties of MOFs. The main advantages of this method over the DFT calculation are the relatively less demanding computational resources, and the possibility of modelling finite temperature[125] and tracking the evolution of system in time domain. By conducting the MD simulation of the MOF-5 (IRMOF-1) structure, Greathouse and Allendorf calculated its elastic modulus which is in good accordance with the result from DFT.[126] But by far, only a limited number of investigations have addressed the mechanical calculations of MOFs using MD due to several reasons including the restrictions of reliable force field and the assumption of rigid frameworks.[127] However, there are promising recent developments on flexible force fields to model the elastic behaviour of MOFs, see Ref. [128], but the study is still limited by the scarcity of efficient sampling schemes for the stimuli-driven phase transitions. Meanwhile, large fluctuation of pressure in MD simulations

could introduce considerable deviation to the calculated properties of MOFs.[129] The flexibility of MOFs can be related to the variation of their mechanical properties, especially for the elastic anisotropy of flexible MOFs such as MIL-47 (V) and MIL-53 (Al), which can be more than 100 times higher than the one of rigid MOFs such as UiO-66 (Zr) and MOF-5 (Zn).[129] Force fields for MOFs with structural flexibility can be used to predict their mechanical properties. For example, the Young's modulus of ZIF-8 obtained using the force field combining quantum chemical calculations and classical Amber force field in Ref. [130] is in a good agreement with the result from the single-crystal nanoindentation experiments reported in Ref. [45].

2.4 Identification of the Failure Modes of MOFs

Investigation of failure mechanisms of crystalline materials at the nanoscales has still rarely been reported, probably this is because there is no specialised technique and model that can be widely applied to a variety of materials. Recent relevant studies in the literature are introduced herein to show the opportunities and challenges that exist in this field.

Indentation on some materials such as silicon may induce very complicated responses because these responses reflect not only the elasticity of materials but also involve the stress-induced failures such as cracking that may lead to fracture.[131-133] Accurate measurement of the Young's modulus may not be possible if the failures have not been properly addressed. There are multiple types of cracks, some of which may occur at the place of highest stress concentration (mostly generated during indenter loading stage) and others, such as lateral crack, usually happens at subsurface parallel to the surface so as to push the surface outwards (often takes effect with the unloading indenter).[131] As a result, pile-up or sink-in may interfere with the precise measurement of contact area. Materials could develop distinct cracking patterns if a sharper indenter tip is employed. A good

example is the radial cracks generated by using a cube-corner indenter tip to indent thin sheets placed on the surface of a hard substrate. This phenomenon was not reproduced employing a blunter tip such as a Berkovich indenter tip.[133]

Important studies on the fracture of the hybrid inorganic-organic framework materials (denser than nanoporous MOFs) have been taken by Tan and co-workers aiming at investigating the structure-property relationships. For instance, by employing the instrumented indentation experiments, they bridged the subsurface fracture morphology with the underlying crystalline structure of a pair of hybrid polymorphs (i.e. CuPA-1 and CuPA-2) and then differentiating their crack initiation mechanisms linked to different crystallographic orientations.[38, 90] It was suggested that the breakage of chemical functional groups and bonds (such as the rupturing of hydrogen bonds) are responsible for the initiation and propagation of the different crack patterns.

There are recent attempts to study the permanent deformation (notably plasticity), defects, and collapse mechanisms/amorphisation of MOF structures using theoretical methods such as MD and DFT. For instance, the MD simulation sheds light on the molecular process of pore collapse[134] and the directional plastic deformation of MOF-5[69] as well as the DFT-based MD simulation elucidates the amorphisation process of ZIF-8[70].

2.5 Investigation on the Mechanical Behaviour of 2-D MOF Structures

2-D metal-organic framework (MOF) nanosheets have attracted increasing attention because of their thin thickness so as to offer highly accessible active sites and thus showing extraordinary advantages in many targeted applications such as capacitance,[135-136] energy storage,[137] electrocatalysis,[138] luminescence,[139] and gas separation[49]. Currently, the widely-used synthesis methods of 2-D MOFs incorporate the sonication exfoliation,

interfacial synthesis, three-layer synthesis, and surfactant-assisted synthesis (summarised in Ref. [140]).

The mechanical characterization of 2-D materials is often difficult owing to the mutual interplay between the adjacent nanosheets and the structural failures. Even so, there have been a number of attempts to mechanically characterise materials in 2-D form. This includes the employment of the AFM nanoindentation on the graphene nanosheets (thickness t ~ 20–50 nm)[141], the instrumented nanoindentation and AFM nanomechanical property mapping (PeakForce^{TM} QNM) on the MnDMS nanosheets (a typical multilayer thickness t ~10 nms)[91]. In addition, the complex moduli of MOF nanosheets can be measured as a function of temperature by conducting the dynamic mechanical analysis (DMA) experiments. For instance, the thermo-mechanical property characterisation of a type of 2-D MOF nanosheets, NUS-8, was reported by Hu and co-workers.[142] In their study, it was observed that the NUS-8 nanosheets experienced substantially higher thermo-mechanical dissipation than the 3-D interpenetrated NUS-16 and this may be attributed to the coupled effect of both interlayer shear sliding deformation and tension/compression out of the plane.[142] However, to date, there is no reliable experiment executed in order to quantify nanoscale mechanical properties of compliant nanosheets, let alone the MOF nanosheets which are apt to be porous thus more compliant. Even though, the depth-sensing indentation techniques have been regarded as a promising approach to explore the mechanical properties at the nanoscale.[143-147] Amongst these techniques, the AFM-based nanoindentation wherein the instrument exhibits extraordinary capability in sensing atomistic force and displacement has been employed in this study. In my work, a novel and reliable technique using AFM nanoindentation has been established to quantify the mechanical properties of nanosheets. Furthermore, the measurement is much more localised (indentation depth is as low as ~4 nm) than the aforementioned techniques.

Chapter 3: AFM-Based Nanoindentation

Amidst a variety of mechanical characterisation techniques, in this study, significant effort has been made on the enhancement of the nanoindentation approach based on an atomic force microscope (AFM). Thanks to the high sensitivity of AFM in detecting small forces and displacements, it is a powerful tool for exploring the nanoscale behaviour of materials. In essence, the microscale mechanical properties of MOFs quantified by the conventional instrumented techniques (introduced in Chapter 2) bridge the gap between the nanoscale properties measured by AFM and the macroscale properties central to engineering applications. In this review chapter, the five key aspects of AFM nanoindentation are considered: (a) operating principles of the AFM instrument; (b) advantages of the AFM-based nanoindentation technique; (c) applications of the technique to mechanically characterise a range of materials; (d) important factors to be addressed in an indentation experiment to yield reliable data; and (e) common analytical models for contact mechanics.

3.1 Atomic Force Microscopy (AFM)

AFM is a type of scanning probe microscopy (SPM), which scans the specimen surface using a physical probe to capture its height topography. The schematic in Figure 3.1 illustrates the fundamental operation principle of an AFM. The most common use is for tracing sample surface *via* the indenter-to-sample interaction force produced by the cantilever deflection. In the imaging mode, the indenter-to-sample force is persistently stabilised at a constant level (the magnitude is dependent on the set-point value input by the user) through an electronic feedback loop. While the AFM tip raster scans a rough surface, the degree of the cantilever deflection fluctuates, thereby resulting in the shift of the projected beam (reflected from the top face of the cantilever) on a photodiode. Depending on the sample surface topography, there are four possible degrees of freedom of the cantilever deflection (see Figure 3.1b). On the other hand, the AFM can also operate in an indentation mode, wherein the cantilever undergoes a vertical bending motion such that the tip penetrates normal into the specimen and generates the force-displacement data (i.e. *P-h* curve, the raw data from indentation experiments).

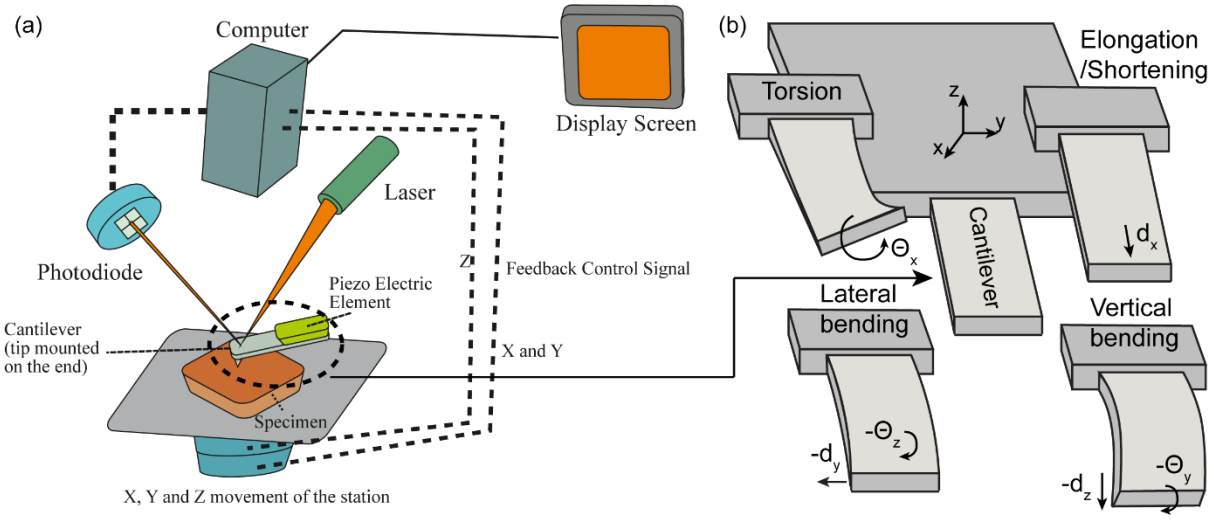

Figure 3.1 (a) Schematic illustrating the operating principle of a typical AFM apparatus. (b) Degrees of freedom of a deflected AFM cantilever.

3.2 Advantages of the AFM-Based Nanoindentation

One of the main advantages of AFM is its ability to control and detect small indentation load (force sensitivity < 0.05 nN) and to apply shallow indentation (displacement sensitivity $\lesssim 0.05$ nm).[148] During indentation, the *P-h* curve is recorded by converting the data of the output voltage on the photodiode as a function of the input voltage applied to the piezoelectric element, which controls the bending motion of the AFM cantilever.

While AFM nanoindentation has been employed to study the mechanical behaviour of a range of soft solids, e.g. polymers, hydrogels and biological samples,[149-150] its applicability to the field of MOF-type materials has not yet been widely demonstrated. Given the aforementioned outstanding sensitivities, the AFM-based nanoindentation technique offers us the opportunity to probe local mechanical properties of small crystals and thin-film samples that were previously inaccessible *via* the instrumented indentation techniques (IIT, see §2.3.1.1). Although some of the instrumented techniques have nanoscale level sensitivity,

in practice it is not feasible to perform indentation as subtle as the AFM, whose load sensitivity is on the picoNewton (pN) range as depicted in Figure 3.2. Not to mention that AFM nanoindentation also enables high-resolution 3-D imaging to map out the surface height topography immediately after the indentation step, thus providing a nearly *in situ* quantification of the shape of the residual indents.

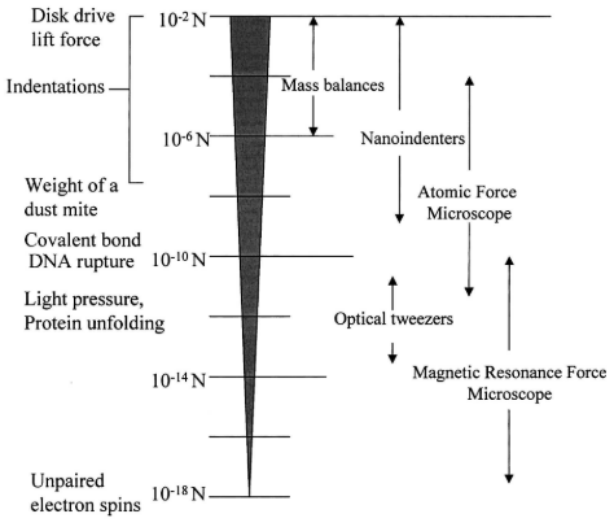

Figure 3.2 Relative magnitude of forces below 0.01 N and the applicable instruments for performing the measurement. Reprinted from Ref. [151] with permission. Copyright (2004) Materials Research Society.

3.3 Example Applications of AFM Nanoindentation

Nanoscale characterisation of the local mechanical properties of nanostructured materials is challenging. For porous crystalline materials like metal-organic frameworks (MOFs) and their nanosheets, the fine-scale behaviours of coordinated metal-organic linkages require even more sensitive instruments such as an AFM to probe. To date, many materials have been tested using AFM nanoindentation, and these include soft matter (biological entities,[152-178] polymers,[149, 179-184] gels,[104-105, 170, 185-187] fibres[188-189] etc.), and relatively harder materials such as graphene,[190-191] as well as materials with distinctive

attributes, such as viscoelastic materials,[180, 192-194] layered materials,[195] anisotropic materials[88, 196] and so forth.

3.3.1 AFM Nanoindentation of Polymers

Knowledge of the mechanical properties of polymers is important to gauge their durability, in the last few decades, there have been many indentation experiments being conducted on polymers. More recently, AFM nanoindentation on polymers has also been reported due to its capability in extracting the local mechanical properties at a much finer scale. For instance, Jee and Lee utilised AFM nanoindentation to measure the Young's modulus and hardness of ten polymers, namely: low density polyethylene (LDPE), high density polyethylene(HDPE), polyvinyl alcohol (PVA), polyvinyl chloride (PVC), ultrahigh molecular weight polyethylene (UHMWPE), polycarbonate (PC), Nylon 6, poly(methyl methacrylate) (PMMA), polystyrene (PS) and polyacrylic acid (PAA).[179] However, the indentation depths on these polymers are in the range of 630–3430 nm, which are comparable with the depth indented using the instrumented indentation techniques (IIT).

Indentation of polymers may be susceptible to various instrumental factors, such as geometrical deviation of the indenter and the varying indentation rate due to viscoelastic response associated with creep and stress relaxation. As Moeller pointed out that sometimes the equivalent circuit models cannot accurately derive the elastic modulus of materials of high viscoelasticity because of the substantial plastic flow contributing to the creep.[180]

Further to the influence of viscoelasticity, soft polymers usually have appreciable adhesion properties, which is challenging to characterise. Polydimethylsiloxane (PDMS), is a representative soft polymer, which is a popular candidate for many applications, especially in medicine and cosmetics. In the last decade, PDMS has been selected as a candidate material to test a number of adhesion models including the well-known

Johnson-Kendall-Roberts (JKR) model.[197] Sirghi and Rossi succeeded in measuring the Young's modulus (1.91 ± 0.33 MPa) and the thermodynamic work of adhesion (0.095 ± 0.023 N/m) of PDMS by utilising a silicon conical indenter (k = 11.5 N/m).[182]

Nevertheless, it is difficult to provide definitive mechanical properties of polymers because they are highly dependent on the degree of curing and crystallinity.[149] What is more troublesome is the aging problem of polymers that could lead to gradual transformation of their initial mechanical properties.[184]

3.3.2 AFM Nanoindentation of Biological Entities

AFM nanoindentation of biological entities have been reported on biological cells,[152-178] microtubules,[198-199] viruses,[153, 200-202] and tissue.[166, 203-205] For example, Roos *et al.* used AFM nanoindentation to characterise the mechanical properties (stretching and bending moduli) and fatigue of viral shells (see Figure 3.3a).[153] Raman *et al.* employed a dynamic AFM technique with high throughput to quantify the nanomechanical properties of living cells. It was claimed that the sampling rate was about a thousand times higher than the conventional quasi-static AFM methods.[156] Using this technique, they acquired stiffness, stiffness gradient and viscoelastic dissipation of a number of living cells. A few examples of the AFM nanoindentation experiments of biological entities are shown in Figure 3.3.

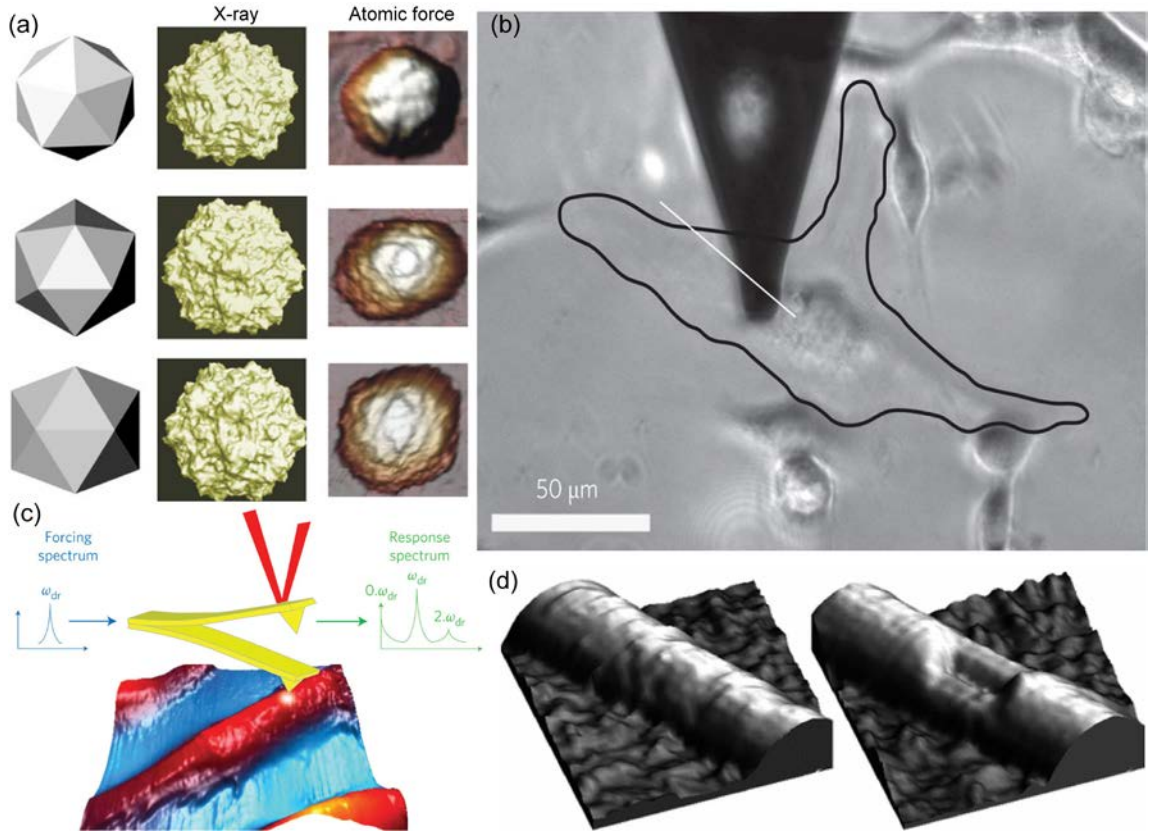

Figure 3.3 AFM nanoindentation of biological entities: (a) from left to right columns, schematic images, X-ray crystallographic images, and AFM images of the oriented capsids of a virus of mice with five-, three- and two-fold symmetry axes. Reprinted from Ref. [153] with permission. Copyright (2010) Springer Nature. (b) Embryo fibroblasts of mice, where the white line indicates the approximate scanning direction. Reprinted from Ref. [157] with permission. Copyright (2012) Springer Nature. (c) A live cell in liquid, nonlinear interaction between the tip and the sample results in the anharmonic frequencies. Reprinted from Ref. [156] with permission. Copyright (2011) Springer Nature. (d) A microtube at a nanoscale before and after being indented. Reprinted from Ref. [199] with permission. Copyright (2003) American Physical Society.

3.3.3 AFM Nanoindentation of Viscoelastic Materials

Optimally, a less sharp indenter tip is favourable to reduce the stress concentration on viscoelastic materials. Moeller developed an AFM creep test using spherical indenters with large apex radii (10 nm to 50 nm) in order to determine the instantaneous elastic moduli of four resins.[180] By using AFM nanoindentation, they quantified the percentages of creep deformation contributed by viscoelastic and plastic flow. According to the results, they

found that strong plastic flow occurred even at small loads (as low as 25 μN). This is because for viscoelastic materials, the *P-h* characteristics could be markedly different with the Hertz contact. To simulate the viscoelastic behaviour of materials, three equivalent circuit models were proposed to calculate the elastic moduli: Maxwell model, Kelvin-Voigt model, and Maxwell-Kelvin-Voigt model.[180, 192] These models can be employed to describe a range of time-dependent behaviours of viscoelastic materials. For instance, the indentation load on PDMS at the displacement holding period drops over time owing to the Maxwell-like stress relaxation, which may lead to the overestimated adhesive force (P_{ad}).[193] But by decreasing the indentation rate, the hysteresis could be alleviated because of the reduction of the dissipated energy during the unloading stage.[194]

3.3.4 AFM Nanoindentation of Anisotropic Materials

The mechanical properties, notably the elastic modulus, measured by indentation on anisotropic materials are essentially weighted magnitudes, *viz.* average properties. As dictated by Fan *et al.*, the indentation imprint involves deformation along all three principal directions.[206] Likewise, for the two of the six representative materials, sapphire and quartz, chose by Oliver and Pharr to verify their well-known Oliver and Pharr (OP) method, are anisotropic.[88] They deduced that the indentation along a specific orientation of an anisotropic material may reveal some average properties owing to the deformation in many other directions. Particularly for AFM nanoindentation, which probes properties at the nanoscale, the interference from other directions could be even more apparent.[196]

Therefore it is envisaged that the effect of anisotropy varies with tip included angles, tip radius of curvature and the indentation depth (also evidenced in Ref. [207]). In theory, the difficulty of predicting the elastic modulus in a specific direction decreases with lower degree of anisotropy. For instance, for transversely isotropic materials indented using a

conical indenter, their elastic moduli in the orthogonal directions of symmetry axes may be approximated on the basis of pressure distribution as proposed by Delafargue and Ulm.[208]

For some materials, the influence from the directions other than the indentation direction can be small. For instance, by using the model that predicts the elastic moduli of ceramics[209] and human tibial cortical bone[210] in specific directions (a conical tip was used), Fan *et al*. evaluated the relatively small effect of anisotropy on nanoindentation experiments, and thus suggesting that the anisotropy of cortical bone is mainly due to the osteonic and interstitial lamellae.[206]

3.3.5 AFM Nanoindentation of 2-D Materials

Another intriguing application of AFM nanoindentation is on the nanoscale study of 2-D materials such as graphene, which is a topical class of atomically thin 2-D material and has been very striking owing to its enormous potentials. Over the last decade, the mechanical properties such as elastic modulus, friction, and fracture behaviour of graphene have been characterised using different techniques.[211] Because the graphene sheets (E ~1 TPa)[212] are usually much stiffer than their substrate, substrate effect may interfere with the stiffness measurement of graphene. As a result, direct measurement by means of traditional instrumented indentation is very difficult. However, despite graphene is one of the strongest materials, whether the localised grain boundaries (synthesised using the chemical vapour deposition method) would reduce its strength was in doubt until the AFM nanoindentation experiments implemented by Lee and co-workers, who confirmed that the grain boundaries have minor influence ($\leq$ 15% reduction compared to its intrinsic value) on the strength of the graphene thin film (Figure 3.4b).[213] Moreover, instead of indenting on the suspended graphene film, Malina performed a number of AFM nanoindentation tests on graphene placed on the SiO_2 (~70 GPa) substrate with varying maximum loads (from 13 μN to 45 μN).[190] One may notice the graphene is still much stiffer than the substrate, but because

the AFM instrument can exert a tiny force and apply much shallower indentation, the substrate effect can thus be minimised. Furthermore, AFM nanoindentation is useful to characterise other properties of graphene, for instance, Nemes-Incze *et al.* came up with an approach using AFM nanoindentation to map the local strain patterning of graphene (Figure 3.4a).[191]

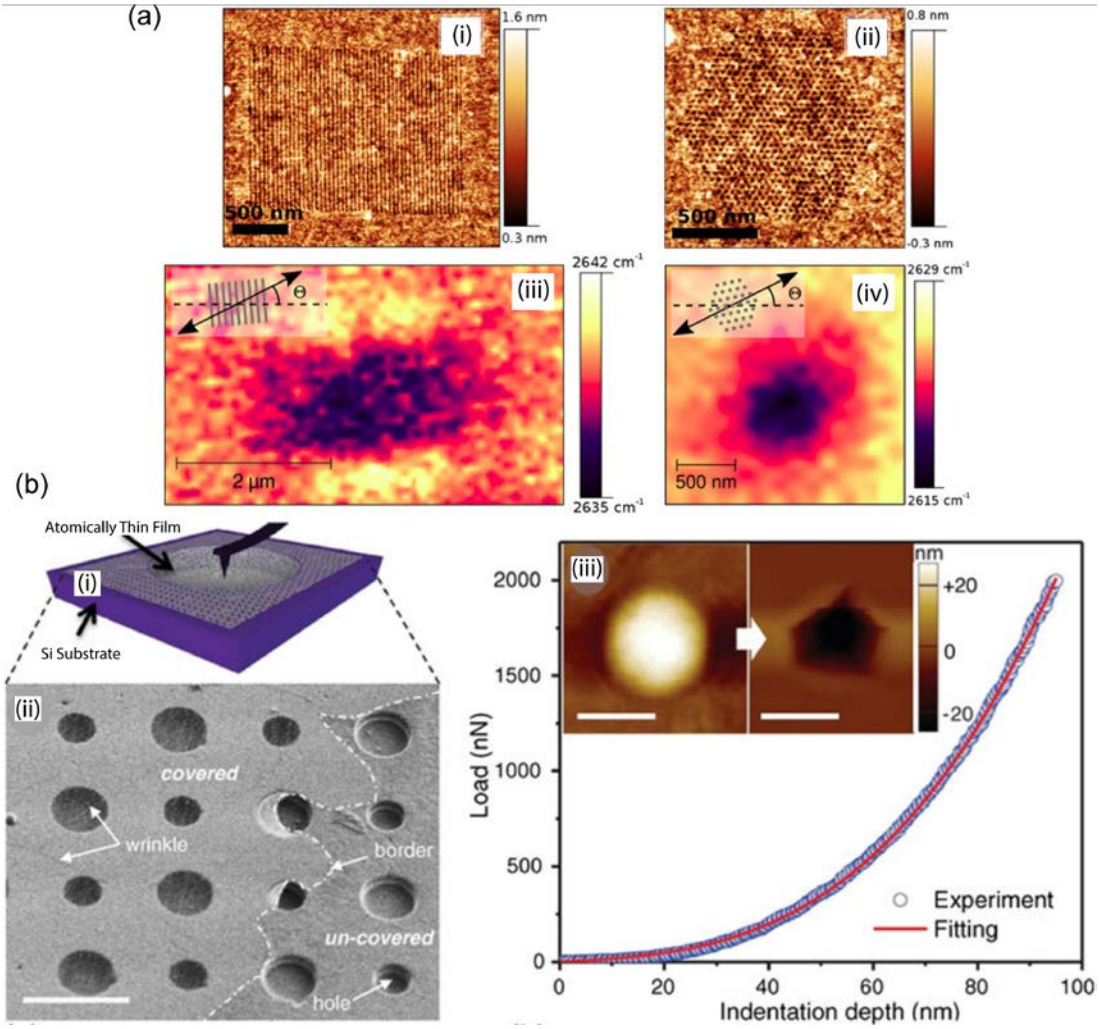

Figure 3.4 (a) The local strain field, (i) a line pattern and (ii) a dot pattern, assisted by AFM nanoindentation is mapped by using Raman spectroscopy, in which AFM shows the stretch orientation of the two patterns, namely (iii) line and (iv) dot. Reprinted from Ref. [191] with permission from the Creative Commons License. (b) Graphene membrane on a perforated silicon substrate: (i) schematic of a graphene membrane indented by AFM; (ii) optical microscopic image; (iii) a *P-h* curve from AFM nanoindentation (insets are the AFM images of part of the graphene membrane suspended over a hole before indentation and after fracture). Reprinted for Ref. [213] with permission. Copyright (2013) The American Association for the Advancement of Science.

Likewise, AFM nanoindentation can also be adopted to study multilayer samples although this type of materials has rarely been investigated because of the uncertainties of the interaction between layers. There still is to some extent breakthrough such as the work in Chapter 7. Another excellent example is the AFM nanoindentation on polyelectrolyte multilayer thin films of varying charge density.[195] Hereby, the elastic moduli of the films were measured ranging from 10^{-2} to 10^{-4} kPa. In consideration of the identical thickness of each layer, the relative Young's moduli of the thin films can be expressed as a function of ionization fraction. Moreover, interestingly, it was found that the thin films of high charge densities are much stiffer (by about two orders of magnitude) than those of low charge densities.[195] Mermut and co-workers suggested that the measurement of Young's modulus can serve as an indicator of the underlying interface and layered architectures, which enabled the comparison of the thin-film internal architectures at different pH conditions. In the course of the study, the feasibility of using AFM nanoindentation to quantify the layer-to-layer adhesive forces has also been demonstrated.[195]

3.4 Factors Affecting the Accuracy of AFM Nanoindentation

AFM-based nanoindentation is a powerful technique for studying the properties of fine-scale materials and nanostructures. However, it also comes with merits and drawbacks since AFM instrument senses the indentation force at least 1000 times lower than the conventional IIT instruments, and thus the smaller forces such as the van der Waals force, capillary force, hydrophobic and hydrophilic forces are no longer negligible. For instance, the elastic-plastic properties vary with changing temperature that will alter the adhesion interaction between the indenter and the sample.[181]

Besides, many other instrumental- and sample-related conditions may also affect the precision and reproducibility of the resulting force-displacement (*P-h*) data. Amongst the foreseeable challenges, a few representative examples are: (i) distorted *P-h* curve results from the interfering factors including the structural failure and fracture of crystalline framework as well as the time-dependent deformation such as creep and thermal drift; (ii) erroneous contact area determination due to the roughness of sample surface; (iii) an AFM probe with a larger tip angle is generally preferred for indentation but at the expense of reduced resolution in 3-D post-indentation imaging; (iv) indentation-triggered effects, such as "pile-up" and "sink-in" at the periphery of the indenter,[76] creep/viscoelasticity and adhesion interactions during indenter unloading.[182]

In order to execute an accurate measurement, a range of factors need to be considered. Factors to be considered prior to or during the indentation experiment are summarised in Table 3.1 and discussed in detail in this section.

Table 3.1 Summary of factors that could affect accurate measurement using AFM nanoindentation along with the corresponding examples in the literature.

	Factors	Influence if overlooked	References
Instrument Calibration	Cantilever's spring constant	False load	[106, 214-220]
	Deflection sensitivity	False displacement	[106, 151]
	Indenter tip geometry	False contact area and unsuitable contact mechanic models	[88, 103-104, 107, 147, 149, 182, 195, 221-232]
	Deflection angle of cantilever	Indentation not normal to sample surface	[228, 233-234]
	Piezoelectric effect	Non-linearity, hysteresis, and creep leading to deviation from the desired displacement and voltage relationship	[235]
	Compliance of the load frame	Erroneous measurement of elasticity	[88, 228]
	Alignment of laser spot*	Offset and noise in force-displacement curve	N/A

Indent-to-Sample Interaction	Post-indentation imaging resolution*	False characterisation of residual indent area and height of pile-up and sink-in	[180, 236]
	Indenter-to-sample contact area*	Erroneous measurement of mechanical properties, e.g. Young's modulus and hardness	[88, 228, 237-239]
	Sample surface roughness	False contact point, inaccurate contact area	[240-244]
	Contact point uncertainty	False indentation depth	[87, 103-104, 173, 185-186, 245-255]
	Poisson's ratio*	Deviated Young's modulus caused by compressibility	[238]
	Pile-up and sink-in*	Inaccurate contact area	[88, 224, 228, 238, 256-264]
Operating Conditions	Loading strain rate*	Creep, thermal drift, fracture, slippage etc. resulting in the distorted force-displacement curve	[106, 265-266]
	Unloading strain rate*	Slope augment (even negative slope) of the incipient segment of the unloading curve, i.e. false contact stiffness	[147]
	Creep effect (hold time)*	Ditto	[147, 180]
	Adhesion effect*	Erroneous measurement of mechanical properties, e.g. Young's modulus	[86, 104, 147, 183, 267-270]
	Substrate effect*	Erroneous of sample stiffness	[103, 107, 157, 263, 271-272]
	Friction	False contact area; inaccurate load-vs-contact area correlation	[239]
	Temperature	Drift causing fluctuation of materials properties	[181, 273-274]
	Hydrated condition	Change of materials properties due to liquid molecule encapsulation; inference on the indent-sample interplay	[65, 275-284]

* Factors with asterisk are elucidated in this subsection.

3.4.1 Substrate Effect

One of the most important applications of AFM nanoindentation is the study of thin films, which are usually coated on a substrate. However, on many occasions, the presence of a substrate may dramatically affect the indentation measurement. Indentation experiments of the same thin film either situated on a harder or softer substrate can produce enormously different results in terms of stiffness, hardness, pile-up or sink-in, and so forth. The substrate effect can be reflected by a normalised *P-h* curve, which can be expressed as either a quadratic or power-law force as a function of depth. In the logarithmic chart of the normalised *P-h* curve, generally it starts to deviate from the linear trend when the indentation depth exceeds ~10% of the sample thickness.[107] Saha and Nix examined the substrate effect of six combinations comprising aluminium and tungsten films adhered to four different substrates: aluminium, glass, silicon and sapphire.[263] For the purpose of minimising the influence from a substrate, a substrate that is much harder than the test specimen is desirable to prevent plastic deformation of the substrate, or such that the plastic deformation can be confined to a negligible degree as long as the indenter does not penetrate the substrate. On the contrary, the measurement of a specimen placed on a soft substrate is in all probability erroneous if the indentation depth exceeds 10% of the specimen thickness since by then the substrate has already been plastically deformed.[263] Therefore, the substrate effect could be avoided under the circumstance of shallower indentation that is below 10% of the sample thickness.

Substrate effect is not only incurred by the spread of the plastic deformation to the substrate, but also caused by its elastic deformation, which explains why the substrate has a significantly greater influence on the measurement of Young's modulus (E) than hardness (H). In other words, the interference of substrate on E is a coupling effect of both

elastic and plastic deformation while on *H* is primarily because of the plastic deformation of the substrate.

In many instances, however, it is required to indent cellular samples over the 10% of their thickness owing to their heterogeneity as well as the cellular cores of interest. To this end, Gavara and Chadwick developed a thickness-independent method called "Bottom effect cone correction (BECC)" on the basis of the Sneddon model (see §3.5.2), which is able to overcome the substrate effect that overestimates *E*.[157] Their experiment was preformed using AFM nanoindentation equipped with a conical indenter to indent cells (e.g. polyacrylamide gels and fibroblasts).

Substrate effect may also occur in the form of binding strength with the specimen. In general, a strong adherence of a specimen to a substrate is wanted during indentation, *P*-*h* curves from experiments on well-bonded and loosely-bonded specimens differ significantly.[271-272] Dimitriadis refined the integral transform methods proposed by Sneddon[285] in order to deal with samples of finite thickness.[103] In the derived force function, the distinction between systems where samples bonded and not bonded to the substrate has been expressed by two parameters as functions of the Poisson's ratio.

3.4.2 AFM Imaging Resolution of Indents

Post-AFM topography imaging of the indentation indent is undoubtedly one of the most widely-used approaches to measure the contact area, profiles of the possible pile-up and sink-in as long as the influence of elastic recovery can be neglected (actually in some cases, the curvature caused by elastic recovery could appreciably modify the projected area as pointed out in Ref. [228]). However, as shown in Figure 3.5a-c, one shall realise that AFM imaging is not perfectly accurate in reconstructing the features of the sample surface since AFM imaging is usually broadening protrusions and narrowing holes during the

tip-sample convolution. Moeller conducted an in-depth investigation of the broadening effect through equipping AFM tips of varying radii to image a type of epoxy polymer. The tips are of small apex-radius from 30 nm to 50 nm and of large apex-radius 451 nm, 553 nm, 642 nm, and 761 nm.[180]

Artefacts from AFM imaging would also affect the clear visualisation of an indent, such as the streaks appearing on an image due to the contamination of the AFM tip (Figure 3.5d), the edge overshoots because of the piezoelectric scanner hysteresis (Figure 3.5e), the image distortion from thermal drift (Figure 3.5f), and the different captured profiles of the same object at different spots (Figure 3.5g) and so on. Therefore, it is important to recognise the image artefacts. To overcome this, Gołek *et al.* suggested an approach to search for the switching lines where the scanning of the sample features switches to tip self-imaging, in order to identify the image artefacts.[236] Additionally, they also summarised other common artefacts that one may encounter during AFM imaging.

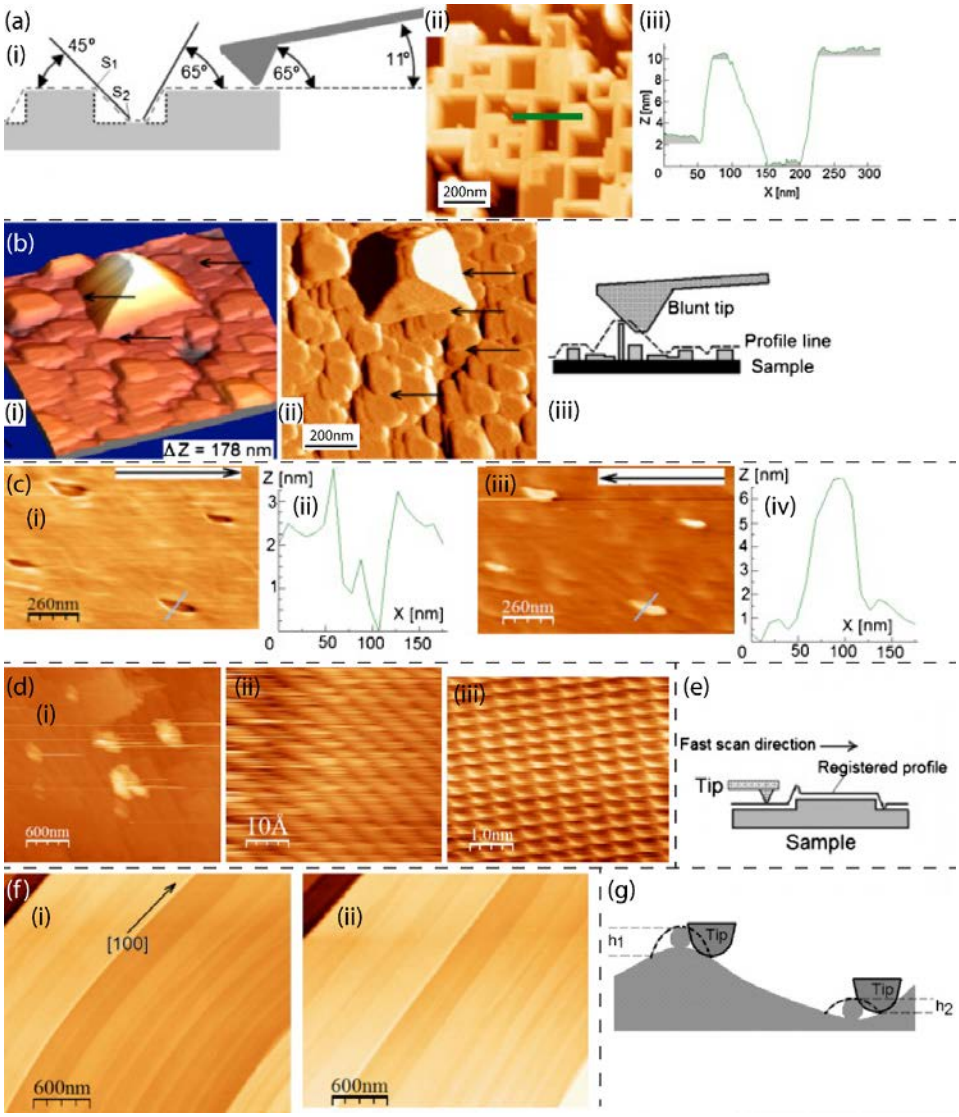

Figure 3.5 (a) (i) Schematic of the broadened protrusion and narrowed groove; S1 and S2 are the switching points indicating the emerging convolution artefacts; (ii) an irregular LiF grid; (iii) height profile along the line labelled in (ii). (b) (i) AFM height image and (ii) error signal image of the broadened image of a slim LiF block coated on Si(001), in which the switching points are marked by arrows; (iii) schematic of the line scanning producing the AFM images in (i-ii). (c) Owing to the artefacts generated by friction, the AFM images obtained from (i) the trace and (iii) the retrace scanning exhibit completely different line height profiles (ii) valley (iv) peak of the same region. (d) (i-ii) AFM images with streaks because of the tip contamination; (iii) AFM image recovered after a noise reduction. (e) Schematic of the edge overshoots. (f) (i) Distorted AFM image due to thermal drift; (ii) AFM image of the same sample with alleviated thermal drift. (g) Two particles of the same dimensions but in different spots can be imaged differently ($h_1 > h_2$), meanwhile the existence of the particles implies the possibility of exfoliated debris on an indent leading to false characterisation of the contact area. Reprinted from Ref. [236] with permission. Copyright (2014) Elsevier.

3.4.3 Tip Geometry (Including Tip-Apex Radius)

Real indenters usually deviate from the ideally presumptive geometry, and this deviation results in erroneous contact area and invalidates the application of idealised contact theories. The influence of non-ideal indenter geometry, especially in terms of its sharpness, included angle, and apex radius of curvature, is more pronounced for shallow indentation, such as AFM nanoindentation. Moreover, pile-up and sink-in are two phenomena, which are closely associated with the geometry of the indenter used. Therefore, efforts have been done to quantify the effect of geometric deviation on mechanical property measurement *via* both analytical[286] and experiment[287] methods.

In fact, accurate measurement of contact area is crucial for calculating the Young's modulus (E) and hardness (H). To this aim, knowledge of the geometry of an AFM indenter prior to indentation is needed. Regarding the effect of different included angles, taking conical indenters as an example, which of larger included angle tends to alleviate the dependence of Young's modulus on indentation depth.[104, 107] Besides, Calabri *et al.* had utilised three different methods: theoretical model, numerical simulation (*via* finite-element method), and experimental method (*via* AFM nanoindentation), which all show that H decreases with the increasing tip included angle.[230] This trend of H can be explained by the theoretical dislocation theory (it is often concerned for metals), which is also referred to as energy dissipation theory wherein H is a function of the surface-to-volume ratio where there is energy dissipated.[288]

For the measurement of E, deviation of radius of curvature by a factor of two could lead to a 41% error for thick samples and it has been demonstrated to be more pronounced for thin samples.[103] A correction factor was proposed by Calabri *et al.* for converting H from an ideal indenter (apex radius $R = 0$) to the value garnered from a real indenter since the tip can be worn somewhat ($R \neq 0$).[230] Apart from the correction on indenter apex radius, in

most theoretical models, asymmetric indenters are assumed. Therefore, for experiments using non-axisymmetric indenters, the correction factor β is required (refer to Ref. [228] for more details).

For specific materials, careful selection of indenters of suitable geometries is important. To enumerate a few examples, flat punches have been proven to be inadequate to study many materials because even the incipient part of the unloading curve is non-linear in most instances due to the continuous elastic recovery in time of unloading.[88, 228] In addition, spherical indenter performs better than sharp indenters if the sample is soft for the reason that sharp indenters generally induce much larger strains that exceed the linear elastic regime. As a result, Young's modulus measured by a non-spherical indenter can be markedly overestimated and the degree can be as much as 20 times.[103] In terms of sharp indenters such as cone and pyramids, the influence of inaccurate geometry is even larger because of its high non-linearity of force-displacement relation.[223] The effect of the indenter geometry is even more obvious when thin film on a substrate is indented.[221] However, it is difficult to identify the precise tip-apex radii of these blunt indenter tips that were worn away.

Of course, it is worthwhile to remember that some contact models (§3.5 and §4.7) are restricted to specific tip geometries. For example, Hertz model is not suitable for indentation by a pyramidal indenter.[104]

There are mainly two ways of acquiring the tip geometry: direct imaging and indirect tip geometry reconstruction. Depending on the tip-apex radius, one may choose a suitable imaging techniques, such as scanning electron microscopy (SEM)[182, 231] and AFM. The latter one prevails by right of its ability to generate 3-D topography. However, direct imaging method by AFM may introduce deviation due to elastic recovery and this issue exists for both true contact area and projected contact area such as the convex curvature reported by

Oliver and Pharr,[228] and the incomplete projected square indent described by Giannakopoulos and co-workers.[224] A prevalent indirect approach is the blind tip geometry estimation algorithm developed by Villarrubia.[226] Basically, this algorithm is based on a fact that while the probe is scanning along sample surface whereon those protrusions of smaller size than the tip-apex radius are actually reversely imaging the probe. Therefore, samples with sharp features (e.g. a NiO pattern)[232] and sufficient height variance (e.g. a calibration grid)[149] serve as good candidates for implementing this algorithm. Indenters made from hard materials such as diamond are often in a less need for frequent tip geometry measurement. For instance, the diamond cube-corner indenter survives after more than 100 indentations without appreciable change of the apex radius (see Figure 4.2g).[147] But quite on the contrary, indenter tips designed to indent soft matters are usually made from less durable materials such as silicon and silicon nitride. Moreover, indenters could be readily contaminated.[195] Overlooking the evolution of the tip geometry and/or artefacts from tip contamination could produce dramatic errors on the contact area.[149]

Nonetheless, there are potential issues that may affect the accuracy of the blind tip estimation algorithm such as the scanning scale and noise from the instrument. Tranchida *et al.* found that instrument noise is apt to underestimate the tip size, whereas larger scanning scale has an opposite effect because the resolution reduces accordingly. Fortunately, the influence of noise diminishes with increasing scanning scale.[229]

Besides the true radius of an AFM probe, scientists have been exploring the concept of effective tip radius, which produces the same shape of indent thus simulating the influence of plasticity on the distribution of pressure under the indenter.[227] Date back to 1993, Hutter and Bechhoefer came up with a non-destructive procedure to deduce an effective tip radius based on the measurements of van der Waals forces (Hamaker constant).[222] However, the effective radius (150 ± 16 nm) was larger than the nominal value (40 nm), and it was

explained that the pyramidal tip apex may end in a line along the edges or the tip had been through a plastic deformation. Thereafter, the "effective indenter shape" had been developed to explain the power-law expression of an unloading curve.[225, 227-228] Amongst the different effective shapes, the paraboloid of revolution that behaves similarly on numerous materials as a rigid cone, or a sphere indenting to shallow depths has been well received.[228] As a matter of fact, many materials exhibit similar unloading behaviour which can be elucidated by a single indenter geometry, i.e. a paraboloid of revolution.[228]

3.4.4 Laser Spot Alignment

Centring the laser spot is a critical step to ensure the force recorded starting from zero when the AFM tip is far away from the sample surface. But the position of the laser spot may drift away from the centre over time, overlook of which will lead to the offset of the *P-h* curve along the ordinate as shown in Figure 3.6b. Apart from the misalignment, laser spot may spill over the cantilever and get reflected off from either the sample surface or the substrate surface so as to interfere with the reflected beam from the cantilever Figure 3.6c. This will cause the wavy artefact of the *P-h* curve, which should be consistently equivalent to zero when there is no interaction between the tip and sample. To solve this problem, the laser need be properly focused, or alternatively by using a laser with shorter coherence length instead, which facilitates the reduction of the laser speckles shown in Figure 3.6c.

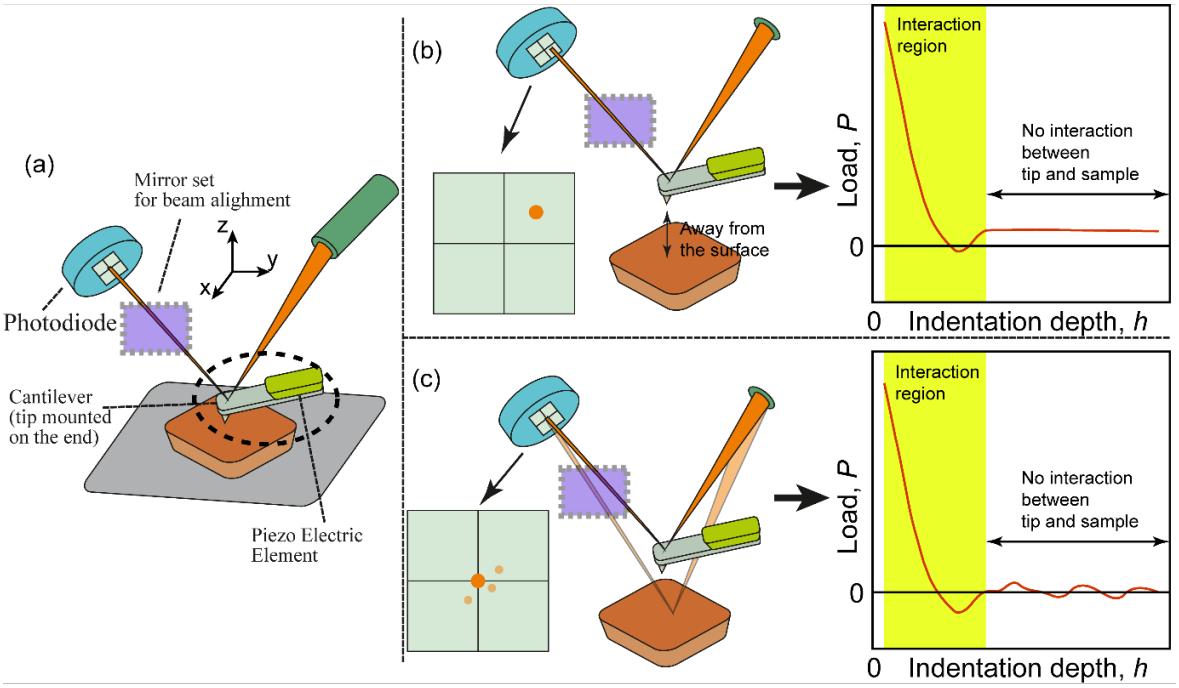

Figure 3.6 (a) Schematic of the operating principle of an AFM instrument. (b) Off-centred laser beam and the consequence of the shifted *P*-*h* curve. (c) Interference of the spilled laser reflected from the sample or substrate surface and the resulting wavy segment of the *P*-*h* curve.

3.4.5 Adhesive Force

In fact, all materials have certain levels of adhesive interaction with the indenter tip. On account of the influence of adhesive force on the mechanical measurement, a number of adhesion models have been developed such as the Johnson-Kendall-Roberts (JKR) and Derjaguin-Muller-Toporov (DMT) models, see §3.5.3 and §3.5.4. These models are able to shed light on both the adhesion characteristics and intrinsic mechanical properties of materials, such as the work of adhesion and elastic modulus.[86]

The presence of adhesive force complicates the mechanical characterisation in different ways. For example, the indenter-to-sample contact area becomes a function of load (P), sample elastic modulus, indenter tip radius, and energy release rate (refer to Ref. [268] for more details), and it tends to be exaggerated if the adhesion effect is neglected. In other scenarios, elastic modulus may be overestimated as well.[270] The deviation would be even

more significant if the sample stiffness and the indentation depth is relatively low. In addition, massive adhesion could offset the identification of the surface contact point because of the "jump-in" contact when the indenter approaches the surface.[104] From the numerical simulation standpoint (in §8.6.2), indenters of different geometries trigger distinctive adhesion effects.

It is advisable to leverage the energy release rate (G) and the work of adhesion (γ) to analyse the adhesive behaviour and this is not merely because of the complication of the force analysis, but also due to the probable imperfections of sample, such as roughness and heterogeneity. It is worth noting that only for a system in equilibrium, G equals to γ since G is loading rate dependent.[183, 269] Otherwise, error of the elastic modulus will occurs as pointed out by Notbohm *et al.*.[183] It is generally recognised that the adhesion effects on the loading and unloading segments are not analogous, and this can be explained from the energy standpoint that γ at the unloading stage is not constant within the contact area but descends from the centre to the periphery.[267] Therefore, sometimes it turns out to be better while applying certain adhesion models (e.g. JKR model) to the loading segment rather than the common option, i.e. the unloading part.[183, 267]

Adhesion effect may differ under the load-controlled or displacement-controlled loading schemes. Through the investigation of G, Notbohm *et al.* found that the displacement-control experiment is more stable than the load-control experiment with respect to the growth of fracture.[183]

3.4.6 Pile-up and Sink-in

Pile-up and sink-in are two common surface phenomena in indentation experiments. Losing sight of both introduces measurement errors on *E* and *H*, and the discrepancy could be as much as 50%. The errors are mainly owing to the deviation of contact areas. A case in point is the well-known Oliver-Pharr (OP) method which neglects the effect of pile-up.[88, 228]

With a view to the fact that plastic deformation plays the major role on the formation of pile-up and sink-in, Bolshakov and Pharr used finite-element (FE) method to explore their influence on a range of materials by simulating them to von Mises solids with discrete yielding as well as linear and isotropic strain hardening.[238] Notably, they discovered that pile-up predominates and increases under either one of the two subsequent conditions: reducing work hardening or the ratio h_f/h_{max} approaches to 1 where h_f denotes the final depth after fully unloading and h_{max} is the maximum depth. In essence, the implication of h_f/h_{max} can be explained by the close relevance of the pile-up and sink-in with the size of the plastic zone. While at $h_f/h_{max} < 0.7$, sink-in happens regardless of the degree of work hardening. But when $h_f/h_{max} > 0.7$, increasing work hardening starts to surpass pile-up, in other words, to stimulate sink-in. The impact of incremental work hardening becomes more pronounced when h_f/h_{max} is larger. These findings, of course, were derived from the study of conventional materials such as metals and ceramics, the applicability of this approach to nanoporous framework materials is not yet clear.

More effectively, Bolshakov and Pharr introduced the ratio between effective elastic modulus and yield stress (E_{eff}/σ_y).[238] They found the plastic zone decreases with decreasing E_{eff}/σ_y alongside the reduction of h_f/h_{max} (see Figure 3.8). In accordance with the aforementioned trend caused by decreasing h_f/h_{max}, once the plastic zone shrinks back to the contact circle, sink-in occurs instead of pile-up because there is only elastic deformation at the outer contact periphery. The concept of the plastic zone can also be used to explain

the inhibiting effect of work-hardening on pile-up because the large extent of the plastic deformation is squeezed to deeper area rather than being spread along the sample surface.[256] In other words, work-hardening of materials constrains the material flow towards the surface. Using the finite-element method, Cheng *et al.* examined the formation of pile-ups while indenting on a number of materials of different work-hardening behaviour.[260-262] They also proposed the possibility to analyse pile-up from an energy standpoint, i.e. the areas under the *P-h* curves.

In order to evaluate the distribution of plastic zone, Giannakopoulos *et al.* reported the elastic-plastic boundary produced by a Vickers indenter using the numerical (i.e. finite-element) and analytical methods.[224] Similarly, Larsson and co-workers utilised the finite-element and experimental methods to evaluate the performance of a Berkovich indenter.[258] Apart from Vickers (tetragonal base) and Berkovich (trigonal base) indenters, Giannakopoulos and Larsson also studied the plastic zone produced by a Knoop (rhomboid base) *via* the classic Drucker-Prager plastic potential to simulate the induced stress field.[259]

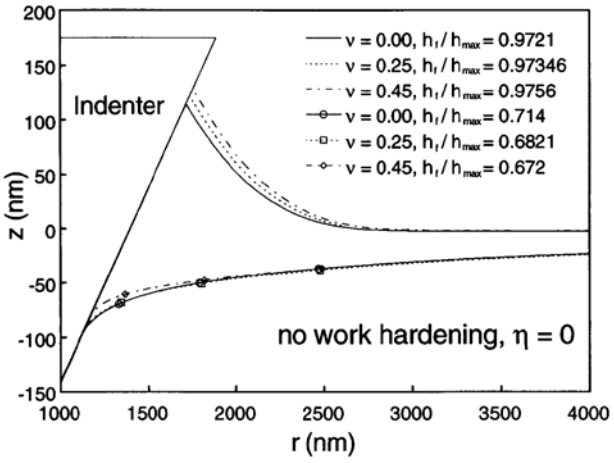

Figure 3.7 Contact profiles of an indentation of materials without work hardening presenting the influences of Poisson's ratio (ν) on the contact geometry. Reprinted from Ref. [238] with permission. Copyright (1998) Materials Research Society.

As Bolshakov *et al.* pointed out, the influence of Poisson's ratio (v) in the range of 0 to 0.45 on the generation of pile-up and sink-in can be broadly neglected.[238] Moreover, for work-hardening materials, the influence is even more subtle.

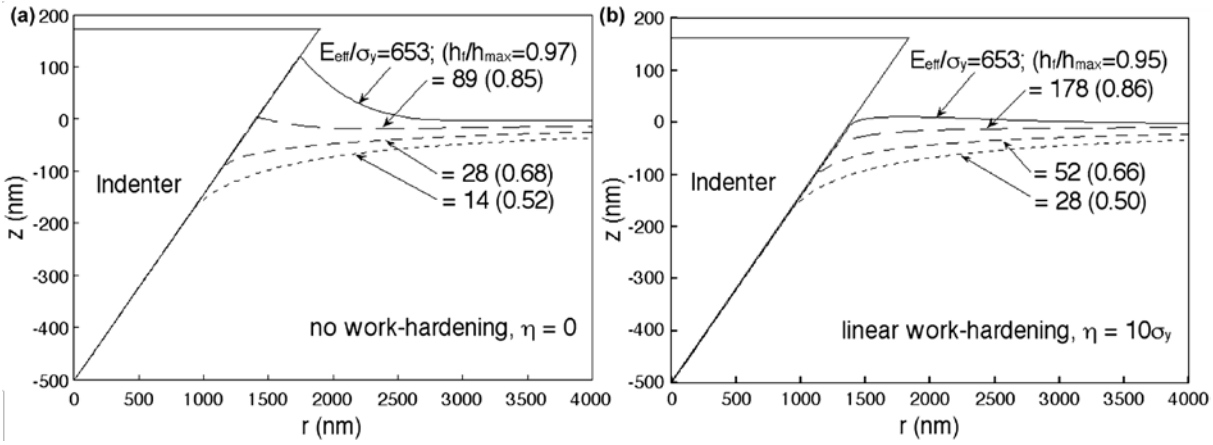

Figure 3.8 Contact profiles revealing the influence of the degree of work-hardening (η) (a) η = 0, (b) $\eta = 10\sigma_y$, as well as the elastic-plastic properties of materials (E_{eff}/σ_y) on pile-ups and sink-ins. Reprinted from Ref. [228] with permission. Copyright (2004) Materials Research Society.

For indentation of films attached onto a substrate, Saha and Nix found that pile-up is easier to form when a soft film situates on a hard substrate. Conversely, indentation tends to induce sink-in.[263] In regard to elastically homogeneous materials, accurate hardness value (considering both pile-up and sink-in) can be obtained on the condition that elastic modulus is known.[257]

Pile-up is not only formed due to plastic deformation, but also probable to generate by other factors, such as the lamellar deformation reported by Bedoui *et al.*, who observed double pile-ups while indenting a semi-crystalline polymer;[264] and the result discussed in Chapter 7. Another good example is the instrumented nanoindentation experiment of an anisotropic hybrid inorganic-organic framework material, $Cu_{1.5}(H_2O)(O_3PCH_2CO_2)$, wherein the extent of pile-up on the {010}-oriented facet is substantially higher than the {100}- and {001}-oriented facets owing to the underlying 2-D layered structures.[90]

3.4.7 Effect of Poisson's Ratio

Generally, for soft matter such as gel-like and biological entities, their Poisson's ratios (v) are assumed to be 0.5 by right of their incompressibility.[104, 170, 289-290] Alternatively, instead of neglecting the uncertainties of compressibility, one may also combine Young's modulus and Poisson's ratio into a single material constant, which is termed the indentation modulus (I). Nevertheless, under many circumstances of indentation, the variance of v ranging from 0 to 0.45 has only a minor impact on the contact profiles in terms of the pile-up and sink-in effect (see Figure 3.7).[238] However, the indentation analysis of materials with a highly anisotropic Poisson's ratio is not well investigated.

3.4.8 Influence of Loading Rate

For soft matter, slow loading rate usually leads to a much deeper indentation under the same load because of time-dependent behaviours, such as creep and thermal drift, as well as due to structural failure and fracture. As a consequence, the accurate measurement of both elastic modulus and hardness could be affected.

In the case of the creep effect, slow loading rate means longer indentation time, which facilitates the further indentation displacement leading to the exaggeration of contact area. To put it differently, indentation performed with a high loading rate tends to increase the measured elastic modulus, resulting in a value that is closer to the true stiffness of the specimen. It has been demonstrated by experiments that high loading rate could help to minimise the viscoelastic effects.[265-266] Moreover, the ascending trend of the elastic modulus with increasing loading rate were also observed in other mechanical property characterisation techniques such as uniaxial tensile test.[106] Therefore, by applying a high loading rate, the elastic moduli of viscoelastic materials can be solely extracted since the viscous component is diminished.

Likewise, the slow unloading rate could also result in the distortion of the unloading curve acquired as discussed in Chapter 5. Recently, it has been demonstrated that the distortion of the unloading curve can be overcome employing high unloading strain rate (see §4.7.3 and §5.3.1).[147]

3.4.9 Creep Effect (Load Holding Time and Unloading Rate)

The importance of an accurate unloading curve is unquestionable since majority of contact models concentrate on analysing its incipient portion. However, as introduced earlier in §3.4, there are several interfering factors that could obstruct the precise acquisition of it. More specifically, these factors tend to deviate the unloading process from the genuine elastic recovery reflecting the elasticity of material, thus leading to distorted unloading curve. More severely, if the unloading strain rate is rather small, the initial segment of the unloading curve would become a negative slope (bulging, see Figure 5.5).[147]

Taking the additional displacement caused by creep effect as an example, the most common way to alleviate it is to apply a stress or load hold period before the tip withdrawal. Moeller investigated the effect of the hold period on the measurement of E using AFM nanoindentation and reported that the measured E was closer to the literature value with increasing hold period.[180]

In addition, creep could also emerge during the entire unloading stage, and thus increasing unloading rate which corresponds to the reduced unloading time, will appreciably increase the residual depth.[180] Another method to diminish the creep effect is to do a cyclic indentation on the same position of a sample as I have demonstrated in Ref. [98]. Both methods are particularly useful for the equipment that cannot apply the hold period such as the Veeco Dimension 3100 AFM instrument. However, this cyclic indentation method might not be suitable for materials of high stiffness but relatively low hardness, e.g. aluminium,

and this is because of the hysteresis loops, namely reverse plasticity.[88] Actually, the hysteresis implies the persistent creep effect since creep deformation is mainly due to viscoplasticity rather than viscoelasticity.[180] Meanwhile, the effect of compaction (densification) should also be considered. Given these shortcomings, in this work the unloading strain rate principle was suggested since a high unloading strain rate was found to be able to surpass these interfering factors (see §4.7.3 and §5.3.1). Note that it differs from the unloading rate implemented in load control indenters.

3.5 Contact Mechanics Models

Note that the contact models directly used in the thesis are summarised in §4.7.

3.5.1 Hertz Model

Date back to 1881, Hertz reported his pioneering work on the pure linear elastic contact between two spheres without considering any form of surface force such as adhesive force or shear force.[291] In this classic contact mechanism, the two surfaces are assumed to be continuous and non-conforming (i.e. small displacements comparing with the dimensions of the contact bodies and no interpenetration). As a result, the contact area (A) can be treated as a flat and circular area, and it is:[232]

$$A = \pi\left(\frac{R_{\text{eff}}P}{E_{\text{eff}}}\right)^{\frac{2}{3}} \tag{3.1}$$

where R_{eff} is the effective radius of the two spheres, $R_{\text{eff}} = R_1R_2 / (R_1 + R_2)$, and R_1 and R_2 are the radii of the two spheres in contact; E_{eff} is the effective elastic modulus (also known as the reduced modulus) of the two spheres, and P is the load.

Hertz also discussed the case that indentation of an elastic 2-D half-space by using a rigid object. Soon after, Boussinesq extended this model to the 3-D cases.[292]

For indentation on a flat surface, Hertz model is valid if the elastically deformed material is isotropic and homogenous at the length scale of the indenter. However, the traditional Hertz model could result in appreciable deviations if the specimen is very thin.[103]

In the original Hertz model, the contact occurs between two semi-infinite spheres. Aiming at more practical uses, considerable efforts have been made to apply the Hertz model to experiments using indenters of other geometries including conical,[107, 170, 293], pyramidal,[294] paraboloid,[293] and hyperboloid.[293] Since an indenter is hardly absolutely sharp, many attempts have also been made to characterise such geometrical imperfections.[104, 107, 295-296]

3.5.2 Sneddon Model

Generalising the contact between two curved surfaces in the Hertz model, Sneddon obtained a more widely-applicable solution describing the contact between an axisymmetric indenter and a flat sample. In this method, the relationship between the loading force, depth, and contact area was expressed. More specifically, five special indenter geometries were discussed, and these incorporate a flat-ended cylindrical indenter, a conical indenter, a spherical indenter, an indenter of a paraboloid of revolution, and an indenter of an ellipsoid of revolution.[285] According to these relationships, the analytical model connecting the load and depth with the sample stiffness can be derived. The following equation is an example of using a conical indenter on an elastic sample:

$$P = \frac{2}{\pi}\tan\left(\frac{\theta}{2}\right)h^2\frac{E}{(1-\nu^2)} \tag{3.2}$$

where θ is the included angle of the indenter.

In light of its generalisation, the Sneddon method can be extended to cases with significant adhesion by appending a linear term of adhesion to the force-displacement equation (see §4.7.1 and §5.4.2).[147, 182]

3.5.3 Johnson-Kendall-Roberts (JKR) Model

On the basis of Hertz model, Johnson, Kendall, and Roberts refined the determination of contact area (*A*) by taking adhesive interaction between indenter and sample surface into account.[197] But only the adhesive forces within the contact area was considered. Regarding the adhesive interaction, the work of adhesion (i.e. the work required to separate per unit area, in J/m^2) can be defined as:[232]

$$\gamma = \gamma_{\text{indenter}} + \gamma_{\text{sample}} + \gamma_{\text{interfacial}} \tag{3.3}$$

where γ_{indenter} and γ_{sample} are the surface energy of the indenter and the sample surface, respectively; and $\gamma_{\text{interfacial}}$ is the interfacial energy.

For adhesive contact between two spheres, the contact area (*A*) and indentation depth (*h*) in the JKR model can be expressed by adding three terms of γ to the classical Hertzian model:

$$A = \pi \left[\frac{R_{\text{eff}}}{E_{\text{eff}}}\left(P + 3\pi\gamma R_{\text{eff}} + \sqrt{6\pi\gamma R_{\text{eff}}P + (3\pi\gamma R_{\text{eff}})^2}\right)\right]^{\frac{2}{3}} \tag{3.4}$$

$$a = \left[\frac{R_{\text{eff}}}{E_{\text{eff}}}\left(\sqrt{\frac{3}{2}\pi\gamma R_{\text{eff}}} + \sqrt{P + \frac{3}{2}\pi\gamma R_{\text{eff}}}\right)\right]^{\frac{1}{3}} \tag{3.5}$$

$$h = \frac{a^2}{R_{\text{eff}}} - \frac{4}{3}\sqrt{\frac{3a\pi\gamma}{2E_{\text{eff}}}} \tag{3.6}$$

Combining equations (3.5) and (3.6), the applied force and indentation depth can be directly correlated and then being used to fit the experimental data.

The pull-off adhesive force provided by the JKR model is:

$$P_{\text{ad}} = -\frac{3}{2}\pi\gamma R_{\text{eff}} \tag{3.7}$$

The JKR model can also be extended to other geometries, such as flat punches, spheres, and cones.[297]

The JKR model is propitious to systems where the indenter tip has a large radius of curvature and the sample surface has both strong and short-range forces with the indenter.[232] Furthermore, in the JKR model, the sample should be compliant enough to permit surface deformation to be attracted towards the indenter (see Figure 3.10).[105]

3.5.4 Derjaguin-Muller-Toporov (DMT) Model

The DMT model differs from the JKR model in the treatment of the adhesive force (P_{ad}). More specifically, in the DMT, P_{ad} is essentially being regarded as the addition of indentation load in order to maintain the shape of Hertzian contact.[298] That is to say that there is no effect of the interfacial forces on contact profile although the contact area increases with deeper indentation.[232] Unlike the JKR model, the DMT model considers the adhesive forces at the exterior region of the Hertz contact area by using the Lennard-Jones potential.[299] And thus P_{ad} in the DMT model is a long-range force in contrast to the one in the JKR.

The contact area allowing for the exterior adhesive force can be written as:

$$A = \pi \left[\frac{R_{\text{eff}}}{E_{\text{eff}}}(P + 2\pi\gamma R_{\text{eff}})\right]^{\frac{2}{3}} \tag{3.8}$$

$$a = \left[\frac{R_{\text{eff}}}{E_{\text{eff}}}(P + \sqrt{2\pi\gamma R_{\text{eff}}})\right]^{\frac{1}{3}} \tag{3.9}$$

$$h = \frac{a^2}{R_{\text{eff}}} \tag{3.10}$$

Thereby, P and h can also be related in this model. The pull-off adhesive force predicted by the DMT is:

$$P_{\mathrm{ad}} = -2\pi\gamma R_{\mathrm{eff}} \tag{3.11}$$

In contrast to the JKR model, the DMT model is suitable for the study of stiff samples exhibiting a low but more long-range adhesive forces, *viz.* shallower indentation and lower indention rate, when an indenter of smaller apex radius is used.

3.5.5 JKR-DMT Transition (Maugis-Dugdale) Model

As the consensus, either the JKR or DMT describes the extremities of the adhesive contact. To better capture the intermediate regime, Tabor's parameter (μ) has been proposed to bridge the JKR and DMT models, which is defined as:[300]

$$\mu = \left(\frac{R_{\mathrm{eff}}\gamma^2}{{E_{\mathrm{eff}}}^2 {Z_0}^3}\right)^{\frac{1}{3}} \tag{3.12}$$

where Z_0 is the equilibrium separation distance between the indenter and the sample surface.

A step forward, in the MD model, Maugis introduced a non-dimensional parameter λ for the JKR-DMT transition, in which the interaction between the contact surfaces was described using the Dugdale model (see Figure 3.10 for visualisation of the different zones attributed to the Hertz, DMT, JKR, and MD models), and λ can be expressed as:[301]

$$\lambda = 1.16\mu = 2\sigma_0 \left(\frac{R_{\mathrm{eff}}}{\pi\gamma {E_{\mathrm{eff}}}^2}\right)^{\frac{1}{3}} \tag{3.13}$$

where σ_0 is the constant adhesive stress.

As shown in Figure 3.9, the applicability of these adhesion models spans along an exclusive range of λ and the normalised load $\bar{P}$.

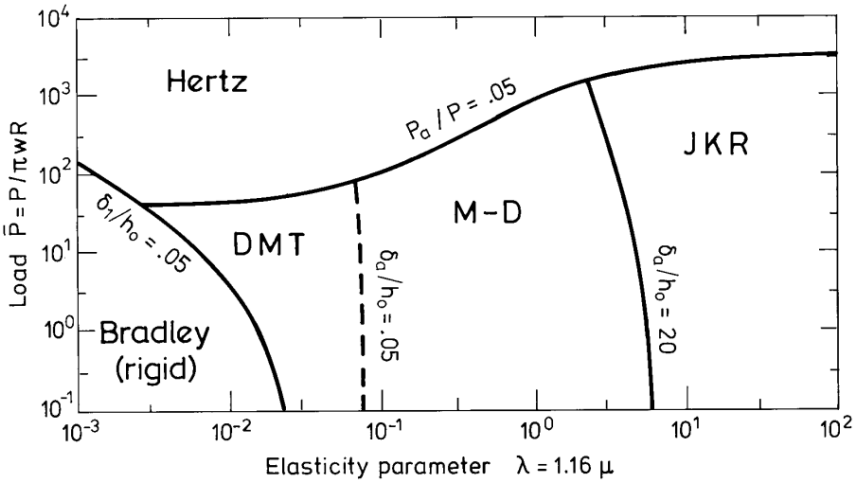

Figure 3.9 Adhesion map. Reprint from Ref. [302] with permission. Copyright (1997) Elsevier.

In order to analytically solve the adhesion effect on the *P-h* curve, Maugis suggested the use of four dimensionless parameters $\bar{P}$, $\bar{a}$, Δ, and m:[301]

$$\bar{P} = \frac{P}{\pi\gamma R_{\text{eff}}} \tag{3.14}$$

$$\bar{a} = a\left(\frac{E_{\text{eff}}}{\pi\gamma {R_{\text{eff}}}^2}\right)^{\frac{1}{3}} \tag{3.15}$$

$$\Delta = h\left(\frac{{E_{\text{eff}}}^2}{\pi^2\gamma^2 R_{\text{eff}}}\right)^{\frac{1}{3}} \tag{3.16}$$

$$m = \frac{c}{a} \tag{3.17}$$

where a is the radius of Hertz contact area and c is the radius of the entire stressed area in the DMT model. By virtue of these parameters, the normalised load ($\bar{P}$) and depth ($\bar{h}$) can be linked up by the following two equations:[301]

$$\bar{P} = \bar{a}^3 - \lambda\bar{a}^2\left[\frac{m^2}{\tan\left(\sqrt{m^2-1}\right)} + \sqrt{m^2-1}\right] \tag{3.18}$$

$$\bar{h} = \bar{a}^2 - \frac{4}{3}\lambda\bar{a}\sqrt{m^2 - 1} \tag{3.19}$$

In view of the difficulty for applying the MD equations to experimental data since *P* and *h* are not explicitly related, Piétrement and Troyon generalised the MD model into the PT model[303] on the basis of the Carpick-Ogletree-Salmeron (COS) equation[239]. The COS equation suggests that the external applied force (*P*) is related to the contact radius. More conveniently, the PT model proposes the direct correlation between *P* and *h* thus facilitating the practical fitting of experimental data. Both COS and PT models are empirical approximations of the MD scenario with reasonably good precision. Generalisation of the PT model benefits from the fact that the determination of contact area is not a prerequisite. Therefore it is easier to be applied to experimental results for working out the interfacial energy and elastic modulus.

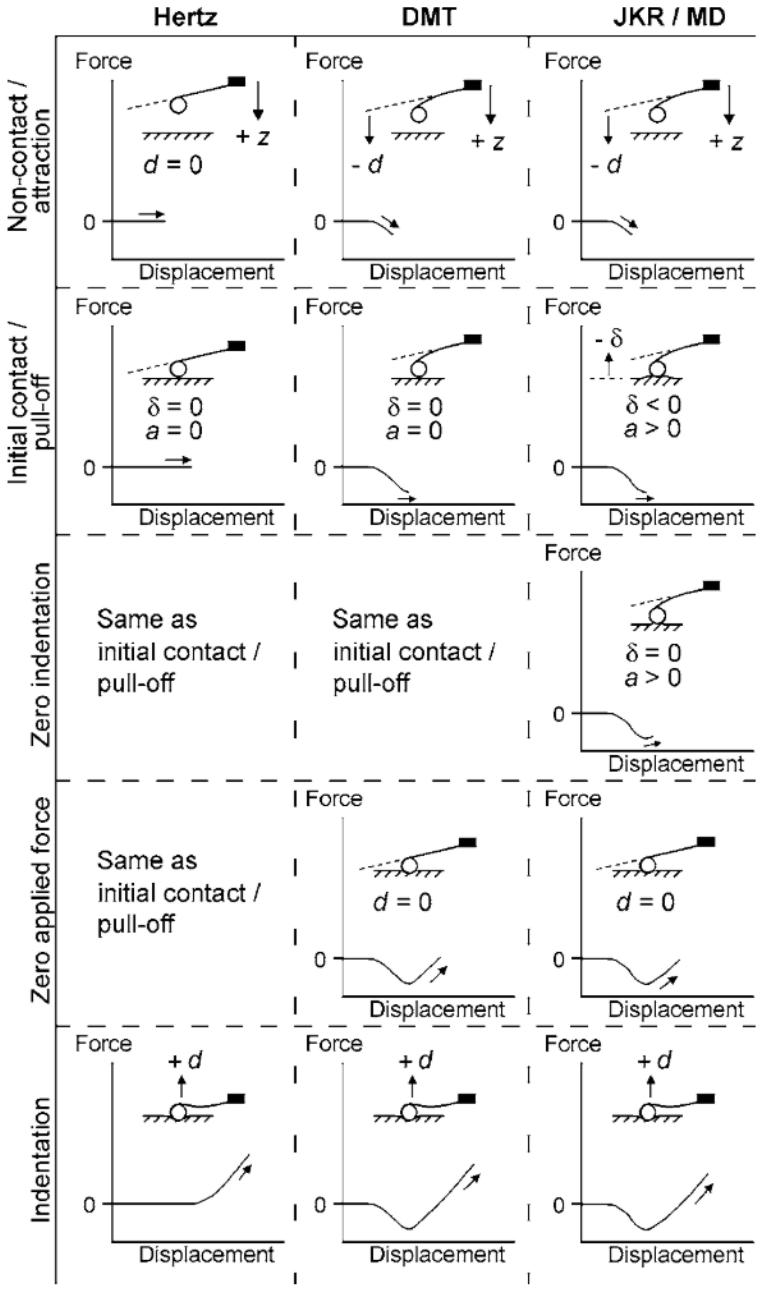

Figure 3.10 Schematic of *P-h* curves based on the four popular models and the later three considers adhesive interactions between the indenter and the sample surface: Hertz, DMT, JKR, and MD models. Reprinted from Ref. [105] with permission. Copyright (2007) American Society of Mechanical Engineers ASME.

Chapter 4: Materials and Methods

In this chapter, the methods used throughout the thesis are summarised. It starts by an introduction of the synthesis approaches of the three model MOF systems: ZIF-8, CuBDC, and HKUST-1, which exhibit distinctive structural characteristics. ZIF-8 crystal represents the nanomaterials of porous crystalline framework architecture with a low elastic anisotropy; CuBDC nanosheet typifies the crystalline nanomaterials in the 2-D form; HKUST-1 crystal epitomises anisotropic nanomaterials showing a strong adhesion property, and more importantly, it shows the auxetic behaviour which has not been properly addressed. Thenceforward, techniques for characterising sample topography *and crystallinity are introduced, which are followed by the techniques aiming at quantifying the nanoscale mechanical properties of MOFs. Amongst them are the instrumented nanoindentation and scratch technique as well as the AFM-based nanoindentation method. Subsequently, the contact models that were employed in the thesis are elucidated and then specifications of the finite-element models are covered. In the end, application of programming languages, viz Matlab and Python, are briefly described for processing the experimental and theoretical data.*

4.1 Sample Preparation: Synthesis of Metal-Organic Framework (MOF) Crystals and Nanosheets

All the reagents and solvents used in the following synthesis methods were purchased from commercial sources without further purification.

4.1.1 ZIF-8

In order to study the size effect of the nanostructural response of ZIF-8 to indentation, crystals of two different length scales were synthesised as follows.

4.1.1.1 Synthesis of Nanocrystals of ZIF-8

The nanocrystals of ZIF-8 used in this study were typically of 300 to 500 nm in diameter, as characterised in Figure 4.1 and Figure 5.1. Such ZIF-8 nanocrystals were synthesised by dissolving 4.5 mmol of zinc nitrate hexahydrate ($Zn(NO_3)_2 \cdot 6H_2O$, 98%, Sigma-Aldrich), and 13.5 mmol of 2-methylimidazole (98%, Sigma-Aldrich) in 60 mL methanol, respectively. The precursors were sonicated until the solutes were completely dissolved, then combined and heated in an oven at 40 °C for 1 hr, resulting in the formation of a white colloidal suspension comprising ZIF-8 nanocrystals. Sonication of the mixture

solution was avoided to prevent growth of ZIF-8 clusters; likewise, increasing the reaction time might lead to the formation of unwanted polycrystalline aggregates. Nanocrystals were isolated by centrifugation at 8000 rpm for 10 min, then the clear solution was removed before re-dispersing the extracted ZIF-8 in fresh methanol. The washing step was repeated 3 times to ensure the complete removal of excess reactants.

ZIF-8 nanocrystals were used to prepare a concentrated suspension in methanol (~5 mL), which was then drop casted onto a dust-free glass substrate held inclined at ~10° to 20° to the vertical direction. Using this approach, a polycrystalline thin film of ZIF-8 with a nominal thickness of ~2 μm was achieved and a root-mean-square roughness of ~80 nm (measured by a non-contact optical profilometer, Alicona InfiniteFocus). Figure 5.1b in Chapter 5 shows the X-ray diffraction pattern obtained from the drop-cast thin film, confirming the high crystallinity and phase purity of the ZIF-8 nanocrystals.

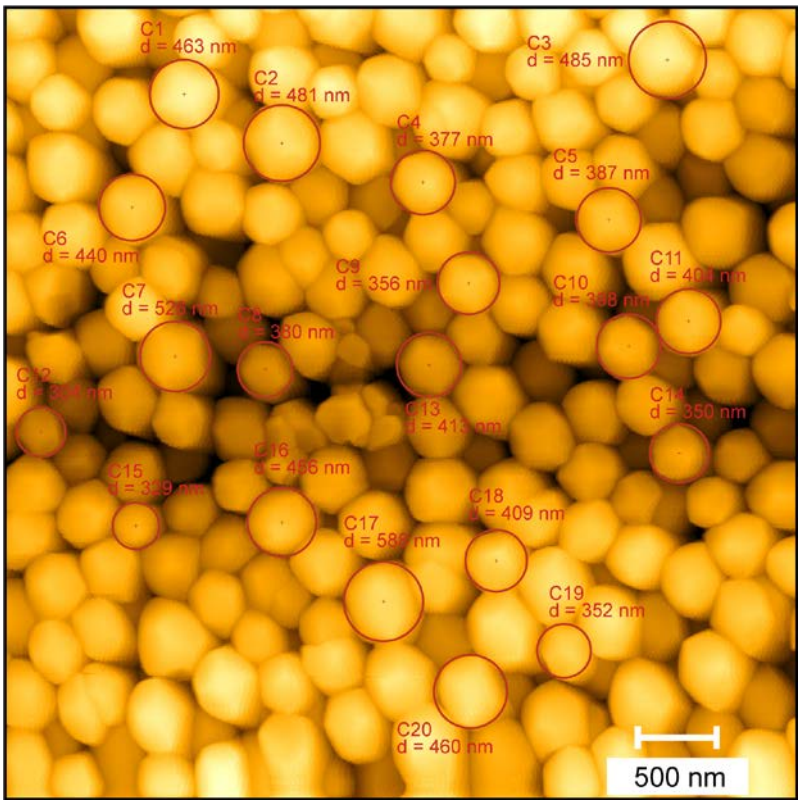

Figure 4.1 Sampling of ZIF-8 nanocrystals from an AFM image obtained using a silicon tip (Tap300Al-G) under the tapping mode. The averaged nanocrystal size was found to be 417.9 ± 170.1 nm, derived from 20 crystals.

4.1.1.2 Synthesis of Micron Crystals of ZIF-8

The micron-sized crystals of ZIF-8 employed in this study had a mean diameter of ~1–2 μm, synthesised using a solvothermal method. Two precursor solutions were prepared by dissolving 1.34 g (4 mmol) of zinc nitrate hexahydrate, and 0.334 g (4 mmol) of 2-methylimidazole in 40 mL of methanol, respectively. A mixture of 80 mL was obtained by combining the two precursor solutions, which was then left (without stirring) for 24 hr at room temperature. The product comprising micron-sized crystals of ZIF-8 (see Figure 5.10a-c in Chapter 5) was washed several times with methanol, centrifuged, and then dried overnight in a vacuum oven at 90 °C.

4.1.2 CuBDC

The CuBDC nanosheets were synthesised by a collaborator using the layering technique reported by Rodenas and co-workers.[49] In detail, 0.29 g of copper(II) nitrate trihydrate (Sigma-Aldrich) was dissolved in a mixture of 5 mL of *N*, *N*-dimethylformamide (DMF) and 10 mL of acetonitrile in a glass vial with the assistance of ultra-sonication. Similarly, equimolar quantity of terephthalic acid (0.2 g, Sigma-Aldrich) was dissolved in a mixture of 10 mL of DMF and 5 mL of acetonitrile. The terephthalic acid solution was placed in a glass test tube. A mixture of 2 mL of DMF and 2 mL of acetonitrile was added on the top of the terephthalic acid layer dropwise to create a separation layer. The copper(II) terephthalate solution was added slowly dropwise as a third layer. The test tube was left in an oven at 40 °C overnight. As a result of the Cu^{2+} ions diffusion to the bottom layer and interaction with terephthalic acid, the CuBDC nanosheet crystals were formed. The CuBDC crystals were centrifuged and washed with DMF three times and then methanol three times with ultrasonication. After drying in a vacuum oven at 40 °C overnight, the yield of CuBDC was determined to be ~18 wt.% (a fractional amount of solvent may remain in the pores, and thus introducing deviations), this relatively low yield is in agreement with Ref. [304].

4.1.3 HKUST-1 (CuBTC)

The submillimetre-sized crystals of HKUST-1 were prepared using a solvothermal method. Similar to the role of the lauric acid (see Figure 2.8), in this method, the glacial acetic acid was used as the modulator and found to be more effective and reproducible.[58] The procedure is summarised below.

0.49 g of $Cu(NO_3)_2 \cdot 3H_2O$ was first fully dissolved in 3 mL of deionized water and then mixed with 3 mL of *N*,*N*-dimethylformamide (DMF) in a scintillation vial (20 mL) forming the $Cu(NO_3)_2$ solution. Meanwhile, 0.24 g of H_3BTC (trimesic acid) was dissolved in 3 mL of ethanol (mild heating to assist with dissolution). Thereafter, the H_3BTC solution and 12 mL of glacial acetic acid were successively added to the $Cu(NO_3)_2$ solution and then the vial was placed in a furnace at 55 ^oC for 3 days. The synthesis resulted in the growth of blue HKUST-1 crystals found on both the wall and the bottom of the vial. The solution then removed and the crystals were immersed in ethanol for a minimum of 3 days for solvent exchange. It is worth noting that the crystals collected from the bottom of vial were susceptible to defect since they were prone to aggregate. Therefore, it is advisable to store the crystals from the wall and the bottom separately in different vials of ethanol. If needed, the crystals can be activated in a vacuum oven at 120 ^oC overnight.

4.2 Topography of Nanomaterials: Atomic Force Microscopy

4.2.1 Atomic Force Microscopy (AFM)-Based Imaging

One of the primary applications of AFM is for imaging, which offers superior resolution (over 1000 times higher than the optical microscope, which is limited by the diffraction limit). In addition to provide the similar level of resolution as those of transmission electron microscopes, AFM is also capable of reconstructing the 3-D height

topography of specimen, which enables quantitative characterisation of surface waviness and roughness at the nanoscale.

However, the topographic image captured by AFM is usually not absolutely precise and the inherent artefacts of AFM imaging are associated with the incomplete convolution between the indenter tip and the sample surface. Typically, certain features of the sample surface, such as protrusions in AFM image become wider than the real ones, likewise holes appear to be narrower and shallower (more details are available in §3.4.2). For the purpose of error reduction, ideally the radius of indenter tip should be smaller than the radius of surface features to be measured. Implementation of a suitable tip deconvolution approach can be used to reduce the imaging errors.[305]

AFM imaging were performed herein using the Veeco Dimension 3100 instrument operating under the tapping mode. Different types of probes have been employed including the silicon probes such as Tap300Al-G (BudgetSensors), Scout 350 and Scout 350 HAR – high aspect ratio (NuNano). In addition to the three silicon AFM probes that were designed for high imaging accuracy, under certain circumstances, a less sharp diamond indenter tip has also been employed for *in situ* imaging of indents at the expense of losing sharpness of the images (accurate characterisation of the indenter tip geometry is given in §4.2.2). The specifications of the cantilevers and tips of the three silicon probes are summarised in Table 4.1.

Table 4.1 Specifications of the AFM imaging probes from manufacturers

AFM Tip	Manufacturer	Tip Apex Radius (nm)	Cantilever Length (μm)	Cantilever Width (μm)	Cantilever Thickness (μm)	Resonance Frequency (kHz)	Spring Constant (N/m)
Tap300Al-G	BudgetSensors	< 10	125	30	4	300	40
Scout 350	NuNano	< 10	125	30	4.5	350	42
Scout 350 HAR (high aspect ratio)	NuNano	< 10	125	30	4.5	350	42

4.2.2 Geometrical Characterisation of the Cube-Corner Indenter Tip

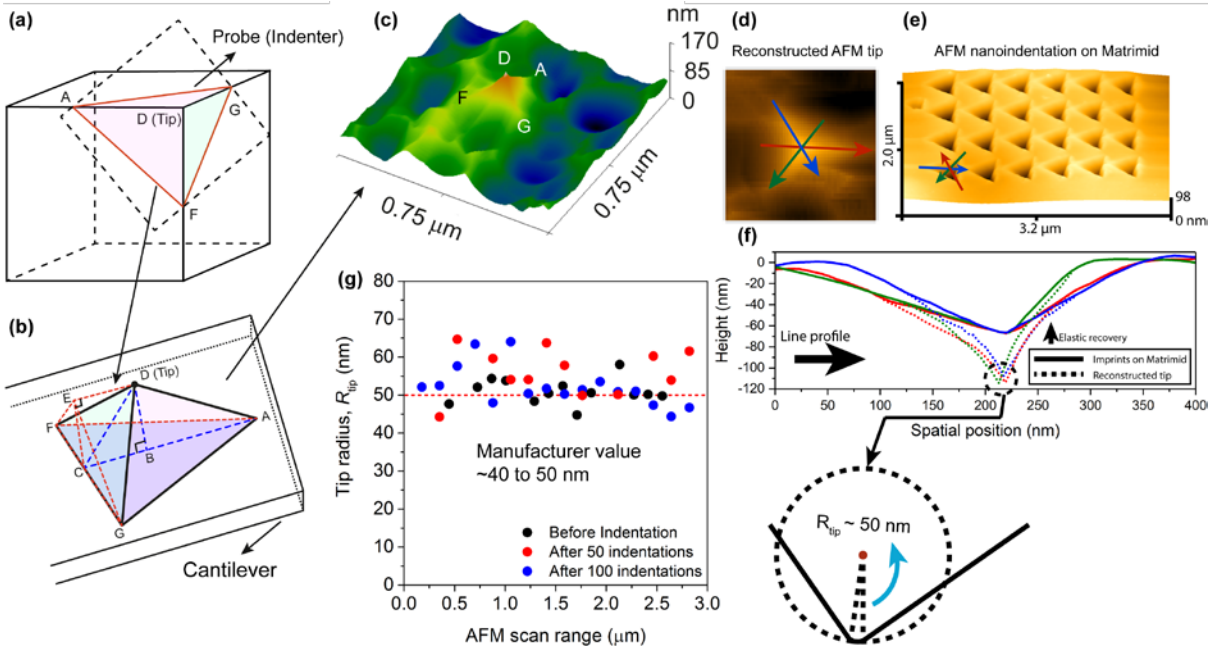

Figure 4.2 (a-b) Schematics of a cube-corner indenter, which can be used to implement both AFM imaging and *in situ* nanoindentation.[147] (c-d) Height topographic images (in two distinguishable modes of colour map) of the indenter tip geometry reconstructed *via* the Villarrubia algorithm.[226] (e) Residual indents generated by the indenter after unloading, and (f) the corresponding line profiles indicating the radius of the diamond indenter apex (r ~50 nm) acquired by the Villarrubia algorithm.

The Villarrubia blind estimation algorithm[226, 306] was adopted to reconstruct the geometry of the indenter tip due to the fact that the indenter could be worn/abraded over a period of time leading to the change of contact area at a certain depth. The algorithm was implemented in the Gwyddion software[307]. Essentially, the blind estimation algorithm is an indenter reconstruction method, which is able to determine similarly represented indenter geometry based on the fact that AFM image of tested sample contains information of both the sample morphology and tip geometry. In order to extract the tip geometry, the algorithm iterates over each point of the input AFM image. The algorithm complies with the rationale that when an indenter tip is imaging a surface feature, such as a protrusion, in the meantime, the surface protrusion is actually scanning the indenter tip in the opposite direction. By

means of the algorithm, it was confirmed as shown in Figure 4.2g that the geometry of the diamond indenter has been consistently intact even after performing more than 200 indentations on relatively soft materials (Young's moduli of the samples tested in this study are < 50 GPa).

As shown in Figure 4.3d, usually the features imaged are broadened compared to the actual features of the sample (more examples are in §3.4.2). Conversely, regarding the scanning as a process to image the indenter by surface protrusions as shown in Figure 4.3c, these protrusions are actually broadened replicas of the indenter. Therefore, as illustrated in Figure 4.3e, an estimated geometry can be obtained by using the blunt indenter as a reference to fit each point of the 3-D image of the sample surface, and then subtracting all the restricted portions (represented as the regions enclosed by the dashed green boundary and the sample surface).

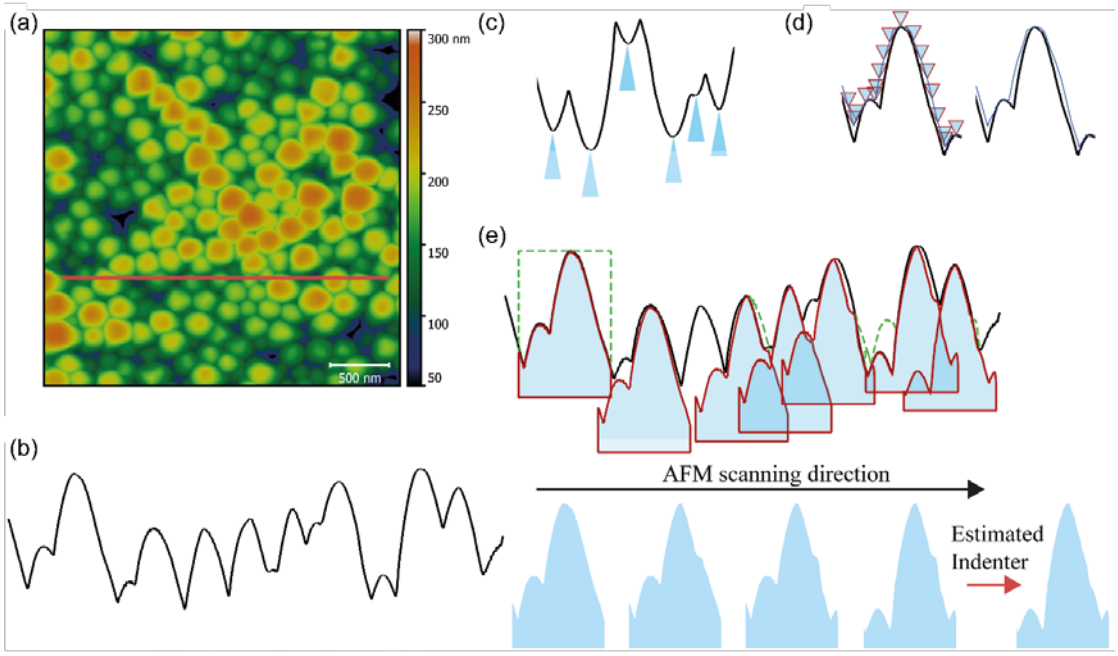

Figure 4.3 (a) Depth image of polycrystalline ZIF-8 nanocrystals (deposited as a thin-film coating on a glass substrate) obtained by using the AFM PDNISP indenter tip, which later served as the input data for the blind tip estimation algorithm. (b) Profile curve is a 1-D topography at the red-line position shown in (a). (c) From a different perspective, AFM tip had been imaged by protrusions of sample surface during the scanning process. (d)

AFM images are broadened replicas of the real surface features. (e) Schematic illustrating the procedure of the blind tip geometry estimation algorithm developed by Villarrubia.[226]

Table 4.2 shows the dimensions estimated for the cube-corner indenter tip used in this thesis, with which the nominal contact area as a function of the indentation depth, $A(h)$, can be determined.

Table 4.2 Dimensions of the diamond cube-corner indenter tip: (left) included angles and (right) side lengths at the indentation depth h_{DB} = 50 μm, they were derived by applying the Pythagorean Theorem.

Angles of the indenter				At indentation depth (μm) h_{DB} = 50	
	$*^1$	$*^2$			
Front angle $\angle_{ADB}$	55 ± 2^o	58.2422^o		Side length L_{AB}	71.4074
Back angle $\angle_{CDB}$	35 ± 2^o	35.1542^o		Side length L_{CB}	35.0104
Side angle $\angle_{CEF}$	51 ± 2^o	49.1985^o		Side length L_{FC} (L_{GC})	61.7449
Equivalent conical angle (2θ)*		91.4667^o		Side length L_{AG} (L_{AF})	123.0332

$*^1$: The manufacturer's specifications

$*^2$: The real-time included angles of the cube-corner tip reconstructed by applying the Villarrubia algorithm.

*: An equivalent conical indenter tip of the included angle is 2θ, which has the same surface area as the cube-corner indenter tip (see the concept of "effective indenter shape" in §3.4.3).

4.3 Topography of Nanomaterials: Electron Microscopy

4.3.1 Scanning Electron Microscopy and Transmission Electron Microscopy

The scanning electron microscopy (SEM) images in this thesis were taken using two instruments, and they are the Carl Zeiss Evo LS15 VP-scanning electron microscope and the Hitachi TM3030Plus tabletop microscope. Both microscopes were equipped with the back-scatter detectors and secondary electron detectors. Charging-up damage could accumulate on the MOF sample surface in both microscopes. To deal with this issue, in the Carl Zeiss SEM, gaseous environment can be created under the environmental SEM mode. For the Hitachi tabletop SEM under a high vacuum condition, a reduced charge-up mode works well in the MOF systems. For improved imaging, a gold sputter coating favours the protection of a sample surface by coating it with a nanoscale gold layer. However, none of the sample surfaces prepared for indentation was sputter coated since it was likely to alter their mechanical properties.

The transmission electron microscopy (TEM) images were collected using a JEM 2100 LaB6 TEM operating at 200 keV. TEM was required to image the ultrathin samples of the CuBDC nanosheets (Chapter 7).

4.4 Topography of Nanomaterials: InfiniteFocus Profilometry

4.4.1 Alicona Profilometer

The majority of the optical images in this thesis were collected using an Alicona InfiniteFocus 3-D profilometer, which is equipped with 5, 10, 20, 50, 100× objectives. Alicona profilometer is also an excellent instrument for acquiring the waviness and roughness of sample surface by right of its non-contact InfiniteFocus technique, which realises the vertical scanning through varying the focal plane. Submicron roughness can be

measured using this instrument (>30 nm). An example of the optical images is for the polished HKUST-1 crystal embedded in a cured epoxy resin (see Figure 8.2b-c).

4.5 Crystallography of Nanomaterials

4.5.1 X-ray Diffraction

For the purpose of confirming the crystallinity of the MOF samples, X-ray diffraction (XRD) has been used. Briefly, as waves of electromagnetic radiation elastically scatter by the electrons of atoms, they are augmented constructively in specific directions. Along these directions, the spacing between diffracting planes and corresponding incident angles can be determined by the Bragg's law.[308]

Two instruments were utilised to perform the X-ray diffraction, they are: Rigaku Smart Lab diffractometer [Cu Kα source (1.541 Å)]. XRD measurements were performed at 1^{o} min^{-1} step speed and 0.01^{o} step size, to confirm the crystallographic structure of the synthesised samples, which were prepared by drop casting of uniform MOF samples onto glass substrates and were activated subsequently *via* heat treatment in a vacuum oven.

4.6 Mechanical Properties of Nanomaterials

4.6.1 Instrumented Nanoindentation Technique (IIT)

For micron-sized materials, the instrumented nanoindentation technique (IIT) was performed using the MTS Nanoindenter® XP (Agilent) to determine the continuous stiffness data. The instrument was well isolated from external perturbation by a buffering platform and a cabinet. The MTS nanoindenter was equipped with a Berkovich indenter of tip apex radius ~100 nm, whose total included angle is ~142.3^{o}. The MTS nanoindenter can sense

load below 50 nN, which determines that it can only be employed for measuring materials of much larger surface area (~4 million times larger) than AFM (load resolution < 0.05 nN).

The maximum indentation load provided by the MTS nanoindenter was usually larger than 1000 μN. In this thesis, samples were consistently indented down to 2 μm since this depth was found to be optimal to avoid any tip geometry calibration errors at shallow depth and minimising damages on MOFs such as cracks at deeper depth.

4.6.2 Instrumented Scratch Technique (IST)

Nanoscratch experiments were also implemented using the MTS Nanoindenter® XP in order to characterise the failure mechanisms and adhesion behaviours of thin film coatings that were composed of MOF crystals. The lateral stresses exerted by scratching into the MOF coatings is able to determine their attachment on different substrates and this is of crucial importance in practical applications. The results are shown in §6.4 of Chapter 6. Likewise, AFM indenter is also capable of doing nanoscratch but at a much smaller area.

4.6.3 Atomic Force Microscopy (AFM)-Based Nanoindentation

4.6.3.1 AFM Nanoindentation Using a Diamond-Tipped Cantilever Probe

AFM nanoindentation experiments were performed using the Veeco Dimension 3100 instrument operating under the indentation mode, equipped with a Bruker PDNISP probe. The AFM probe consists of a 350 μm long stainless steel cantilever, at the end of which mounted a cube-corner diamond indenter tip. Its spring constant and contact sensitivity have been calibrated by the manufacturer, and given as 152.285 N/m and 256.6 nm/volt, respectively.

Establishing accurate geometry of the indenter tip is extremely important for enabling quantitative measurements of the fine-scale mechanical properties since it is often necessary to accurately measure the true contact area established between the indenter tip

and material. Herein to ascertain the actual tip geometry, the blind tip estimation algorithm developed by Villarrubia was adopted (Figure 4.3),[226] which has been validated by experiments.[306] The dimensions of the cube-corner indenter tip are shown in Table 4.2 in §4.2.2.

4.6.3.2 Loading Scheme of the Veeco Dimension 3100 AFM Instrument

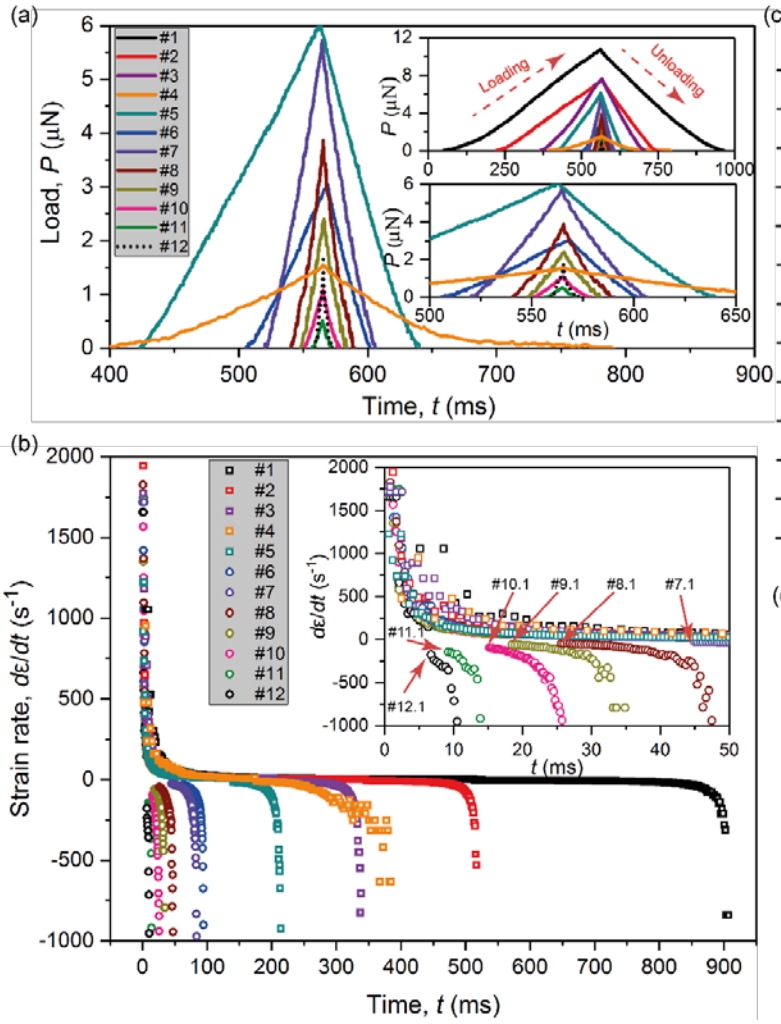

(c)

Numbering	Loading rate dP/dt (μN/ms)	Unloading rate dP/dt (μN/ms)
#1	0.02510	-0.03000
#2	0.02317	-0.04409
#3	0.04226	-0.05888
#4	0.01134	-0.01506
#5	0.04377	-0.08815
#6	0.05074	-0.09653
#7	0.13045	-0.14747
#8	0.18254	-0.15720
#9	0.13883	-0.13596
#10	0.07475	-0.10079
#11	0.06247	-0.06555
#12	0.24631	-0.21234

(d)

Numbering	Unloading strain rate $d\varepsilon/dt$ (s^{-1})
#7.1	-25.98156
#8.1	-45.79584
#9.1	-59.19862
#10.1	-94.95218
#11.1	-144.62021
#12.1	-178.45653

Figure 4.4 Loading versus time plot illustrating the loading scheme of the AFM instrument

As shown in Figure 4.4, the strain rate decreases continuously with indentation depth during the loading stage. Then after the singularity, i.e. the deepest point (h_{max}), the strain rate increases at the opposite direction until the detachment between the indenter and the

specimen occurs. This phenomenon explains why the occurrence of the negative-gradient curve only exists at the incipient segments of the unloading curves. In other words, the increasing unloading strain rate over time is favourable to minimise the creep effect.

The indentation strain rate (s^{-1}) can be correlated to the vertical displacement of the indenter tip, penetrating into the surface:

$$\frac{d\varepsilon}{dt} = \dot{\varepsilon} = \frac{\dot{h}}{h} \tag{4.1}$$

In the Veeco Dimension 3100 AFM instrument, the load variation over indentation time, $\dot{P} = \partial P/\partial t$, can be maintained constant during each of the indentation cycle (Figure 4.4). In the experiments, the magnitude of $\dot{P}$ during the loading and unloading test segments can be tuned by varying the AFM scan rate (V) and the cantilever probe deflection (δ). The strain rate at the maximum indentation depth can be determined from $\dot{\varepsilon} = \dot{P}/P_{max}$,[309] coinciding with the initial point where the indenter starts to unload.

Therefore, in this work, the loading rate ($\dot{P}$) is a controllable parameter. Assuming that hardness (H) of ZIF-8 crystals is homogeneous, i.e. invariant during the entire indentation process, the mathematical expression of the strain rate can be simplified into:

$$\begin{aligned} \dot{\varepsilon} = c_1\left(\frac{\dot{h}}{h}\right) = c_1\left(\frac{1}{h}\cdot\frac{dh}{dt}\right) = c_1\left(\frac{\sqrt{c_2 H}}{\sqrt{P}}\cdot\frac{1}{\sqrt{c_2 H}}\cdot\frac{1}{2}\cdot\frac{1}{\sqrt{P}}\cdot\frac{dP}{dt}\right) \\ = c_1\left(\frac{1}{2P}\cdot\frac{dP}{dt}\right) = \frac{c_1}{2}\cdot\frac{\dot{P}}{P} = c_3\cdot\frac{\dot{P}}{P} \end{aligned} \tag{4.2}$$

In equation (4.2), P is the indentation load that can be expressed in terms of the contact area (A) and hardness (H) as:

$$P = A\cdot H = \frac{\pi h^2 tan\theta}{cos\theta}\cdot H = c_2 h^2 H \tag{4.3}$$

Thus, the indentation depth that can be substituted into equation (4.2) is:

$$h = \frac{\sqrt{P}}{\sqrt{c_2 H}} \tag{4.4}$$

where θ in equation (4.3) is the equivalent conical half-angle, and c_1 to c_3 are material constants that are sample dependent.

4.7 Contact and Adhesion Models

A suitable contact model that precisely describes the response of material to indentation is central to extract mechanical properties of interest. There are a number of contact models formulated in the literature to adapt to the different complexities of different contact problems. In the thesis, twelve prevailing contact models have been summarised in Chapter 3 and Chapter 4, and they can be divided into two categories. Models in the first category (§3.5) are relevant but not being directly used in my study, they are: Hertz model,[291] Sneddon model,[285] Derjaguin-Muller-Toporov (DMT) model,[298] Johnson-Kendall-Roberts (JKR) model,[197] and Maugis-Dugdale (MD) model.[301] The remainders are the models either being adopted or further expanded in this work (§4.7): the adhesion model developed based on Sneddon method, Oliver and Pharr (OP) model,[88, 228] unloading strain rate principle, Lennard-Jones (LJ) model,[299] Derjaguin's approximation,[310] Carpick-Ogletree-Salmeron (COS)[239] and Piétrement-Troyon (PT)[303] approximations, as well as the numerical simulation method.

4.7.1 The Adhesion Model Based on the Sneddon Method

Adhesion usually has significant influence on the unloading process of AFM indenter, which exerts and senses nN-μN level forces. Under the coupling effect of elastic and adhesive forces, the resulting force-displacement (*P*-*h*) curve is often distorted from the pure elastic-plastic deformation. The true interaction force between the indenter and the sample is given by the following equation:[182]

$$P = P_{\text{elastic}} + P_{\text{adhesive}} \tag{4.5}$$

The cube-corner geometry can be converted into equivalent conical indenter geometry based on the same contact area criterion (a type of "effective indenter shape", see §3.4.3 and Table 4.2).

$$R_{\text{contact}} = f(h_{\text{contact}}) \tag{4.6}$$

Due to the possible sink-in, the real indentation depth of the contact surface is a function of displacement from the sample surface:[182]

$$h_{\text{contact}} = (1 - \epsilon_2)h \tag{4.7}$$

where $\epsilon_2 = 1 - \frac{2}{\pi}$ for a conical indenter-to-sample contact mechanism. According to the Sneddon solution of elastic behaviour for a conical indenter,[285] elastic force on the sample can be represented by a function of the indentation depth:

$$P_{\text{elastic}} = \left(\frac{2E^*}{\pi}\right) tan\,\theta \cdot h^2 \tag{4.8}$$

The correlation of the true indenter-to-sample contact area and indentation depth for the equivalent conical indenter of semi-vertical included angle θ is:

$$A_{\text{contact}} = \frac{\pi \cdot tan\,\theta}{cos\,\theta} \cdot {h_{\text{contact}}}^2 \tag{4.9}$$

In order to investigate the influence of adhesive force on the sample behaviours in response to indentation, the energy of adhesion is considered as follows:[182]

$$W_{\mathrm{ad}} = -\gamma A_{\mathrm{contact}} \tag{4.10}$$

where γ is the thermodynamic work of adhesion.

Substituting equations (4.4), (4.6) and $\epsilon_2 = 1 - \frac{2}{\pi}$ into equation (4.7), an expression for the energy of adhesion can be derived. Subsequently, differentiating energy with respect to the indentation depth gives the adhesive force, which is:

$$P_{\mathrm{adhesive}} = -\gamma \cdot \frac{8tan\,\theta}{\pi cos\,\theta} \cdot h \tag{4.11}$$

Therefore, substituting equations (4.5) and (4.8) into equation (4.2) returns the true interaction force produced between the indenter and the sample:

$$P = \frac{2E \cdot tan\,\theta}{(1-v^2)\pi} \cdot h^2 - \gamma \cdot \frac{8tan\,\theta}{\pi cos\theta} \cdot h \tag{4.12}$$

In this work, the thermodynamic work of adhesion, can be expressed as a linear function of indentation depth, which is:

$$\begin{aligned} P &= \frac{2E \cdot tan\,\theta}{(1-v^2)\pi} \cdot h^2 - (k_1 h + k_2) \cdot \frac{8tan\,\theta}{\pi cos\theta} \cdot h \\ &= \left[\frac{2E \cdot tan\,\theta}{(1-v^2)\pi} - \frac{8k_1 tan\,\theta}{\pi cos\theta}\right] \cdot h^2 - \frac{8k_2 tan\,\theta}{\pi cos\theta} \cdot h \end{aligned} \tag{4.13}$$

4.7.2 Oliver and Pharr (OP) Method

Normally, four quantities can be extracted from an undistorted *P*-*h* curve, they are: (i) the maximum indentation depth, $h_{\max}$; (ii) the maximum load, $P_{\max}$, developed at $h_{\max}$; (iii) the final (residual) indentation depth after complete unloading, h_{f} ; (iv) the elastic contact stiffness, $S = \mathrm{d}P/\mathrm{d}h$, corresponding to the slope of the incipient segment of the

unloading curve. To determine *S*, the unloading curve fitted with the power-law relation shown below is differentiated:[228]

$$P(h) = a(h - h_{\text{final}})^b \tag{4.14}$$

where *a* and *b* are the curve fitting constants.

As Oliver and Pharr mentioned in Ref. [88], unloading curves including the initial parts of most materials are nonlinear, which invalidates many models at the early stage, such as the Doerner-Nix method.[311] As a result, it became a controversial issue to which fraction of an unloading curve should be fitted. With regard to this issue, the power law fitting is recommended to derive the contact stiffness.[285] First derivation of the power law equation on the initial portion suggests that the upper 1/3 portion[311] of an unloading curve can be fitted to determine the contact stiffness of material.

In the standard OP model,[228] indentation of the elastic half-space by a rigid axisymmetric indenter was used to model the contact periphery sink-in of an elastic material, but the pile-up effect caused by elastic-plastic deformation has been neglected. In this case, the indentation depth is given by:

$$h_{\text{contact}} = h_{\max} - h_{\text{sink-in}} = h_{\max} - \epsilon_1 \frac{P_{\max}}{\left(\frac{dP}{dh}\right)} \tag{4.15}$$

where ϵ_1 is a geometrical constant, equivalent to 0.75 for an effective indenter shape that is resembling a paraboloid of revolution.[285] Therefore, the contact area can be defined as:

$$A_{\text{contact}} = f(h_{contact}) \tag{4.16}$$

Some AFM instruments are equipped with accurate depth-sensing and contact-point recognition capabilities, to facilitate the determination of $f(h_{\text{contact}})$ provided that the tip geometry is known. In the analysis, the criterion for contact point to be established was

applied when the contact stiffness, $S \geq 25$ N/m. The value of contact area can then be found and applied for calculating the "indentation hardness", defined by:

$$H = \frac{P_{\max}}{A_{\text{contact}}} \tag{4.17}$$

Likewise, accurate determination of the magnitude of contact area is important for quantification of the effective (reduced) modulus:[228]

$$E_{\text{eff}} = \frac{1}{2\beta} S \frac{\sqrt{\pi}}{\sqrt{A_{\text{contact}}}} \tag{4.18}$$

where β is a dimensionless correction factor to account for the non-symmetrical pyramidal shape of the indenter tip. Using finite-element analysis and analytical method, Hay *et al.* developed the following expression to approximate the β parameter for an equivalent conical indenter:[312]

$$\beta = \frac{\pi \left[\frac{\pi}{4} + 0.1548 \, cot \, \theta \, \frac{1-2v}{4(1-v)}\right]}{\left[\frac{\pi}{2} - 0.8312 \, cot \, \theta \, \frac{1-2v}{4(1-v)}\right]^2} \tag{4.19}$$

where θ is the included half-angle of the indenter. Because the axisymmetric equivalence of the cube-corner indenter is a cone, for the indenter tip used in this thesis the value of θ was 45.7333° (see Table 4.2). In Chapter 5, the Poisson's ratio (v) of ZIF-8 was taken as 0.4, corresponding to that of a polycrystalline (isotropic aggregate) ZIF-8.[7] Applying equation (4.19), returns β = 1.1093.

Because the stiffness of the diamond indenter tip (1141 GPa) is substantially higher than that of the MOF samples to be probed (typically in the range of several GPa as reported in Ref. [38]), the effective modulus equation can be simplified as follows:

$$\frac{1}{E_{\text{eff}}} = \frac{1 - {v_{\text{sample}}}^2}{E_{\text{sample}}} + \frac{1 - {v_{\text{indenter}}}^2}{E_{\text{indenter}}} \approx \frac{1 - {v_{\text{sample}}}^2}{E_{\text{sample}}} \tag{4.20}$$

Thus the elastic modulus of the sample can be expressed as:

$$E_{\text{sample}} = \frac{1}{2\beta}(1-\nu^2)S\frac{\sqrt{\pi}}{\sqrt{A_{\text{contact}}}} \tag{4.21}$$

Another advantage of the OP method is its extensive applicability since it is not only suitable for geometrically self-similar sharp indenter tips, but also fits majority of axisymmetric ones. The parameter β was introduced to correct the errors caused by the deficiency of asymmetry of the indenters. More importantly, Oliver and Pharr delivered an in-depth discussion about the concept of "effective indenter shape" (see §3.4.3 and §4.2.2).[228] This concept has been used in my studies to transform some mathematical expressions and simplify the finite-element models.

However, in spite of the foregoing merits of the OP method, there are some limitations of it generally associated with the possible distortions of *P-h* curves. For example, since it is not explicit to the degree of the influence from other orientations rather than the indented orientation on the measure value of the elastic modulus, the OP method is normally inadequate for samples of high elastic anisotropy. A good evidence is the ZIF-8 crystals studied in Chapter 5 and Chapter 6. Even though they exhibit a relatively low elastic anisotropy,[7] the effect of such anisotropy on the measured Young's modulus as shown in Figure 5.6. In addition, for indentation on materials of high viscoelasticity such as polymers[313-315] as well as on those susceptible to fracture such as MOFs,[147] the OP method is no longer applicable because the initial portions of unloading curves may be severely distorted. Similarly, the method is also not appropriate for indentation producing massive plastic deformation.[106] In regard to plasticity, the relationship between hardness and elastic modulus (the ratio *H/E*) can be regarded as an indicator to tell whether an indenter-to-sample system is elasticity or plasticity governed (see Figure 4.5).[260, 316]

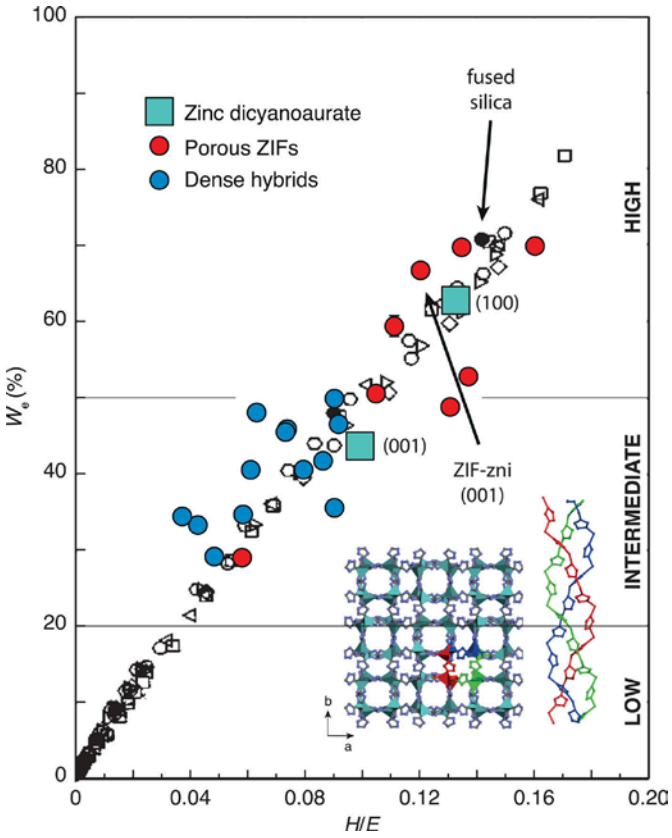

Figure 4.5 Empirical relationship between elastic recovery (W_e) and *H/E*. Data are provided for three types of materials: zinc dicyanoaurate, porous ZIFs, and dense hybrids. For the purpose of comparison, conventional materials such as ceramics, summarised by Ref. [260], are included (data symbols in black and white). What stands out are these porous ZIFs showing significant elastic recovery. Zinc dicyanoaurate has negative compressibility behaving as if dense hybrids when stress is exerted on the {001}-oriented facet, but similar to an open MOF-type system when compressed along the {100}-oriented facet. Reprinted with permission from Ref. [316] under a Creative Commons Attribution License.

Another limitation of the OP method is that the underlying pile-up is not taken into account albeit sink-in is corrected, both of which would introduce considerable errors in contact area determination. Moreover, it is not an appropriate model for a system where there is a recovered displacement owing to reverse plasticity in the course of tip unloading although the reversing effect is often insignificant.[227] Furthermore, since adhesion is neglected, as depth increases, hardness measured usually exhibits an ascending trend.[263]

4.7.3 Oliver and Pharr Method with the Unloading Strain Rate Principle

Accurate implementation of the OP method is on the basis of reliable *P-h* data, which as mentioned above, can be susceptible to some interfering factors such as creep, thermal drift, and cracking. These factors could dramatically distort the *P-h* curves leading to an erroneous measurement. These interfering factors are common while indenting on porous frameworks such as MOFs. Given this, an unloading strain rate principle was proposed to guide the indentation experiment.[147] As demonstrated in Chapter 5, a sufficiently high unloading strain rate is effective to surpass the interfering factors thus garnering reliable measurement of the Young's modulus of ZIF-8 crystals. Additionally, as introduced in §4.6.3.2, the strain rate can be readily controlled by tuning the two AFM operating parameters: scan rate and cantilever probe deflection. This principle has also been extended to study the CuBDC nanosheets in §7.6.3 of Chapter 7.

4.7.4 Lennard-Jones Potential

The Lennard-Jones potential is a model that mathematically describes the interplay between two neutral atoms or molecules. The local pressure (p) of atomic interaction between two objects in the Lennard-Jones potential can be defined as:[302, 317]

$$p(h) = \frac{8\gamma}{3\varepsilon}\left(\frac{\varepsilon}{h}\right)^9 - \left(\frac{\varepsilon}{h}\right)^3 \tag{4.22}$$

where ε is the length parameter representing the range of interaction.

This model has been employed in the numerical simulation method in §4.7.6.

4.7.5 Derjaguin's Approximation

For indentation experiment, the specimen of interest usually possesses a flat surface other than the surface of curvature. With this in mind, the Derjaguin's approximation was utilised to construct the numerical simulation, which governs the interaction between two planar surfaces at a distance of the potential-related separation within a finite domain. In this

method, the repulsive force between the two objects and shape of the gap conforms to the Hertz model and the adhesive force is deemed to be the energy consumed in order to separate the two contacting objects. Separation between the two objects can be expressed by:[270, 310, 318]

$$h(x,y) = -\alpha + \varepsilon + h_0 + \frac{1}{\pi E_{\text{eff}}} \iint_{\Omega} \frac{p(x',y')dx'dy'}{(x-x')^2 + (y-y')^2} \qquad (4.23)$$

where α is the displacement of indenter and h_0 is the initial separation between the two surfaces; Ω determines the scope of the domain in-plane of the sample surface.

This model has been adopted in the numerical simulation method in §4.7.6.

4.7.6 Numerical Simulations

The numerical simulation method was reported by Jin *et al.* for the purpose of overcoming the limitations of other analytical adhesion models due to the lack of general applicability in terms of the tip geometry.[270, 319] For instance, the traditional JKR method can only be adopted when a perfectly spherical indenter is used (or assumed). The method has been adopted to study the HKUST-1 crystals in 8.6.2 of Chapter 8.

The numerical simulation is on the basis of two theories, they are: the Lennard-Jones potential (§4.7.4) and the Derjaguin's approximation (§4.7.5). The former is an empirical model to describe the atomic interplay between two curved surfaces.

In order to transform the solutions from the two theories into a pure mathematical problem, the terms of the equations (4.22) and (4.23) need to be replaced by the dimensionless (namely normalised) variables (added overbars): $\overline{h}$, $\overline{p}$, $\overline{\alpha}$, $\overline{h_0}$, $\overline{x}$, and $\overline{y}$.

$$\overline{h} = \frac{h}{\varepsilon} - 1 \quad ; \quad \overline{\alpha} = \frac{\alpha}{\varepsilon} \quad ; \quad \overline{h_0} = \frac{h_0}{\varepsilon} \quad ; \quad \overline{p} = \frac{p\varepsilon}{\gamma} \quad ; \quad \overline{x} = x\frac{n}{\varepsilon m} \quad ; \quad \overline{y} = y\frac{n}{\varepsilon m}$$

Equation (4.23) can be re-written in a vector form as follows:[270]

$$\vec{\vec{h}} = -\overline{\alpha} + \overrightarrow{\overrightarrow{h_0}} + \frac{\mu^{\frac{3}{2}}}{\pi} C\vec{\vec{p}} \tag{4.24}$$

where *C* is the influential coefficient, which denotes the tessellation of the adhesion domain.

Further on, the model can be transformed to a dynamic system using a virtual state relaxation (VSR) method.[270, 319] The function of the dynamic system is:

$$f\left(\vec{\vec{h}}\right) = \frac{d\vec{\vec{h}}}{dt} = \vec{\vec{h}} - \overline{\alpha} + \overrightarrow{\overrightarrow{h_0}} + \frac{\mu^{\frac{3}{2}}}{\pi} C\vec{\vec{p}} \tag{4.25}$$

Apparently, the state described in equation (4.24) is the equilibrium of the dynamic system. The problem is transformed to the root-finding iteration of function $f\left(\vec{\vec{h}}\right) = 0$.

After executing the iterative bisection algorithm using Matlab (§4.9.1), we can get the value of $\vec{\vec{h}}$. Consequently, according to the Lennard-Jones theory, the discrete interactive potential field (see Figure 8.10) can be determined by substituting $\vec{\vec{h}}$ into the following equation, which is the equation (4.22) with dimensionless variables:

$$\overline{p} = \frac{8}{3}\left(\overline{h} + 1\right)^{-9} - \left(\overline{h} + 1\right)^{-3} \tag{4.26}$$

Given that the Tabor parameter (μ) represents the response of sample to adhesive interaction with the indenter, which is clearly depending on the intrinsic attributes of the entire indenter-to-sample system, it is essential to determine μ for the tested sample (i.e. HKUST-1 in Chapter 8). The normalised force ($\overline{P}$) versus normalised displacement ($\overline{h}$) in Figure 8.9a shows the variance of response of materials with different μ to the attractive forces. $\overline{P}$ can be derived from the following equation integrating the local pressure over the specific domain Ω:

$$\overline{P} = \frac{1}{3\pi}\iint_{\Omega} \overline{P}(\overline{x},\overline{y})d\overline{x}d\overline{y} \tag{4.27}$$

As deduced by Jin *et al.*, for the Berkovich and cube-corner indenters in the numerical simulation, the functions of the normalised force ($\overline{P}$) and Tabor parameter (μ) are as follows:

$$\overline{P} = \left(\frac{n}{m}\right)^2 \frac{P}{3\pi\gamma\varepsilon} \tag{4.28}$$

$$\mu = \left(\frac{m}{n}\frac{\gamma}{E_{\text{eff}}\varepsilon}\right)^{\frac{2}{3}} \tag{4.29}$$

where P is the load which can be measured on the P-h curves from AFM nanoindentation; m is the side length and n is the effective height of the Berkovich indenter. Whereas for the cube-corner indenter, the base triangle is not equilateral. And hence the arithmetic mean of the three sides of the base triangle was taken as the magnitude of m.

To remove the length parameter ε, which cannot be readily determined from the experiment, the equations (4.28) and (4.29) can be combined to output the adhesion energy:

$$\gamma = \left[\left(\frac{n}{m}\right)^3 \frac{\mu^{\frac{3}{2}} P E_{\text{eff}}}{3\pi\overline{P}}\right]^{\frac{1}{2}} \tag{4.30}$$

Furthermore, one may notice that adhesion energy (γ) cannot be directly measured from the experimental P-h curves. Therefore, the equation (4.30) needs to be rewritten by means of the following equations because it contains two important parameters that are measured from the numerically simulated $\overline{P}$-$\overline{h}$ curve (see Figure 8.9a) and the experimentally measured P-h curve (see Figure 8.5c). These two parameters are the displacement from the point at zero load to the point at the pull-off force, *viz.* $\overline{P}_{\text{pull-off}}$ (normalised pull-off force) and $P_{\text{pull-off}}$ (experimental pull-off force from AFM nanoindentation): $\Delta\overline{h}$ and $\Delta\alpha$, respectively.

$$\Delta\alpha = \Delta\overline{h}\varepsilon \tag{4.31}$$

Substituting the equation (4.29) into (4.31) to replace ε, gives:

$$\gamma = \frac{n}{m}\frac{\Delta\alpha E_{\text{eff}}\mu^{\frac{3}{2}}}{\Delta\overline{\alpha}} \tag{4.32}$$

Then the effective modulus can be derived by combining equation (4.30) and (4.32):

$$E_{\text{eff}} = \frac{n}{m}\left(\frac{\Delta\overline{\alpha}}{\Delta\alpha}\right)^2 \frac{P}{3\pi\mu^{\frac{3}{2}}\overline{P}} \tag{4.33}$$

Therefore, the elastic modulus can be determined by employing equation (4.33).

4.7.7 Carpick-Ogletree-Salmeron (COS) and Piétrement-Troyon (PT) Methods

A pioneering study conducted by Tabor, pointed out the contradiction of the JKR and DMT models and proved they are actually two extreme limits of the adhesion theory.[300] Thereafter, in the Maugis-Dugdale (MD) model, the insight of the JKR-DMT transition zone (also known as the MD zone) has been further enhanced by regarding the surface adhesive force as a constant in a Dugdale cohesive zone rather than utilising the Lennard-Jones potential that describes the true adhesive force between surfaces.[301] However, owing to the deficiency of a direct correlation between indentation load (P) and depth (h), meanwhile the dimensionless elasticity parameter λ (see §3.5.5) is *a-priori* unknown, the MD model can only be solved *via* a lengthy iteration with no guarantee of convergence. Considering the *P*-*h* data is the prime output of an indentation experiment, Carpick, Ogletree, and Salmeron introduced the COS empirical equation that directly links P with contact radius, i.e. associated with h, and they also suggested the derivation of λ.[239] Based on the COS equations, Piétrement and Troyon proposed the PT empirical equation by bridging the contact stiffness with adhesion energy.[303] The equation describing the *P*-*h* relation is rearranged as follows:

$$h = \frac{{a_0}^2}{R_{\text{eff}}}\left[\left(\frac{\alpha+\sqrt{1+\frac{P}{P_{\text{ad}}}}}{1+\alpha}\right)^{\frac{4}{3}} - (-2.160\alpha^{0.019} + 2.753\alpha^{0.064} + 0.073\alpha^{1.919})\left(\frac{\alpha+\sqrt{1+\frac{P}{P_{\text{ad}}}}}{1+\alpha}\right)^{\frac{2}{3}(0.516\alpha^4-0.683\alpha^3+0.235\alpha^2+0.429\alpha)}\right] \quad (4.34)$$

Fitting above equation to the experimental data, the values of $a_0{}^2/R_{\text{eff}}$, α can be obtained given the magnitude of adhesive force (also known as pull-off force, P_{ad}) can be measured from the experimental *P*-*h* curve. In order to relate the force and displacement data, the two dimensionless parameters are introduced: $\overline{P_{\text{ad}}}$ and $\overline{a_0}$.[303] In the PT method, the following equations were derived:

$$\frac{P_{\text{ad}}}{\overline{P_{\text{ad}}}} = \pi\gamma R_{\text{eff}} \quad (4.35)$$

$$\overline{a_0} = -0.451\alpha^4 + 1.417\alpha^3 - 1.365\alpha^2 + 0.950\alpha + 1.264 \quad (4.36)$$

$$\overline{P_{\text{ad}}} = 0.267\alpha^2 - 0.767\alpha + 2.000 \quad (4.37)$$

As introduced before, γ is the adhesion energy, i.e. the work done by adhesive force in order to counteract the tensile force which pulls apart two objects. In Chapter 8, Figure 8.12b suggests tensile force could either lead to surface detachment or splitting fracture of one surface adhering to another one. γ can be acquired by substituting equation (4.37) into (4.35).

In the MD zone, the effective elastic modulus can be expressed by the non-dimensional contact radius, normalised curvature of the indenter apex, and the adhesion energy:

$$E_{\text{eff}} = \left(\frac{\overline{a_0}}{a_0}\right)^3 \pi\gamma {R_{\text{eff}}}^2 \quad (4.38)$$

Since we know (note that this is not equivalent to the E_{eff} in §4.7.2 and §4.7.5):

$$\frac{1}{E_{\text{eff}}} = \frac{4}{3}\left(\frac{1-{v_{\text{indenter}}}^2}{E_{\text{indenter}}} + \frac{1-{v_{\text{HKUST-1}}}^2}{E_{\text{HKUST-1}}}\right) \tag{4.39}$$

Therefore, Young's modulus of the HKUST-1 framework along different orientations can be obtained. Additionally, the elasticity parameter (λ) and Tabor parameter (μ) associated with the adhesive response during indentation is defined as:

$$\lambda = 1.16\mu = -0.913\ln(1 - 1.018\alpha) \tag{4.40}$$

Tabor parameter (μ) is a quantity that depicts the elastic deformation that is normal to the indented surface generated exclusively by attractive forces.

In order to construct the adhesion map in Figure 8.8, the normalised force ($\overline{P}$) in both MD and PT methods can be derived as follows:[320]

$$\overline{P} = \frac{P}{\pi\gamma R_{\text{eff}}} \tag{4.41}$$

4.8 Finite-Element (FE) Method

In general, we use analytical equations to describe physical and engineering phenomena, and to resolve unknown quantities of interest. However, we are not always able to find satisfying analytical solutions for all the phenomena encountered in real life applications. To solve these physical or engineering problems, finite-element (FE) method, a versatile numerical simulation has been introduced as early as the 1940s by Hrennikoff and Courant.[321-322] Today, the FE method is widely used in diverse fields in order to solve complex physical problems.

In this thesis, I have adopted the FE method in simulating the indentation experiment for the purpose of gaining a better insight of the underlying contact mechanics for the two MOF systems: CuBDC nanosheet and HKUST-1 submillimetre-sized crystal.

4.8.1 CuBDC Nanosheets

Elastic-plastic properties of the CuBDC nanosheet were simulated using ABAQUS/CAE 2016 (Explicit solver)[323] by inputting the Young's modulus (obtained from the AFM nanoindentation in §7.4), and the stress-strain relation (acquired by implementing the iteration method in §7.5). Four distinctive indenter-sheet assembly models were created representing the four different responses while indenting the CuBDC nanosheet stacks. The sheet parts in the FE models are: a continuum part (Figure 7.3), lamella stacks bound with cohesive layers (Figure 7.5), lamella stacks with fracture criterion defined (Figure 7.6). The CuBDC lamella was meshed using the 8-node linear brick elements (*C3D8R*) with reduced integration and hourglass control, and the indenter was modelled as an equivalent conical discrete rigid part, in which a curved apex of dimensionless radius 0.7 was allocated to avoid the excessive distortion of the meshes. The damage criterion of the cohesive layer was based on the maximum nominal stress criterion (Maxs Damage) using a traction-separation

description implemented in ABAQUS.[323] Moreover, the Johnson-Cook fracture criterion was used to model the failure of the CuBDC lamellae.[324]

4.8.2 CuBTC (HKUST-1) Submillimetre-Sized Crystals

The elastic anisotropy of the HKUST-1 crystals was simulated using ABAQUS/CAE 2016 (Explicit solver)[323] by importing the single-crystal elastic stiffness coefficients obtained from the DFT calculations (C_{11} = 27.719, C_{12} = 25.722, and C_{44} = 5.399) in Ref. [8]. The continuum model was meshed by utilising the 8-node linear brick elements (*C3D8R*) with the reduced integration and hourglass control. In the indenter-crystal assembly, the indenter was modelled as a spherical discrete rigid part. In the FE model, the indentation proceeds normal to the two crystallographic facets: (100) and (111), without considering plasticity of HKUST-1. More details are explained in §8.4.

4.9 Programming Codes

4.9.1 Matlab and Python

I wrote a package of Matlab scripts on Matlab R2018a[325] to process the great majority of experimental data, especially for data from AFM nanoindentation. The efficacy of the scripts include data acquisition, data transformation, curve fitting of the experimental data, theoretical modelling, iterative calculation such as the operation of the root-finding algorithm employed in the numerical simulation (in Chapter 8). Data processing and data graphing were conducted using the software Origin 2017[326-327].

Python 3.6[328] has also been leveraged to refine the finite-element models to realise the analysis of more complex systems in ABAQUS reported in Chapter 8.

Chapter 5: Elastic-Plastic and Adhesion Properties of ZIF-8 Crystals

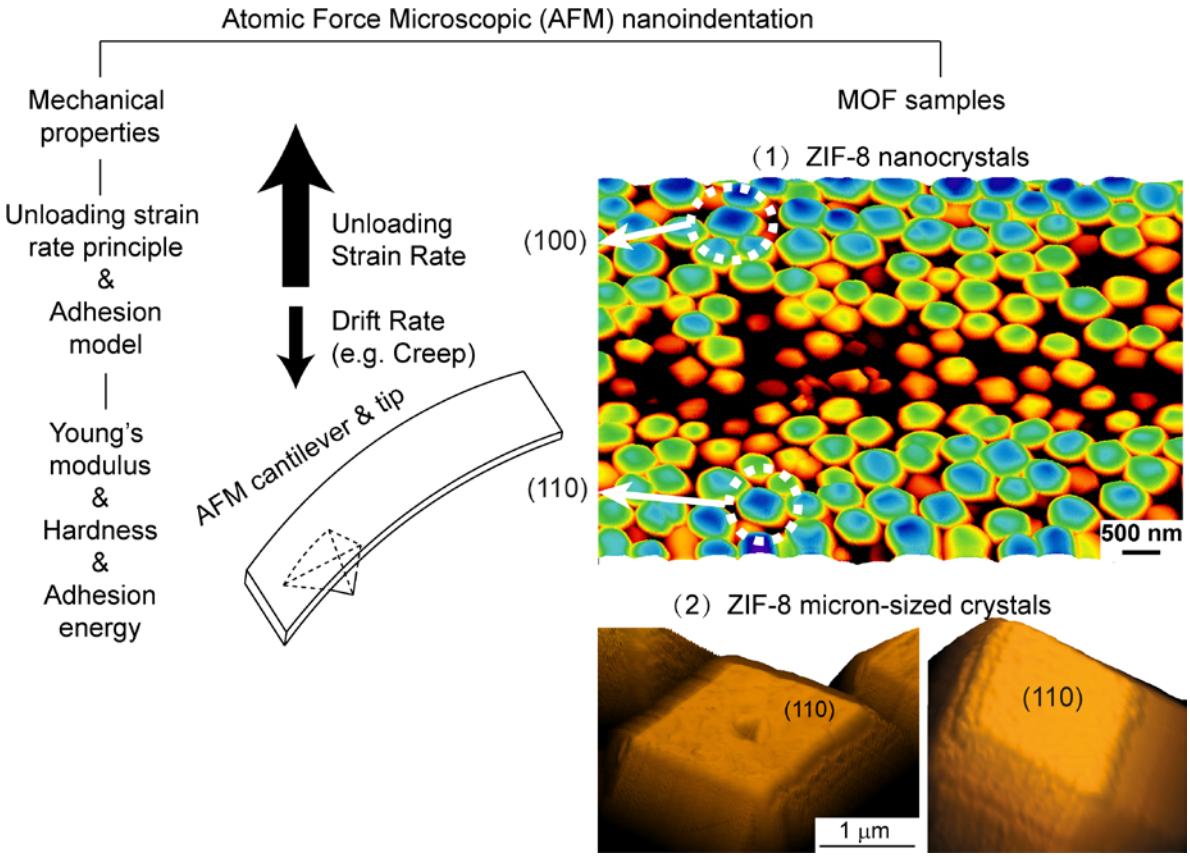

The mechanical properties of individual nanocrystals and small micron-sized single crystals of metal-organic frameworks (MOFs), hitherto, cannot be measured directly by employing the conventional instrumented nanoindentation techniques (IIT). Here the application of atomic force microscopy (AFM)-based nanoindentation technique is proposed. The instrument was equipped with a calibrated diamond cube-corner indenter tip to quantify the Young's modulus, hardness, and adhesion energy of a zeolitic imidazolate framework (ZIF-8) porous material. ZIF-8 was selected as a model MOF system to develop AFM nanoindentation by leveraging the concept of unloading strain rate, so as to critically assess the practicality and technical limitations of AFM to achieve quantitative measurements of fine-scale MOF crystals. Herein, the advantages of using a high unloading strain rate ($\dot{\varepsilon}$>60 s^{-1}) to yield reliable force-displacement data in the few μN load range have been demonstrated, corresponding to a shallow indentation depth of ~10s nm. It was found that the Young's moduli (~3–4 GPa) determined by AFM nanoindentation of the nanocrystals (<500 nm) and micron-sized crystals (~2 μm) are in agreement with magnitudes derived previously from other techniques, namely instrumented nanoindentation and Brillouin spectroscopy (but these methods requiring large 100-μm sized crystals), and also in line with density functional theory predictions of an idealised ZIF-8 crystal.

5.1 Introduction

In this chapter, the first use of AFM nanoindentation to accomplish quantitative characterization of the mechanical properties of ZIF-8 [$Zn(mIM)_2$, mIM = 2-methylimidazolate],[13] which features a porous sodalite framework architecture (Figure 5.1d) is presented. Accurate measurements have been performed on the nanocrystals (<500 nm) and isolated micron-sized (~1–2 μm) crystals of ZIF-8, whose averaged size was about one thousand times smaller[7, 45] than those quantifiable utilizing the established instrumented nanoindentation approach. By monitoring the strain rates of the AFM indenter tip during the indentation process, the strategy to determine reliable Young's modulus and hardness values using very small crystal samples has been demonstrated. Furthermore, the effects of adhesive forces developing at the indenter-to-sample interface have been elucidated.

The synthesis methods of the nanocrystals and micron-sized crystals of ZIF-8 have been presented in Chapter 4 — §4.1.1.

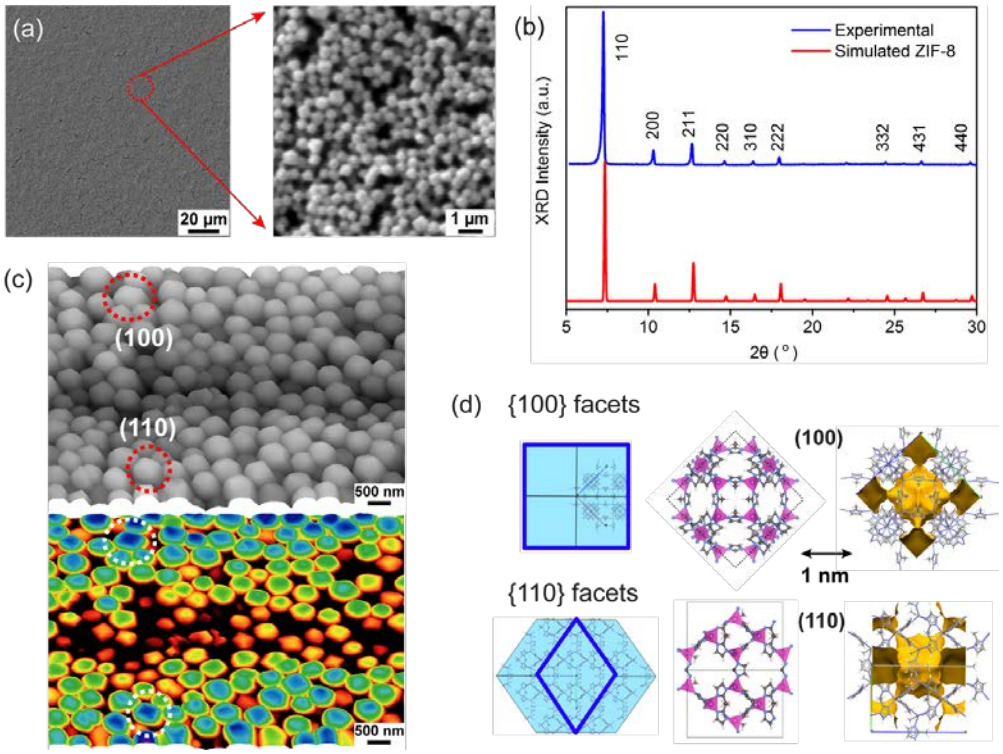

Figure 5.1 (a) Scanning electron microscope (SEM) images of a polycrystalline thin-film coating prepared by drop casting of uniform ZIF-8 nanocrystals. (b) X-ray

diffraction pattern of the drop-cast ZIF-8 film, matching all the simulated *hkl* Bragg peaks of an ideal ZIF-8 structure. Intense diffraction attributed to the (110) crystallographic planes. (c) AFM height topographic images acquired using an imaging silicon tip (Tap300Al-G). Contour maps revealing the crystallographic orientation of the nanosized crystals, where the {110}-oriented rhombic facets are prevalent and with the occasional detection of the (100) square facets. (d) Crystal habits of the ZIF-8 crystal, where in this study the majority consisted of rhombic dodecahedron with {110}-oriented facets. Porous crystalline framework architecture of ZIF-8, where the purple tetrahedron represents the ZnN_4 coordination environment bridged by the 2-methylimidazolate (mIM) organic linkages; (far right) the yellow surfaces designate the solvent accessible volume (porosity) in a cubic unit cell of ZIF-8 viewed down the [100]- and [110]-axes, respectively.

5.2 AFM Nanoindentation Methodology and *P-h* Data Analysis

The AFM nanoindentation measurements yield a set of indenter force-displacement (*P-h*) curves, from which the mechanical properties particularly the Young's modulus (*E*) and hardness (*H*) can be quantified. In this study, the Oliver and Pharr (OP) method[228] (see §4.7.2) has been adopted, which is applicable to the cube-corner indenter geometry. The approach developed in this study, therefore, is different from the common methods typically implemented for the analysis of AFM nanoindentation data, namely the Hertz, JKR (Johnson-Kendall-Roberts) and DMT (Derjaguin-Muller-Toporov) contact models,[329] which have simplified the analysis by assuming a spherical-tip indenter geometry. The aforementioned methods (OP included) share certain limitations: firstly, they assume an isotropic material response[90] and disregard the effects of pile-up and/or sink-in;[76] secondly, they disregard any time-dependent deformation mechanisms, such as creep or viscoelastic effects.

Importantly, herein the unloading strain rate of the indenter tip, $\dot{\varepsilon}$, has been demonstrated as a leading parameter to control during AFM nanoindentation of compliant materials, to allow reliable measurements of the Young's modulus of nano- and micron-sized crystals of ZIF-8. Moreover, I show that the loading and unloading strain rates

can be tuned by varying the AFM scan rate (V) and the cantilever probe deflection (δ) in the Veeco Dimension 3100 AFM. Given that this is a basic AFM setup, it is envisaged that the proposed approach will be easily adapted to other more sophisticated systems. The strain rate at the maximum indentation depth can be determined from $\dot{\varepsilon} = \dot{P}/P_{\max}$ (see detailed explanations in §4.6.3.2),[309] coinciding with the initial point when the indenter starts to unload. By applying this AFM nanoindentation methodology, I have measured the local mechanical properties of MOF crystals over a wide range of unloading strain rates. In the meantime, in order to address the influence of adhesive forces on mechanical properties measurement, I also proposed an improved method that successfully reduces the deviations of the Young's moduli of micron-sized ZIF-8. First attempts in the fine-scale characterisation of fracture mechanism as well as interfacial strength between ZIF-8 polycrystals have been undertaken, by virtue of the superior sensitivity conferred by the AFM-based nanoindentation approach.

5.3 AFM Nanoindentation of ZIF-8 Nanocrystals

AFM nanoindentation experiments were performed in accordance with the strain-rate controlled approach outlined, to study thin film samples (Figure 5.1) prepared *via* drop casting of (submicron sized) ZIF-8 nanocrystals. I have conducted indentation measurements with a surface penetration depth (h) ranging from 10 nm to 80 nm, corresponding to an applied load (P) of between 0.3 μN and 15 μN. Figure 5.2a shows a set of representative *P-h* curves for indentation depths of just ~10 nm to 30 nm onto the top facets of the individual nanocrystals, whose size is *ca*. 300 to 500 nm. These shallow indentations lie within the recommended 10% rule of the sample thickness,[330] *vis-á-vis* the size of the rhombic dodecahedron nanocrystals of ZIF-8, so as to avoid any substrate effects.

Figure 5.2b shows the relatively deeper *P*-*h* indentation curves, for a surface penetration depth of up to h_{max} ~60 nm. Direct 3-D mapping of the residual indents using AFM topographic imaging was found to be not attainable for the shallow indentation measurements described above, because of two factors: (i) the large elastic recovery upon tip unloading is clearly evident in Figure 5.2a where the final depth after fully unloaded $h_f \lesssim 10$ nm, and (ii) the 50 nm tip radius (r) of the diamond cube-corner probe (§4.2.2) is not sufficiently sharp for imaging the very shallow residual indents (~few nm) after elastic recovery, because $h_f \lesssim r$.

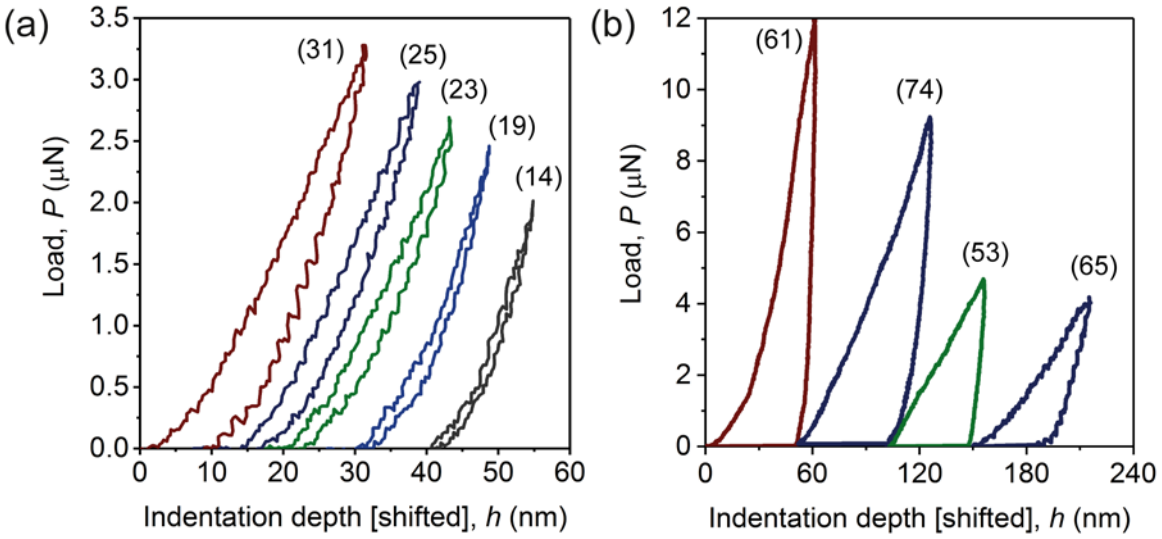

Figure 5.2 AFM nanoindentation force-displacement (*P*-*h*) curves of individual nanocrystals of ZIF-8 showing (a) shallow indents with $h_{max} \lesssim 30$ nm, and (b) relatively deeper indents with $h_{max} \approx 60$ nm. Note that the displacement axis on the abscissa has been shifted for clarity. Note that the numbers in the brackets represent the maximum indentation depths in nm.

Localised indentation on a polycrystalline specimen is complicated because of the interaction between neighboring crystals. In the perspective of energy storage and dissipation, the work done by the indenter might be consumed by either the plastic deformation of the crystalline structure or due to the slippage between the neighbouring crystals. Due to this complexity, the *P*-*h* curves obtained from the indentation on the

polycrystalline coatings show a range of variabilities, some examples are shown in Figure 5.3.

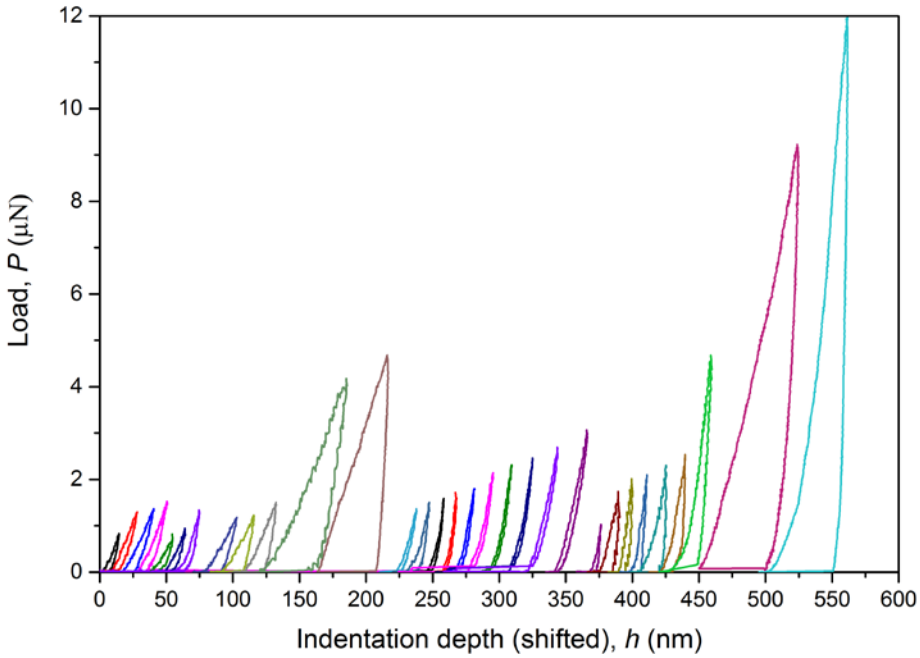

Figure 5.3 AFM nanoindentation measurements performed on the different regions of the (submicron sized) ZIF-8 nanocrystals, deposited as thin-film coating on a glass substrate (Figure 4.1).

As shown in Figure 5.4, there are two primary AFM instrument parameters controlling the indentation strain rate ($\dot{\varepsilon}$), specifically: the scan rate of the cantilever probe (V is speed of indenter spanning the load-unload motion of the piezo-electronics), and its pre-set vertical deflection (δ) of the cantilever tip. In this study, the load-unload strain rates ($\dot{\varepsilon} = \dot{P}/P$) of the probe for each individual indentation test (see Figure 4.4 in §4.6.3.2) could be controlled. It can be seen in Figure 5.4a-b that a high unloading strain rate approaching 140 s^{-1} could be achieved by raising the scan rate V to ~1 Hz, while reducing the cantilever deflection δ to under 10s nm. There is a reasonably good control over the unloading strain rates of the AFM indenter; for example, Figure 5.4c shows the upward trend of $\dot{\varepsilon}$ with different pre-set scan rates, whereas an inversed scaling relation can be observed in

Figure 5.4d with respect to the cantilever deflection of varying scan rates. Together, the results revealed that optimal combinations of V and δ parameters do exist, as presented in the contour plot of Figure 5.4e. In essence when indenting soft materials and/or compliant interfaces, one should maximise the unloading strain rates to yield an $\dot{\varepsilon}$ which is sufficiently high to surpass any unwanted creep effects (to be elucidated below), as well as to prevent extensive fracture of porous frameworks that will result in an erroneous contact area attributed to distorted *P-h* curves (see Figure 5.5). In this study, it is validated that by maintaining a high unloading strain rate (Figure 5.4), it is possible to alleviate the negative-gradient test segment of unloading curves when measuring small-sized crystals of ZIF-8.

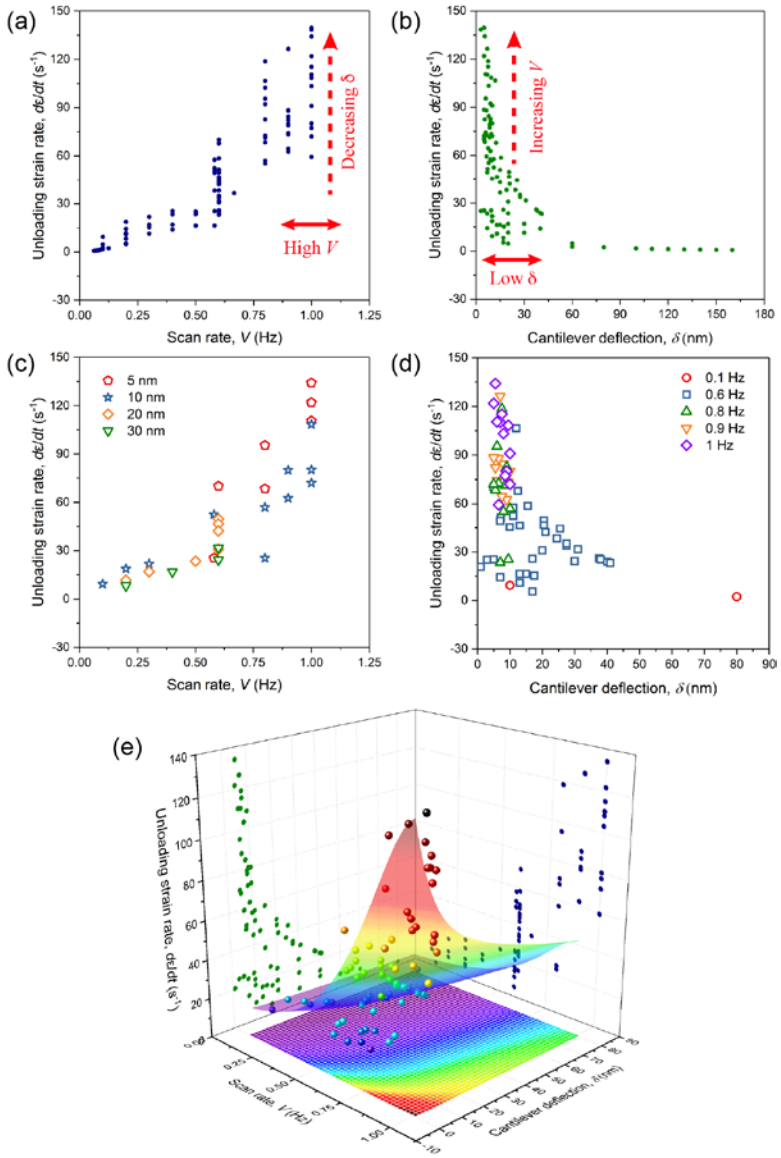

Figure 5.4 (a) Unloading strain rate ($\dot{\varepsilon}$) of the AFM indenter probe as a function of the cantilever scan rate V. (b) $\dot{\varepsilon}$ as a function of the cantilever deflection δ. Data plotted in (a) and (b) were obtained from a total of 72 measurements conducted on individual ZIF-8 nanocrystals like those depicted in Figure 5.1. Selected data highlighting the effects of increasing (c) the cantilever deflection from 5 – 30 nm, and (d) the scan rate between 0.1 – 1 Hz. (e) Contour plot of all 72 indention experiments, showing the combined effects of different scan rate and cantilever deflection, in which the red region marks the desired strain rates for overcoming the creep effects upon unloading of the indenter tip.

The Young's modulus (E) of the ZIF-8 nanocrystals has been determined by analysing the individual P-h curves, using the equations set forth in §4.7.2. The results obtained from a total of 72 indentation experiments are plotted in Figure 5.6, allowing us to

understand the effects that the unloading strain rate ($\dot{\varepsilon}$) and/or the maximum indentation depth (h_{max}) might have on the quantified values of E. In fact, the Young's modulus of ZIF-8 is well-established in the literature, both using instrumented nanoindentation technique on a significantly larger ~150 μm crystal ($E_{[110]}$ = 3.2 GPa)[45] and by Brillouin spectroscopy technique validated by density functional theory ($E_{[110]}$ ~3 GPa and E_{VRH} = 3.15 GPa, the latter is the Voigt-Reuss-Hill averaged value for a polycrystalline ZIF-8 sample). The cubic symmetry of ZIF-8 also exhibits elastic anisotropy, where E_{max} ~3.8 GPa and E_{min} ~2.8 GPa corresponding to the Young's moduli of the {100}- and {111}-oriented crystal facets, respectively (NB. readers should consult Ref. [7] about the source of elastic anisotropy and associated mechanisms).

In the light of this, ZIF-8 was chosen as the "model system" to develop the AFM nanoindentation technique based on the concept of unloading strain rate, in order to critically assess the feasibility and technical limits of this AFM approach, and, to understand its applicability to probe fine-scale MOF crystals. Notably it can be seen in Figure 5.6a that when the applied $\dot{\varepsilon}$ is exceeding ~60 s^{-1} the measured E values start to converge towards the known literature value of ~3 GPa. In contrast, it is evident that there are major overestimations (up to 900%) of the elastic moduli when the $\dot{\varepsilon}$ is below 25 s^{-1}. Particularly it was found that when $\dot{\varepsilon} < 3\ s^{-1}$, the incipient unloading curves began to develop a negative-gradient segment indicating that the creep rate is becoming significantly higher than the indenter unloading rate (see Figure 5.5); notably when creep dominates the initial unloading stage this will result in a spuriously high Young's modulus value. The adverse effects of creep deformation to AFM nanoindentation measurements are well recognised in viscoelastic solids and polymers.[180, 331]

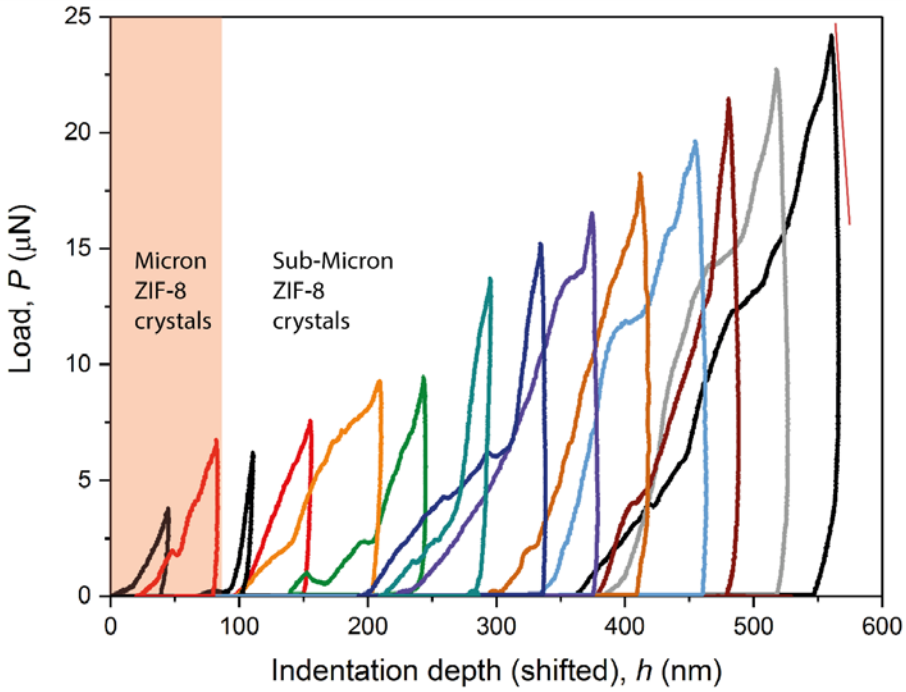

Figure 5.5 Force-displacement (*P*-*h*) curves for nanoindentation measurements performed using a high cantilever deflection. Note that the incipient segments of the unloading curves show a negative gradient, −d*P*/d*h*.

Apparent strain-rate sensitivity effect was observed in ZIF-8 thin film coatings when the unloading strain rate is less than ~60 s^{-1} (Figure 5.6a). It is proposed that this strain-rate effect is relevant to the negative gradient at the incipient unloading curve as shown in Figure 5.5. More specifically, indentation with smaller unloading strain rate than a certain threshold value (this is also likely to be material dependent, for instance, 60 s^{-1} for ZIF-8 and 140 s^{-1} for CuBDC introduced in Chapter 7), the gradient of the incipient segment of the unloading curve starts to increase, which corresponds to the increasing contact stiffness measured until the negative gradient occurs and invalidates the OP model (the power law equation in this method cannot fit the negative-gradient segment of the unloading curve).[228] Therefore bulging of the unloading curves of ZIF-8 thin film coatings was observed under imposed high loading conditions, i.e. excessive cantilever deflection.

Briscoe *et al.* pointed out that at the incipient segment of the unloading stage, the indentation depth continuously increases slightly with the decreasing forces due to the creep effect.[309] This means that the creep rate at the opposite direction surpasses the unloading rate even at the peak force where the highest unloading rate is reached (see Figure 4.4). Cohen *et al.* suggested that this bulging appears due to the fact that a time lag between the change in stress and the induced strain of testing material.[148] In other words, the material has residual "memory" of increasing stress during the incipient stage of unloading. Typical method to eliminate the undesired effect is to hold the maximum indentation load until a mechanical equilibrium is reached (typically adopted in the test procedures of instrumented nanoindenters). It is worthwhile to mention that the creep effect is apparent in viscoelastic materials such as polymers.[180]

Post-processing, computational approaches can also be used to remove this effect by correcting for the contact mechanisms, for example see Refs. [[309] and [332]]. Negative-gradient unloading curve was also reported on hard materials, such as ceramics, because of grain dislocation. Materials showing viscoplasticity could also be susceptible to this effect leading to a bulging curve in the incipient unloading test segment. Another undesired effect, thermal drift, could accompany the creep effect, and this is indistinguishable from the creep contribution.

5.3.1 Young's Modulus and Hardness Quantification of the ZIF-8 Nanocrystals

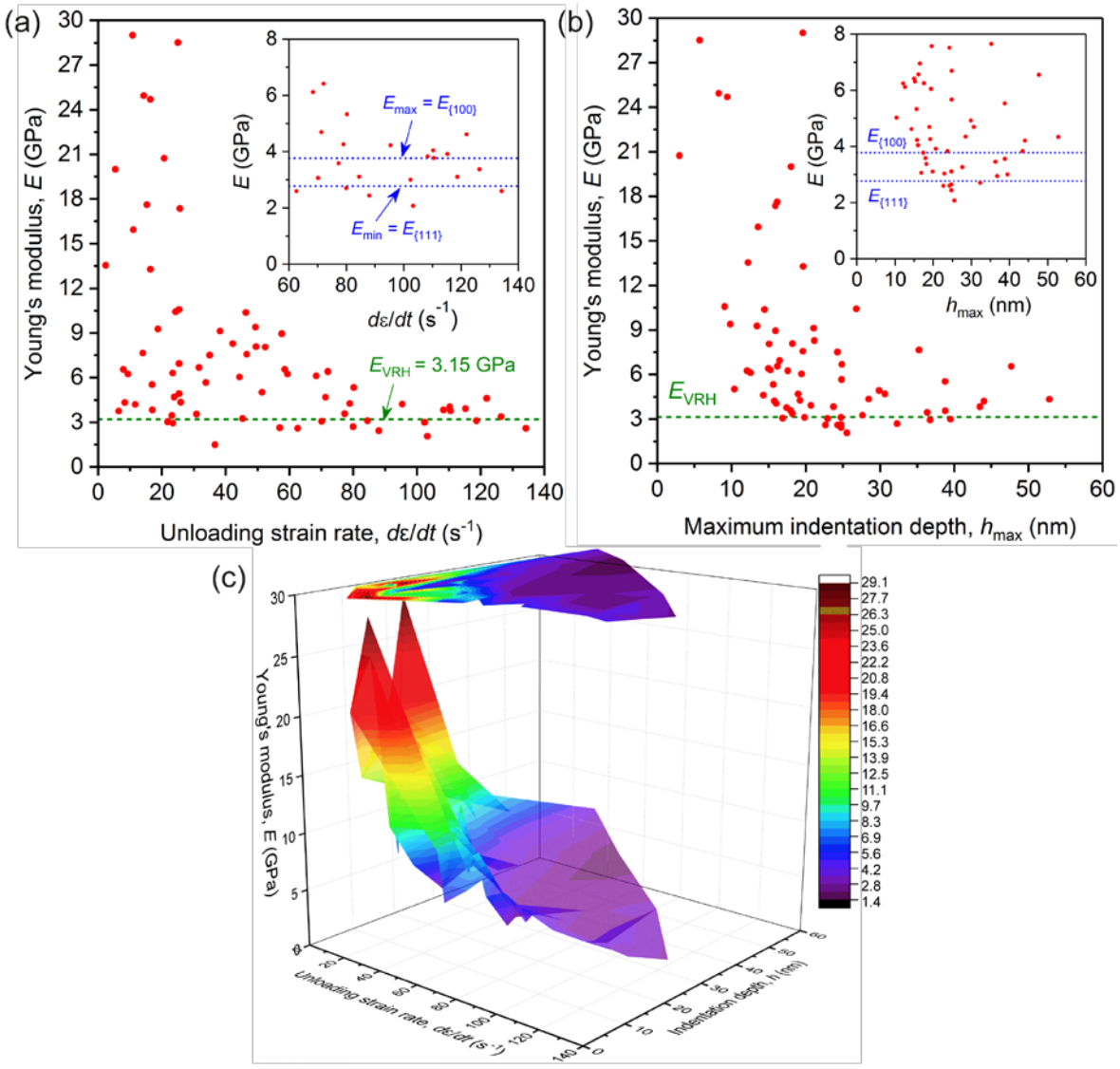

Figure 5.6 (a) Young's modulus, *E*, plotted as a function of the (initial) unloading strain rate of the indenter tip, where a higher unloading strain rate stabilises the magnitude of the measured moduli coinciding with the literature value for ZIF-8 (the green line is the literature value,[7] assuming an isotropic polycrystalline ZIF-8 sample). The inset compares the AFM results against the reported upper bound $E_{[100]}$ and the lower bound $E_{[111]}$ of a ZIF-8 single crystal due to elastic anisotropy. (b) The variation of *E* plotted as a function of the maximum indentation depth. (c) Contour plot correlating Young's modulus with the two indicative parameters, i.e. unloading strain rate and maximum indentation depth. Projection of the contour plot is placed on the top for clarity.

As shown in Figure 5.6b akin to instrumented nanoindentation data, the results of Young's modulus acquired from the AFM nanoindentation method can also be presented as a function of the maximum indentation depth, i.e. h_{max}, determined at the point of indenter unloading. Although a reasonable agreement to the literature value (E ~ 3 GPa) can be attained when h_{max} is much deeper than ~30 nm, it was found that the correlation to the unloading strain rate is more important (Figure 5.6a). This is because the unloading strain rate is a more versatile parameter to be tuned when indenting compliant materials susceptible to creep deformation (such as an aggregate of MOF nanocrystals), where the $\dot{\varepsilon}$ parameter can be varied to obtain a consistently high value of >60 s^{-1} across a range of indentation depths. The hardness (H) property of the ZIF-8 nanocrystals can be obtained in accordance with the definition: $H = P_{max}/A$. Because the contact area established under the maximum load is determined only by the maximum indentation depth (h_{max}) of the loading test segment, hardness derived from AFM nanoindentation is thereby independent of the unloading strain rate. The hardness results are given in Figure 5.7, showing a convergence towards the literature value for indentation depths of much greater than ~30 nm. This is a remarkable improvement given that the reported hardness (H ~500 MPa) required the use of a considerably larger single crystal (150 μm) of ZIF-8, whose results were averaged over depths of 100-1000 nm.[45] Significantly, in this work, nanocrystals (300–500 nm) which are about 1000× smaller have been indented and yet I have established comparable H values for an indentation depth of between ~30–80 nm. The rapid rise in the hardness values for depths of below ~30 nm might be linked to the indentation size effects,[288, 333] evidenced also in instrumented nanoindentation studies[334] (but typically detected at < 200 nm, see Figure 5.7 inset).

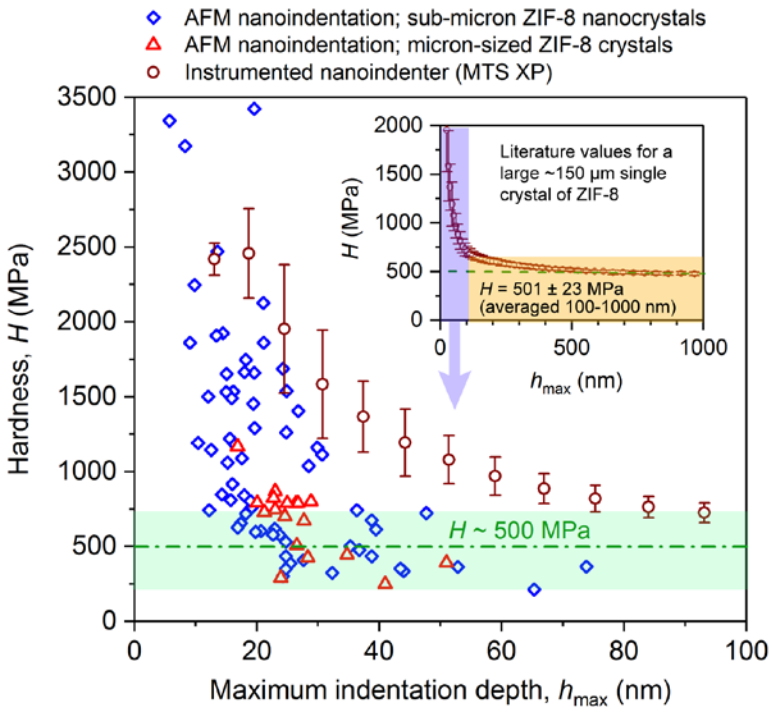

Figure 5.7 Variation of the hardness of ZIF 8 single crystals as a function of the maximum indentation depth. Blue diamonds represent AFM measurements on nanocrystals of ZIF-8 (size < 500 nm), while red triangles are results for micron-sized crystals (~1–2 μm), for a total of 97 and 18 indentation experiments respectively. The green dotted line designates the averaged hardness value reported by Ref. [45], but note that this value was obtained using a much larger (~150 μm) single crystal of ZIF-8 to enable testing using an instrumented nanoindenter as shown in the inset (adapted from Ref. [45]).

For the first time, the AFM approach has offered us the unique opportunity to selectively indent individual sub-micron sized MOF crystals, hitherto, not possible utilising an instrumented nanoindenter setup that will require the preparation of a considerably larger crystal size, of at least ~100 μm.[73, 89] The study shows that direct quantification of the AFM nanoindentation data is possible to achieve reliable measurements of the *E* and *H* values, consistent with instrumented nanoindentation tests but requiring only crystals that are about 1000× smaller. There are other advantages for using AFM-based nanoindentation to study MOF mechanics: the load sensitivity of the AFM is about three orders of magnitude better than that of an instrumented nanoindenter,[148] hence enabling precise deformation of

relatively pliant porous structures such as MOFs. Moreover, because of the implementation of screw-driven translation stages in instrumented indenters, their spatial positioning accuracy is limited to ~1 μm, thereby not suitable to accurately locate and probe standalone nanoparticles and sub-micron scale crystals.

It is worth emphasizing that the successful AFM nanoindentation of sub-micron crystals (nanocrystals) will depend on several factors: (a) High surface roughness of polycrystalline films and coatings could affect the stability of the indentation measurement, therefore minimum sample roughness is desirable to avoid error in contact area determination; (b) Accurate calibration of the indenter geometry and tip radius is important to prevent erroneous results when analysing the Young's modulus and hardness based on the *P*-*h* curves. (c) High unloading strain rates are necessary to overcome time-dependent deformation, such as creep effects that may lead to spurious stiffness values.

5.4 AFM Nanoindentation of Micron-Sized ZIF-8 Crystals

AFM nanoindentation was also conducted on isolated single crystals of ZIF-8, specifically on the {110}-oriented facets, whose lateral dimensions are *ca*. 1–2 μm as depicted in Figure 5.8, Figure 5.9, and Figure 5.10a-c. To put this work into context, while the micron-sized crystals concerned are about 10× bigger than the nanocrystals, notably they are at least 100× smaller than that of a ZIF-8 single crystal previously quantifiable *via* instrumented nanoindentation technique.[45] Figure 5.10d presents the representative *P*-*h* data measured by the AFM approach, demonstrating the indentation of 16 individual micron-sized crystals of ZIF-8. It can be seen that the surface penetration depths were approximately 20–30 nm (satisfying the 10% depth rule to mitigate substrate effects[330]), corresponding to indentation loads measured in the few μN levels. It is worth noting that there was no sign of sample movement by comparing the positions of crystals before and

after the indentation process, because crystals were well attached on the substrate after evaporation of solvent and became immobilised for indentation under the AFM probe. Otherwise, the corresponding force-displacement curves will exhibit abnormal behaviour, such as the "pop-in" phenomenon when crystals are not securely mounted onto substrate. This finding also reflects the advantage of AFM nanoindentation whose loading increment is on the pN level, thereby allowing direct probing of small crystal samples prepared *via* drop casting.

The micron-sized crystals of ZIF-8 studied in this work were approximately 3 μm in height, and thus the measurement of mechanical properties, especially the Young's modulus is not affected by the substrate (indentation depth < 10% sample thickness).

The position of the indent is very important to accurately quantify the mechanical properties. As shown in Figure 5.8 and Figure 5.9, indentations made near to the edges of crystals had resulted into crystal fracture. Mechanical properties such as the Young's modulus and hardness derived using such *P-h* curves will be erroneous. Transverse AFM profiles of the four residual indents in Figure 5.8 and Figure 5.9 can be used to characterise the degree of pile-up and/or sink-in, which will result in deviation of the contact area calculated.

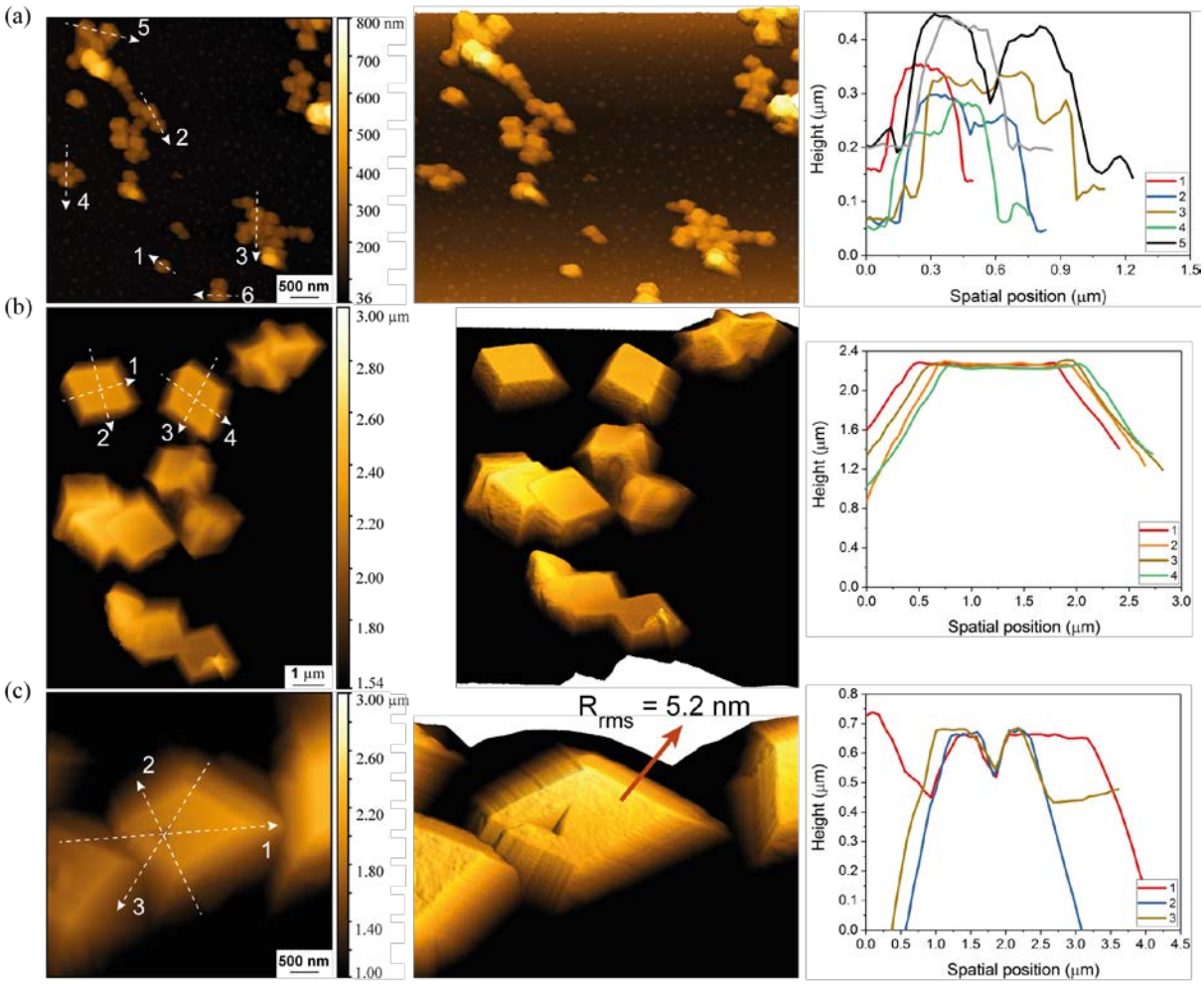

Figure 5.8 AFM images of the individual ZIF-8 crystals: 2-D images (left) and 3-D images (middle). (a-b) Crystals without being indented. (c) Indented crystal. Note that the root-mean-square roughness (R_{rms}) of the crystal surface in (c) was derived before the indentation. Profile plots are shown on the right panels.

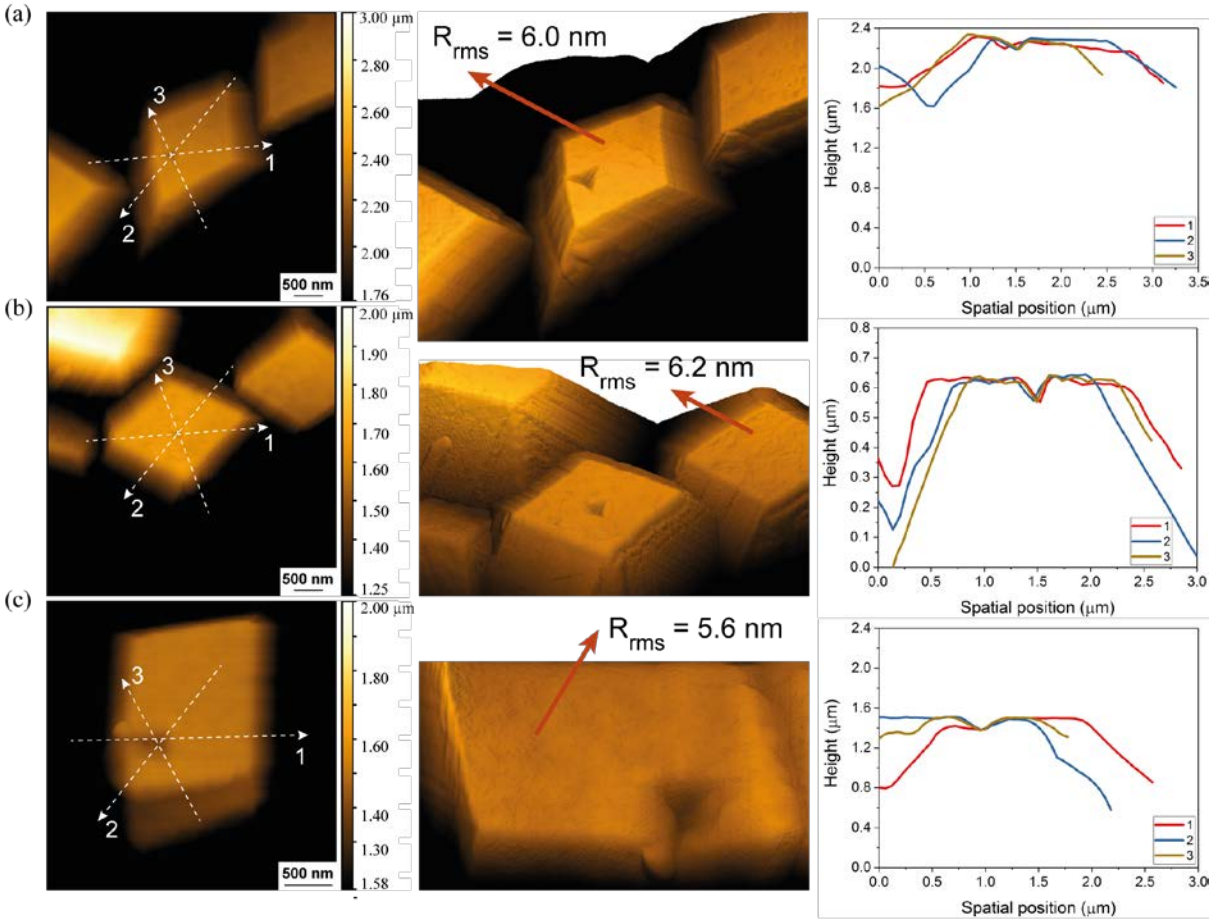

Figure 5.9 AFM images of indents on individual crystals of ZIF-8: 2-D images (left) and 3-D images (middle); root-mean-square roughness (R_{rms}) of surface before indentation. Profile plots (right).

5.4.1 Young's Modulus and Hardness of Micron-Sized ZIF-8 Crystals

The basic methodology applied to derive the magnitudes of the Young's modulus (E) and hardness (H) properties of micron-sized crystals based on the measured P-h data is identical to the one implemented for analysing the nanocrystal counterparts. The results of E and H properties obtained as a function of unloading strain rate and indentation depth, are plotted in Figure 5.10e and Figure 5.7 respectively. The Young's modulus determined, is in fact: $E_{[110]}$, which is in good agreement with the literature value of ~3 GPa (*via* instrumented nanoindentation of a larger 150 μm crystal, Brillouin scattering and DFT calculations[7]). Unlike AFM nanoindentation of the nanocrystals (see Figure 5.6a) that exhibits a strong

dependence towards the unloading strain rate (ideally $\dot{\varepsilon} > 60\ s^{-1}$), in the case of micron-sized crystals no direct correlation between E and the $\dot{\varepsilon}$ parameter (Figure 5.10e) was observed because of the absence of interparticle sliding prevalent in the polycrystalline sample. Indeed, the results suggest that a ~10 nm deep indent is sufficient to yield a reliable E value. This finding shows that AFM nanoindentation can be developed into an excellent mechanical characterization tool for probing few-micrometer sized MOF crystals and other nanostructured compounds, which cannot be directly measured by instrumented nanoindentation technique. Furthermore, as shown in Figure 5.7 the hardness values determined are consistent with the literature (H ~500 MPa, obtained from a large ZIF-8 crystal),[45] albeit with a stronger dependence on the indentation depth. The clear advantage here, however, is the ability to quantify hardness by employing a MOF crystal whose dimension is a hundred times smaller than the minimum size[76] previously required to enable reliable nanoindentation measurements.

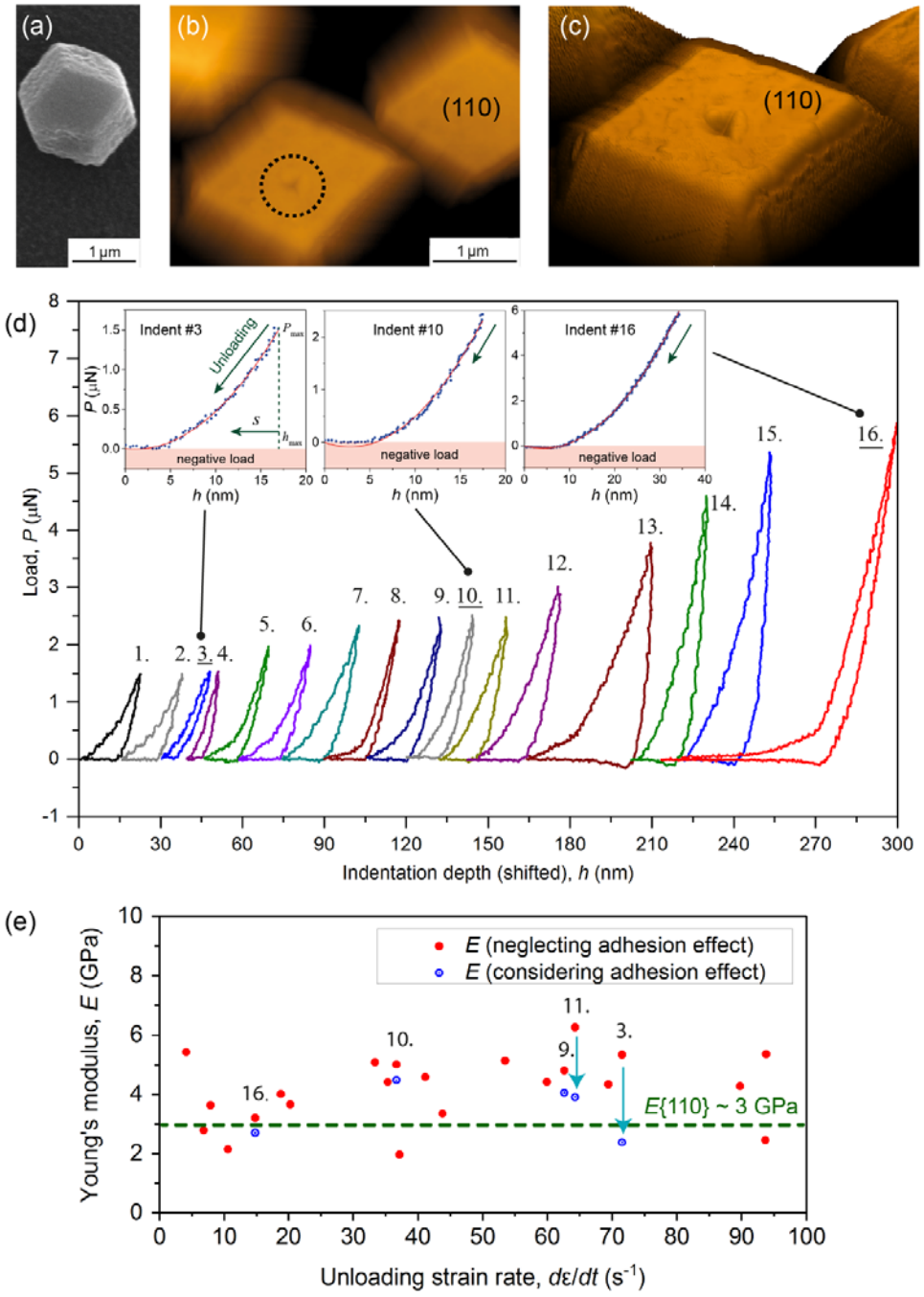

Figure 5.10 (a) SEM image of an isolated micron-sized single crystal of ZIF-8 used in the AFM nanoindentation study. (b-c) AFM topographic images showing the residual indent on the {110}-oriented crystal facets. This sample corresponds to the *P-h* curve of indent #4 shown in panel (d). (d) Representative *P-h* curves of indentation measurements performed on 16 individual crystals. The insets show three examples of unloading data with the adhesion segments (negative load), which were fitted using the adhesion model in equation (5.1). Note that numbers in brackets are the indentation depths in nm. (e) Young's modulus as a function of the unloading strain rate, in which each data point was determined from an individual single crystal whose sample # is matching the *P-h* curve in panel (d). The green dotted line indicates the literature value of $E_{[110]}$, based on Ref. [7].

5.4.2 Contact Adhesion Forces at the Nanoscale

In this section, the additional effects due to contact adhesive forces at the nanometer length scale have been considered, and the forces are established between the indenter tip and crystal surface during the unloading stage of tip withdrawal (from $h_{\max}$ to h_f). Herein, the adhesion contact model proposed by Sirghi and Rossi[182] was implemented. In the model, they demonstrated that the total interaction force at unloading which accounts for both elastic and adhesive interactions, can be expressed as:

$$P = \frac{2E \cdot tan\,\theta}{(1-\nu^2)\pi} \cdot (h - h_{\text{final}})^2 - \gamma \cdot \frac{8tan\,\theta}{\pi cos\theta} \cdot (h - h_{\text{final}}) \qquad (5.1)$$

where γ is termed the thermodynamic work of adhesion[335] developed between the indenter and the sample surface in contact. More details are presented in §4.7.1.

Equation (5.1) together with the measured *P*-*h* data (Figure 5.10d) have been applied to solve for the magnitudes of γ. For example, the analysis of the values of γ for these selected indents: #3, #9, #10, #11 and #16, has been taken since all of these indents exhibit negative loads in their unloading test segments (see Figure 5.10d insets) signifying the effects of adhesion interactions. The insets of Figure 5.11a-b show the values determined for the thermodynamic work of adhesion; first by letting γ to be a constant (i.e. independent of depth),[182] and, subsequently I propose the use of γ that scales linearly with the surface penetration depth such that $\gamma \propto h$. The latter approach was shown to result in a more realistic response demonstrating the local variation of adhesion interactions (~ J/m^2) with respect to the indenter position *s* during tip unloading, see Figure 5.11b inset. The magnitudes of the thermodynamic work of adhesion determined are broadly found in the range of ~$0.4 - 3.3$ J/m^2, whereby its precise value is dependent on the local nature of the indenter-to-surface contact. And interestingly by comparison to the situation where there is no indenter interaction, the "free" surface energy (γ_s) of ZIF-8 has been estimated by DFT

to be ~0.28 J/m^2.[71] Not surprisingly, the thermodynamic work of adhesion obtained are markedly higher than those found on soft polymers (with low Young's modulus and hardness), for example polydimethylsiloxane, PDMS (γ is 0.095 J/m^2 and E ~2 MPa)[182] and for a polyimide interface whose γ ~0.11 J/m^2.[336]

Upon indenter unloading, it follows that the *release* of the energy of adhesion W_{ad} (negative sign) can be determined from:

$$W_{ad} = -\gamma A \tag{5.2}$$

where A is the actual indenter-to-sample surface contact area.

The relation for an equivalent conical indenter with an included angle of 2θ is given by:

$$A = \frac{\pi \cdot tan\,\theta}{cos\,\theta} \cdot h^2 \tag{5.3}$$

Adhesion energies determined based on the assumptions of, either a constant $\gamma_{adhesion}$ or a linear correlation of γ, are presented in Figure 5.11a-b, respectively. The difference between the two approaches becomes even clearer while comparing their first derivatives, i.e. the slope dW_{ad}/ds, as demonstrated in the matching Figure 5.11c-d. Taking the linear correlation of γ, variation in adhesion energy was detected, and this can be used to elucidate the salient nature of the indenter-to-surface contacts as illustrated in Figure 5.11d inset, where: (i) the elastic work (W_{el}) > plastic work (W_{pl}) for P-h curves featuring a predominantly elastic recovery (*e.g.* indents #3, 16), whereas (ii) W_{el} < W_{pl} for an elastic-plastic dominated response experienced in the unloading test segment (*e.g.* indents #9, 10,11).

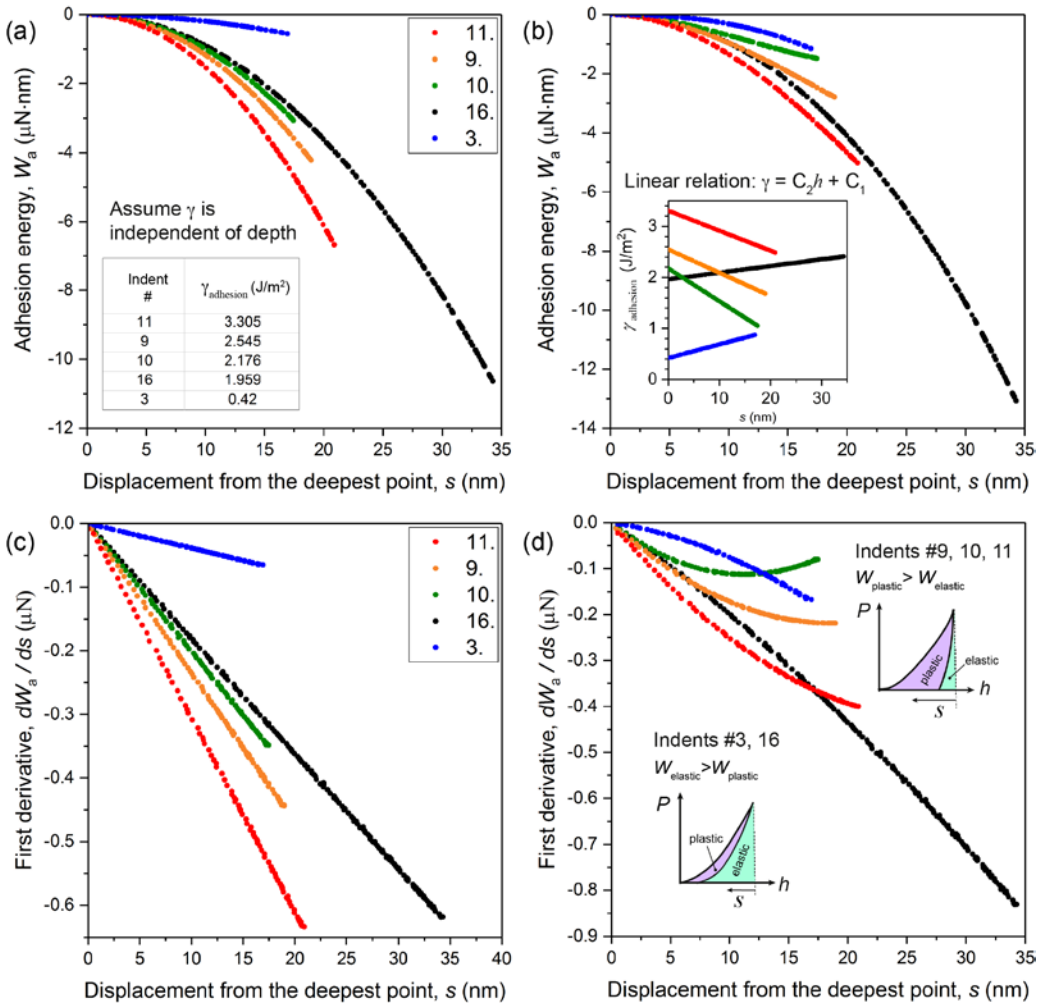

Figure 5.11 Top panels: (a-b) Reduction in adhesion energy ($-W_{ad}$) as a function of the position of the indenter tip measured from the deepest point of contact, here designated as *s*. The insets show the values of γ, derived from equation (5.1), first by letting γ to be a constant in accordance with Ref. [182], and by assuming as a linear function of indentation depth. Bottom panels: (c-d) Plots of dW_{ad}/ds as a function of the tip withdrawal distance from the maximum indenter penetration depth. The indentation numbers # correspond to the *P*-*h* curves in Figure 5.10d.

As presented in Figure 5.10e, the Young's modulus (*E*) corrected for adhesion interaction has a relatively lower magnitude than the ones derived using the standard OP method. It was found that when the adhesive forces are hindering the unloading process, the magnitude of *E* determined may be overestimated by as much as ~1–2 GPa; by correcting for the influence of adhesion, this discrepancy could be addressed. The Young's moduli

determined, *i.e.* data points in Figure 5.10e, with and without considering the contribution from adhesive forces are compared in Table 5.1.

Table 5.1 Young's moduli measured by using the OP method to process load-displacement data obtained from AFM nanoindentation of micron-sized crystals of ZIF-8. Note that the numbering of indents corresponds to the ones in Figure 5.10.

Indentation number #	**Young's Modulus E (GPa)**	**E with adhesion correction (GPa)**	$\frac{W_{\text{elastic}}}{W_{\text{plastic}}}$
1	5.365		0.753
2	4.279		0.847
3	5.339	2.385	2.638
4	2.455		0.979
5	4.594		1.370
6	4.343		1.260
7	4.427		0.807
8	4.425		2.120
9	4.807	4.050	1.064
10	5.013	4.485	1.254
11	6.264	3.903	0.857
12	5.140		0.734
13	3.347		0.168
14	1.971		0.607
15	5.088		0.378
16	3.197	2.698	1.828

5.5 Summary of the Chapter

It has been demonstrated, for the first time, the efficacy of the AFM nanoindentation approach to achieve quantitative measurements on the fine-scale crystals of a prototypical MOF material: ZIF-8. The primary results are summarised below.

- General AFM nanoindentation methodologies have been established for individual MOF nanocrystals (~300 to 500 nm) and *isolated* micron-sized MOF crystals

(~1 to 2 μm), which to date cannot be characterised accurately using the instrumented nanoindentation techniques (IIT), because of the very small crystal size.

- AFM nanoindentation enables the acquisition of force (few μN) versus displacement (10s nm) measurements at a significantly higher resolution, from which to derive quantitative mechanical properties such as the Young's modulus and hardness properties. Moreover, AFM allows direct imaging of the residual indent to study surface deformation right after unloading.

- The work elucidates the optimal combination of the AFM instrument parameters, specifically the probe scan rate and the cantilever deflection can be tuned to maximise the unloading strain rate ($\dot{\varepsilon}$). It was found that $\dot{\varepsilon} > 60$ s^{-1} is necessary to surpass the effects of creep deformation (e.g. in ZIF-8) upon unloading of a compliant sample, to enable accurate determination of the contact stiffness (and subsequently the derived Young's modulus).

- It was shown that the high sensitivity of the AFM force transducers (pN) enables the characterisation of adhesive force interactions between the indenter tip and the MOF crystal, with which the thermodynamic work of adhesion was determined to be of the order of a few J/m^2.

- The methodologies described in this study will be applicable to the fine-scale mechanical characterisation of other porous MOFs, 3-D framework crystals, 2-D nanosheet materials and polycrystalline films. Specifically, the application of AFM nanoindentation technique to quantify the mechanical properties of 2-D nanosheets of CuBDC and submillimetre-sized crystals of HKUST-1 will be discussed in Chapter 7 and Chapter 8, respectively.

Chapter 6: Failure Modes of ZIF-8 Crystals Under Indentation

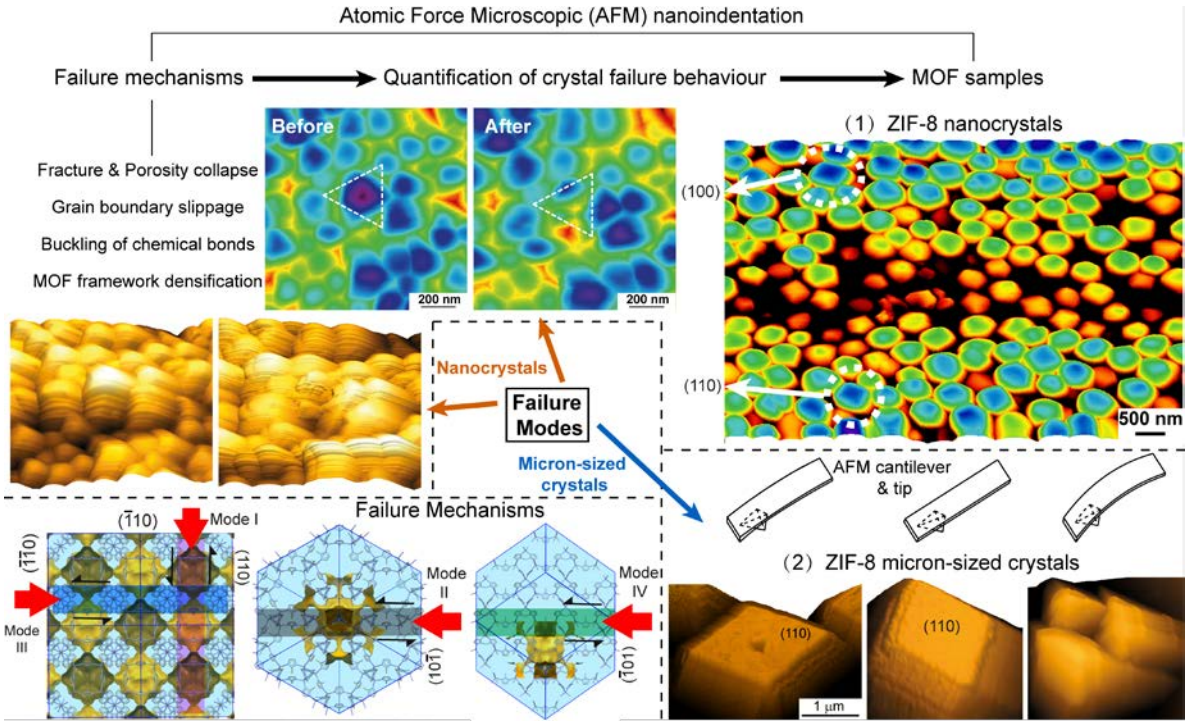

This chapter will focus on the failure mechanisms of ZIF-8 nanocrystals and micron-sized single crystals. To maintain consistency, the ZIF-8 samples used herein are the same as the ones employed in Chapter 5. To the best of my knowledge, this is the first attempt to develop a systematic approach to quantify the nanoscale mechanical failure modes of MOFs. By harnessing the force and displacement sensitivities of atomic force microscopy (AFM)-based nanoindentation, four distinctive failure modes of individual crystals of ZIF-8 were studied. Besides, I also investigated the interfacial strength of the closely-packed ZIF-8 nanocrystals. This was achieved on account of the fact that the measured threshold loading conditions of these failure modes can be understood by examining the distortions of the loading portion of the force-displacement (P-h) curves, thus disclosing the interfacial and fracture strengths of ZIF-8. Moreover, the AFM-based characterisation technique established here has been applied to other challenging systems: the MOF nanosheets in Chapter 7 and the anisotropic and auxetic MOF crystal in Chapter 8.

6.1 Introduction

MOFs, unlike the dense hybrid frameworks, often possess very high porosity with promising functionalities. It is obvious that mechanical robustness is important because structural failures of the underlying framework could affect the performance of MOF products. In order to investigate the failure modes and the threshold triggering conditions, the high-resolution nanoindentation technique employing the AFM instrument has been developed. The aim is to identify and quantify the failure modes of porous MOF structures, by probing closer to the scale of the constituent components and nanoporosity. In this chapter, the study of the failure modes is focused on the ZIF-8 materials.

6.2 Identification of Framework Failure based on the *P-h* curves

This work shows that the AFM-based nanoindentation method can be adapted to quantify the interfacial mechanical properties of a polycrystalline thin-film material, comprising a compact "coating" of MOF nanocrystals as shown in Figure 5.1c. The cube-corner AFM diamond probe was used to generate significantly deeper indentations, for example with $h_{max} > 100$ nm to be able to measure the collective response of a polycrystalline film. It was found that the occurrence of failures usually causes severe distortions of the force-displacement (*P-h*) curves, as exemplified in Figure 6.1 and Figure 6.2. These failures can originate from either the individual crystals or the polycrystalline structures. For instance, Figure 6.3 shows the residual indent obtained from a 270 nm deep indentation experiment, it is clear that the response measured here could no longer be associated with that of a single crystal alone. The *P-h* curve reveals a distinctive "pop-in" effect[91] that can be attributed to interfacial sliding or interparticle slippage of adjacent polycrystalline aggregates due to shear-induced glide.

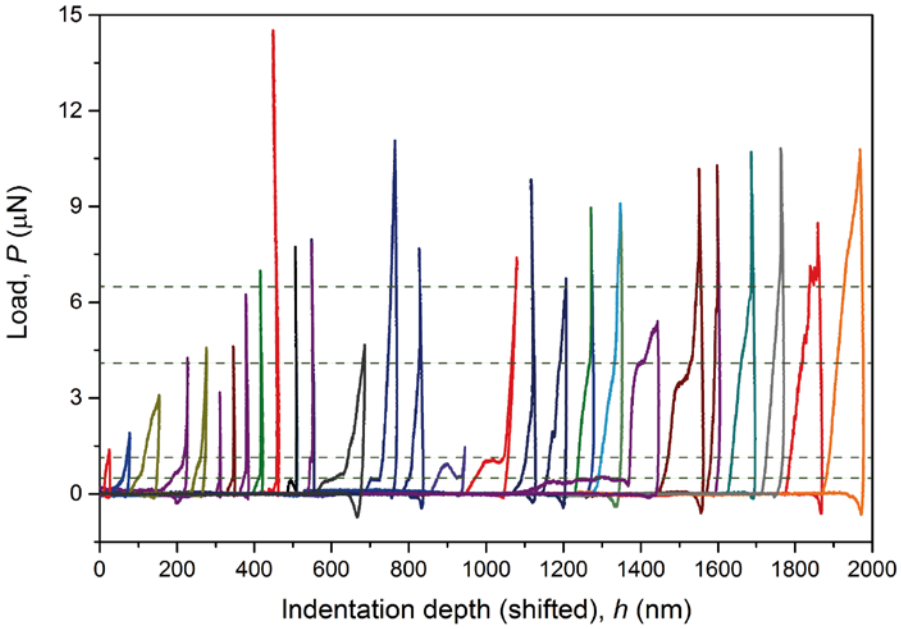

Figure 6.1 Examples of the distorted *P-h* curves obtained from indentation on individual micron-sized crystals of ZIF-8, indicating different failure events. The proposed failure modes are presented in Figure 6.14.

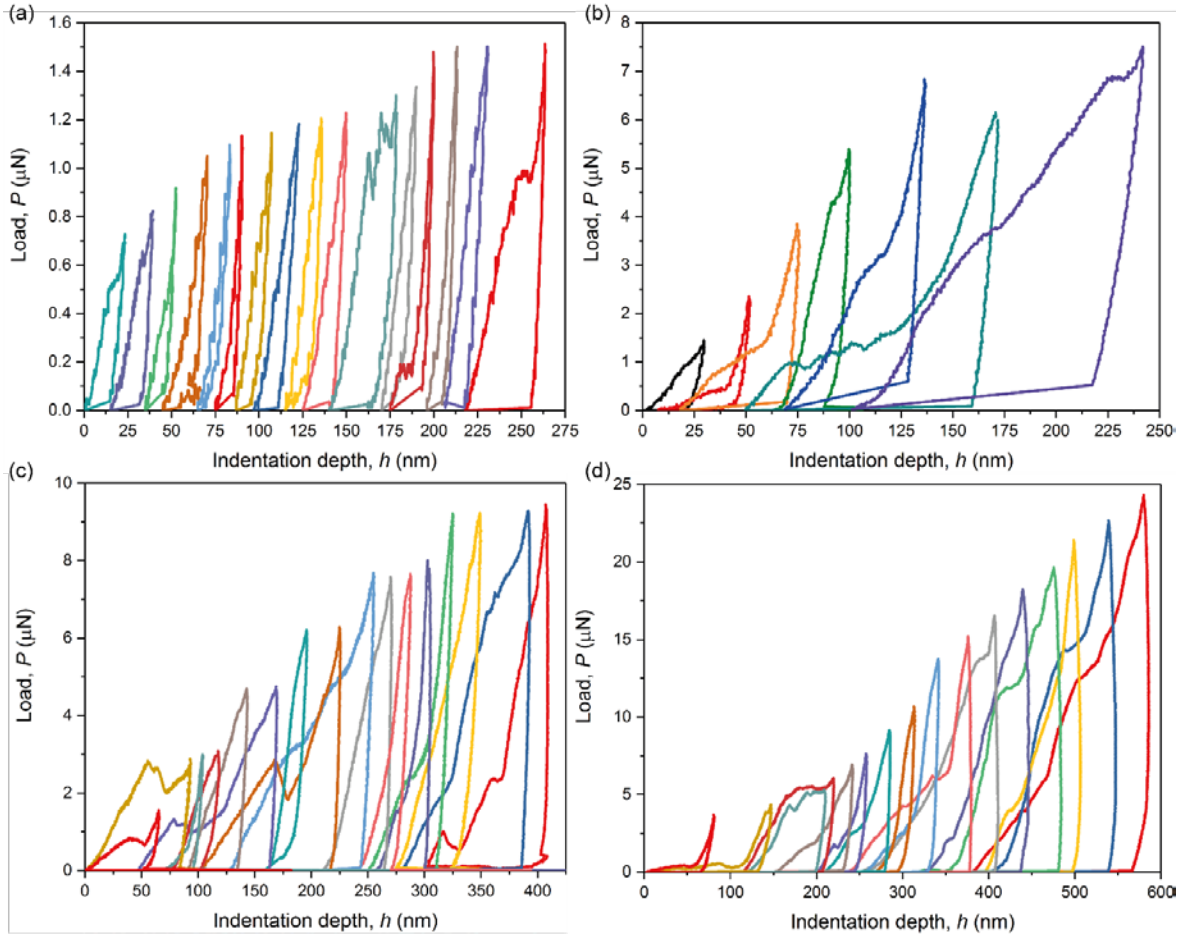

Figure 6.2 Examples of the distorted *P-h* curves on polycrystalline ZIF-8 nanocrystals, indicating different failure events; see the proposed modes in Figure 6.5.

It was found that such interfacial deformation on a polycrystalline film can yield a much larger surface penetration depth, achieved even with a relatively small indentation load. To illustrate this effect, at the equivalent P_{max} of 12 μN, a 60 nm indentation depth was detected without slip (see Figure 5.2b for a single-crystal response) compared to the 270 nm deep indent in Figure 6.3a associated with a deformation dominated by polycrystalline sliding. Of course, if there is a substantial polycrystalline interfacial contribution to the overall indentation process, it is important to note that the hardness calculated from $H = P_{max}/A$ will become erroneously low because the contact area becomes significantly larger from interfacial sliding combined with pop-in deformation.

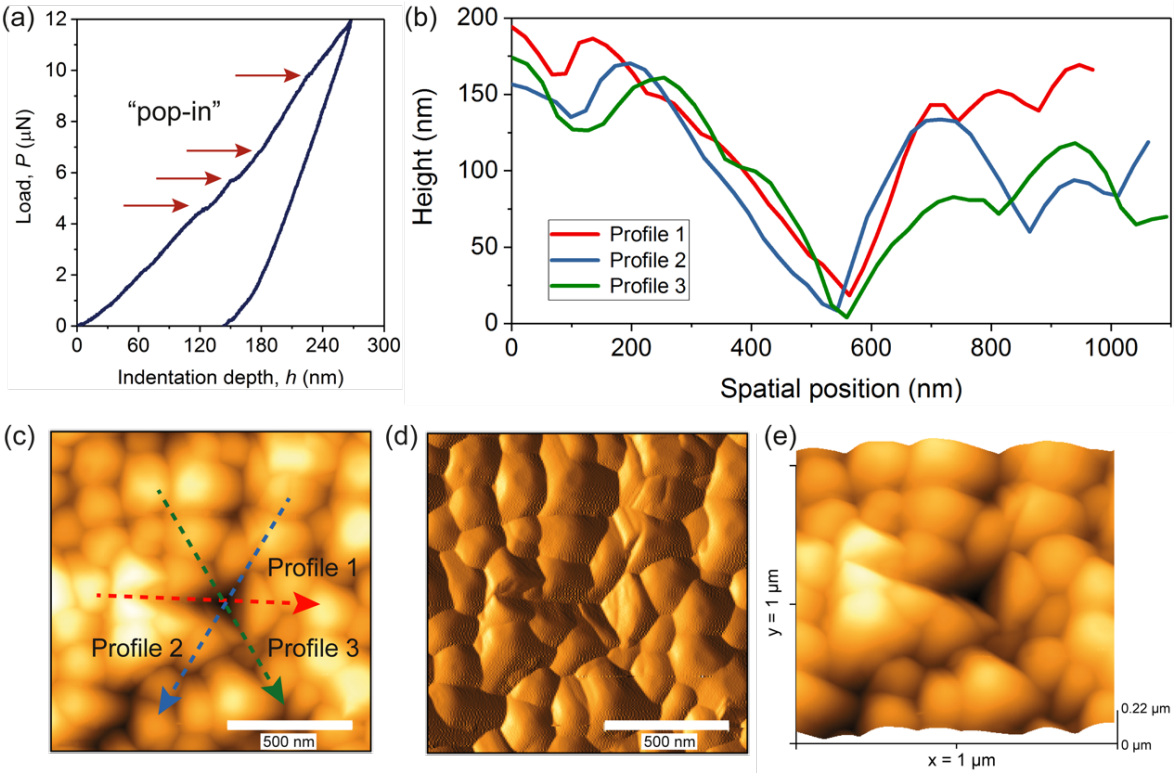

Figure 6.3 (a) An example of a 270 nm deep indent on the polycrystalline film comprising nanocrystals of ZIF-8, where pop-ins can be associated with the interfacial sliding of adjacent nanocrystals occurring in the periphery of the indenter. (b) AFM topographic scans corresponding to the 3-D height images in (c) and (e), height mapping was achieved using the indenter probe. (d) AFM amplitude image revealing the pyramidal-shape of the residual indents.

The characterization of the interfacial sliding effects occurring at the grain boundary interface of adjacent polycrystals is discussed here, when the cube-corner AFM probe was used to indent the polycrystalline film fabricated by drop casting technique. Figure 6.4a shows three example experiments in which the indents of the residual indents were imaged by using the AFM PDNISP indenter tip. It is proposed that the deformation mode associated with interfacial sliding of polycrystals can be represented by the schematic in the bottom panel of Figure 6.4b, in which shear-induced sliding and compaction of the nanocrystals will accommodate the large penetration of the tip. Figure 6.4c-d present the scenario whereby the load-displacement curves of indents *P1* and *P2* indicate a final penetration depth of ~200 nm, but the maximum load of the former indent was relatively lower. Intriguingly, while the maximum load of indent *P3* was ~7 μN resembling that of indent *P1*, its maximum indentation depth was nearly three times lower.

The data, therefore, revealed that the exact nature of the sliding deformation underpinning a polycrystalline film (constituting MOF nanocrystals) is a complex phenomenon. It may be triggered by a small external load, of an order of just several μN. Irregularity detected in the *P-h* curve can be analysed by comparing it to the ideal function (without pop-in), with the form of $P(h) = Ah^2 + Bh$, given by the red curves in Figure 6.4c-e. This approach can be used to pinpoint the threshold depth (h^*) at which an interfacial sliding deformation occurs, see highlighted regions marked in Figure 6.4f-h. It was found that h^* is ranging from ~50-80 nm for the polycrystalline film of ZIF-8, which indicates that grain-boundary slippage can be triggered by an indentation depth that is not exceeding 1/3 of the size of the smallest individual nanocrystal (~300 nm).

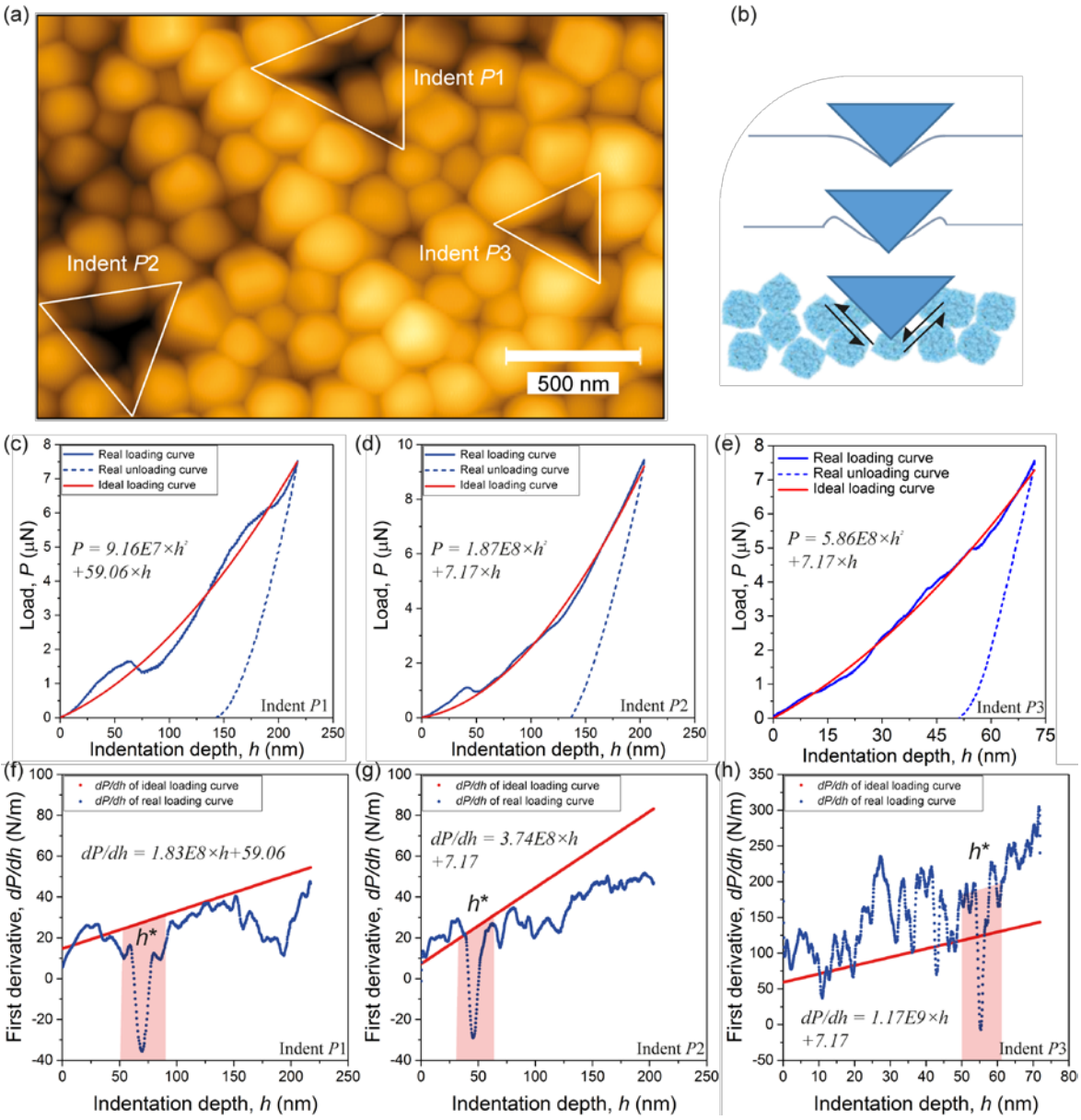

Figure 6.4 (a) AFM scans showing three residual indents on the polycrystalline film comprising ZIF-8 nanocrystals. (b) Schematic (top to bottom) illustrating the common sink-in or pile-up deformations against the grain-boundary sliding of polycrystals occurring under the indenter tip. (c-e) Force-displacement (*P-h*) curves comparing the measured data to the idealised *P-h* curve in accordance with the relation $P(h) = Ah^2 + Bh$, where *A* and *B* are curve fitting coefficients. The indent numbering *P#* corresponds to the ones denoted in panel (a). (f-h) Pop-in/sink-in phenomenon where the first major slip events are highlighted, identified by tracking the sharp decline in the contact stiffness, d*P*/d*h*.

6.3 Quantitative Measurements of Interfacial Sliding and Fracture Strengths of ZIF-8 Nanocrystals (Thin Film Coatings) Using AFM Nanoindentation

The application of AFM nanoindentation can be extended to characterise the mechanical failure modes of polycrystalline ZIF-8 nanocrystals. Six examples of the topographic images collected by AFM are shown in Figure 6.5, Figure 6.6, and Figure 6.7, along with the method presented in Figure 6.8 to identify the distortions/turning points on the *P-h* curves. The results are compiled in Figure 6.5c-d. Pile-up and sink-in phenomena can be observed in Figure 6.5a-b, which was confirmed by tracking the evolution of the surface topography before and after each indentation measurement. It can be seen that the deformation behaviour is complex, and this will be dependent upon the interfacial strength of the grain boundary between adjacent crystals and the local packing pattern in the vicinity of the indenter tip (Figure 6.5c-d).

The representative failure modes are presented in Figure 6.5e-f. For instance, the first hump of the loading curve of the indent *P5* in Figure 6.5d was due to the combined effects of crystal fracture and crystal slippage, as evidenced by the AFM image and the height profiles in Figure 6.5b. These failure modes could lead to a reduction in the Young modulus and hardness values measured in the experiment.[337] Subsequently the corresponding threshold stresses for the four distinctive failure modes A-D were determined, and plotted as a failure map shown in Figure 6.5h. It can be seen that Mode A due to grain boundary slippage could occur at a relatively shallow penetration depth of under ~50 nm, while Mode B is linked to polycrystalline fracture where a failure strength of up to 1 GPa has been determined. Mode C indicates the accumulated compaction of porous materials during indentation, while Mode D suggests the continuous buckling of bonds along the

indentation direction (resembling the buckling response of highly-aligned carbon nanotubes under compression[338]).

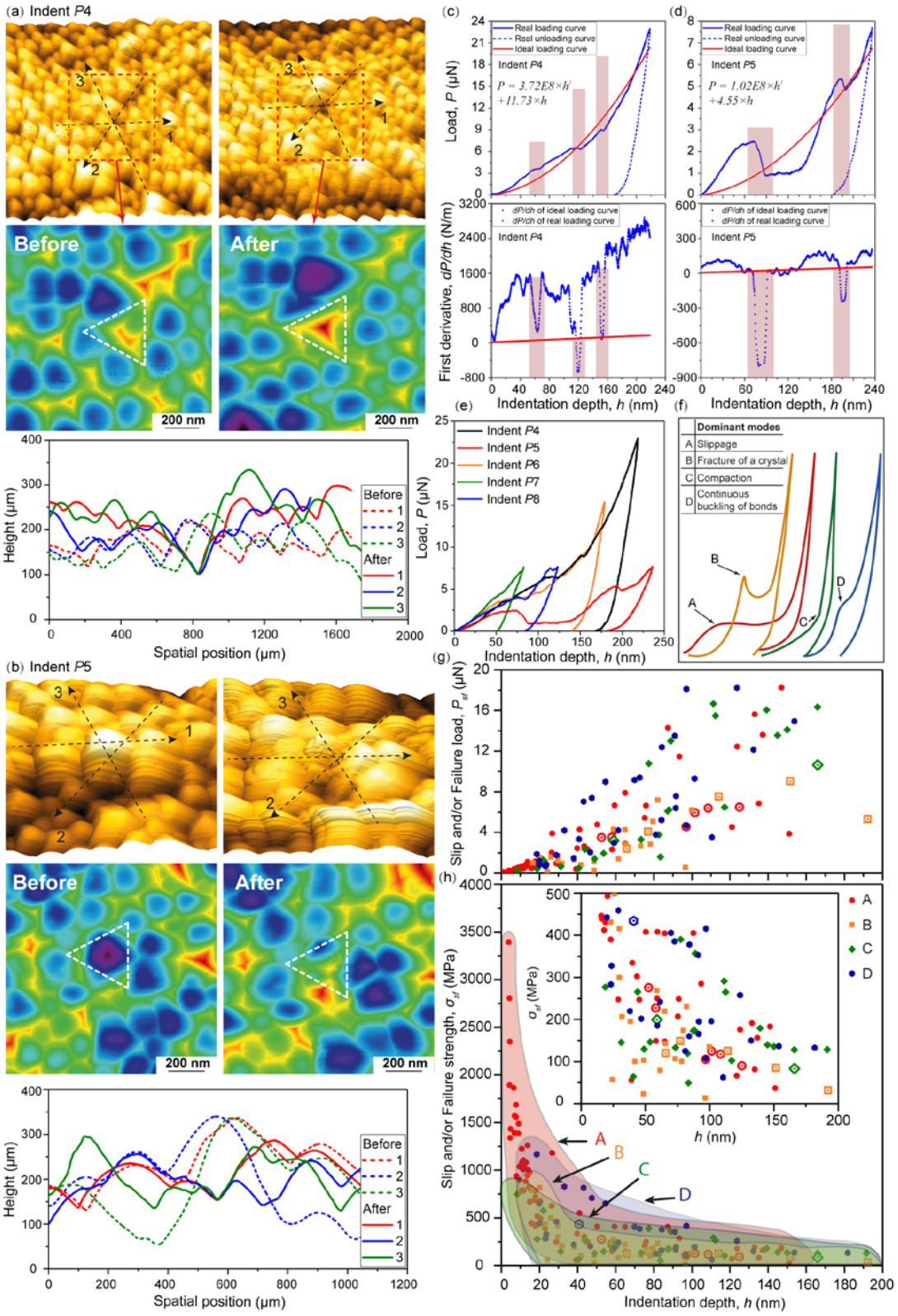

Figure 6.5 AFM nanoindentation on the polycrystalline ZIF-8 nanocrystals in the form of a thin-film coating (example #1 and #2): (a) Interfacial slippage-dominant indentation,

where the contour map and profiles show the displacement of the surrounding nanocrystals. (b) Crystal facture-dominant indentation, where the contour map and profiles show the fragmentation of a crystal and subsequent slippage. (c-d) Force-displacement curves comparing the measured data to the idealised *P-h* curve in accordance with the relation $P(h) = Ah^2 + Bh$, where *A* and *B* are curve fitting coefficients. Interfacial slippage and crystal fracture are highlighted, identified by tracking the sharp decline in the contact stiffness, d*P*/d*h*. (e) Force-displacement curves. (f) Schematic illustrations of the proposed dominant failure modes. (g) Threshold loads that resulted in interfacial slip and crystal fracture modes, and, (h) the corresponding stresses of the different failure modes. Note that the open symbols in (g-h) correspond to the data extracted from indents marked *P4-P8* in panel (e). Note that the indent contour maps, profiles, and *P-h* curves for indents *P6-8* are shown in Figure 6.6, Figure 6.7, and Figure 6.8 respectively.

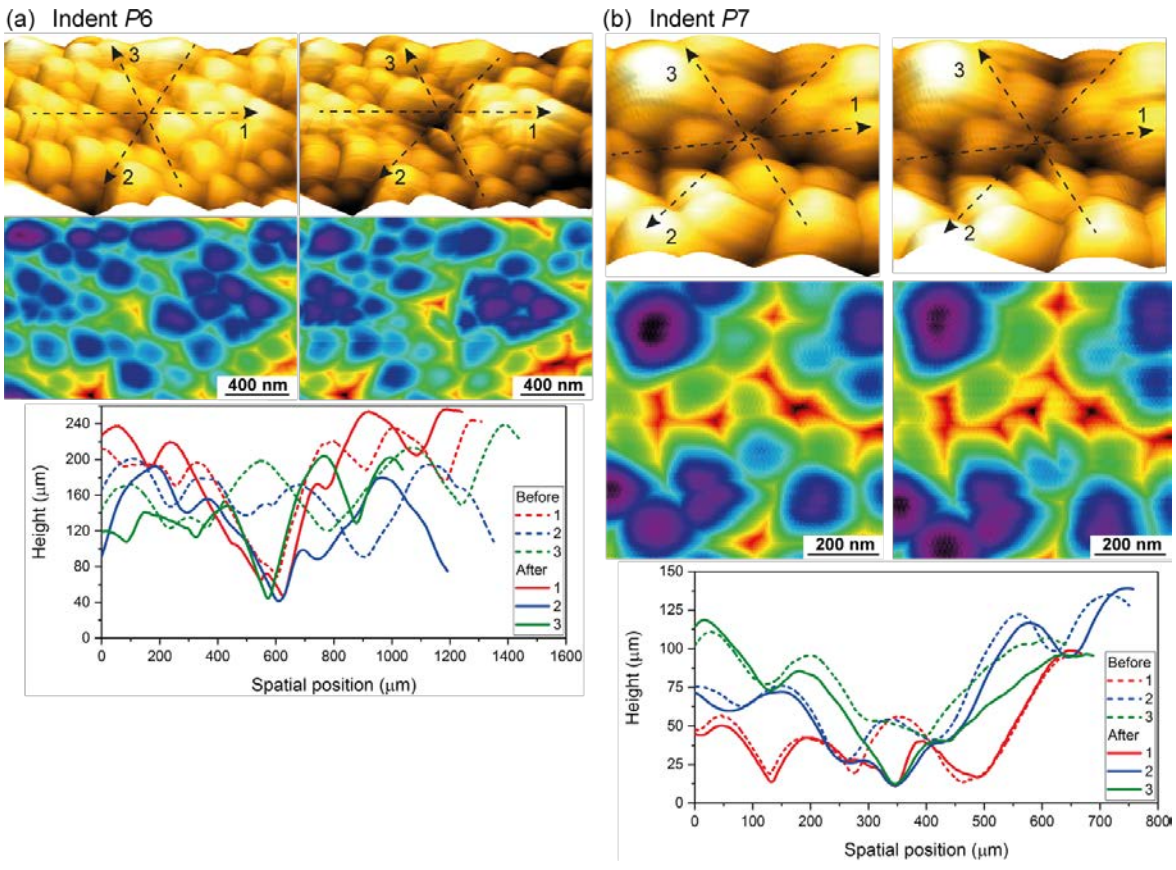

Figure 6.6 AFM nanoindentation on the polycrystalline coatings comprising nanocrystals of ZIF-8 (example #5 and #6): (a) Fracture and interfacial slippage; (b) Cleavage of a ZIF-8 crystal.

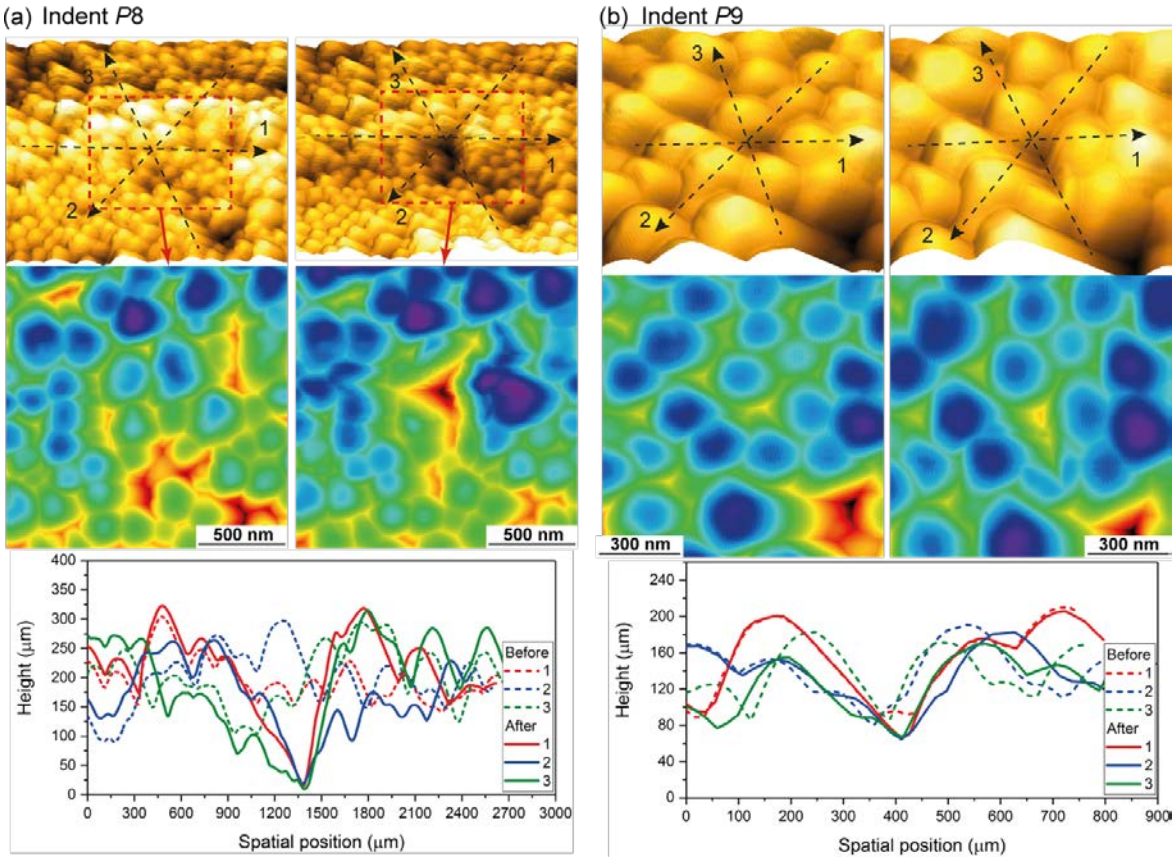

Figure 6.7 AFM nanoindentation on the polycrystalline coatings comprising nanocrystals of ZIF-8 (example #3 and #4): (a) Fracture-dominant failure; (b) Indentation on the interface between two neighboring ZIF-8 crystals.

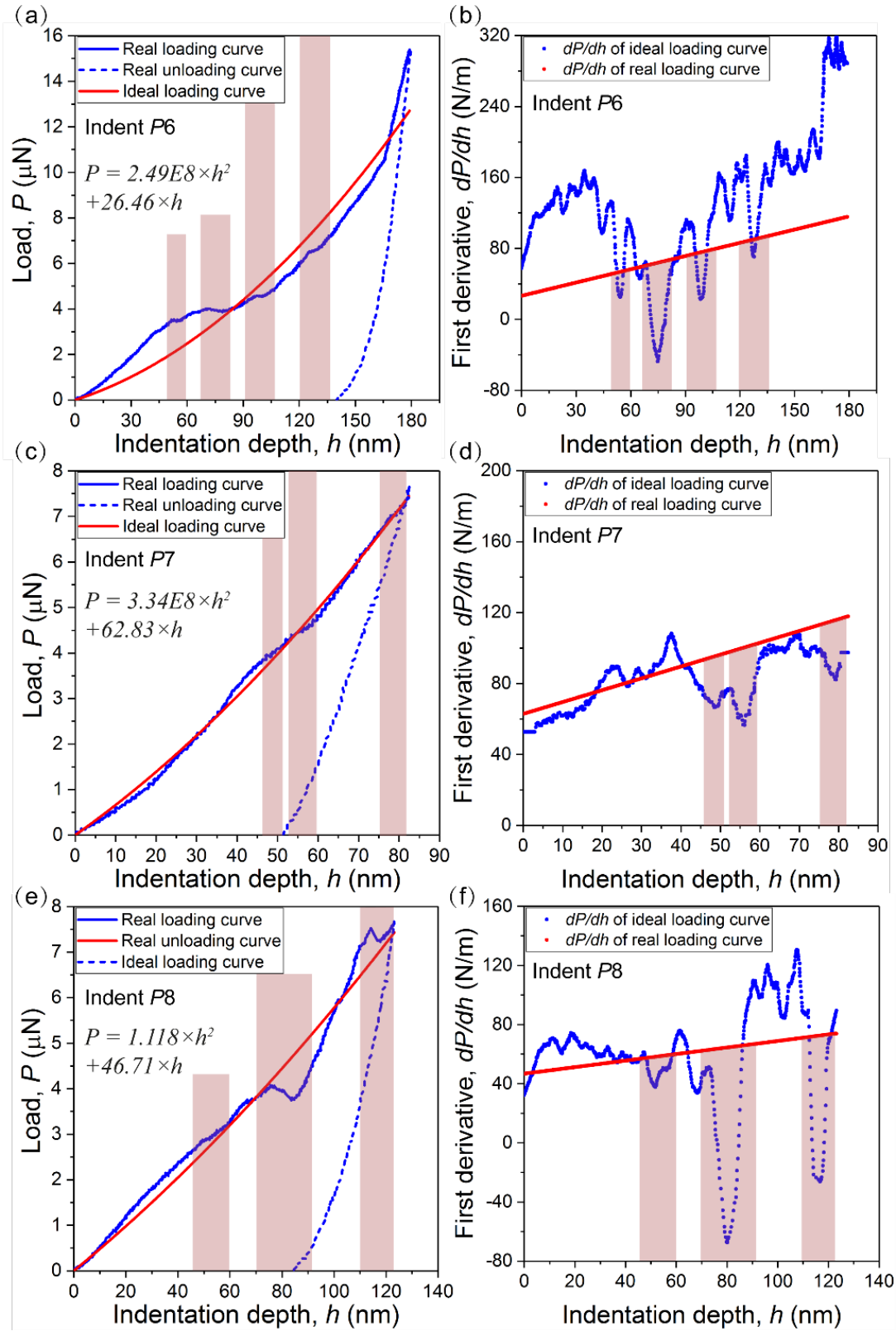

Figure 6.8 (a, c, e) Force-displacement curves comparing the measured data to the idealised *P*-*h* curve in accordance with the relation $P(h) = Ah^2 + Bh$, where A and B are curve fitting coefficients. The indent numbers P# correspond to the ones denoted in Figure 6.6 and Figure 6.7. (b, d, f) Pop-in/sink-in phenomenon where the major events are highlighted, identified by tracking the sharp decline in the contact stiffness, d*P*/d*h*.

6.4 Quantitative Measurements of Film-to-Substrate Adhesion Strength of ZIF-8 Nanocrystals (Thin Film Coatings) Using Instrumented Scratch Technique

Nanoscratch experiments using the instrumented scratch technique (IST) is a relatively more established approach to qualitatively characterise the failure mechanisms. It works by imposing the lateral and normal stresses simultaneously to study the adhesion behaviour of thin film coatings, which is one of the crucial factors to be considered for constructing robust thin film products.[82] For instance, the antireflection coating of a thin-film photovoltaic cell should attach on a glass substrate firmly without debonding when subjected to a shear deformation or bending moments.

I have carried out the nanoscratch experiments on the ZIF-8 polycrystalline thin-film coatings. These experiments were conducted using the MTS NanoIndenter® XP fitted with a Berkovich diamond tip. There were 30 nanoscratch experiments conducted to ensure the consistency of the results. The schematic in Figure 6.9 illustrates the ramp-load test procedure conducted in four steps.

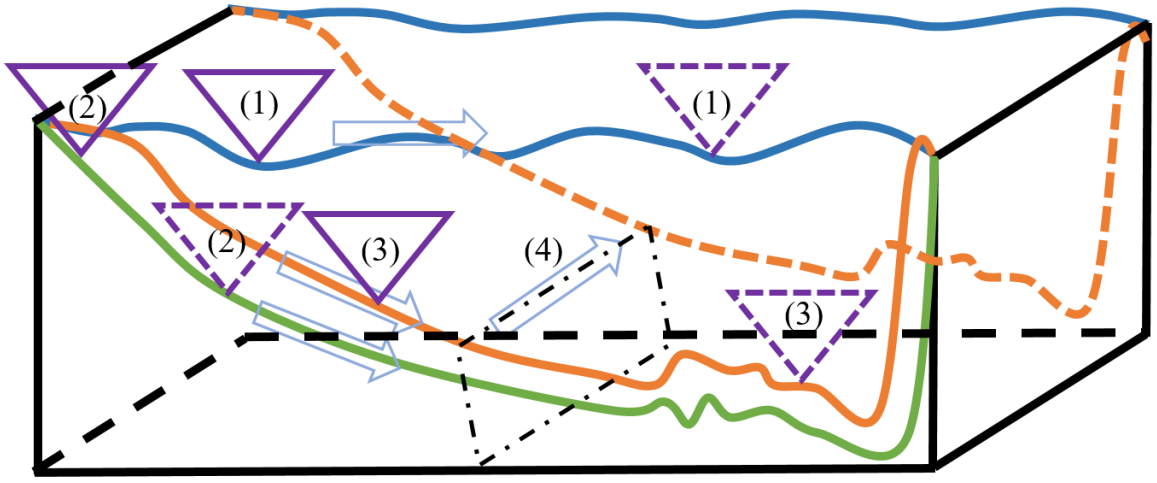

Figure 6.9 Schematic illustrating the four steps of the scratch test. Step #1 – topological scan of the coating surface (in blue). Step #2 – ramp-load scratch (in green). Step #3 – topological scan of the residual deformed surface to detect recovery after scratching (in orange). Step #4 – transverse scan to capture the cross-sectional profile at the middle of scratch track.

In the IST experiment, a ramp-increasing normal load was precisely controlled. In fact, nanoscratch test measures not only the adhesion strength; more importantly, it probes the coupled deformations of both the thin film coating and the substrate. As shown in Figure 6.14, the ZIF-8 polycrystalline thin-film coatings with an average thickness of ~2 μm were scratched along both the edge-forward (ploughing) and face-forward (pushing) directions of the Berkovich tip. Because the Berkovich probe is sharper than a spherical one it has been widely applied in scratch test, it results in better-defined plastic deformation with smaller threshold load into the coatings, as exemplified in Figure 6.10 using a smooth polymer film (Matrimid).

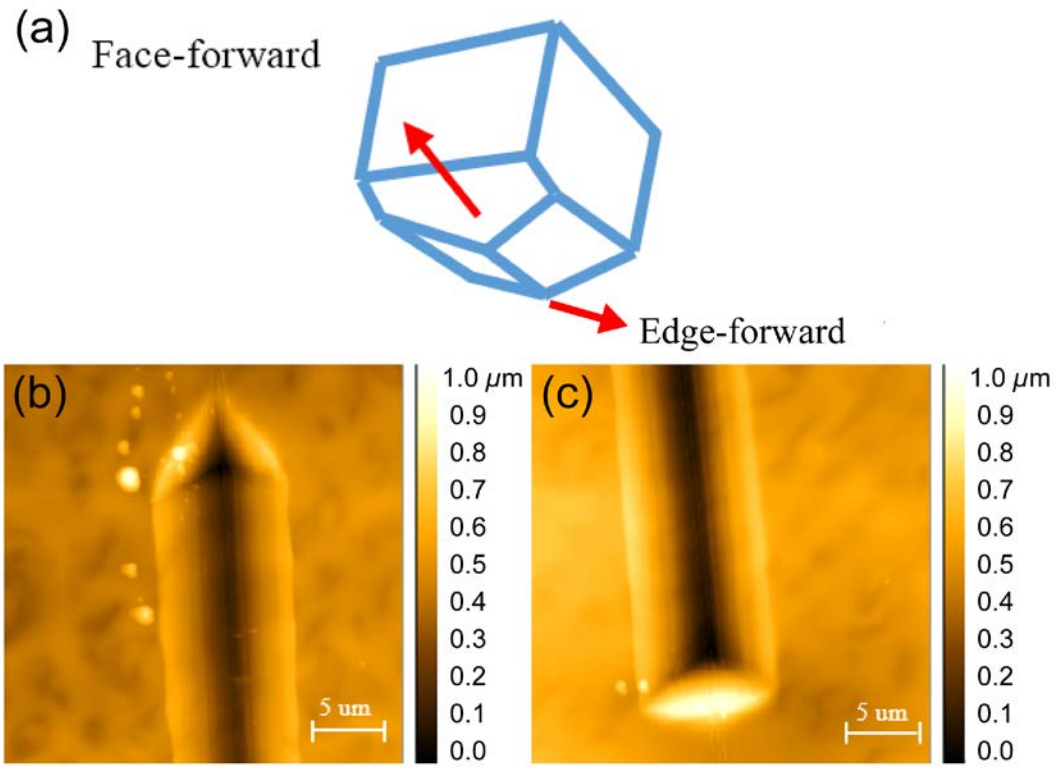

Figure 6.10 (a) Schematic showing the two scratching modes on the smooth (root-mean-square roughness ~20 nm) Matrimid coatings to characterise the scratch tracks. AFM height topographic images of the (b) edge-forward scratch, and (c) face-forward scratch.

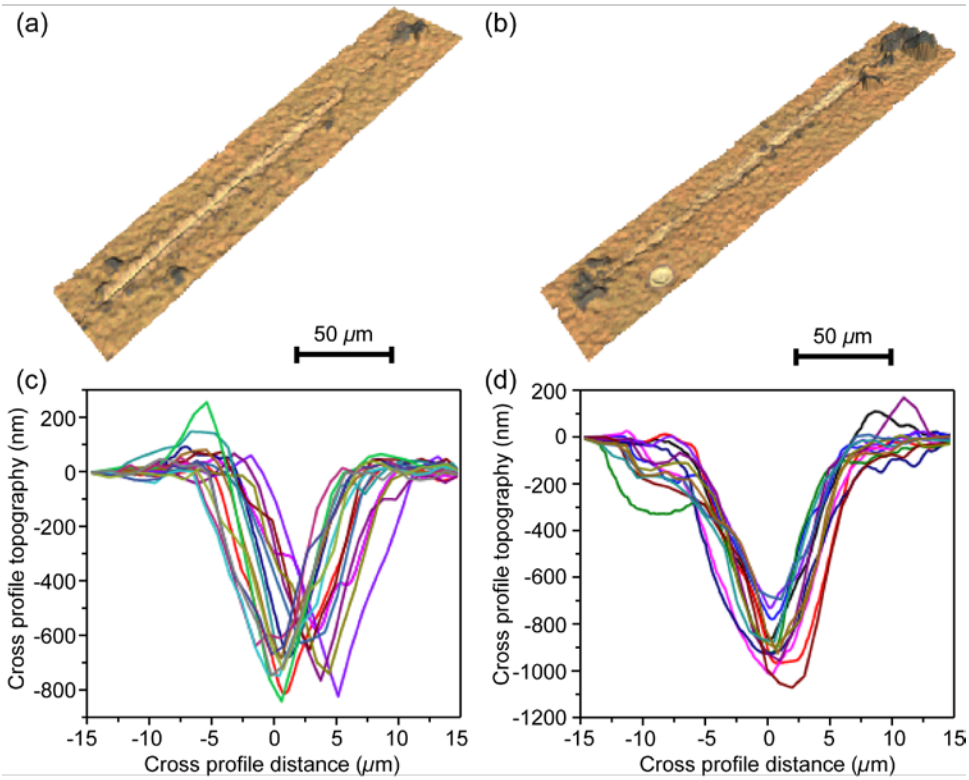

Figure 6.11 3-D topographic images collected using the Alicona InfiniteFocus technique (see §4.4) for the (a) edge-forward and (b) face-forward scratches. Corresponding cross-sectional profiles at the middle of the scratch tracks made on the ZIF-8 coatings.

Inspection of Figure 6.11 shows that under the same loading condition, the scratch in the face-forward direction is penetrating deeper into the surface compared with the experiment along the edge-forward direction since the ploughing action (edge-forward) produces higher stress through the thickness and thus more likely to propagate the minor cracks in the coating and compress the ZIF-8 crystals against the underlying substrate. To put it differently, in contrast to the ploughing scratch, the pushing scratch exerted higher lateral force that releases the stored elastic energy thus leading to a more localised, or even gross spallation along the slide track.

Nevertheless, through a series of experiments at the varying operating conditions in terms of the load rate and scratching direction, I found the quality of the scanned residual topography of the edge-forward scratch is quite unstable as observed in Figure 6.12a. This

can be attributed to the crushing and collapse of the polycrystalline structure underneath the scratch track. Therefore, this work mainly focuses on the results from the face-forward scratch tests, and plastic deformation was found to be predominant leading to delamination failure (see Figure 6.12c). Besides, Figure 6.12b shows the significant plastic deformation before failure.

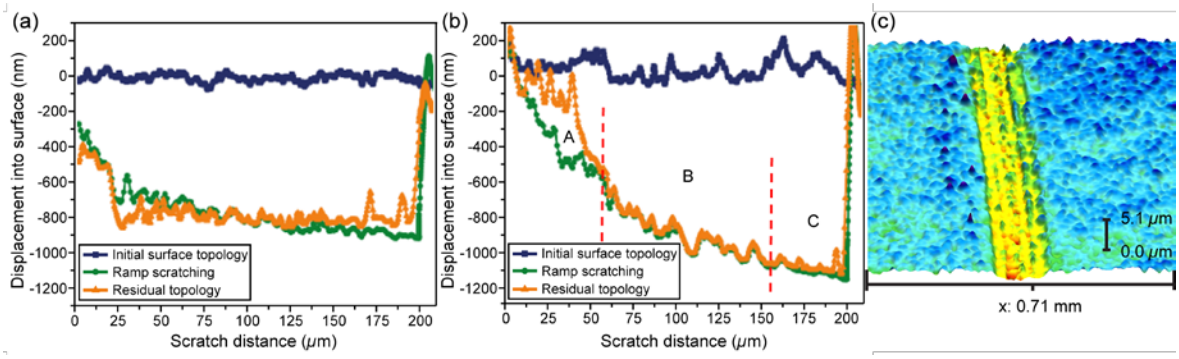

Figure 6.12 Maximum normal load P_{max} = 5 mN and scratch distance S_x = 200 μm along different scratch directions: (a) edge-forward and (b) face-forward. A is designated as the elastic-plastic region, while B denotes the plastic-dominated region, and C is the region where the delamination failure of the coating occurs. (c) Delamination failure caused by the face-forward scratch (the glass substrate exposed along the scratch track is mapped in yellow).

Nanoscratch on the ZIF-8 coatings often crushes the nanocrystals into the underneath layers above the substrate, and this was reflected by the segments of the curves enclosed by the red dashed lines in Figure 6.13. This phenomenon was also reported in the nanoscratch experiment on the HKUST-1 thin film coatings.[82]

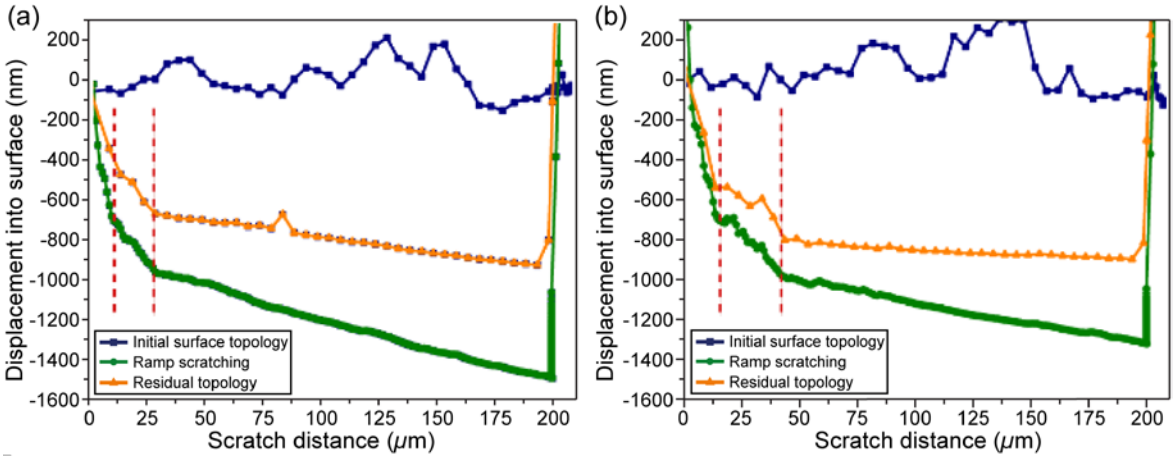

Figure 6.13 Nanoscratch on the ZIF-8 polycrystalline thin film coatings. (a-b) The resulting curves of the scratch displacement into sample surface as a function of the scratch distance.

The threshold load leading to the delamination failure was found to be loading rate dependent. It was observed that the threshold load decreased with the reduction of the loading rate. More specifically, the threshold loads from the scratch tests here employing the different loading rates (in mN/s) 0.50, 0.38, 0.25, and 0.13, are ~3.44, ~2.98, ~2.59, and ~1.49 mN, respectively.

Changing the scratch speed may also alter the threshold load. For tests with the same loading rate in the direction normal to the sample surface but distinct scratch speeds, the displacement into surface was larger as the scratch speed increases. However, no apparent variance was observed in the threshold load when the scratch speed was in the range of 1 μm/s and 10 μm/s. The load/scratch distance ratio (dP/dL) is an important parameter in analysing the data from scratch tests. Herein, it was found that with a decreasing dP/dL ratio, the threshold load reduced accordingly. This phenomenon has also been reported by Steinmann who suggests it is due to the increasing defective adhesion as the dP/dL ratio decreases.[339] This evidences the tendency of decreasing threshold load with the reduction of loading rates when the scratch speed remains constant. This tendency may not be valid in

testing thin film of nanoscale thickness as reported by Beake *et al.*,[340] who found no obvious variance of the threshold load of an 80 nm tetrahedral amorphous carbon film on silicon wafer under different decreasing load/scratch distance ratios. In addition, film roughness may also affect the threshold load, but this impact could be negligible compared with other factors, such as the film thickness.[341]

6.5 Quantitative Measurements of Interfacial Sliding and Fracture Strengths of Individual Micron-Sized Crystals of ZIF-8 Using AFM Nanoindentation

AFM nanoindentation can also be used to study the failure modes of individual micron-sized crystals of ZIF-8 as shown in Figure 6.14. It was observed that the cube-corner diamond indenter can cause brittle fracture as illustrated for the example of "Crystal A" in Figure 6.14a-b; this is not surprising because: (i) the pointy tip geometry generates a large stress concentration onto an unconstrained crystal surface to initiate cracking, and (ii) Mode I→III→IV indicating the corresponding failure loads of each mode. This type of failure measurements was performed on a total of 40 micron-sized crystals to pinpoint their failure modes, whose results are collated in Figure 6.14e. These data, in fact, can be better represented as failure strength (σ_f), see Figure 6.14f, calculated by dividing the individual failure load by its corresponding contact area, $\sigma_f = P_f/A$.

Figure 6.14f shows that the majority of the failure events have been detected at under σ_y ~600 MPa, which was designated as the "yield strength" of ZIF 8, collectively for Modes I, III, and IV. In fact, the failure strength of Mode I is relatively lower at under ~400 MPa. In contrast, Mode II extends to a significantly higher value of exceeding 2 GPa. It was reasoned that the failure mechanisms of the different modes could be explained by considering the local alignment of the indenter axis, in relation to the underlying framework

structure of the ZIF-8 crystal. The four plausible failure mechanisms are depicted in Figure 6.14g, in which the local indenter axis is pointing normal to the {110}-oriented facets. Mode I and IV may be linked to the rupturing of mIM organic linkages *via* shearing of the ZnN_4 coordination clusters,[7] which is a failure mechanism that can be triggered at a relatively low level of stress. Mode II could be explained by buckling of the mIM organic linkages thereby resulting in detection of a distinctive peak load. Mode III may be associated with the breakage of the ZnN_4−mIM−ZnN_4 coordination linkages, followed by sequential pore collapse and material densification (akin to a collapsing foam)[342] thus causing a sharp rise in indentation force. Nonetheless, further confirmation of the precise failure mechanism warrants the application of theoretical approaches, such as large-scale molecular dynamics simulations (see examples in Refs. [[69] and [134]]) that are beyond the scope of the current work. Conversely, the failure strengths measured in my study will be useful for the validation of theoretical models as a follow on to this research.

In addition, automated identification of the failure modes can be achieved according to the gradient change of the distorted *P*-*h* curves. More specifically, the height and width of the peak as well as the depth and width of the valley in the plot (as shown in Figure 6.8) of the first derivative (d*P*/d*h*) as a function of the indentation depth (*h*) can be used to form the automated identification criteria.

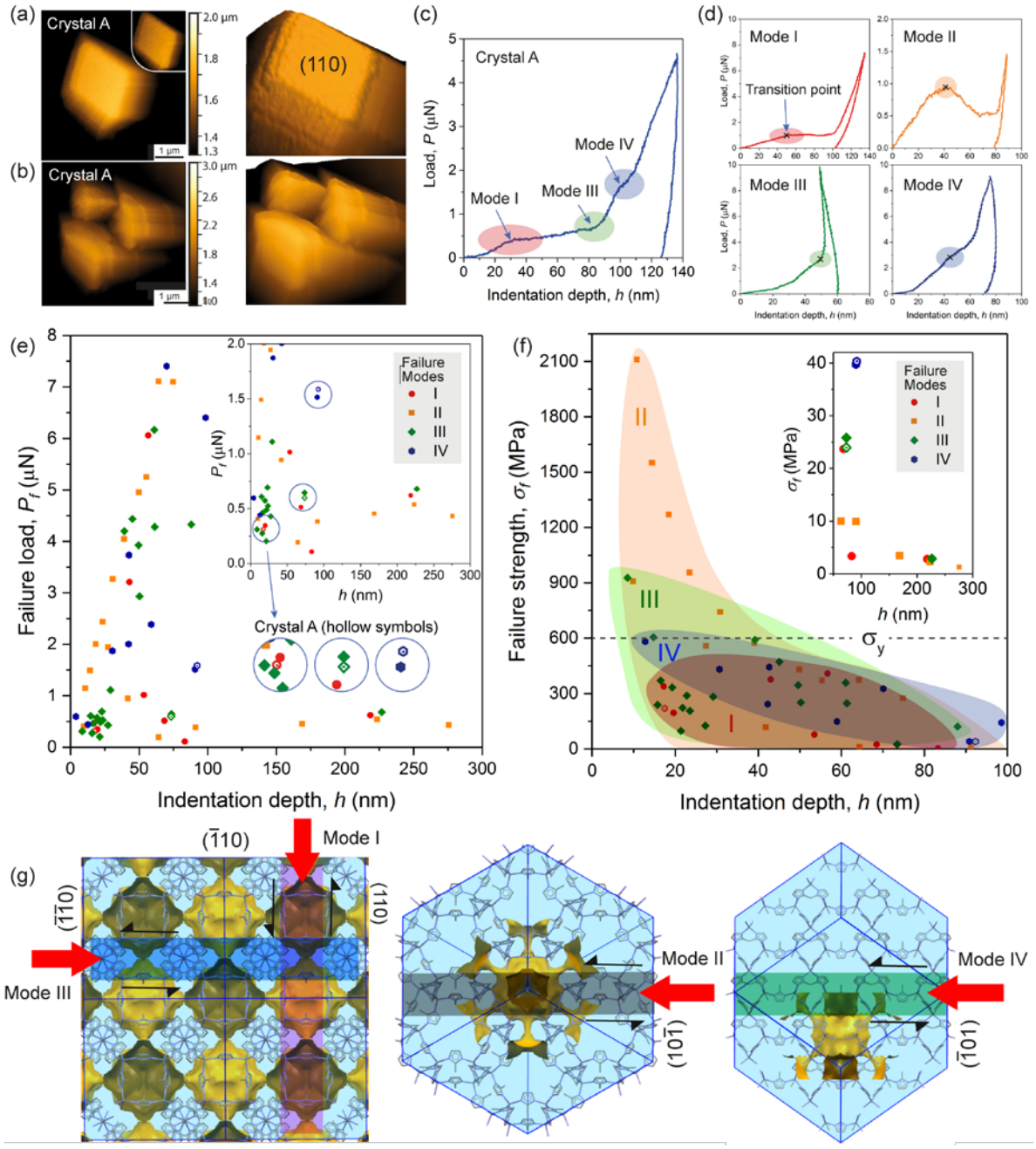

Figure 6.14 Failure modes of micron-sized crystals of ZIF-8 induced by AFM nanoindentation. (a) AFM topographic scans of (a) the micron-sized crystal "A" with the top (110) facet before indentation test, and (b) post-indentation leading to crystal fracture. (c) *P-h* curve of crystal A, revealing the three different failure modes. (d) Representative *P-h* curves showing the four failure modes identified in ZIF-8. (e-f) Fracture loads and fracture strengths obtained by indenting 40 individual samples of micron-sized crystals of ZIF-8, in which the four failure modes are colour coded. (g) Proposed failure modes normal to the indented {110}-oriented crystal facets. The red arrow designates the position of the indenter axis relative to the local crystal structure of ZIF-8. The yellow surfaces represent the porosity (solvent accessible volume) of a 2×2×2 super cell.

6.6 Summary of the Chapter

The characterisation of the different failure mechanisms of MOFs (using ZIF-8 as the model material system) at the micro and nanoscale has been achieved. The results of this study will be relevant to the design of MOFs to make them suitable for practical applications. The major results can be summarised as follows:

- It has been demonstrated that the AFM indenter probe is effective for inducing grain-boundary interfacial sliding of a polycrystalline MOF film to investigate the pop-in and slippage phenomena.

- AFM nanoindentation can be employed to probe the local failure modes of micron-sized MOF crystals, and to enable quantitative measurements of fracture strengths of tiny crystals. The four failure modes being observed or proposed are: grain boundary slippage, fracture of the crystalline structure, densification of the porous frameworks, and buckling of the chemical bonds.

- The methodologies described in this chapter can also be extended to study to the fine-scale failure mechanisms of other porous MOFs, 3-D framework crystals, 2-D nanosheet materials and polycrystalline films. Further to this work, I also developed a larger-scale toughness measurement method to probe porous organic polymers using the MTS instrumented nanoindentation (see Ref. [98]).

- Using the instrumented scratch technique, failure mechanisms of MOF polycrystalline thin-film coatings under simultaneous lateral and normal stresses have been characterised. The current results suggest the possibility for using the AFM instrument to scratch MOF systems at an even finer scale.

Chapter 7: Mechanical Behaviour of Two-Dimensional CuBDC Nanosheets

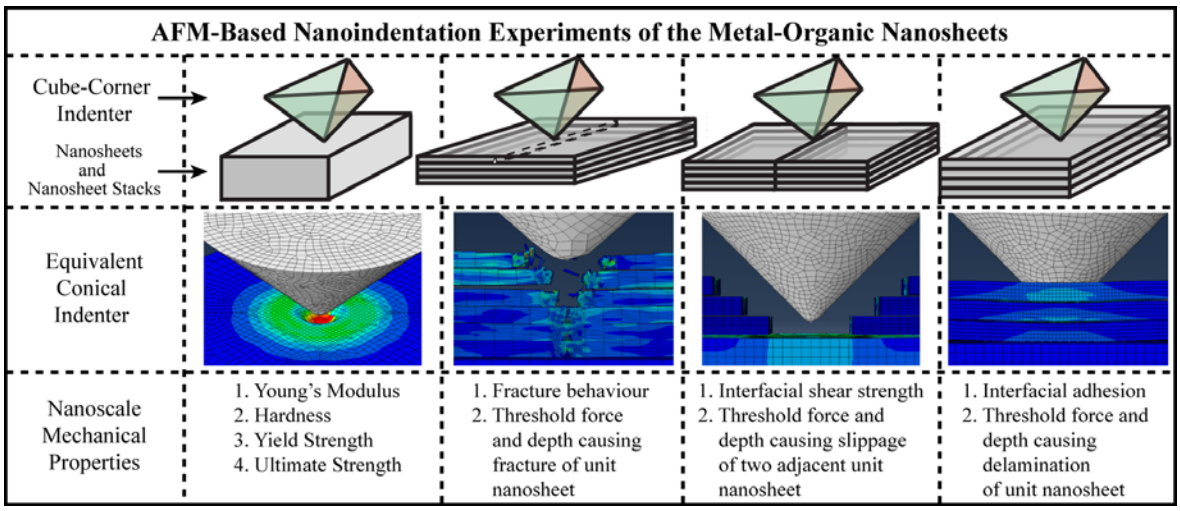

Mechanical properties measurement of porous nanosheets at the nanoscale faces tremendous challenge in spite of its importance. In the light of this, herein AFM nanoindentation of nanosheets has been developed together with the implementation of new data analysis tools to quantify the nanoscale mechanical properties of a representative metal-organic nanosheet material, termed CuBDC [copper 1,4-benzenedicarboxylate]. The sample thickness was ranging from ~2 nm comprising a stack of a few monolayers, up to ~400 nm for a thick multilayered sample. The Young's modulus (~23 GPa), hardness (~2 GPa), yield stress (~448 MPa), and ultimate strength (~674 MPa) have been measured in the through-thickness direction. Three failure modes have been proposed: interfacial sliding, framework fracture, and delamination mechanism of the CuBDC nanosheets and the threshold indentation forces and corresponding indentation depths leading to these failure modes have been determined: 42.6 nN (6.5 Å), 70.4 nN (6.4 Å), and 56.0 nN (5.8 Å), respectively. To gain additional insights into the proposed failure mechanisms, finite-element models were developed with cohesive layers to simulate the debonding of the adjacent nanosheet layers. To sum up, an all-around characterization of nanoscale mechanical properties of the CuBDC nanosheets has been achieved and it is envisaged that the technique is also applicable to other nanosheet materials.

7.1 Introduction

The CuBDC nanosheet, an example of metal-organic nanosheets (MONs), has been selected as the model material to develop the comprehensive AFM nanoindentation technique to quantify the mechanical properties of thin 2-D structures.[2, 6] As a type of MOF nanosheets, CuBDC, the abbreviation of copper 1,4-benzenedicarboxylate, is composed of the square-planar Cu(II) dimers coordinated to benzenedicarboxylate organic ligands.[48] The CuBDC nanosheet has a layered crystalline structure that is porous (see Figure 7.1 and §2.2.2), thereby promising for fabricating 2-D functional devices, for instance, a composite membrane made from exfoliated CuBDC embedded in a polymer matrix shows excellent CO_2 separation from the mixture containing CH_4.[49]

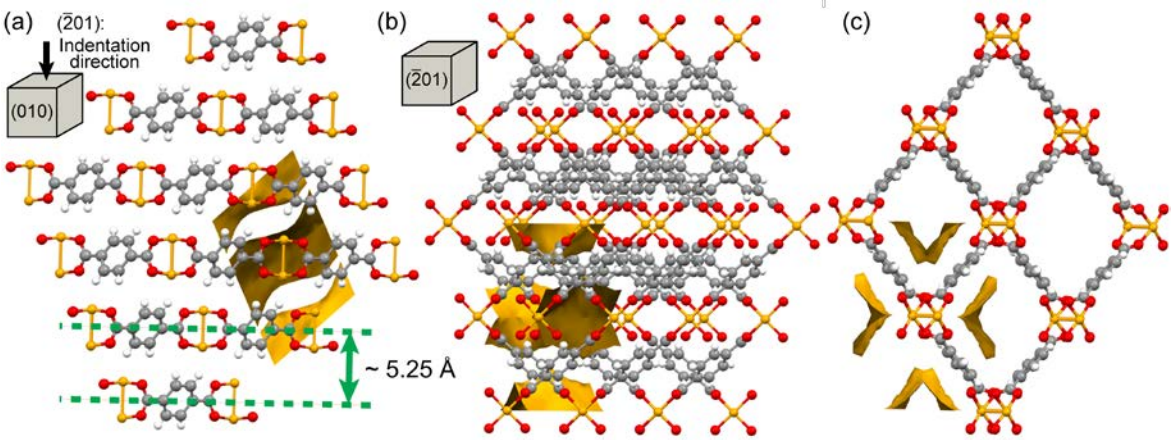

Figure 7.1 Crystalline framework structure of CuBDC, where the yellow atom represents the copper centers coordinated by the terephthalate organic ligands; the yellow surfaces designate the solvent accessible volume (porosity). The crystallographic structure (a) viewed down the [010]-axis, thus showing the stacking direction, and AFM nanoindenter penetrates along the $[\bar{2}01]$-axis (the arrow pointing downwards); (b) viewed down along the $[\bar{2}01]$-axis; (c) viewed down the pore channel, respectively. Oxygen, hydrogen and carbon atoms are shown in red, white and grey, respectively. The crystalline structure was based on Ref. [49].

The CuBDC nanosheets are thin 2-D crystals as shown in Figure 7.2. The constituent CuBDC layers stack along the $[\bar{2}01]$-axis and extend to form well-defined CuBDC nanosheets. As shown in the AFM close-up images, thickness of the CuBDC nanosheets ranges from 2 nm (*viz* the thinnest nanosheet consists of ~ 2 monolayers as shown in Figure 7.1b) to 400 nm (comprises hundreds of monolayers). It is worth noting that exfoliation of thin nanosheets out of the thicker nanosheet stacks is very important since these thin nanosheets may well become a remarkable source of building blocks in novel 2-D applications, especially in thin-film electronics and miniaturised energy storage devices.[343]

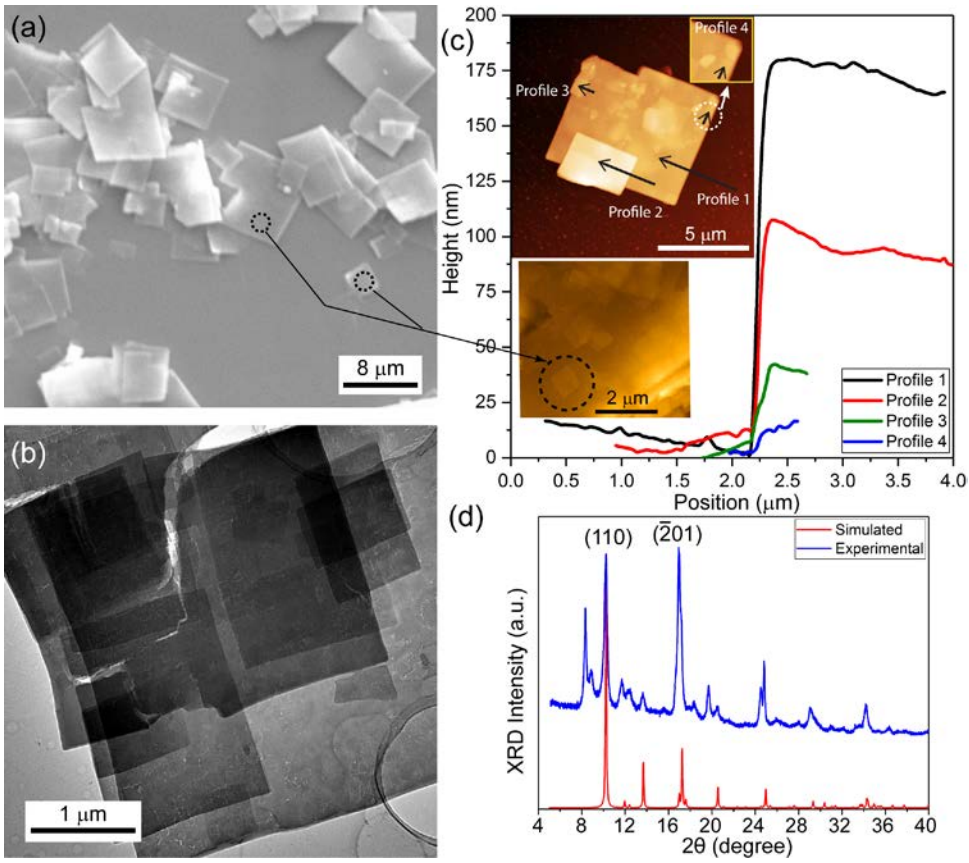

Figure 7.2 The CuBDC nanosheets. (a) Scanning electron microscope (SEM) image (collected by a collaborator). (b) Transmission electron microscope (TEM) image (collected with a collaborator). (c) Atomic force microscope (AFM) images of the multilayered CuBDC nanosheets such as the one marked by Profile 4. (d) Experimental and simulated XRD patterns; the two extra peaks at $2\theta \sim 8.3°$ and ~ 8.9° are ascribed to thermal desolvation of the framework.[304] More specifically, as reported in Ref. [304], full desolvation at 220 °C will maximise the two extra peaks and surpass the other XRD peaks indicating the distortion

and expansion of the crystalline structure but it was suggested the nanosheet still has the similar structure and also reversible after adding specific solvent molecules. As shown in §4.1.2, the activation temperature was as low as 40 °C and thus it is rational to assume that the sample indented has limited degree of distortion and expansion from the structure shown in Figure 7.1.

The stack of CuBDC nanosheets are bonded together by van de Waals forces, and thus there is risk of delamination as well as other forms of interfacial failure (e.g. the movement of nanosheets relative to one another). Therefore, design and fabrication of functional devices integrating CuBDC nanosheets require a better understanding of not only common mechanical properties such as the elastic modulus and hardness, but also the underlying interfacial and 2-D failure modes since the rupture of nanosheets will impede the accurate measurement using the depth-sensing indentation techniques. These factors could result in either distortion of the force-displacement (*P*-*h*) data or erroneous indenter-to-sample contact area in the experiment. This chapter will address the above challenges, and by doing so opened up the possibility for more accurate experimental determination of the intrinsic mechanical properties of nanosheets and to quantify the threshold failure modes of metal-organic nanosheets.

7.2 AFM Nanoindentation Using a Diamond-Tipped Cantilever Probe

AFM nanoindentation was performed using the Veeco Dimension 3100 instrument operating under the indentation mode, equipped with the Bruker PDNISP probe (cube-corner diamond tip). The probe has a 350 μm long cantilever made of stainless steel. And a cube-corner indenter tip made from diamond is mounted at the end of the cantilever. The spring constant and contact sensitivity of the probe have been calibrated, and given as

152.285 N/m and 256.6 nm/volt, respectively. More details regarding the specifications and characterisation of the indenter tip are available in §4.2.2).

7.3 AFM Nanoindentation Methodology and *P-h* Data Analysis

7.3.1 Oliver and Pharr Method

Each AFM nanoindentation experiment generates a force-displacement (*P-h*) curve, based on which the mechanical properties such as Young's modulus (*E*) and hardness (*H*) can be determined. In this work, the Oliver and Pharr (OP) method (§4.7.2) was used to derive the Young's modulus of the CuBDC nanosheets,[228] every data point of which (in Figure 7.14b) was obtained from individual indentation cycle, *viz* a single loading-unloading method. The mechanical properties of CuBDC are primarily dependent on the ligand−ligand and ligand−metallic centre interactions.[344] The representative *P-h* curves in Figure 7.14a are highly reproducible, and thus they represent the genuine response of the material.

7.3.2 Unloading Strain Rate Principle

Indentation on materials that are either porous or brittle and either viscoelastic or defective, usually exhibits failures or creep, which can introduce significant distortion on the *P-h* curves and under the circumstances, the OP method is no longer suitable. As demonstrated in the Ref. [147] (i.e. §5.3), the additional displacement along the indentation direction still dominates the overall movement overwhelming the elastic recovery towards the opposite direction. As a consequence, the resulting unloading curve, whose incipient segment is usually tilted anticlockwise resulting in an overestimation of the Young's modulus. To put it differently, the incipient segment of the unloading curve no more reflects the specimen's ability to resist deformation in response to the applied indentation load. Furthermore, excessive curve distortion may result in an unloading curve with a negative

gradient. In contrast to the nanocrystals and micron-sized crystals of ZIF-8 presented in Chapter 6, more failure modes for nanosheets were observed in this study (discussed in greater details in §7.6), thus leading to more severe deviation. Given this, the unloading strain rate principle (see §4.7.3) has been adopted for the purpose of retrieving the *P-h* curves reflecting the genuine elastic-plastic response of the nanosheets. In the unloading strain rate principle, higher strain rate on the unloading segment of indentation, especially at its initial stage, helps to diminish or even eliminate the additional indentation displacement induced by time-dependent phenomenon such as creep and the effect of material fracture.[147] It is worth noting that for nanosheets, the in-plane stretch may also affect the measurement of stiffness.[107]

7.3.3 Finite-Element Modelling

For the purpose of predicting the plastic deformation of the CuBDC nanosheet, a numerical technique simulating the indenter-to-sample contact is required. With this intention, I have adopted the finite-element (FE) method which has rarely been selected to model the characteristics of MOFs, in principle the FE model can be extended to a macroscopic scale to simulate the mechanical response of the entire framework of MOFs as reported in Ref. [345] but at the expense of losing the definition of the small-scale inorganic-organic-inorganic linkages. In this chapter, a continuum model meshed by an 8-node linear brick element with reduced integration and hourglass control (*C3D8R*) was used to represent the CuBDC nanosheet in ABAQUS/Explicit[323] since the explicit procedure is usually more suitable in terms of resolving complicated contact problems. It is noteworthy that the oscillations of *P-h* curves reported in Refs. [346-347] on geometrically continuous materials have been overcome by applying a more refined mesh. In the indentation assembly, the indenter in the FE model is an equivalent conical discrete rigid part, in which a curved

apex of a dimensionless radius 0.7 was created in order to avoid the excessive distortion of the FE mesh.

In addition, the FE method with the ABAQUS/Explicit solver has also been employed to imitate the patterns of distortions caused by the failures of the CuBDC nanosheets during the loading stage as well as the recovery and pop-out phenomena during the course of unloading (more details in §7.6). In these FE models where the nanosheet interfacial failures were defined, the interaction between nanosheets was modelled as a cohesive layer (Figure 7.5) whose damage under stress initiates based on the maximum nominal stress criterion (Maxs Damage) using a traction-separation description in ABAQUS.[323] Moreover, the Johnson-Cook fracture criteria[324] has been selected to define the fracture of the nanosheets under the penetration of the indenter. The Johnson-Cook fracture criteria was initially proposed for metals but has also been applied to polymer-like materials.[348] In this criteria, the impact of the strain and strain rate can be easily defined.

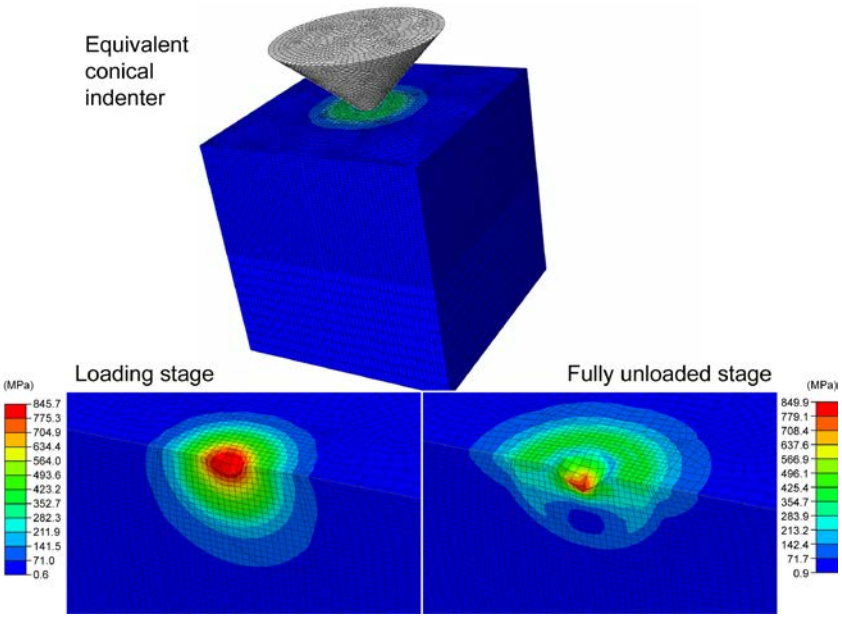

Figure 7.3 The FE model with the von Mises stress contour showing the indentation of an equivalent conical indenter (same contact area over depth as the cube-corner indenter, see the "effective indenter shape" in §3.4.3 and §4.2.2) on a continuum CuBDC model . The input material properties include elasticity (from the AFM nanoindentation experiment) and plasticity (from mathematical iteration method based on the height of pile-ups in §7.3.5).

In order to diminish the influence of the mesh system on the resulting value of the ratio *s/h*, the mesh convergence check was taken as shown in Figure 7.4.

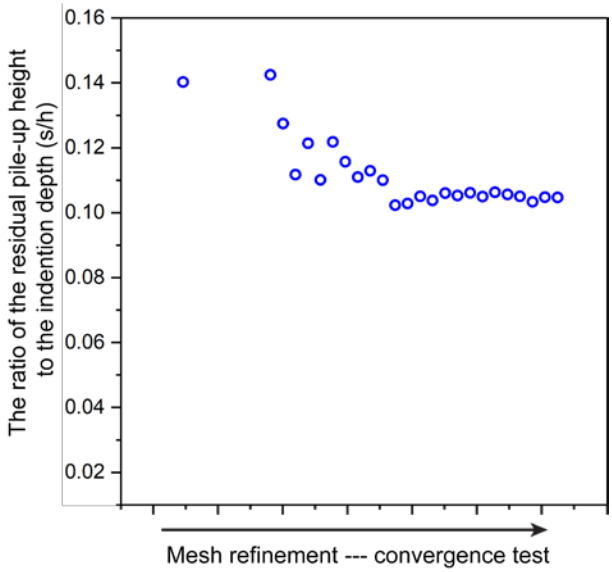

Figure 7.4 Mesh convergence plot showing that the mesh system is sufficiently fine to avoid the influence to the ratio of the pile-up height (*s*) to the indentation depth (*h*).

Table 7.1 Dimensionless parameters of the materials properties in the FE model for the failure-free indentation.

Elasticity Behaviour		**Plastic Behaviour**	
Young's Modulus	Poisson's Ratio	Yield Stress	Plastic Strain
22900	0.4	448	0
From AFM Nanoindentation	Assumption	From the iteration method: $\sigma_y = 863.521 \cdot {\varepsilon_p}^{0.173}$	

The cohesive layer represents the bonded interaction between the adjacent nanosheets. In the FE model, the cohesive layer was modelled as a thin sheet of 1% thickness of the CuBDC monolayer model. Separation of the layer occurs when the displacement reaches a designated threshold value. As just mentioned, the layer follows a linear-traction separation response. In the CuBDC nanosheet model, the cohesive layer starts to "degrade" (or fail) when the maximum nominal stress reaches a threshold in either normal or shear directions. Therefore by adopting this approach in conjunction with AFM nanoindentation experiments, both interfacial sliding (in shear direction) and delamination (in normal

direction) can be investigated. The FE models simulating the three failure modes were not quantitative but were created to verify the distinct distortion patterns when different failure modes occurred. Although the specifications of the damage criteria of the cohesive layer and the fracture model are summarized in Table 7.2, the absolute values in the table do not necessarily corresponding to the actual failure attributes of the CuBDC nanosheets.

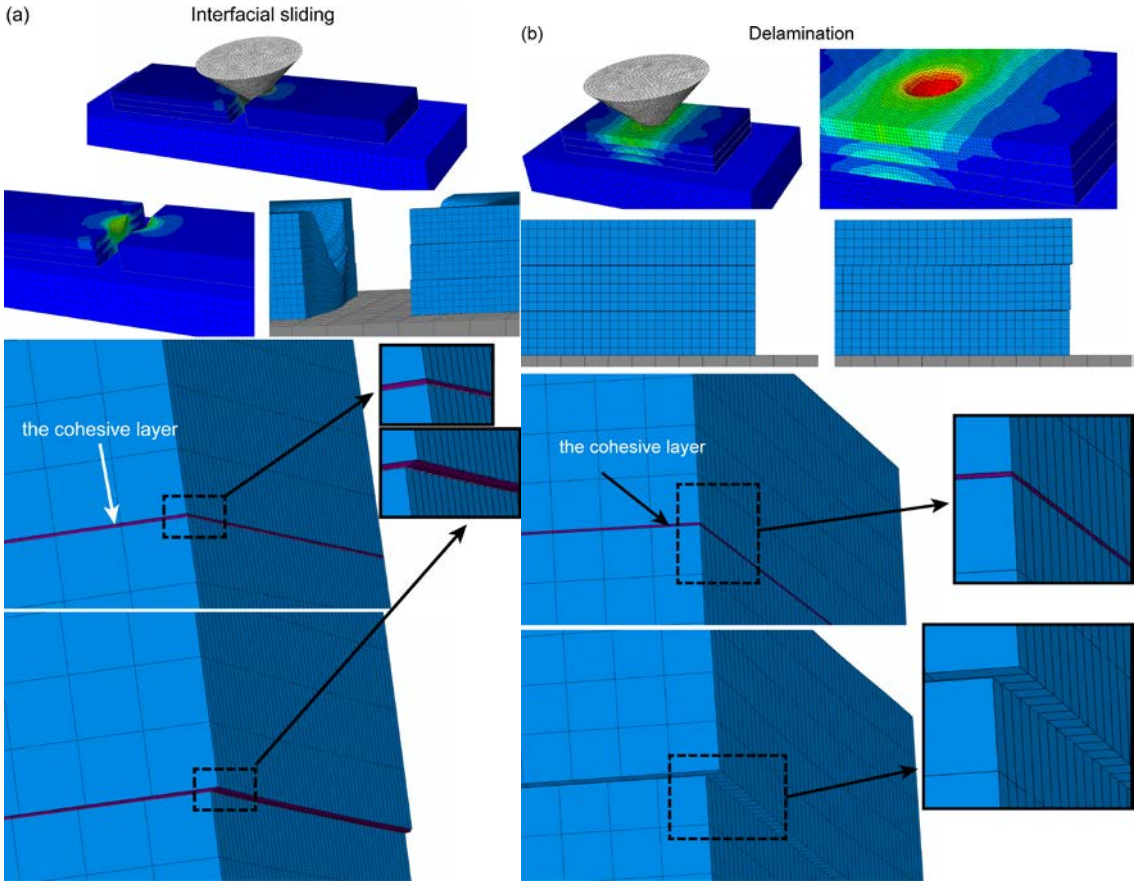

Figure 7.5 The FE model with the von Mises stress contour showing (a) the sideward/interfacial sliding and (b) the delamination caused by the penetration of the indenter (the cohesive layers are shown in purple).

Table 7.2 Dimensionless parameters of the maximum nominal stress criterion (Maxs Damage) and the Johnson-Cook Damage criterion. Note that the values presented herein are not the absolute mechanical properties of the CuBDC nanosheets and refer to Ref.[323] for the details regarding the parameters in the table.

Cohesive layer		**Fracture Model**	
Maxs Damage	Values	Johnson-Cook Damage	Values
Tolerance	0.05	Failure Parameters: d_1, d_2, d_3, d_4, d_5	-1, 1.1, 0.4, 0.001, 0
Nominal Stress Normal-Only Mode	0.0001	Melting Temperature	0
Nominal Stress First Direction	0.0001	Transition Temperature	0
Nominal Stress Second Direction	0.0001	Reference Strain Rate	1
Damage Evolution – Displacement	Degradation: Maximum; Displacement at Failure: 0.0002	Damage Evolution – Displacement	Degradation: Maximum; Displacement at Failure: 1.0E-007
Damage Stabilization Cohesive	Viscosity Coefficient: 1.0E-006		
Mass Density	8.6E-010	Plastic – Johnson-Cook Hardening	A = 300; B = 110; n = 0.4; m = 1; Melting Temperature = 0; Transition Temperature = 0.
Elastic – Traction	E/E_{nn} = 1000; G_1/E_{ss} = 1000; G_2/E_{tt} = 1000.	Rate Dependent	C = 0.003; $\dot{\varepsilon}_0$= 1.

The plasticity model shown in Figure 7.6 was built based on the Johnson-Cook hardening model, the static yield stress (σ^0) of which is given by:[324]

$$\sigma^0 = [C_1 + C_2(\bar{\varepsilon}^{pl})^n]\left(1 + C_3 ln\frac{\dot{\varepsilon}}{\dot{\varepsilon_0}}\right)[1 - (T^*)^m] \quad (7.1)$$

where $\bar{\varepsilon}^{pl}$ is the equivalent plastic strain and C_1, C_2, m, n are material parameter that can be derived from the experiment. $\dot{\varepsilon}$ and $\dot{\varepsilon}_0$ are the current and reference strain rate, respectively.

T^* is the temperature constant that is defined as $T^* = \frac{T-T_t}{T_m-T_t}$, where T_t and T_m are the material transition and melting temperatures, respectively.[324, 349] If the current temperature $T \leq T_t$, the mathematical expression of σ^0 is independent on temperature, i.e. $T^* \equiv 0$ (assumption in the FE model). Determination of these parameters normally requires a series of quasi-static and dynamic tests, such as tensile test with high triaxiality.[349] However, it is practically impossible to implement these tests on the nanoscale CuBDC nanosheets. Therefore, in this work, the fracture model of CuBDC nanosheets being implemented was aimed at gaining a semi-quantitative insight into which part of the *P-h* curve distortion that can be linked to the fracture of materials.

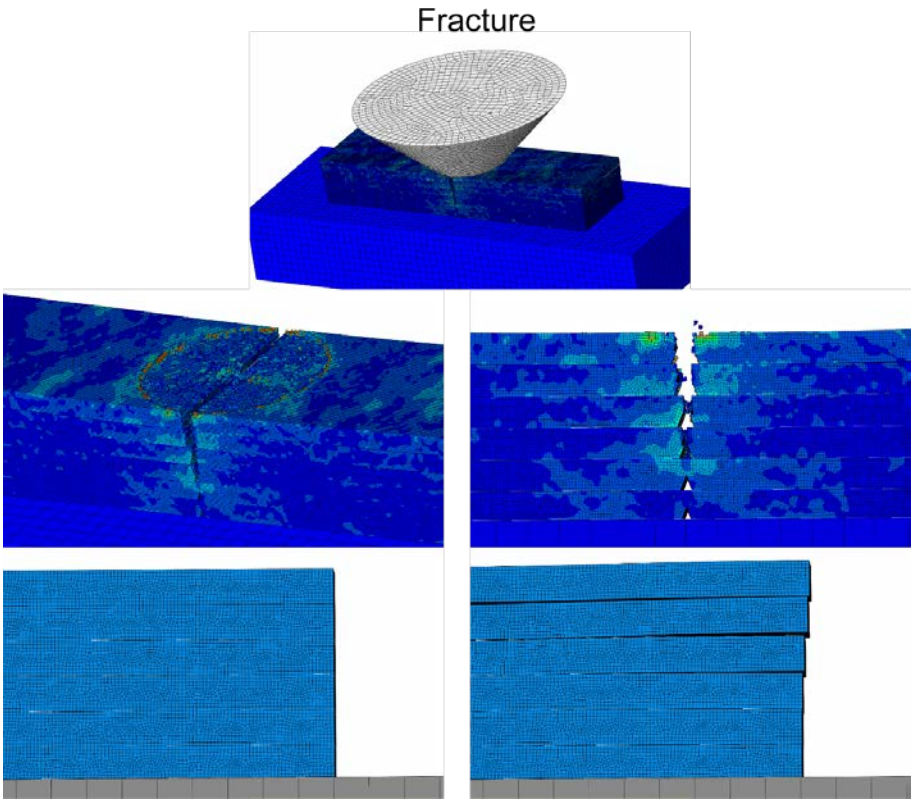

Figure 7.6 The FE model with the von Mises stress contour showing the fracture of the CuBDC nanosheets caused by stress concentration induced by the sharp indenter tip.

7.3.4 Characterisation of the CuBDC Nanosheets and Residual Indents from the AFM Nanoindentation Measurements

Figures 7.6-7.10 show the residual indents present on the surface of the nanosheet specimens after being probed using a cube-corner indenter tip. It can be seen that the CuBDC nanosheets exhibit differential deformation behaviour, further reflected by the resulting *P-h* curves in Figure 7.17d and Figure 7.19a. The different loading forces and the irregular nature of contacts between the indenter tip and specimen may be attributed to the packing of the CuBDC nanosheets and microstructural defects (e.g. Figure 7.10).

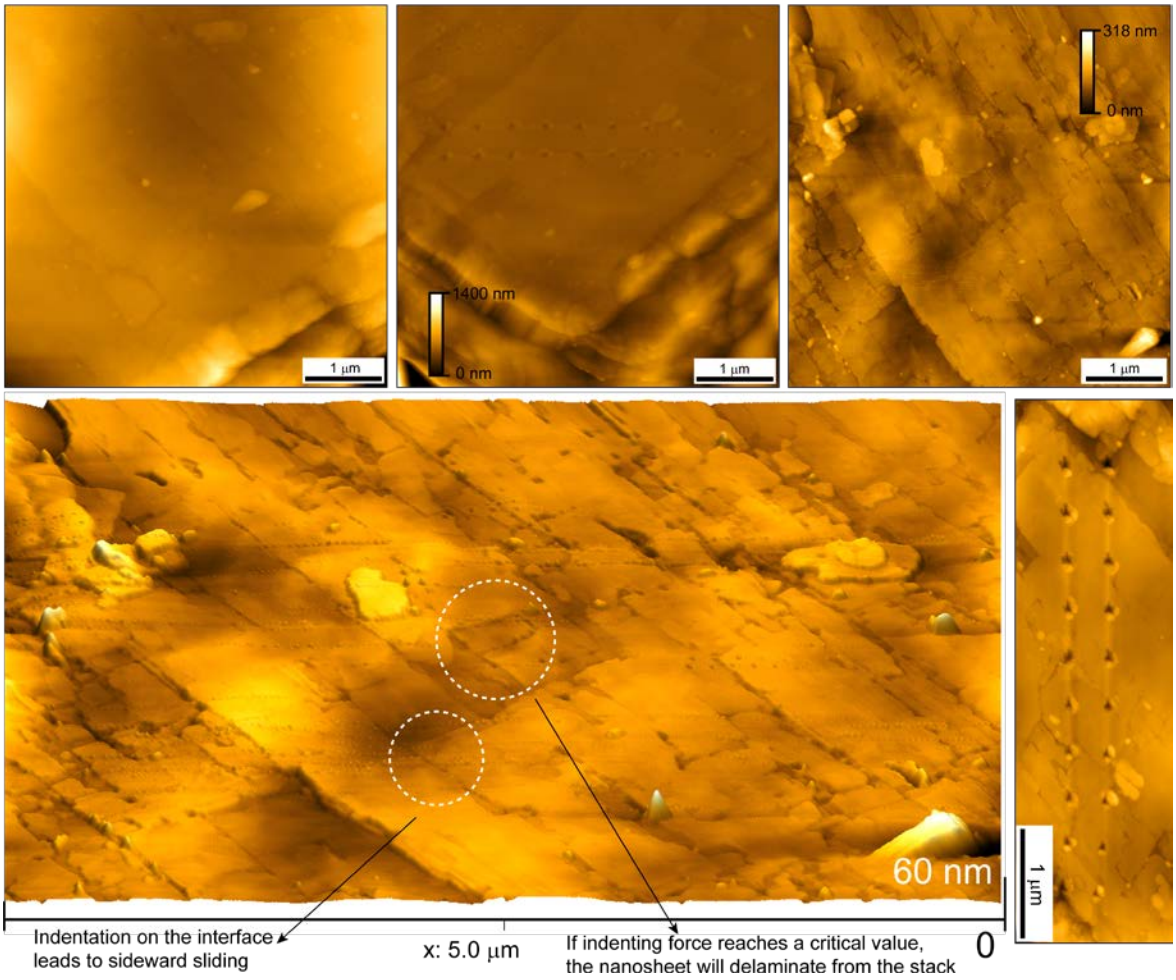

Figure 7.7 AFM images of stacks of CuBDC nanosheets, on which can be seen the two columns of residual indents created by a cube-corner indenter.

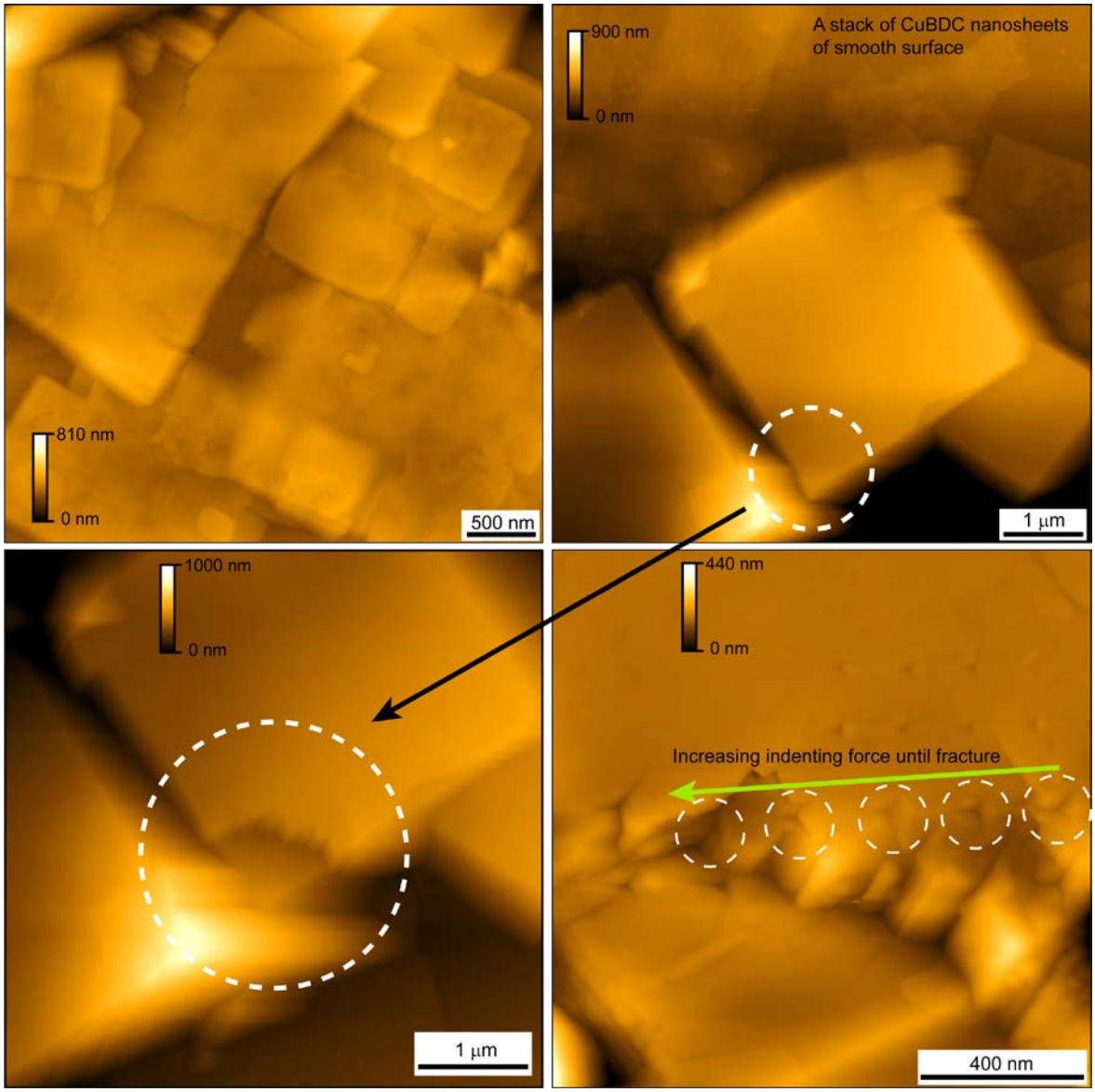

Figure 7.8 AFM images of stacks of CuBDC nanosheets with a smoother surface comparing with the ones shown in Figure 7.7 and the fracture of a CuBDC nanosheet.

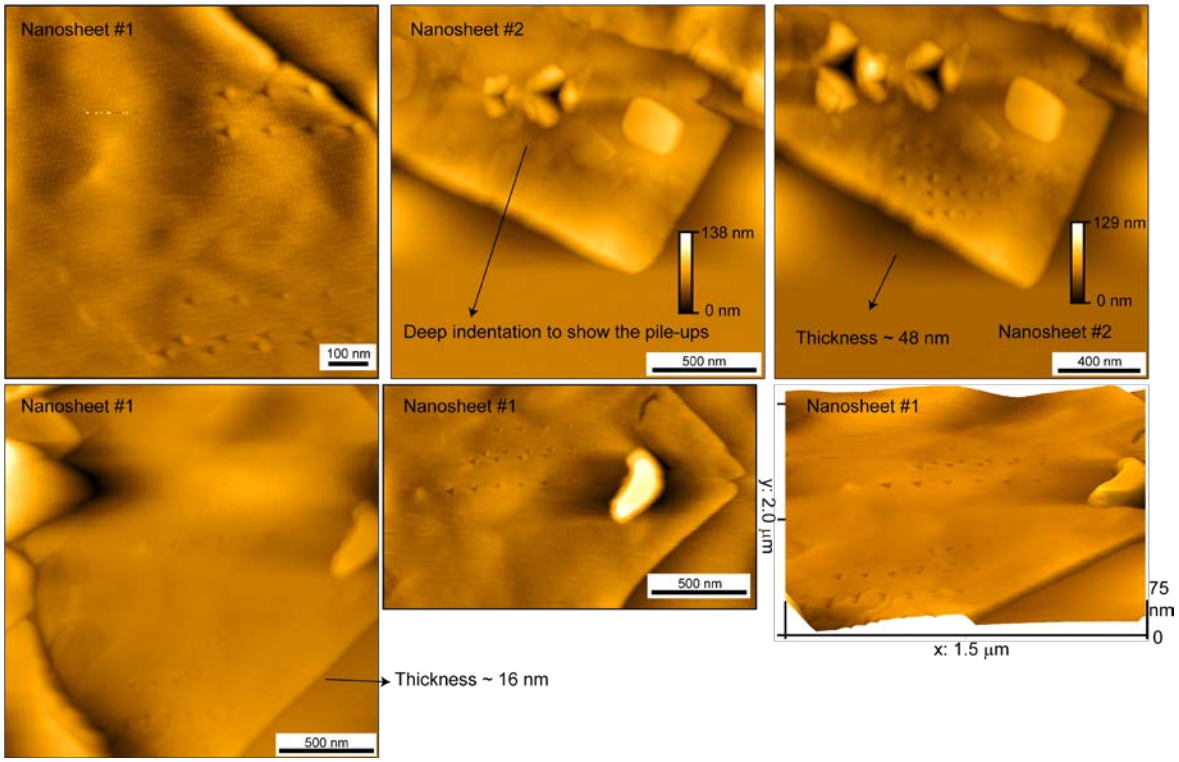

Figure 7.9 AFM images of two CuBDC nanosheets, where sample #1 is thinner than #2.

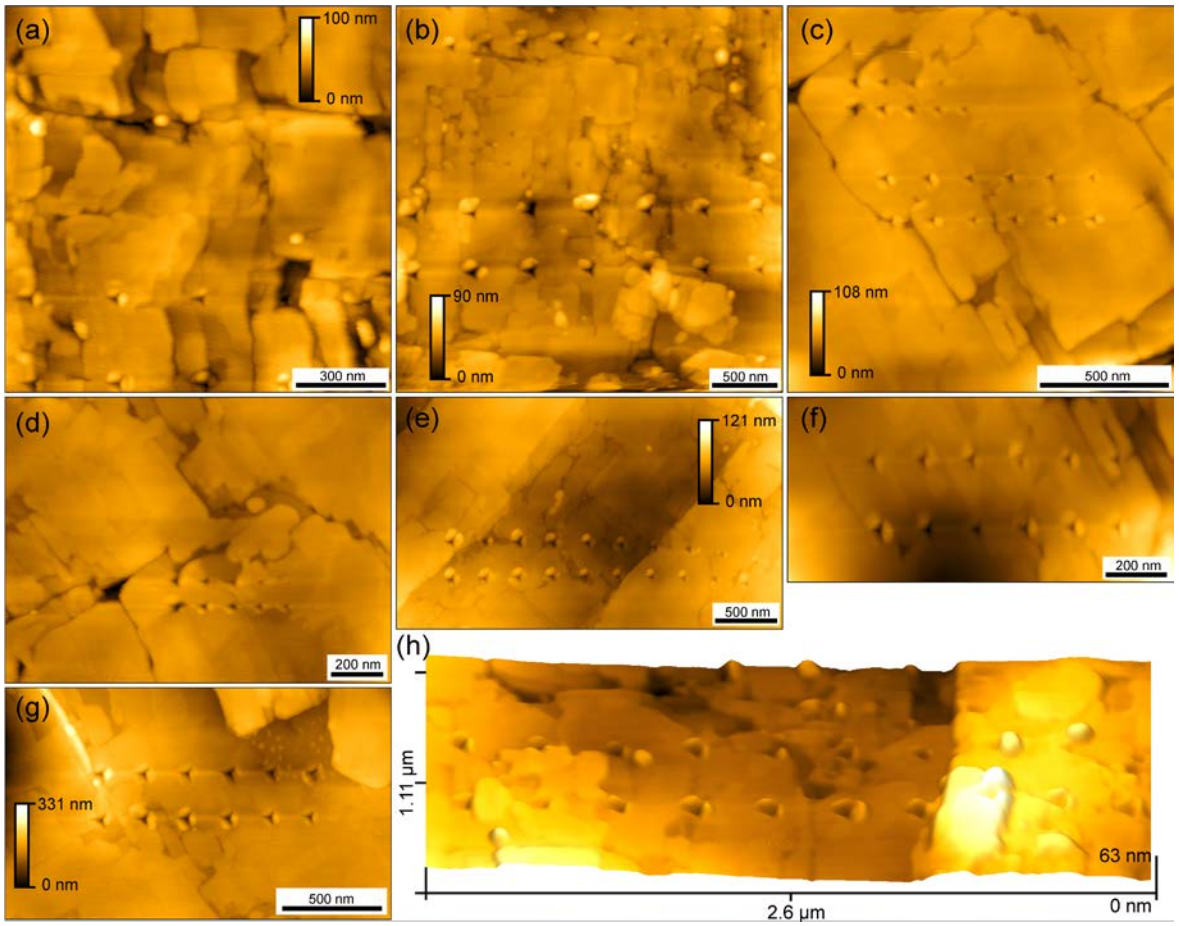

Figure 7.10 (a-g) AFM images of stacks of CuBDC nanosheets, on which the residual indents can be observed. AFM nanoindentation equipped with the cube-corner indenter was

applied to the specific sites of the stacks to identify the failure modes. (h) A 3-D height image of the AFM nanoindentation experiments on a CuBDC nanosheet stack.

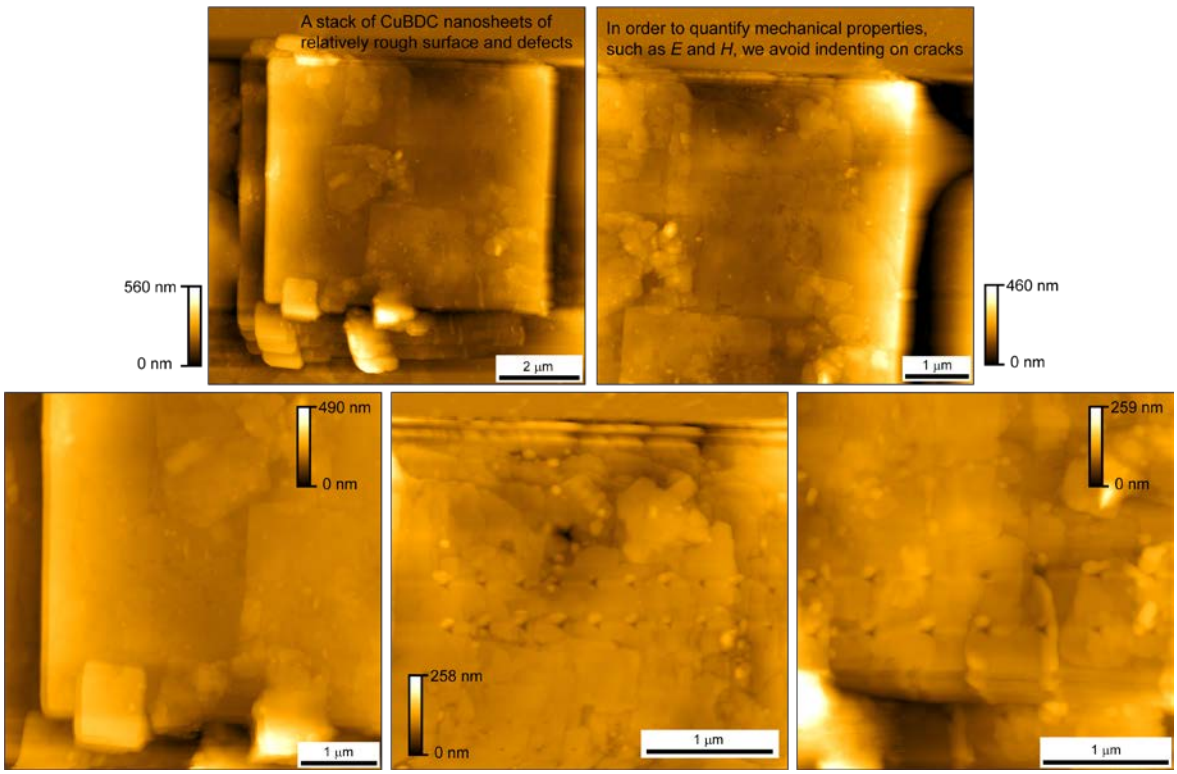

Figure 7.11 AFM images of a bulky stack of CuBDC nanosheets and the residual indents on the sample surface.

7.3.5 Pile-Up and Yield Stress Using an Iteration Method

Plastic deformation is a nontrivial factor to be considered in the indentation experiments. Systematic discussion about the analysis of pile-ups during indentation has been done by Taljat and Pharr.[350] In this study, I developed a novel iteration method to acquire the plasticity of the nanosheets on the basis of the correlation between the plasticity and the height of the pile-ups on the periphery of the indents. The flow chart shown in Figure 7.13h elucidates the iteration procedure, in which the results obtained from both AFM nanoindentation and FE method were utilised.

The materials input of the FE model comprise the elastic and plastic properties. For elasticity, the Young's modulus can be measured using AFM nanoindentation. For plasticity,

the work-hardening behaviour was defined as a power law relation using the Hollomon's equation. The work-hardening efficient of a material is an important factor that exerts an influence on the height of the pile-ups and such fundamental behaviour is able to inhibit the formation of pile-ups.[228] In detail, the hardening of the material near the indenter actually restrains the rising flow to the specimen's surface.[228] For this reason, the work-hardening property of the CuBDC nanosheets was considered. The relationship between the stress and plastic strain in the Hollomon's equation is shown as follows:[351]

$$\sigma = k \cdot {\varepsilon_{\mathrm{p}}}^{n} \tag{7.2}$$

where σ stands for the stress, ε_{p} is the plastic strain, k is the strength coefficient, and n is the strain hardening exponent.

Since at the end of the elastic regime of a stress-strain curve, the strength coefficient k can also be defined based on the elastic modulus:

$$k = \frac{\sigma_{\mathrm{y}}}{\varepsilon^{n}} = \frac{\sigma_{\mathrm{y}}}{(\frac{\sigma_{\mathrm{y}}}{E})^{n}} \tag{7.3}$$

According to the empirical relation proposed by Matthews:[352]

$$\frac{s}{h} = \frac{1}{2}\,(\frac{2+n}{2})^{2(1-n)/n} - 1 \tag{7.4}$$

where s is the height of a residual pile-up after the withdrawal of the indenter tip, and h is the indentation depth from the free surface (i.e. at the maximum load). The value of s can be measured from the AFM images of the indents (see Figure 7.13a-b). The study of 32 indents gave the arithmetic mean value of s/h = 1.0551, and thus n = 0.17275 (see Table 7.3).

Table 7.3 The ratio (*s/h*) of the height of a residual pile-up (*s*) to the indention depth (*h*) of the pile-ups (pile-ups on the three sides of a residual indent are illustrated in Figure 7.12). Note that for some indents produced by the cube-corner indenter on the nanosheet stacks, there were pile-ups on only one or two sides, to which the zero values in the table are ascribed. It is necessary to mention that considerable standard deviation of the pile-up height implies that the values of hardness, yield stress, and ultimate stress are of certain level of uncertainties.

	Pile-up Back	**Pile-up Left Side**	**Pile-up Right Side**
s/h	0.07231	0.05984	0.10518
	0.09783	0.09395	0.14726
	0.05209	0.21101	0.06862
	0.08015	0.11748	0.13084
	0.04578	0.05602	0.08195
	0.05057	0.08526	0.14407
	0.07009	0.04258	0.12177
	0.03106	0.14186	0.11498
	0.02553	0.24621	0.11707
	0.04715	0.00000	0.07270
	0.03021	0.00000	0.09536
	0.05085	0.00000	0.10523
	0.05314	0.00000	0.08961
	0.05737	0.00000	0.11113
	0.11416	0.00000	0.08008
	0.16024	0.00000	0.11598
	0.14629	0.00000	0.13464
	0.20887	0.00000	0.05957
	0.17102	0.00000	0.07836
	0.06580	0.00000	0.07039
	0.11675	0.00000	0.15866
	0.16534	0.00000	0.00000
	0.15110	0.00000	0.00000
	0.20377	0.00000	0.00000
			Mean of the *s/h* ratio of all the pile-ups
Mean*	0.09448	0.11713	0.10493	0.10551
Standard Deviation*	0.05724	0.07090	0.02850	

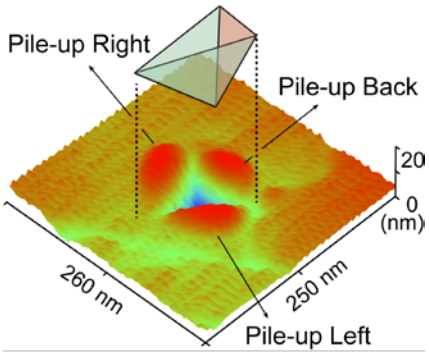

Figure 7.12 Schematic illustration of a residual pile-up

* The values were obtained by only considering the nonzero values of the pile-up height.

In the iteration procedure, a stochastic initial value of the yield stress (σ_y) has been discreetly allocated into equation (7.3) acquiring the initial value of *k*. Subsequently, by substituting the values of *k* and *n* into the equation (7.2), gives the first predicted plasticity property of the CuBDC nanosheet. Inputting the elastic (Young's modulus from AFM

nanoindentation) and plastic property into the FE model, gives a new ratio of *s/h*. The yield stress of the nanosheet was determined through an iterative process, until the updated input yield stress in the FE model gives the same *s/h* as obtained from the AFM nanoindentation experiments (see Figure 7.13f-g).

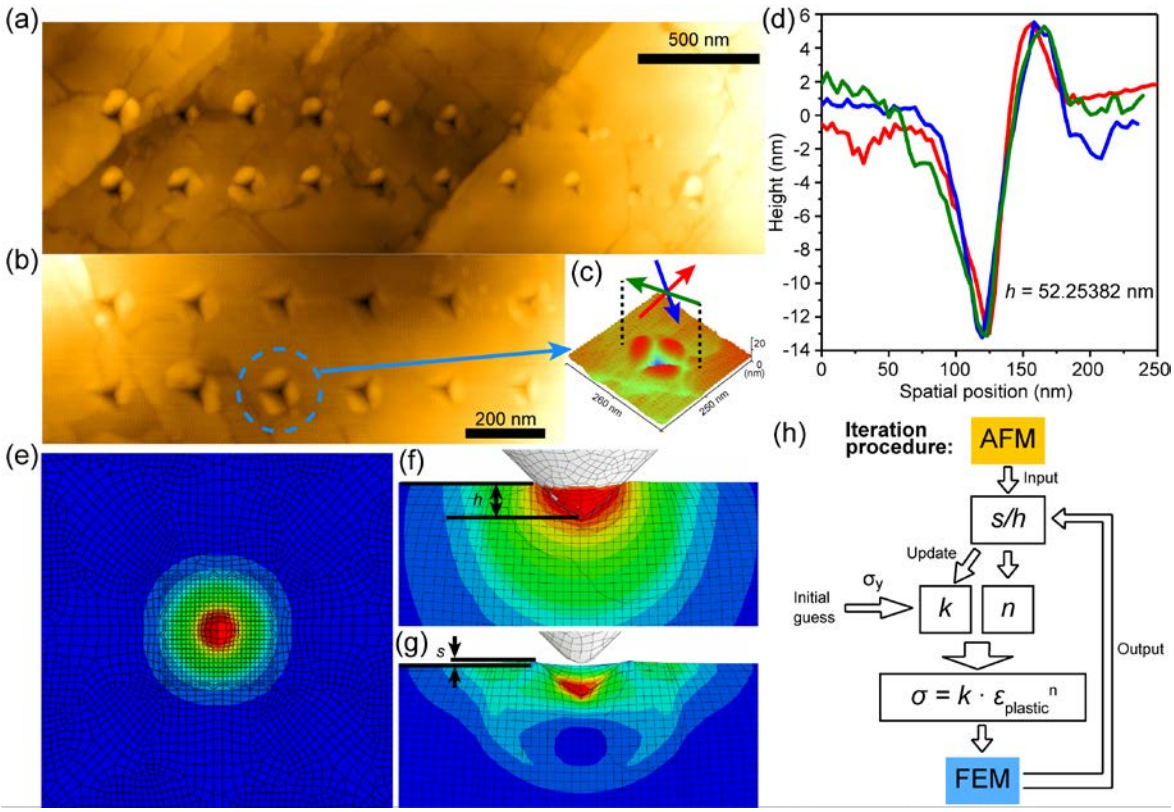

Figure 7.13 (a-b) AFM topographic images of indents on two CuBDC nanosheet stacks, where pile-ups generated by the cube-corner indenter are clearly visible. (c) A 3-D height image in depth colour map, where the three sectional profiles marked by the arrows are plotted in (d). A FE model (the von Mises stress contour plot) of the indentation on the CuBDC using a contact-area equivalent conical indenter (the conical angle 2θ is 91.4667°, see Table 4.2)[147] in order to avoid the excessive distortion of the meshes (refer to the concept of the effective indenter shape in Ref. [228]): (e) the top view (the indenter is hidden) and (f) the front view at the point of the maximum load; (g) the model at the fully unloaded state. (h) The procedure of the iteration method.

7.4 Quantification of Through-Thickness Elastic Behaviour

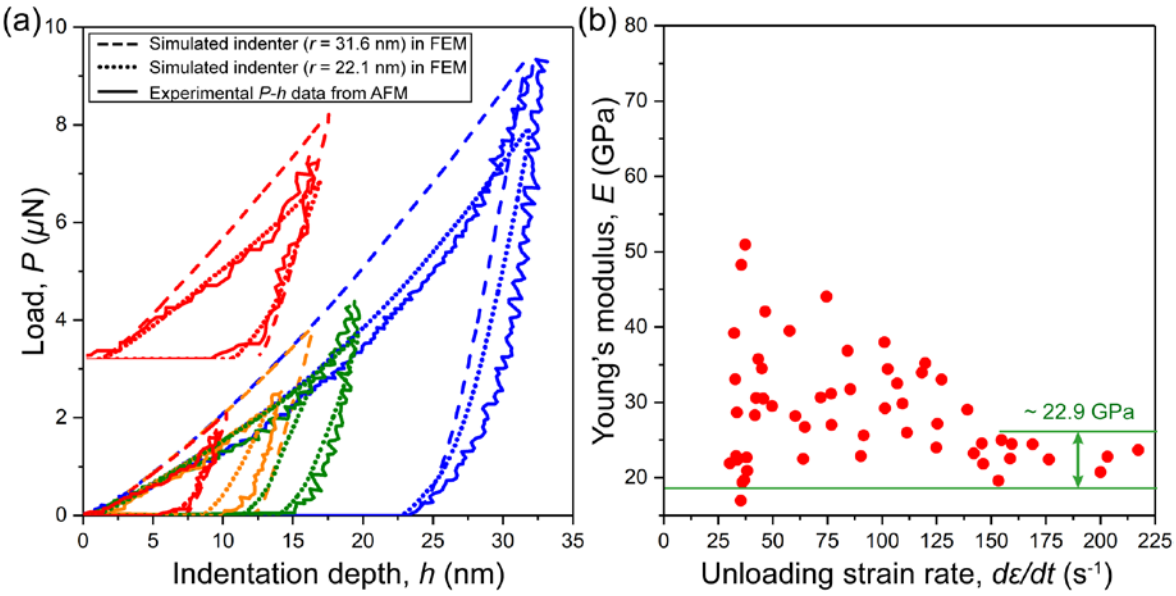

Figure 7.14 Representative *P-h* curves from the AFM nanoindentation experiments (solid lines) and the FE method (dashed and dotted lines for indentation using the two simulated indenter tips of apex radii $r \approx 31.6$ nm and ≈ 22.1 nm, respectively). It shows that both the elastic and plastic behaviors of the CuBDC nanosheet models created using ABAQUS are in accordance with the experimental data. (b) The Young's modulus (E) as a function of the unloading strain rate ($d\varepsilon/dt$). The arithmetic mean value of E after convergence is ~22.9 GPa.

The Young's modulus measured at low unloading strain rate is massively scattered and overestimated up to ~52 GPa due to the framework failure and the time-dependent deformation that contribute to the exaggeration of stiffness. An augmented unloading strain rate method (§4.7.3) was used so as to overcome these side effects. By doing so, the Young's modulus starts to converge with the increasing unloading strain rate. In terms of the CuBDC nanosheets, after unloading strain rate reaches ~140 s^{-1}, the Young's modulus settles down to the steady state (arithmetic mean ~22.9 GPa). The Poisson's ratio of CuBDC was taken herein as 0.4 since it has a relatively small influence on the Young's modulus (Figure 7.15).

The dashed and dotted curves in Figure 7.14a refer to the resulting *P-h* curves from the FE model with no material failure. The material property defined in the model

incorporates the elasticity derived from the AFM nanoindentation experiments and the plasticity obtained from the iteration method. The *P-h* curves simulated by the FE model are in good agreement with the *P-h* curves resulted from the AFM nanoindentation experiments.

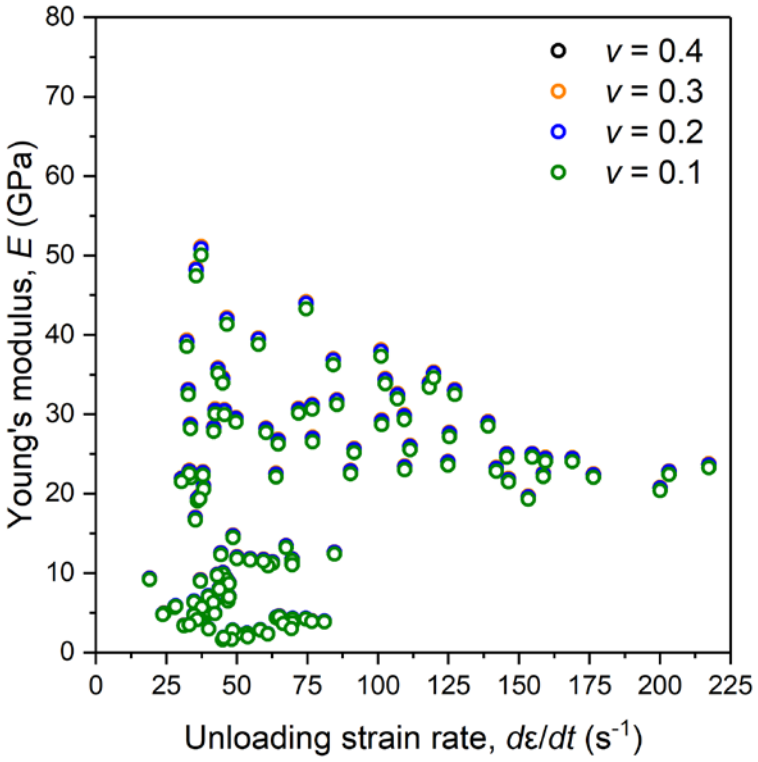

Figure 7.15 Young's modulus (*E*) versus unloading strain rate plot assuming ν = 0.1, 0.2, 0.3, 0.4 to demonstrate the negligible influence of ν on *E*.

7.5 Quantification of Plasticity

7.5.1 Stress-Strain Curve

Based on the iteration method proposed in §7.3.4, the yield stress has been determined to be σ_y ~ 448 MPa (Figure 7.16) since the FE model with this input value gives the identical height of pile-ups (s/h ~ 0.10551) measured from AFM nanoindentation. Figure 7.16 shows the stress-strain relationship of CuBDC established using this approach. Herein, the linear elastic regime was determined according to the Young's modulus from the AFM nanoindentation experiments.

7.5.2 Hardness

Hardness measurement using AFM nanoindentation on a layered structure is usually influenced by interlayer sliding movement, therefore the indentation depth can no longer be used to indicate the genuine resistance of the nanosheet to plastic deformation. However, given the characterised strain-hardening effect (Figure 7.16), it is possible to obtain an plausible estimate of the hardness of the CuBDC nanosheet because the yield stress of a material is generally related to its hardness using the expression as follows:[353]

$$\sigma_{\mathrm{y}} = \frac{0.1^{n} \cdot H_{\mathrm{Vickers}}}{3} \tag{7.5}$$

where H_{Vickers} is the Vickers hardness number. The unit of the yield stress in equation (7.5), is kilogram-force per square millimetre ($\mathrm{kgf \cdot mm^{-2}}$), which can be converted into the unit of Pascal by multiplying 9806650.

Likewise, the ultimate strength (σ_{u}) of CuBDC can be estimated by the following equation:[354]

$$\sigma_{\mathrm{u}} = \frac{H_{\mathrm{Vickers}}}{2.9}(1-n)\left(\frac{12.5n}{1-n}\right)^{n} \tag{7.6}$$

Given that the yield stress (σ_{y}) and the strain hardening coefficient (n) are known, the Vickers hardness number ($H_{Vickers} \sim 204$) was obtained, which corresponds to the absolute hardness $H \sim 2$ GPa (Figure 7.16b). Furthermore, the ultimate strength was determined as 674 MPa (Figure 7.16a).

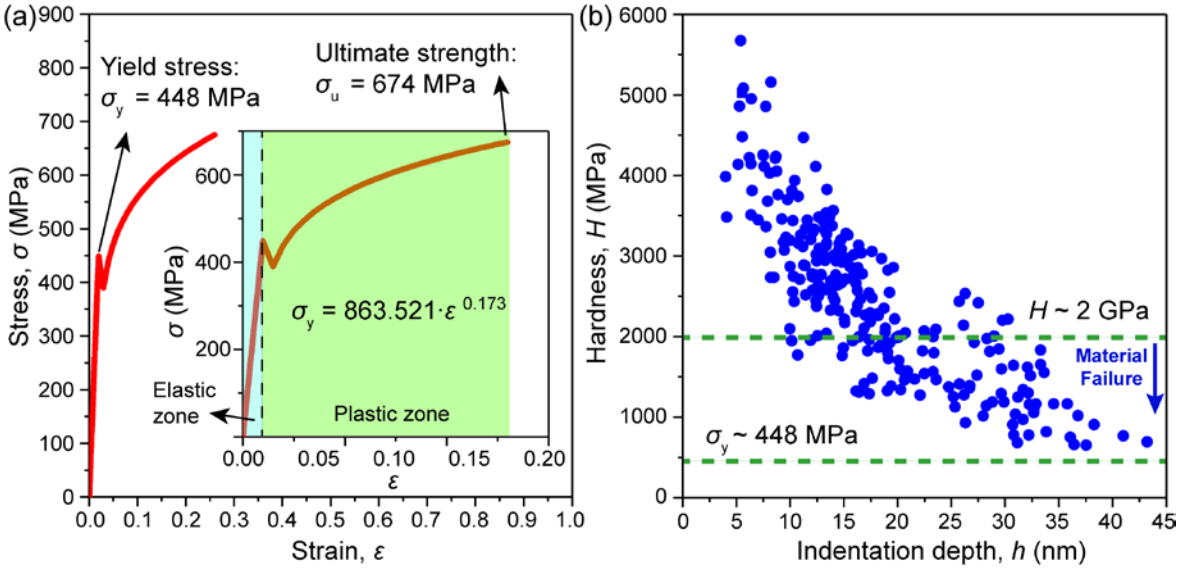

Figure 7.16 (a) Stress-strain (σ-ε) curve showing the yield behaviour of the CuBDC nanosheet. (b) Hardness (H) plotted as a function of the indentation depth (h) and the yield stress (σ_y) and hardness of the CuBDC nanosheets.

7.6 Identification of Different Failure Modes

7.6.1 Large-Scale Failures Leading to Distinct Distortions of the *P-h* Curves

AFM nanoindentation was employed to characterise the mechanical failures of the CuBDC nanosheets, with the aim to understand the origin and characteristics of failure modes under different loading conditions. In comparison with the small-scale failures that take continuous effect thus resulting in the different *P-h* curves as shown in Figure 7.19a, the distortions of the *P-h* curves from indentation experienced the large-scale failures can be directly visualised (Figure 7.17). Herein, three distinctive failure modes of CuBDC nanosheets at the indentation loading stage are proposed: Mode I – slippage of nanosheets; Mode II – fracture of nanosheets; and Mode III – delamination of nanosheets (Figure 7.17).

In Mode I, the coplanar nanosheets could be separated by the penetrating indenter and then the separated nanosheets slide sideward with the further indentation. The separation occurs only if the coplanar nanosheets were initially bound together. Typically, the sliding

of nanosheets produces the stepwise distortion of the *P*-*h* curves, which echoes the "pop-in" phenomenon observed in other 2-D materials.[91] During the slippage, a force analysis (in §7.6.2) has been conducted to shed light on the underlying mechanism. In Mode II – the CuBDC framework fractures were due to the stress concentration induced by the indenter, and the phenomenon can be detected as "humps" in the *P*-*h* curves; in Mode III – during the indenter loading stage, bending of a nanosheet can lead to its delamination from the nanosheet underneath and this is ascribed to the bending moment arising from the peripheral regions of the indent. In other words, as illustrated in Figure 7.18b, the stretch of the cohesive layer is normal to the nanosheet plane eventually causes the damage of the layer, which simulates weak interactions between the adjacent nanosheets. In addition, the pop-out and recovery phenomena at the unloading stage have been observed (discussed in §7.6.2).

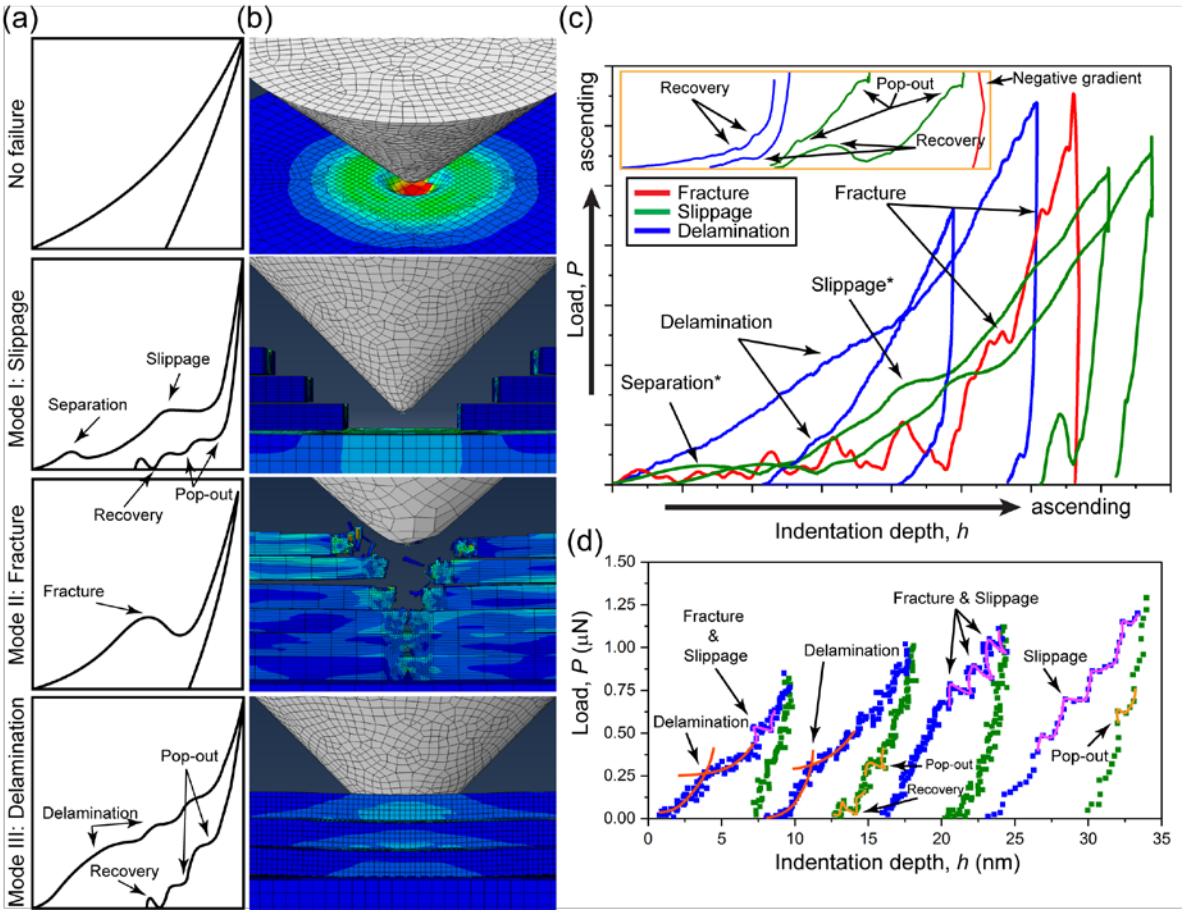

Figure 7.17 (a) Schematics illustrating the observable distortions of the *P*-*h* curves from indentation inducing material failures. The exception is the first schematic depicting the

AFM nanoindentation on a nanosheet stack (*viz.* firmly-bonded multilayers) that is not susceptible to failures such as fracture, interfacial slippage and delamination. (b) The FE models correspond to the resulting *P-h* curves in (c), which support the characteristic distortions observed on the experimental *P-h* curves in (d) measured by AFM nanoindentation. The inset in (c) shows the enlarged view of the unloading curves. Note that the asterisked (*) modes will be discussed in §7.6.2.

7.6.2 Force Analysis of the Failure Modes

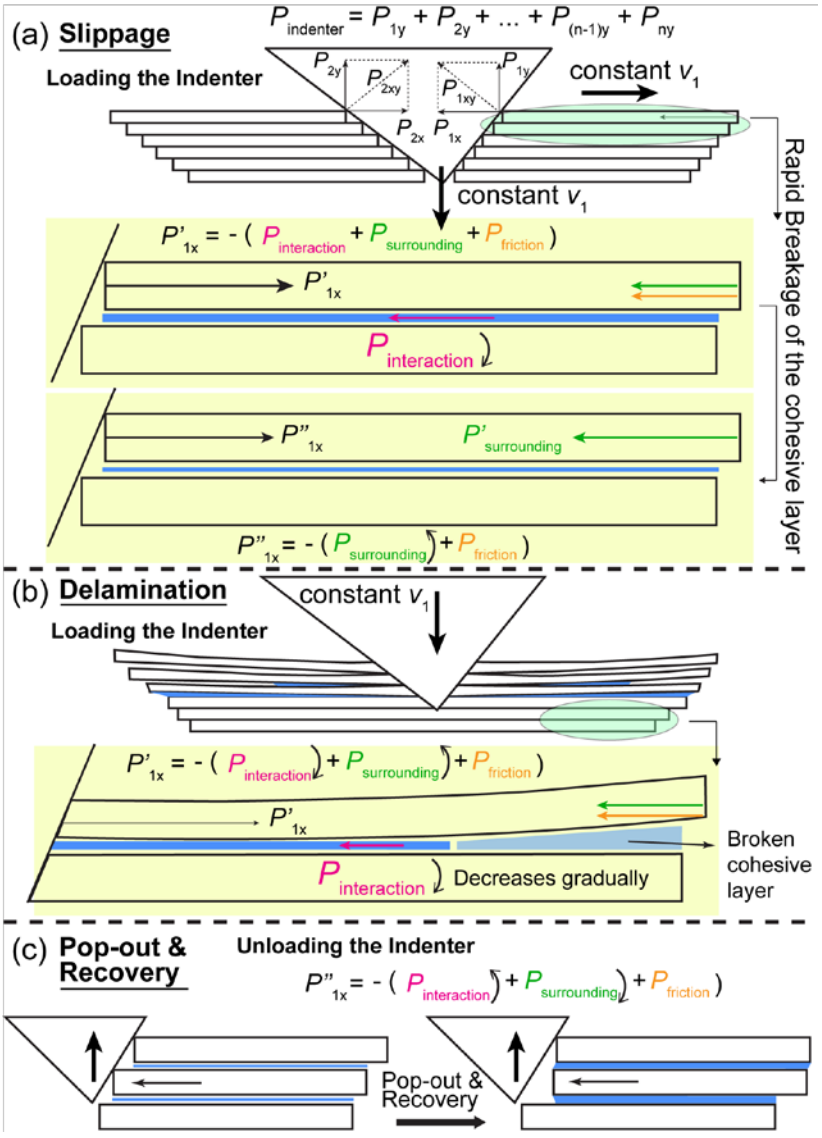

Figure 7.18 Schematic illustrating the evolution of the resolved forces between the indenter and a stack of nanosheets as well as between adjacent nanosheets under different failure modes: (a) Mode I – slippage, (b) Mode III – delamination. (c) Mechanisms of pop-out and recovery phenomena during the unloading stage. Note that the enlarged views of the interactions between the cohesive layers (shown in blue) are highlighted in yellow background.

Figure 7.18a-b illustrate the origin of the distortions in the *P-h* curves owing to the slippage and delamination mechanisms, respectively. In regard to the interfacial slippage, initially, the indenter overcomes the adhesive forces that binds the nanosheets together on the same layer (*i.e.* separation of the nanosheets). The breakage of this constraint is indicated by the first broad hump in the schematic *P-h* curve of Figure 7.17c (i.e. separation*). Subsequently, the indenter starts to push the nanosheets sideward. The cohesive layers start to deform owing to the shear forces until the complete failure. During the process, the increment of the resolved indention forces (P'_{nx}, n = 1, 2, 3, …, n, stand for the numbering of the nanosheets) between the indenter and nanosheets decrease because of the growing detachment of the cohesive layer, and that is to say $P_{interaction}$ decreases gradually until the cohesive layer is fully damaged, which evidences the second pop-in segment of the *P-h* curve (i.e. slippage* in Figure 7.17c). By contrast, the breakage of the cohesive layers proceeds much slower in the delamination mode than in the slippage mode because the bending stress that induces the delamination spreads much slower than the shear stress taking place while nanosheets sliding relative to one another (Figure 7.21g). Therefore, the gradient of distorted loading curve in delamination is reducing at lower rate compared with the more abrupt stepwise pop-in deformation.

In the AFM nanoindentation, the pop-out phenomenon was also observed at the unloading stage. It was because of the formation of a new cohesive layer or the restoration of the broken cohesive bonds, which introduces the additional interaction forces between the nanosheets. The resolved counter-acting force from the indenter (P'_{nx}) is equivalent to the summation of the forces provided by the new cohesive layers $P_{interaction}$, the restraining forces exerted by the surrounding materials $P_{surrounding}$, and the friction force $P_{friction}$ (actually, $P_{friction}$ also changes with the vertical movement of the indenter owing to the change of the normal force, and it can also affect the resulting *P-h* curves)[264]. The model in Figure 7.18c

shows that as the unloading of the indenter proceeds, the interaction force from the new cohesive layer ($P_{\text{interaction}}$) increases, along with the descending force from the surrounding material ($P_{\text{surrounding}}$), thus the interplay between the indenter and material thus resulting in a quasi-equilibrium state, which brings about the pop-out distortion of the unloading curve (see Figure 7.17). Interestingly, a force recovery process was witnessed in experiment emerging right before the indenter-to-sample interaction was reduced to zero (Figure 7.17d). The reason of the recovery is similar to the pop-out phenomenon, but instead of reaching the force equilibrium, the augmentation of $P_{\text{interaction}}$ was overwhelming comparing with the reduction of $P_{\text{surrounding}}$, thus showing the temporary rise in the resultant force (Figure 7.18c). The recovery only appeared when the unloading of the indenter was nearly completed, and at that moment $P_{\text{surrounding}}$ was close to be fully relaxed.

Instead of indenting directly on a few monolayers of CuBDC nanosheet (thickness $t \sim 2$ nm), on which the substrate effect[330] is prone to arise, the AFM nanoindentations were performed on the multilayered nanosheet stacks. Moreover, a few of the AFM nanoindentation experiments were performed on two thin CuBDC nanosheets ($t \sim 16$ nm and ~48 nm) placed on a glass substrate in order to investigate the plasticity on the upper surface of nanosheets. There were no visible radial cracks from the residual indents (Figure 7.8), which suggests the relatively resilient nature of the surrounding CuBDC framework. That is to say, the surrounding CuBDC framework has an impact (i.e. $P_{\text{surrounding}}$) on the indent area, and this supports the force analysis shown in Figure 7.18. In comparison, the indentations using sharp indenter tips (e.g. a cube-corner tip) on thin but stiffer sheets such as the silicon sheet ($t = 50$ nm, see Ref. [133]) and the hybrid YAS-GNP coating ($t = 169 \pm 10$ μm) on a silicon carbide substrate (see Ref. [355]) were reported to generate dramatic radial cracks.

7.6.3 Small-Scale and Continuous Failures

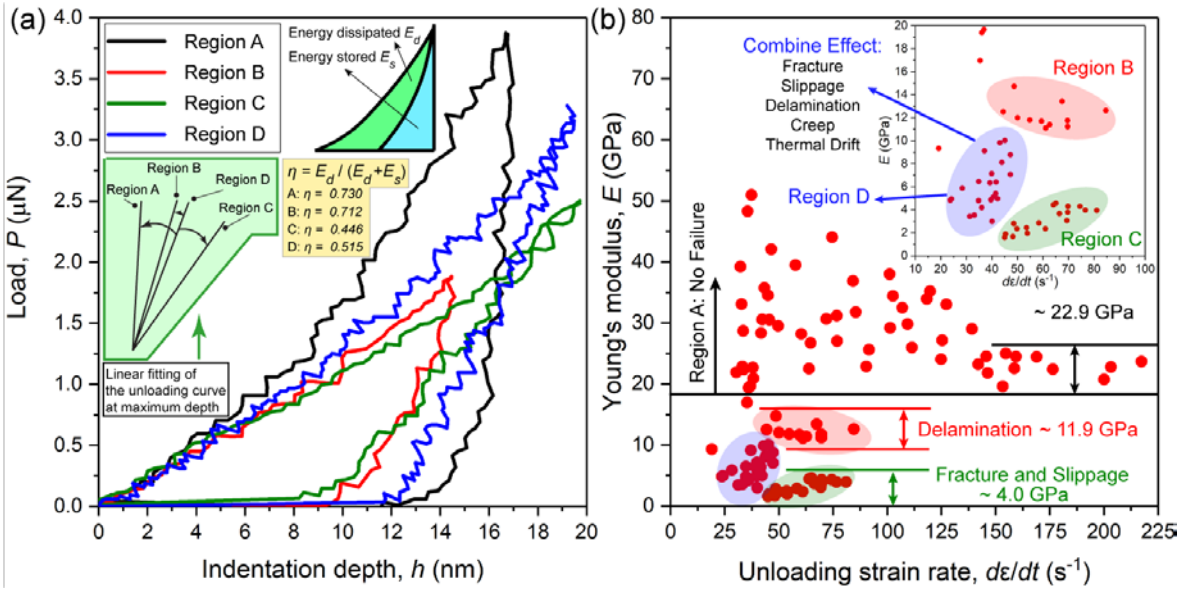

Figure 7.19 (a) Representative *P-h* curves from AFM nanoindentation of the CuBDC nanosheets respectively representing the indentations that cause no failure (curve in black: Region A), the delamination of nanosheets (curve in red: Region B), coupling effect of the slippage and fracture of nanosheets (curve in green: Region C), and combined occurrence of all possible time-dependent response such as creep, thermal drift, and failure modes (curve in blue: Region D). The linear fittings of the incipient unloading curves are highlighted in the green panel. The percentage of the energy dissipated accounting for the total energy is highlighted in the yellow panel. (b) Young's modulus measured by processing the unloading curves of the four types of *P-h* curves in (a) using the OP method showing a significant reduction in Regions B, C, D, comparing with Region A.

In Figure 7.19a, the *P-h* curve in black obtained from AFM nanoindentation typifies the response of the CuBDC nanosheet without experiencing a failure mode. While the other three representative *P-h* curves show distinct responses when indentation stress induces different failure modes or time-dependent responses. Such difference is embodied in the distribution of the Young's modulus in Figure 7.19b, observation of which shows that the distribution of Young's moduli falls into four regions, in which only Region A describes the CuBDC framework's intrinsic property without significant stress-induced framework failure and other time-dependent deformation (creep and thermal drift). Otherwise, the CuBDC

framework undergoes stiffness loss and hardness reduction (designated as Regions B, C, and D) at different degrees depending on the failure modes, resulting from the additional indenter penetration displacement. Additionally, the energy loss (see Figure 7.19a) of the AFM nanoindentation experiments in Regions B, C, D was observed lower than in Region A. The results suggest that in the scenarios described by the Region B, C, D, a part of deformation was contributed by other forms of material behaviours (e.g. fracture, sliding, delamination) that dissipate less energy than only plastic deformation.

Regions B and C are the subsequently steady states of Region D as the unloading strain rate increases. Similar to the effect of surpassing the time-dependent behaviours such as creep and thermal drift in the indention direction, high unloading strain rate also reduces the creep in the horizontal direction along P'_{nx}, and thus contributing to the convergence of the Young's modulus from Region D to Region C. With this in mind, the unloading strain rate principle can also be extended to fracture mode since high loading-unloading strain rate shortens the time for cracks propagation. Figure 7.19b also shows that the indentations in Region D were implemented at a relatively lower unloading strain rate, therefore the excessive additional indentation displacements were generated by a combination of factors: fracture, sliding, delamination, creep, and thermal drift. Nevertheless, the effect of these failure mechanisms can be overcome by increasing the unloading strain rate (converging to Regions B and C).[147]

7.7 Quantification of the Loads Resulting in the Failures Modes

The Young's modulus in Regions B, C, and D in Figure 7.19b are all derived from *P-h* curves that have no visible distortions, implying that the occurrence of the failures is a subtle effect compared with the history of the entire *P-h* curve. However, in some cases, *P-h* curves from AFM nanoindentation consistently show large-scale distortions as discussed in §7.6.1. By carefully characterising these distortions, it is proposed that the threshold forces that give rise to the failures of CuBDC nanosheets in the atomic scales can be quantified (see Figure 7.20).

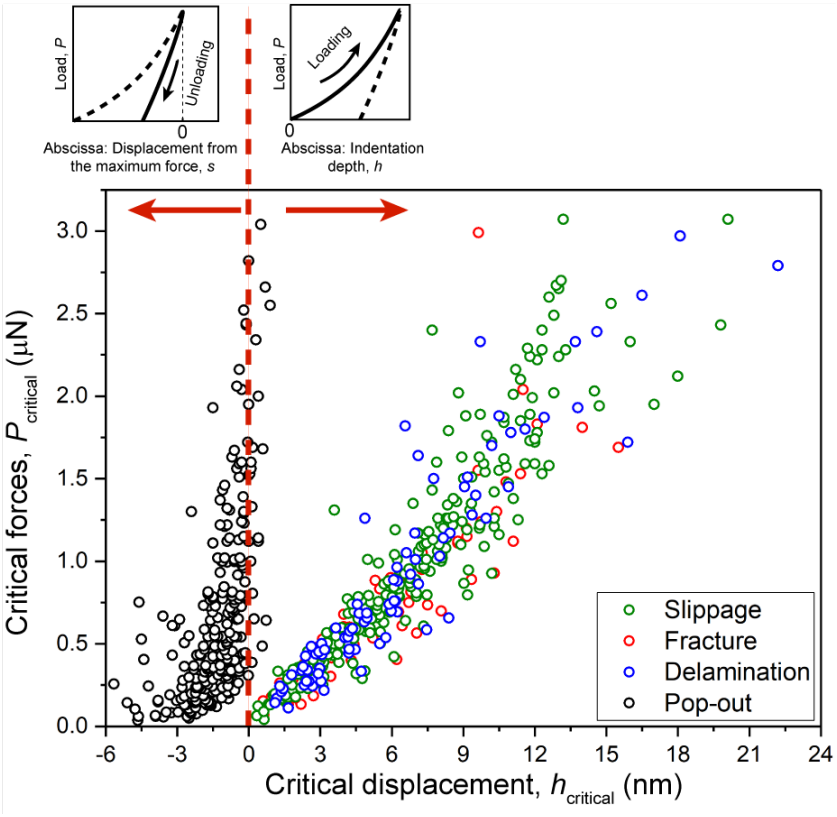

Figure 7.20 The threshold forces resulting in the three failure modes during the loading stage as the function of the threshold depths; and the threshold forces leading to the pop-out phenomenon as a function of the displacement from the maximum force during the unloading stage (because it is in the opposite direction, the displacement has a negative value). Note that a small portion of the data points for the pop out are positive due to the distortion of the incipient unloading curves.

The data points in Region B might correspond to delamination of the CuBDC nanosheets (Mode III) caused by the AFM indenter. This inference is based on the observation that delamination introduces less additional indentation displacement than other two failure modes, and thus brings about less stiffness loss. In comparison, indentation in Region C is on account of the coupling effect of the interfacial sliding (Mode I) and the fracture (Mode II) of the nanosheets that results in a considerable stiffness loss due to the additional indentation displacement. The interfacial sliding in this study mainly refers to the horizontal sliding (*viz* sliding plane normal to the indentation), although the interfacial sliding along indentation direction may also cause stiffness loss, such as reported in the literature.[337]

The speed of stress spreading within the nanosheet plane is a good indication to evaluate the growth of the failure modes in the continuous indentation experiments. Moreover, the speed varies when different failure modes occur. An ideal scenario that the area of the stress field stays constant with increasing penetration depth, hence the idealised threshold forces and threshold depths triggering the failure modes can be estimated. Regarding the idealised force and depth, they are obtained by proportionally increasing the unit idealised force and corresponding depth that cause any one of the three failure modes to form the data points (blue and green in Figure 7.21c-e) in the linear pattern. It was found only these data points based on the genuine unit force and depth leading to the failure modes of a single layer of the CuBDC nanosheet (thickness $t \sim 0.8$ nm, see Figure 7.1b) are able to define the lower bound of the experiment data points (red in Figure 7.21c-e). Using this approach, the threshold indentation force and the corresponding indentation depth were determined for the three failure modes (summarised in Table 7.4). However, in reality, as the cube-corner indenter continues to penetrate into the material, the stress spreads constantly thus the affected area is continuously growing. As illustrated in Figure 7.18,

higher force is needed in order to overcome the counter-acting force from the cohesive layer, whose area increases rapidly with stress spreading. Therefore, the experimental threshold forces causing interfacial sliding where stress spreads more rapidly (see Figure 7.21g) and hence increases faster than the idealised values by contrast with fracture (Figure 7.21d) and delamination (Figure 7.21e).

Table 7.4 Threshold values of the indentation force, depth, project indent area, area of the stress field (derived from Figure 7.21g), and stress (force/area of the stress field) leading to the three distinctive failure modes of a monolayer of the CuBDC nanosheet. Possible uncertainties are dependent on the localised distinct nanosheet stacking conditions.

Thresholds / Failure Modes	Force (nN)	Depth (Å)	Projected Indent Area (nm^2)	Area of the stress field (nm^2)	Stress (MPa)
Slippage	42.6	6.5	1.1	~ 2290	9.3
Fracture	70.4	6.4	1.1	~ 23779	3.0
Delamination	56.0	5.8	0.9	~ 3421	16.4

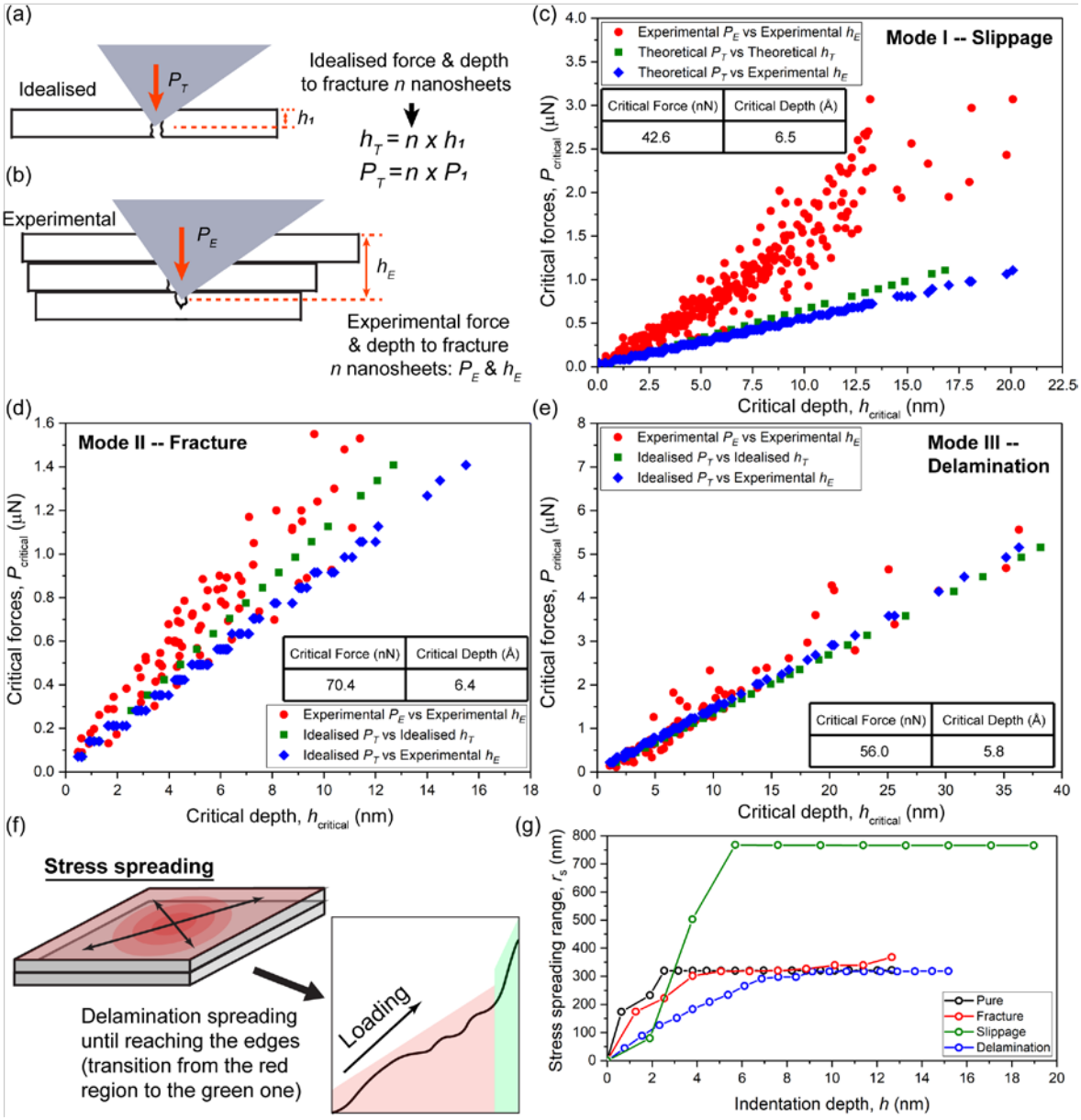

Figure 7.21 Schematic illustrations of the (a) idealised (i.e. analytically modelled) and (b) experimental forces and depths, respectively. Comparison between the idealised and experimental data in the plot of threshold forces as a function of threshold depth leading to the failure modes: (c) Mode I – slippage, (d) Mode II – fracture, (e) Mode III – delamination. Stress spreading: (f) in the exemplar of delamination, the sketch illustrates the influence of planar stress extension on the resulting *P-h* curve; (g) the planar stress spreading range with increasing depth acquired from the FE model.

7.8 Summary of the Chapter

In this work, a new approach was demonstrated for using the AFM-based nanoindentation to measure the mechanical properties of the CuBDC nanosheet. The main results are summarised as follows:

- The elastic-plastic properties including the Young's modulus, hardness, yield strength, and ultimate strength have been characterised. And the unloading strain rate principle has been applied and found to be effective for improving the accuracy of the measurements.

- Three characteristic failure modes at loading of the nanosheets have been proposed, and the failure modes are governed by bending deformation and the interlayer shear mechanisms. The three failure modes are the interfacial sliding, framework fracture, and delamination. The pop-out and recovery phenomena at unloading are explained.

- Furthermore, the threshold indentation forces and threshold indentation depths leading to the failure modes have been quantified.

- The finite-element method has been employed to simulate the AFM nanoindentation on the MOF nanosheets to gain insights into the plastic deformation and the proposed failure modes.

- Although the CuBDC nanosheet was used as the model material to establish the novel efficacy of the AFM-based nanoindentation in investigating the nanoscale mechanical behaviour of MOF nanosheets, the methodologies developed should be applicable to quantitatively study the nanoscale mechanical properties of a wide range of nanomaterials, nanosheets in particular, which are often considered to be difficult to study.

Chapter 8: Mechanical Behaviour of HKUST-1 (CuBTC) Crystals

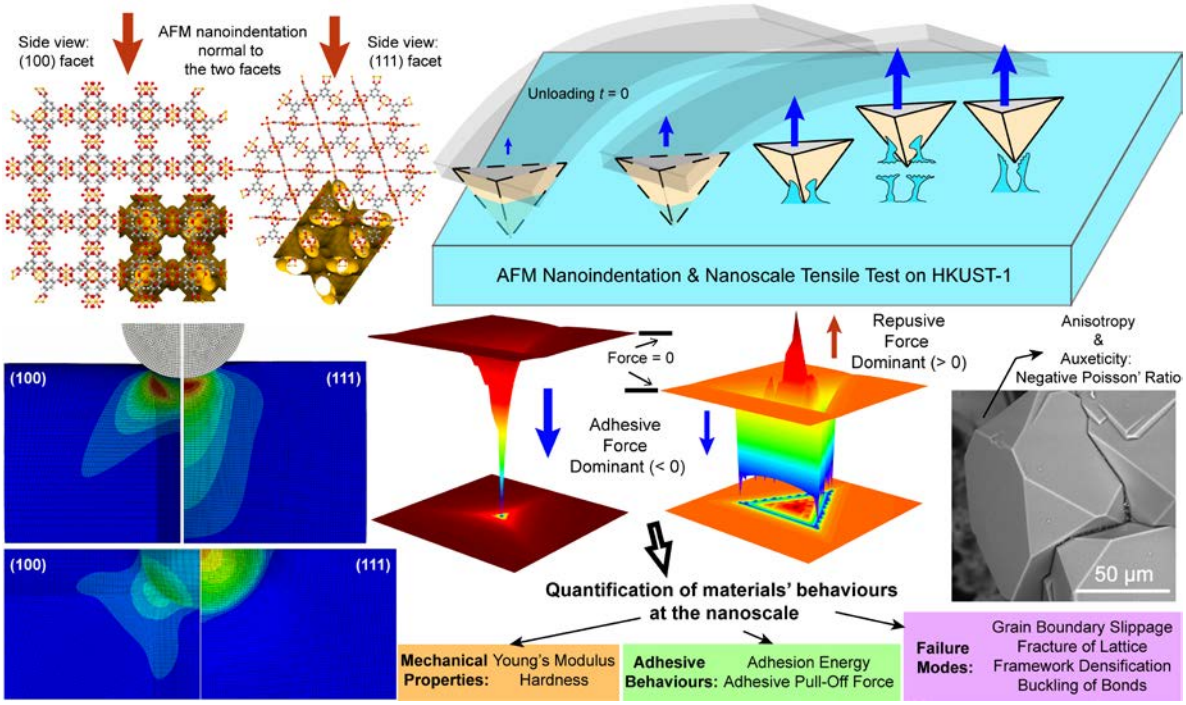

This chapter focuses on characterising the nanomechanical properties of the submillimetre-sized crystals of $Cu_3(BTC)_2$ (more well-known as HKUST-1), using the AFM nanoindentation technique equipped with the calibrated diamond cube-corner indenter tip. For the first time, the experimental results of the elastic-plastic properties (e.g. the Young's modulus and hardness) of HKUST-1 have been characterised together with the four structural failure modes (i.e. slippage, fracture, densification of the porous framework, buckling of bonds) during the indenter loading stage as well as the two distinctive pop-out phenomena reflecting the recovery of the Cu−BTC−Cu linkages during the unloading stage. The structural failures caused by the indenter could introduce significant distortions on the resulting force-displacement (P-h) curves while indenting on the porous MOF structure. This work demonstrates that the distortions can be circumvented by leveraging two adhesion models (analytical and numerical), which improve the quantification of the Young's modulus, adhesive force, and adhesion energy of HKUST-1. Furthermore, a novel nanoscale "tensile test" has been developed by using the AFM indenter to apply tension to the crystal surface. The role of auxeticity (viz. negative Poisson's ratio) of HKUST-1 at the nanoscale has also been studied.

8.1 Introduction

In this chapter, the copper paddle-wheel MOF structure, called HKUST-1 has been chosen, due to its well-ordered nanoporous structure and promising structure-based functionality.[50] HKUST-1 exhibits exceptional performance in many aspects including catalysis,[356] preferential adsorption,[52-54] storage of energy,[55, 357] and electronics[56] benefited by its metallic dimer, Lewis acid sites, and outstanding porosity (pore diameter ~0.6 nm).[358] For instance, HKUST-1 shows excellent catalytic activity due to the existence of the Lewis acid sites that immobilise the redox-active polyoxometalate[356] and the tuneable electrical conductivity when the nanopores encapsulate conjugated guest molecules.[359] Moreover, after densification and shaping of HKUST-1, the capacity of natural gas (mostly methane) adsorption has been demonstrated to be elevated to an unprecedented level of 259 cm^3 (STP) cm^{-3} at 65 bar.[55] Because of the many promising properties of HKUST-1, having detailed information and understanding about its mechanical properties will be advantageous for future applications.

MOFs show apparent fragility comparing with metallic and ceramic materials, in addition to that, experimental evidence of the (DFT predicted)[8] auxetic attribute (negative Poisson's ratio) of HKUST-1 is even more challenging to probe under an indentation setting. In this study, the nanomechanical properties of HKUST-1 have been quantified by employing both the IIT (see §2.3.1.1) and the AFM (see Chapter 3) nanoindentation techniques. The majority of the reported studies using the AFM technique provided only the basic indications of the localised mechanical properties (mostly Young's modulus, hardness, and yield stress) through a small number of indentations.[153, 180] In contrast, in this study as many as 846 indentations have been performed in order to systematically explore the intrinsic nanomechanical properties of HKUST-1. In addition to the nanoindentation experiments, a suite of analytical, empirical, and numerical methods has been developed to

analyse the experimental data so as to achieve the accurate mechanical characterisation of HKUST-1. The influence of the elastic anisotropy and the possible contribution from auxeticity have also been addressed.

8.2 Structure and Synthesis

The HKUST-1 crystal has cubic symmetry as shown in Figure 8.1. According to the calculation from the *ab initio* density functional theory (DFT),[8] the HKUST-1 crystal structure is predicted to exhibit directional auxeticity. Its negative thermal expansion and low shear moduli have already been experimentally confirmed in recent studies.[51, 360-361] Details regarding the crystallographic structure, predicted material properties, and applications have been discussed in §2.2.3. The submillimetre crystals of HKUST-1 studied herein (300 μm or more) were synthesised by low-temperature solvothermal method augmented by glacial acetic acid (see §4.1.3).

It should be noted that the submillimetre-sized crystals of HKUST-1 are actually about two orders of magnitude larger than the micron-sized ZIF-8 (in Chapter 5 and Chapter 6) with a view to avoid the influence of the confinement from the surrounding epoxy resin (Struers Epofix) on the characterisation of the elastic anisotropy. These crystals were mounted by two different methods. (i) By embedding the crystals into an epoxy resin stub, which was then fully cured before the crystal surface (designated as $_{\text{polished}}$HKUST-1, see Figure 8.2b-c) was carefully ground/polished following the established methodology[45] to expose the {100}- and {111}-oriented facets for nanoindentation experiments. The prepared crystal surface was cleaned with ethanol and then desolvated at 90 ^{o}C. (ii) The second way to immobilise the crystal was to apply the mounting wax (melted at 60 ^{o}C and cured at room temperature) around the periphery of the bottom of the crystals (entitled as $_{\text{fixed}}$HKUST-1,

see Figure 8.2d-g). There is no difference observed for crystals immobilised using (i) and (ii) when being indented using the IIT and AFM. This observation indicates that the crystals are large enough to eliminate the effect of the confinement imposed by the cured epoxy resin.

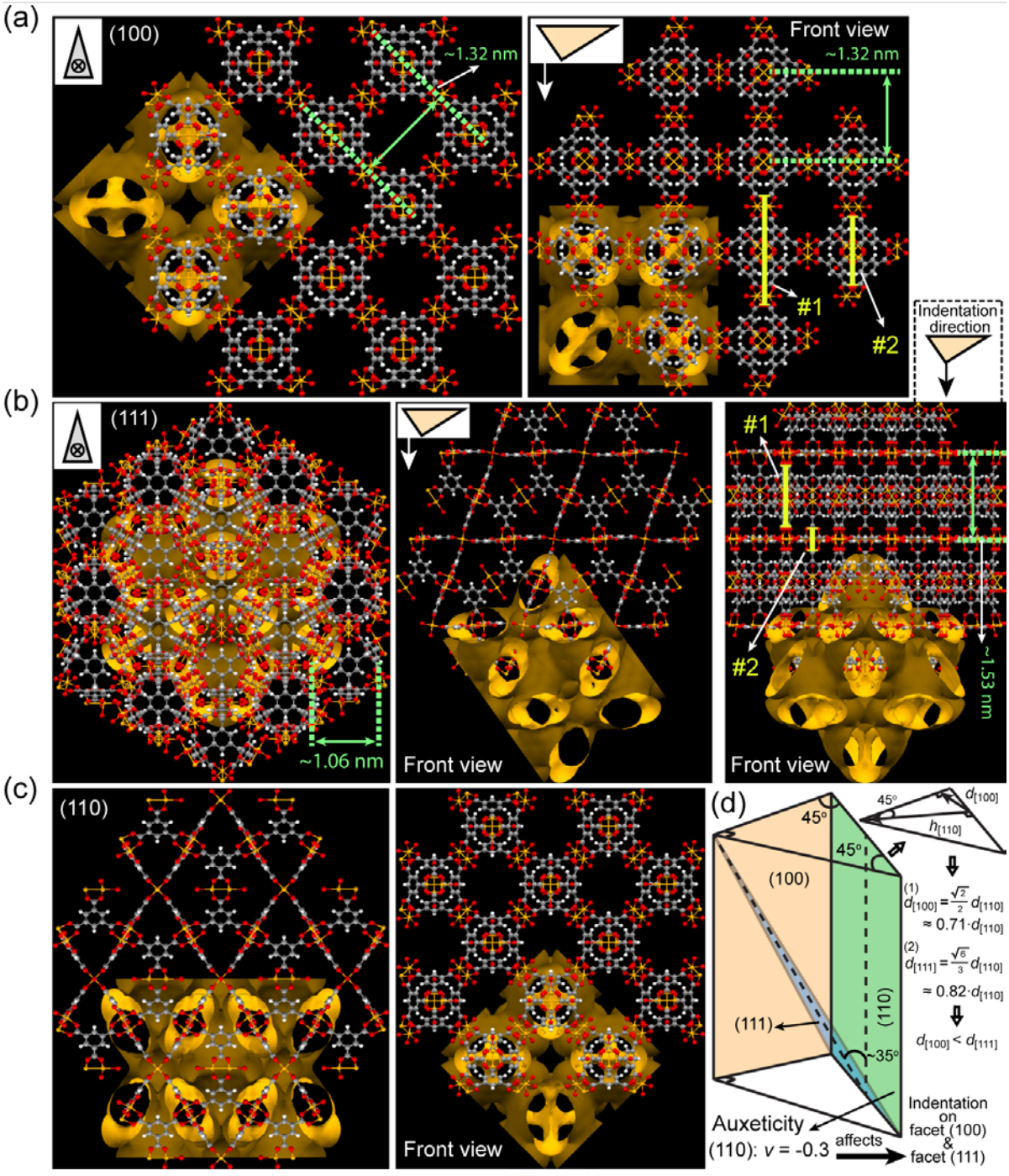

Figure 8.1 Crystal structure of HKUST-1. Nanoindentation of the (a) (first row) {100}-oriented, (b) (second row) {111}-oriented facets. Auxeticity of HKUST-1, the Poisson's ratio (ν) along the (c) (third row) [110]-axis: ν = –0.3 according to the DFT calculations in Ref. [8]. Indentation directions are illustrated by the insets (crosses denote

the indentation into the page). The vertical markers (highlighted in yellow) indicate the unit length scale wherein the failure modes occur on a HKUST-1 unit cell (see Table 8.1 in §8.9). (d) Schematic showing the influence of auxeticity along the [110]-axis (explained in §8.7). The inclination of the {110}-oriented facet relative to the other two orientations where nanoindentation was performed. The counter-acting deformation imposed by the {110}-oriented facet to the other two facets is denoted as *d*. This influence of auxeticity was also observed in the measurement of hardness (see the inset in Figure 8.6b).

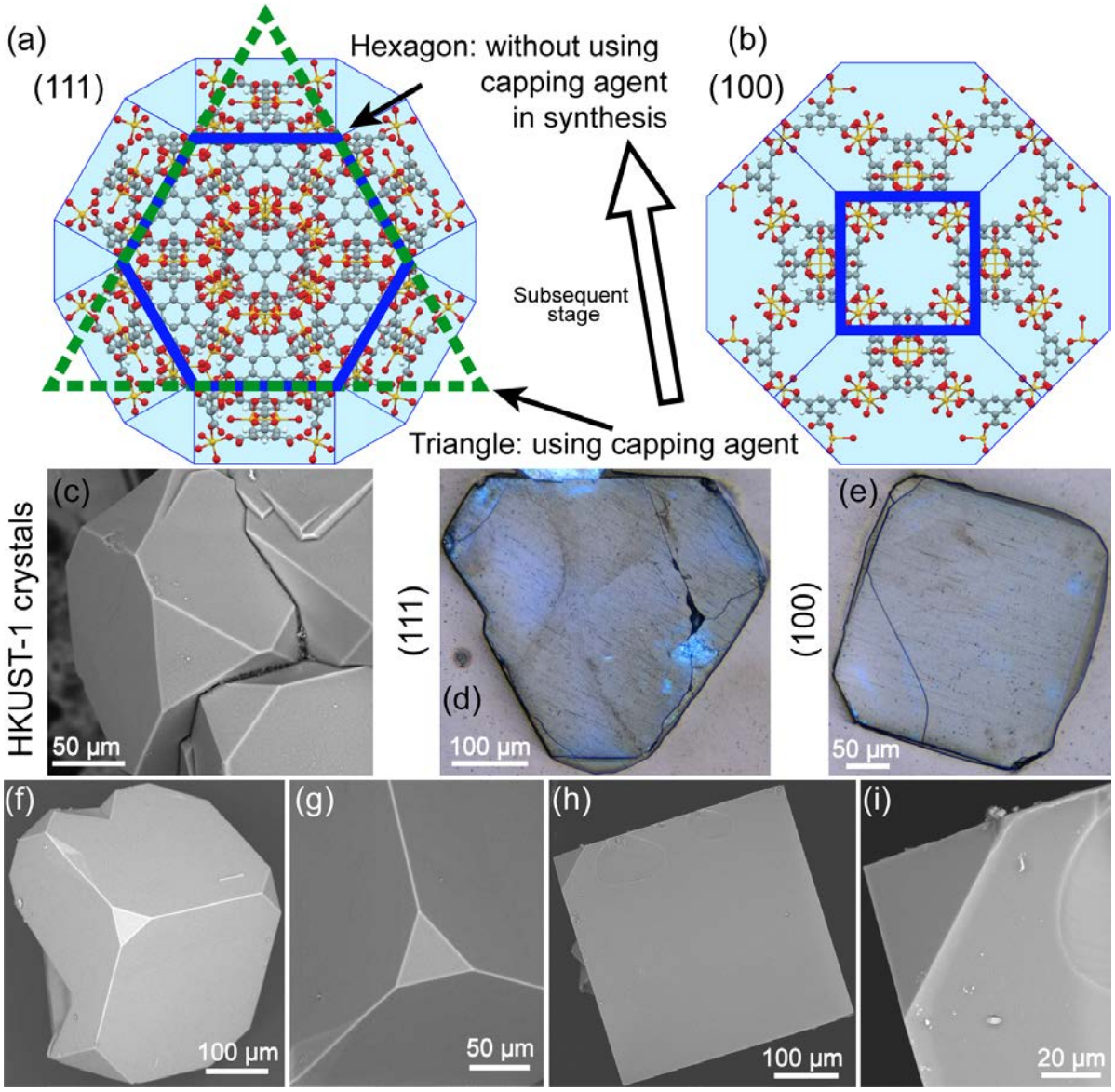

Figure 8.2 (a) Crystal morphologies of HKUST-1 (a) {111}-oriented and (b) {100}-oriented facets. The modulator, glacial acetic acid (see §4.1.3) also acts as a capping agent that inhibits the growth of the (111) plane from the triangular geometry (green) to the hexagon (blue) and also changes the growth rate of the crystals. X-ray diffraction pattern of a single crystal of HKUST-1 can be found in Figure 2.9. (c) The SEM image of the aggregated submillimetre-sized crystals of HKUST-1. Optical images of the two $_{\text{polished}}$HKUST-1 crystals embedded in the fully-cured epoxy resin stub showing the (d)

{111}-oriented and (e) {100}-oriented crystallographic facets, on which minor cracks could be generated during the polishing process using the diamond suspension (0.1 μm, Struers). The SEM images of the $_{fixed}$HKUST-1 crystals with (f-g) {111}-oriented (triangular) and (h-i) {100}-oriented (square) facets facing up.

8.3 Nanoindentation Techniques

The force sensitivity of the (conventional) instrumented indentation technique (IIT) are normally of the tens of nanoNewtons (nN) level. For instance, the force sensitivity of the MTS Nanoindenter® XP is ~50 nN while the Hysitron Triboindenter can detect load as low as 1 nN,[99-100, 362] although in practice the peak loads imposed by the IIT instruments are usually 100s to 1000s μN.[45, 90, 101-102] In comparison, the AFM instrument is capable of sensing significantly smaller forces (force sensitivity < 0.05 nN) and could apply a shallower indentation depth (vertical displacement sensitivity $\lesssim$ 0.05 nm). Because of this, AFM nanoindentation complements the IIT in probing more localised properties.

In this study, the IIT experiment and AFM-based nanoindentation were performed using the MTS Nanoindenter® XP equipped with a Berkovich indenter tip and the Veeco Dimension 3100 instrument fitted with the cube-corner indenter tip (same as the one in previous chapters), respectively.

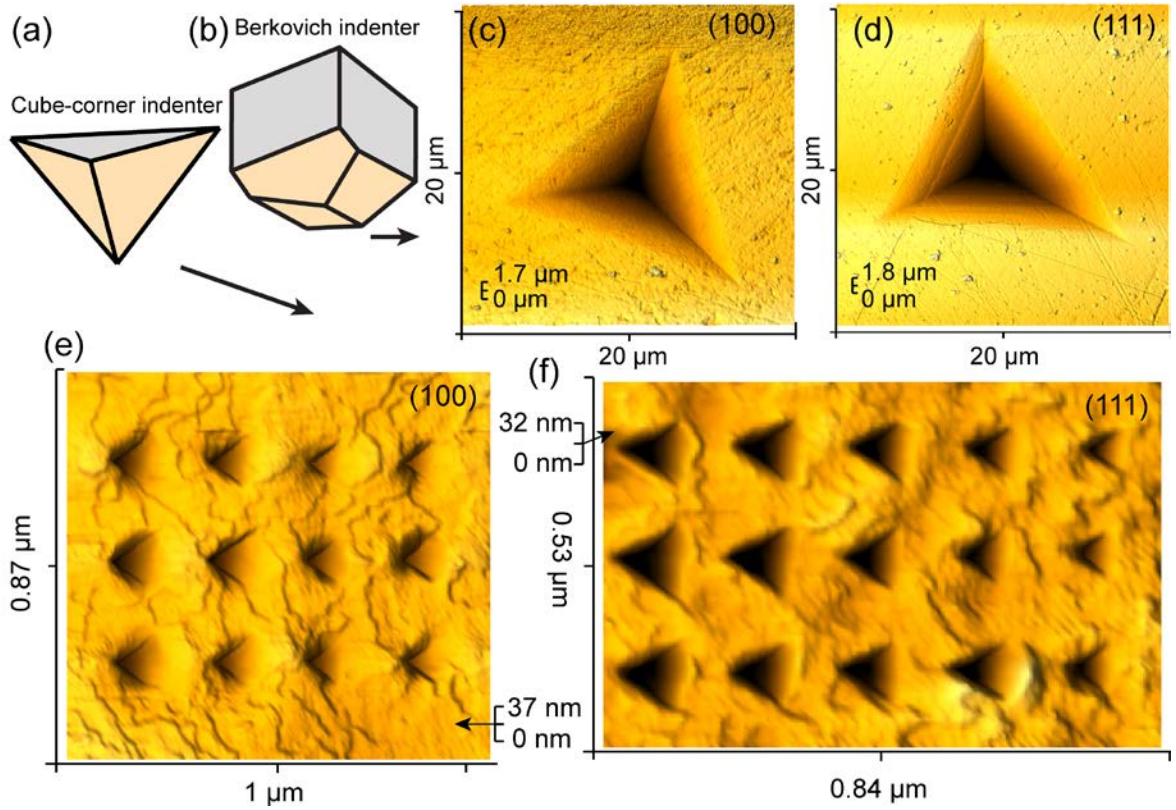

Figure 8.3 Schematic illustrating the (a) cube-corner (for the AFM nanoindentation experiments) and (b) Berkovich (for the IIT experiments) indenter tips, respectively. The 3-D AFM height topographic images (captured using an imaging silicon tip, namely Tap300Al-G, see §4.2.1) of the indents were produced by the IIT experiments on the two crystallographic facets of the HKUST-1 crystals: (c) (100) and (d) (111). The 3-D AFM height topographic images of the indents which were generated in the AFM nanoindentation experiments on the (e) (100) and (f) (111) crystal facets. The images in (e) and (f) were in situ captured using the cube-corner indenter tip. It is assumed that the synthesis procedure and heating treatment (see §4.1.3) have removed residual reactants from the crystal porosity, and thus there is negligible influence on the indentation experiments. However, given that the indentation experiments were not conducted under dry and vacuum environment, the underlying effect of the re-encapsulated water molecules from the atmosphere may contribute to a limited degree of deviation.

8.4 Finite-Element Method

In order to simulate the elastic anisotropy of the HKUST-1 crystals, the finite-element (FE) method implemented in ABAQUS has been employed to model the indenter-to-sample contact interactions. In this work, a continuum model meshed by an

8-node linear brick element with the reduced integration and hourglass control (*C3D8R*) was used to mesh the HKUST-1 crystals (treated as a continuum) in ABAQUS/Explicit.[323] In the indentation assembly, the indenter is a spherical discrete rigid part rather than the cube-corner geometry adopted in the actual AFM nanoindentation. The spherical design is selected to avoid the excessive distortion of the meshes and to remove the geometrical influence of the cube-corner shape, thus concentrating on the elastic anisotropy of the crystal itself.

The elastic constants of the continuum model were based on the C_{ij} stiffness coefficients from the reported DFT calculations (C_{11} = 27.719, C_{12} = 25.722, and C_{44} = 5.399).[8] Obvious differences of elastic response shown by the {100}- and {111}-oriented crystallographic facets can be seen from the von Mises stress fields in Figure 8.4. Moreover, in Figure 8.6a, the overlap of the initial portions of the *P-h* curves for both facets suggests that anisotropy is less important when the plastic deformation is relatively small (h < 7.5 nm). With increasing indentation depth, the experimental *P-h* curves remain in agreement with the *P-h* curves acquired from the FE model, until the depth reaches h ~ 20 nm for the {111}-oriented facet and h ~ 25 nm for the {100}-oriented facet. This is due to the excessive plastic deformation starting to collapse the framework and densify the fragments into the underlying framework. This hypothesis is supported by the evolution of the *P-h* curves along the [100]-axis, where the slope of the loading curve gradually approaches the one along the [111]-axis. In other words, after the plastic deformation reaches a threshold, the framework begins to lose its resistance against the incoming indenter, meanwhile, the effect of anisotropy also diminishes. Besides plastic deformation, other interfering factors such as time-dependent response (creep and thermal drift) as well as crystal failures and fracture, will also distort the shape of the *P-h* curve

(creep can cause a negative gradient at unloading, see §3.4.9), and this was also observed on the ZIF-8 crystals (see Figure 5.5).

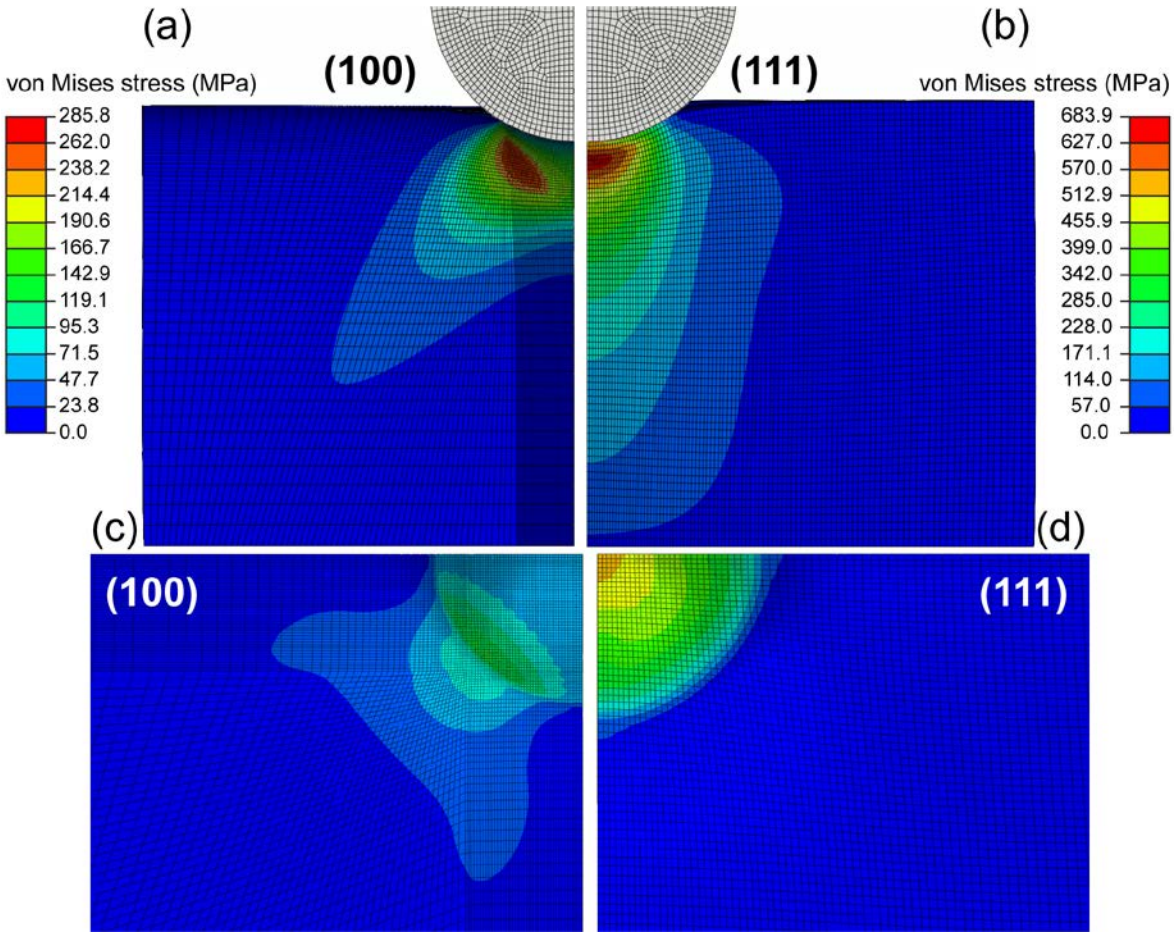

Figure 8.4 The von Mises stress fields in (a-b) showing the anisotropic mechanical response of HKUST-1 under indentation along the [100]- and [111]-axes viewed from the front side. (c-d) are the top views of the stress fields for indentation along the [100]- and [111]-axes (indenter not shown for clarity).

8.5 Nanoscale Mechanical Properties of HKUST-1

8.5.1 Force Curve Quality Evaluation: P/S^2

In general, the force-square contact stiffness ratio (P/S^2) stays constant irrespective of indentation depth (h) and the pile-up or sink-in behaviours.[257] By virtue of this, a new approach is proposed to evaluate the quality of the resulting force-displacement (P-h) curves from the indentation experiments. Specifically, as shown in Figure 8.5a and Figure 8.5c, the

slope lines through the origin are deduced to indicate the ideal slopes of the incipient segment (starting from the peak load) of the unloading curves. The slope lines can be generated by equation (8.1),[257] which gives the ideal slopes (*S*) at different peak loads. The input values of the Young's modulus (*E*) and hardness (*H*) can be obtained from the indentation experiments.

$$\frac{P}{S^2} = \frac{\pi}{(2\beta)^2}\frac{H}{E^2} \tag{8.1}$$

More specifically, the slope lines serve as an indicator as a means for evaluating whether an unloading process is free from the interfering factors (previously introduced in §3.4) causing the distortion of the unloading curves (see examples in Figure 8.5c). With this in mind, one can assert that the *P*-*h* curve #1 (shown in the inset of Figure 8.5a) is free from the influence of interfering factors. These slope lines can also be regarded as the ideal unloading curves integrating information of both the Young's modulus (*E*) and hardness (*H*) of the HKUST-1 crystals, in contrast, the finite-element (FE) model only involves *E* (i.e. the C_{ij} stiffness coefficients).

In the IIT experiment, the indentation depths were ~2000 nm. The force-displacement (*P*-*h*) and stress-indentation depth (σ-*h*) curves can be seen in Figure 8.5a-b. Whereas as shown in Figure 8.5c, the AFM-based nanoindentation performed at much smaller scale returns the *P*-*h* curves exhibiting the distinctive behaviour of HKUST-1. Regarding the AFM nanoindentation on HKUST-1, in contrast to the experiment of the same instrument setup on the smooth and flat Matrimid® 5218 (a glassy polyimide) thin film (thickness $t \sim 1\ \mu$m), AFM nanoindentation produces consistently reproducible *P*-*h* curves and exhibits a harmonic oscillation. Unlike the nanoporous HKUST-1, it is reasoned that the cross-linked structure of Matrimid is more isotropic and impose a more uniform resistance to the aforementioned interfering factors. In fact, the chaotic oscillations (more

severe in Figure 8.14) of some indentations of HKUST-1, reflect the different failure modes of the framework, which will be discussed in greater details later in §8.9 of this chapter.

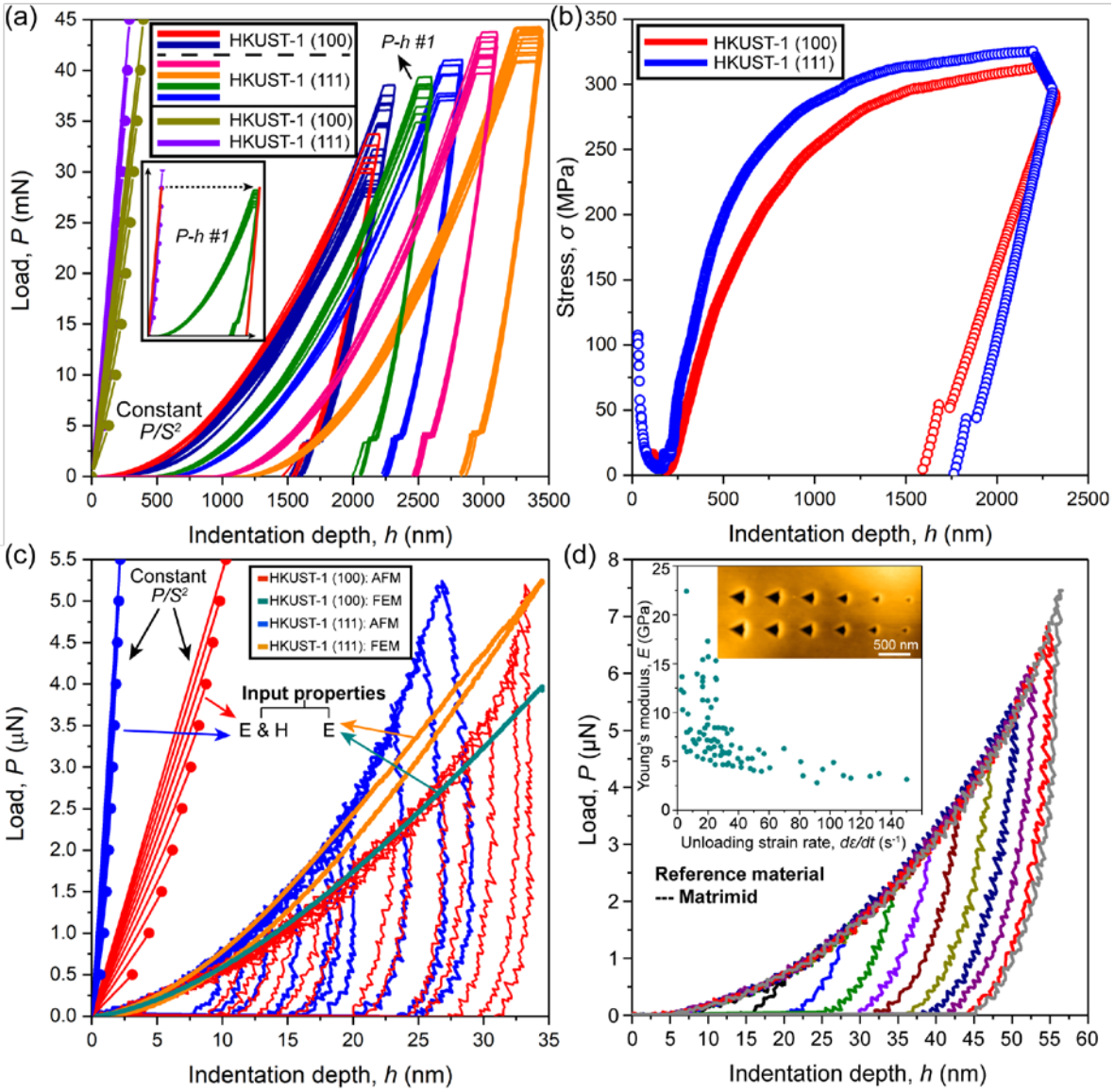

Figure 8.5 (a) (right) Force-displacement (*P*-*h*) curves from the IIT of the {100}- and {111}-oriented crystallographic facets of HKUST-1; (left) the slope lines derived from equation (8.1), and the input values of *E* and *H* in the equation are from the IIT experiments. (b) Stress (σ) induced by the IIT experiments as a function of the indentation depth (*h*). (c) (right) Two types of *P*-*h* curves: one was from the AFM-based nanoindentation (a few representative ones are shown here taken from the 846 indentations in total) and another one was acquired from the elastic FE model on both facets (see Figure 8.4); (left) the slope lines derived from equation (8.1), and the input values of *E* and *H* are from the AFM nanoindentation experiments. (d) *P*-*h* curves from the AFM nanoindentation experiments on a reference sample, *viz.* Matrimid thin film and the measured *E* as a function of the unloading strain rate is shown in the inset.

8.5.2 Hardness (*H*)

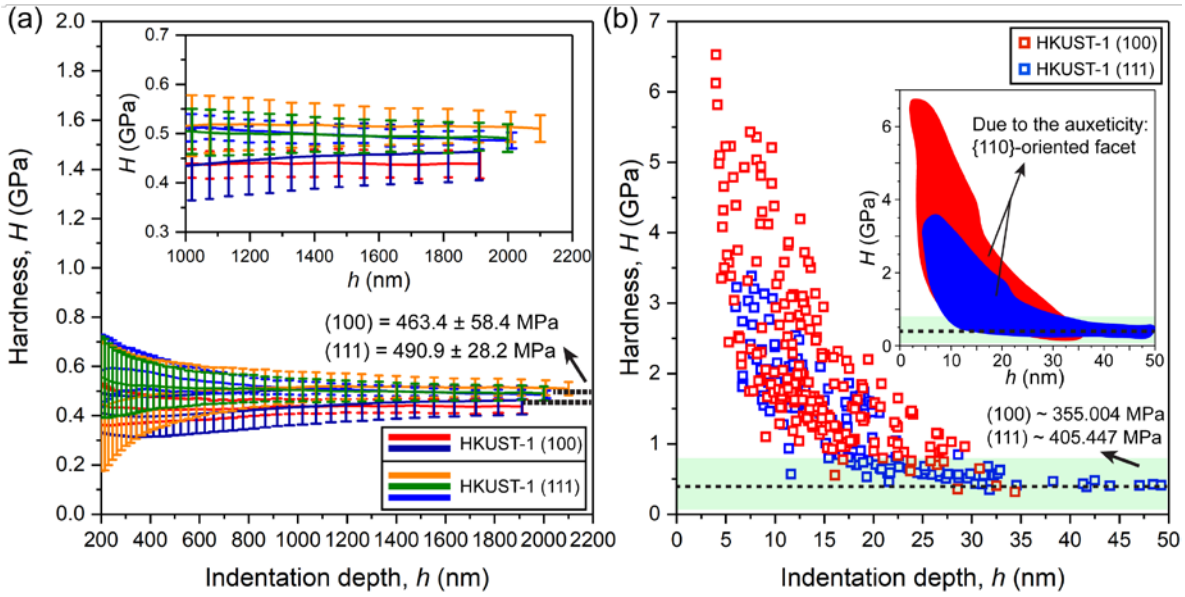

Figure 8.6 Hardness (*H*) measured by (a) the IIT and (b) the AFM-based nanoindentation experiments as a function of indentation depth (*h*), *H* was obtained by its definition: $H = P_{max}/A_{contact}$. The inset in (a) shows the enlarged view, and (b) regions marking the distinctive tendencies of *H* measured as the indenter penetration increases. The dashed lines designate the mean values of *H* for the (100) and (111) crystallographic facets after the value of *H* converges.

By means of the IIT, the values of the hardness along the [100]- and [111]-axes have been measured: $H_{[100]} = 463.4 \pm 58.4$ MPa and $H_{[111]} = 490.9 \pm 28.2$ MPa, respectively, which are in good agreement with the measurement of the polycrystalline monolith of HKUST-1 ($H = 460 \pm 30$ MPa).[55] Nevertheless, close inspection of the *P*-*h* curves in Figure 8.5a, one can observe the apparent variance of the peak loads indicating the partial loss of hardness, and this is also evidenced by the scattering of the measured hardness values shown in Figure 8.6a. The inconsistency of the hardness measured can be ascribed to the propagation of cracks, *viz.* fracture of the framework, as well as the possible subsurface crystal defects produced during either the synthesis or the surface polishing of some of the crystals. This is supported by the AFM height topographic images of the indents in Figure 8.3c-d.

One may perceive that the variance of hardness would be more severe in the case of the AFM-based nanoindentation, which is equipped with the smaller and sharper indenter (cube-corner tip) so as to induce a much higher stress concentration. Although the AFM-based nanoindentation measures the hardness at a significantly shallower depth, the result suggests a considerable hardness loss (see Figure 8.6b). Additional possible reason to the hardness loss is that the intense stress concentration actually facilitates the plastic deformation as well as the foregoing interfering factors such as creep and structural failure. The hypothesis has been corroborated by the indication of the slope lines in Figure 8.5c, which also contains the information of H as explained in §8.5.1. As the indentation depth increases, one can easily see the deviation between the slope lines and the incipient segments of the unloading curves obtained from the AFM nanoindentation experiments.

8.5.3 Young's Modulus (E) using the Oliver and Pharr Method

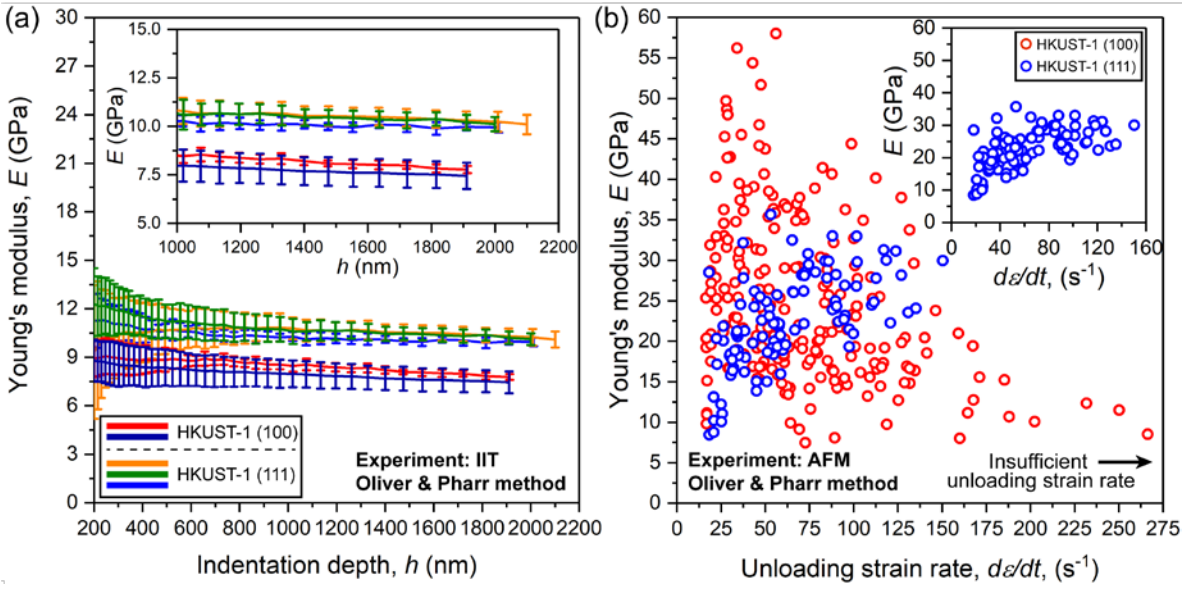

Figure 8.7 Young's modulus (E) measured by (a) the IIT as a function of the indentation depth (h) and (b) the AFM-based nanoindentation as a function of the unloading strain rate ($\dot{\varepsilon}$), the P-h curves was analysed using the Oliver and Pharr (OP) method. The insets in (a) and (b) showing the enlarged views.

The unloading strain rate principle (§4.7.3) in applied here, which has been demonstrated to be effective in overcoming the distortion to the unloading curves.[147] Using this approach, a sufficiently high value of $\dot{\varepsilon}$ is needed (limit of the specific AFM instrument) to minimise creep and other time-dependent effects.

Similar to the measurement of the hardness, both IIT and AFM nanoindentation experiments were performed to indent the two crystallographic facets of HKUST-1: (100) and (111). Young's modulus obtained from the IIT experiments for the {100}- and {111}-oriented facets are $E_{[100]} = 7.4 \pm 0.6$ GPa and $E_{[111]} = 10.4 \pm 0.8$ GPa, respectively. In the chapter, Poisson's ratio, v is taken to be zero and thus the Young's modulus (E) mentioned herein is actually equivalent to the indentation modulus (I). Densification could slightly increase E of HKUST-1, which is akin to the compacted polycrystalline HKUST-1 monolith whose $E \sim 11.5 \pm 0.4$ GPa (taking $v = 0$).[55] There is a discrepancy between the results from the IIT experiment and the theoretical values of $E_{[100]} \sim 2.96$ GPa and $E_{[111]} \sim 15.15$ GPa *via* the theoretical DFT calculations at the B3LYP level of theory in the literature, although the DFT values were predictions at 0 K.[8] In generally, the Young's moduli of MOFs decrease with the increasing temperature since the restoring force that returns the deformed bond to its equilibrium state is normally lower at high temperature.[125] Another possible reason, as pointed out by Oliver and Pharr, is that the *P*-*h* curves collected by indentation of a specific crystallographic orientation does not represent the true elastic response because of the complex tip geometry, previous experiments suggested that the elastic modulus of anisotropic materials are only average values (see §3.3.4). That is to say, during the indentation normal to the intended crystal facet, the deformation along other orientations also take effect in resisting the penetration of the indenter.[88] Additionally, the contribution from other crystallographic orientations may be considerable because of the

predicted atomic-scale 'trampoline-like' deformation and the Cu paddle-wheel dynamics of HKUST-1 (phonons).[8]

However, as indicated by the P/S^2 slope line in Figure 8.5c, in the AFM-based nanoindentation, severe creep and fracture (without excluding the other interfering factors) lead to the appreciable overestimation of the Young's modulus (see Figure 8.7b). With the increasing unloading strain rate ($\dot{\varepsilon}$), the Young's moduli measured begin to converge. Nonetheless, the maximum unloading strain rate (up to 275 s^{-1}) was limited by the piezoelectric element of the AFM instrument, and thus the resulting *P-h* curves, were still slightly distorted. Given that the upper segment of the unloading process, *viz.* subsequent to the peak load, is more susceptible to the interfering factors, in this chapter, two methods were explored wherein the lower segment of the unloading curves was analysed instead of the initial segment. For the lower segment at unloading, adhesive force becomes more significant while approaching the indenter-to-surface detachment. With this in mind, the lower segment was divided into two stages: the first unloading stage until the load reaches a zero value (i.e. region #1 in the inset of Figure 8.9b), and the second unloading stage until the adhesive force becomes the most negative value (corresponding to the pull-off force, $P_{\text{pull-off}}$, see region #2 in the Figure 8.9b inset).

8.6 Implementation of the Adhesion Models for Improved Analysis of the Young's Modulus

The first method is an empirical approximation of the Maguis-Dugdale (MD) analytical model[301] developed by Carpick, Ogletree, and Salmeron (COS method)[239] and subsequently improved by Piétrement and Troyon (PT method).[303] Due to the direct correlation between the contact stiffness and the adhesion energy, the PT method has been

implemented in this chapter. The PT method mainly analyses the range of an unloading curve from its lower segment to the $P_{\text{pull-off}}$ point (see Figure 8.9b).

The second method is a numerical simulation method, which markedly extends the applicability of the indenter-to-sample systems of interest by discretising the interplay between the indenter and the sample into tessellation. This method circumvents the limitation of many analytical methods that are only applicable to indenters of particular geometries (see §3.5 and §4.7).

Details regarding the two methods are elucidated in Chapter 4.

8.6.1 Selection Criterion of the Analytical Models

By applying the empirical approximation (the PT method, see §4.7.7) of the analytical method (the MD method, see §3.5.5) to the AFM nanoindentation data (see the curve fitting results in Figure 8.9b), the relationship between the normalised force ($\overline{P}$) and the two adhesion parameters (λ and μ) for the two HKUST-1 facets has been obtained. Careful inspection of Figure 8.8 reveals that although the majority of λ for HKUST-1 situates at the MD zone, it still widely extends to the JKR zone. This is evidenced from the potential field reconstructed by the numerical simulation in Figure 8.10 (see §8.6.2), where the adhesive force outside the contact periphery has been neglected and the elastic stresses that are reflected by the potential field tend to be infinite at the contact periphery. On the contrary, the Derjaguin-Muller-Toporov (DMT) model[298] takes the interaction forces outside the contact area into account. Therefore, the observation of λ closer to the JKR zone suggests the HKUST-1 framework is relatively compliant and has the short-range interaction with the indenter comparing with materials of λ at the DMT zone. The wide span of the value of λ can be ascribed to the variance of the localised interaction between the HKUST-1

framework and the indenter since the framework has nanoscale porosity as presented in Figure 8.1.

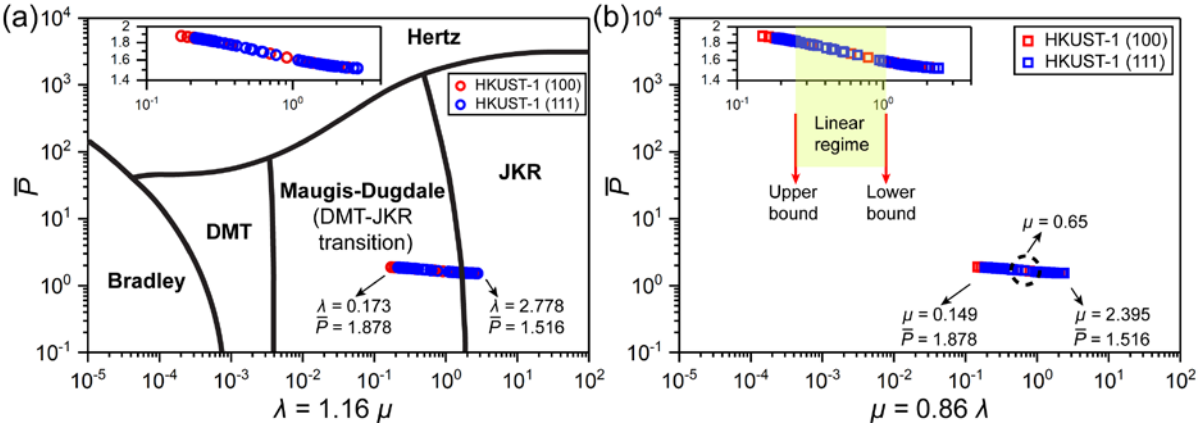

Figure 8.8 The adhesion map: the normalised force ($\overline{P}$) as a function of the (a) elasticity parameter (λ) and (b) Tabor parameter (μ).[300, 320] The relations of the three parameters are shown in equations (4.40) and (4.41) of Chapter 4. The adhesion property of HKUST-1 along the [100]- and [111]-axes situated at the Maugis-Daugdale (MD) zone and are closer to the JKR zone. The segmentation of the adhesion map in (a) was adapted from Ref. [320] (see §3.5.5 for more details).

In this chapter, the PT method was not only used for calculating the mechanical properties, but also was employed to calculate the adhesion property of HKUST-1, and thus the Tabor parameter (μ) obtained in the PT method was imported into the numerical simulation discussed later. Interestingly, it was found that the arithmetic median μ of the linear portion (highlighted in Figure 8b) of the data string in the logarithmic plot of $\overline{P}$ versus μ was the value that reflects the adhesive behaviour of HKUST-1. Given this finding, a new method is proposed to determine μ of porous materials. In this method, the relationship between $\overline{P}$ and μ within the linear regime can be defined as:

$$s' = \frac{\log \frac{\overline{P}_{\text{lower\_bound}}}{\overline{P}_{\text{upper\_bound}}}}{\log \frac{\mu_{\text{lower\_bound}}}{\mu_{\text{upper\_bound}}}} \tag{8.2}$$

where s' is the constant slope of the linear regime marked out in Figure 8.8b.

As a consequence, the value of μ was determined to be 0.6528 (derived by taking the median magnitude of the lower bound 0.2696 and the upper bound 1.0360 which define the boundaries of the linear regime). $\mu \approx 0.65$ has also been demonstrated by the numerical simulation which gives the Young's moduli of the two HKUST-1 facets in good agreement with the DFT calculations in Ref. [8] (see §8.6.3).

8.6.2 Numerical Simulation Method

In the numerical simulation, the relationship between $\overline{P}$ and $\overline{h}$ in the adhesion-dominated region (i.e. negative resultant force) for materials of different μ is shown in Figure 8.9a. Unlike the PT method, which requires the input of both the unloading curve regimes #1 and #2 for curve fitting purposes (see Figure 8.6b), only two parameters from the AFM-based nanoindentation data are required in the numerical simulation, they are: the pull-off adhesive force ($P_{\text{pull-off}}$) and the indenter-to-sample separation distance ($\Delta\alpha$, in this chapter, it is also called the stretch displacement).

The evolution of the normalised force fields between the cube-corner indenter and the sample surface (whose Tabor parameter, $\mu \approx 0.65$) were derived using the numerical simulation method (see Figure 8.10). More details are covered in 4.7.6 of Chapter 4.

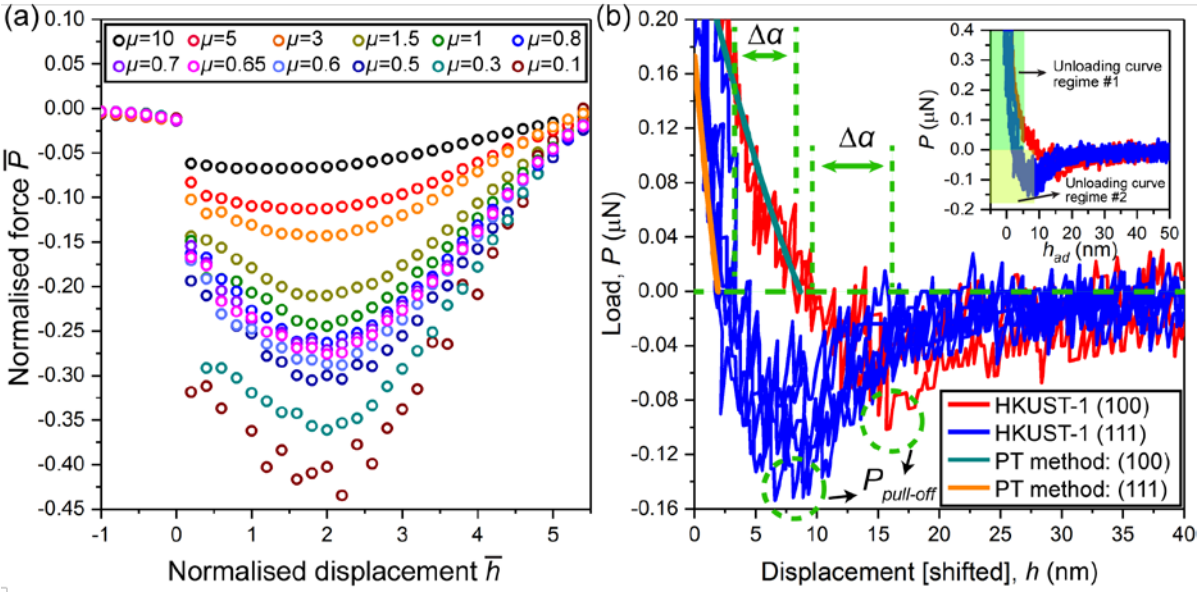

Figure 8.9 (a) The normalised force ($\overline{P}$) as a function of the normalised depth ($\overline{h}$) at the unloading stage in the numerical simulation method for the cube-corner indenter while the indenter-to-sample interaction force becomes negative (when adhesive force is dominant). The adhesive force is material-dependent varying with the different adhesion properties, and thus the $\overline{P}$-$\overline{h}$ curves were explored using a range of Tabor parameters (μ) where $\mu \approx 0.65$ were determined for HKUST-1 using the PT method. (b) Representative unloading curves (focusing on the lower segment, *viz.* unacted on the aforementioned interfering factors in §3.4) for both crystallographic facets. The indenter-to-sample separations ($\Delta\alpha$) from the point where the resultant force equals to zero to the point where the force reaches its minimum magnitude ($P_{\text{pull-off}}$). Superimposed on the data are the fitted curves for both facets obtained by using the PT method.

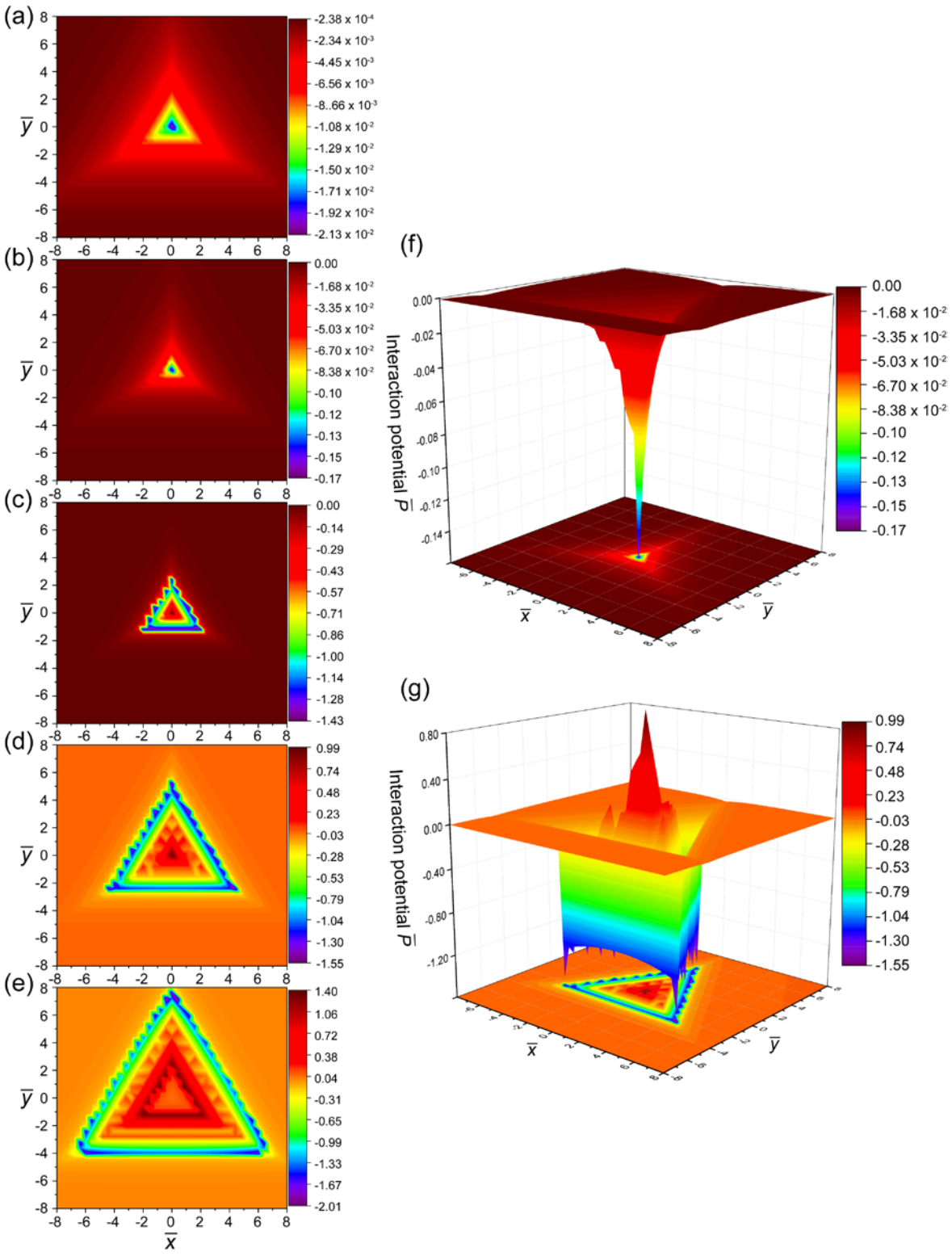

Figure 8.10 The normalised force ($\overline{P}$) distribution map of the interaction between a cube-corner indenter and a planar sample surface in the dimensionless numerical simulation domain [–8 8] × [–8 8]. Selected normalised force distribution maps at certain normalised indentation depth ($\overline{h}$): (a) $\overline{h}$ = –2, (b, f) $\overline{h}$ = –1, (c) $\overline{h}$ = 0, (d, g) $\overline{h}$ = 1, (e) $\overline{h}$ = 2. Negative interaction potential indicates the adhesive force dominates over the resultant force (combination of the adhesive force and the repulsive force).

8.6.3 Young's Modulus Determined by Applying the Adhesion Models

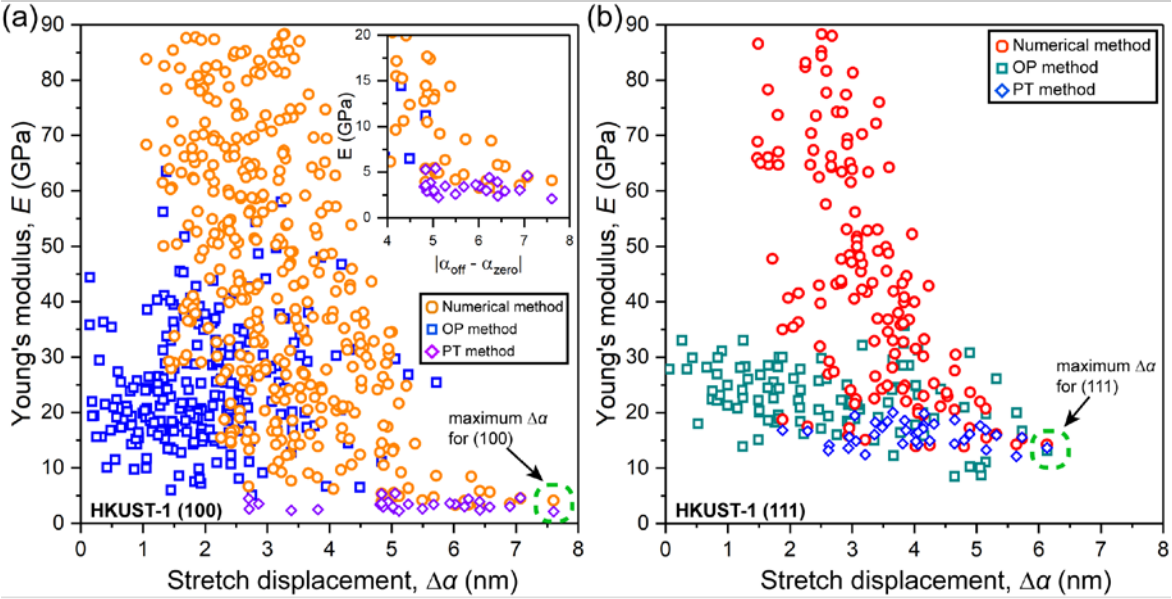

Figure 8.11 Young's modulus (E) versus stretch displacement ($\Delta\alpha = |\alpha_{off} - \alpha_{zero}|$) data were derived from the three different methods, they are: the Oliver and Pharr (OP) method, the PT method, and the numerical simulation method for HKUST-1 on (a) the {100}-oriented facet and (b) the {111}-oriented facet.

In Figure 8.11, it is obvious that the Young's modulus (E) obtained from the OP method is not in connection with the stretch displacement ($\Delta\alpha$) since the OP method concentrates on the incipient segment of the unloading curves rather than the lower segment. In contrast, the Young's moduli of both HKUST-1 facets measured using the numerical simulation method converge to $E_{[100]}$ ~ 4.08 GPa and $E_{[111]}$ ~ 14.28 GPa as the stretch displacement increases. The measured Young's moduli using the PT method has an excellent agreement with the one from the numerical simulation as shown in Figure 8.11. The minor discrepancy between the Young's moduli from the AFM-based nanoindentation and the DFT calculations in Ref. [8] (where $E_{[100]}$ ~ 2.96 GPa and $E_{[111]}$ ~ 15.15 GPa) may be attributed to the temperature effects (0 K DFT vs. 300 K experiments).[125] As one may notice that in the numerical simulation method, the Young's moduli can be easily overestimated when the stretch displacement is relatively small, and this is on account of the

interference of oscillation noise when the unloading curves have a small stretch displacement.

8.7 Anisotropy and Auxeticity

By virtue of its superior force and displacement sensitivity, AFM nanoindentation is very appropriate for the exploration of the nanoscale behaviour of MOFs. Conversely, the measured material properties from IIT literally average out the total properties at a larger area (micrometre lengthscale), this could be the reason why the auxetic deformation on the inorganic-organic-inorganic linkages cannot be accurately probed by IIT.

Herein, the AFM nanoindentation data suggest that the auxeticity of HKUST-1 might have played a role at the nanoscale, especially on the [110]-oriented plane, which has an apparent influence on the AFM nanoindentation along the [100]- and [111]-axes. As shown in Figure 8.1d, the {110}-oriented facet forms angles with the [100]- and {111}-oriented facets of 45^{o} and $\sim 35^{o}$, based on which the counter-acting deformation (*d*), namely the resistance from the (110) orientation, can be resolved into the deformations along the other two crystallographic axes of indentation, i.e. [100]- and [111]-axes. As shown in Figure 8.1d, the resistance (in the form of the counter-acting deformation) from the {110}-oriented facet to the indentation perpendicular to the {100}-oriented facet is weaker than to the {111}-oriented facet. This phenomenon explains the more abrupt reduction of hardness measured of the facet (100) than the facet (111) (see the inset in Figure 8.6b).

Although in theory, the Young's moduli of materials along specific orientations of opposite Poisson's ratio (i.e. the same absolute value but different signs) should be the same, the plastic deformation and failure mechanisms of the MOF linkages under stress are usually different because the linkage bends in the opposite directions.

8.8 Nanoscale Tensile Test

8.8.1 Surface Detachment and Splitting Fracture

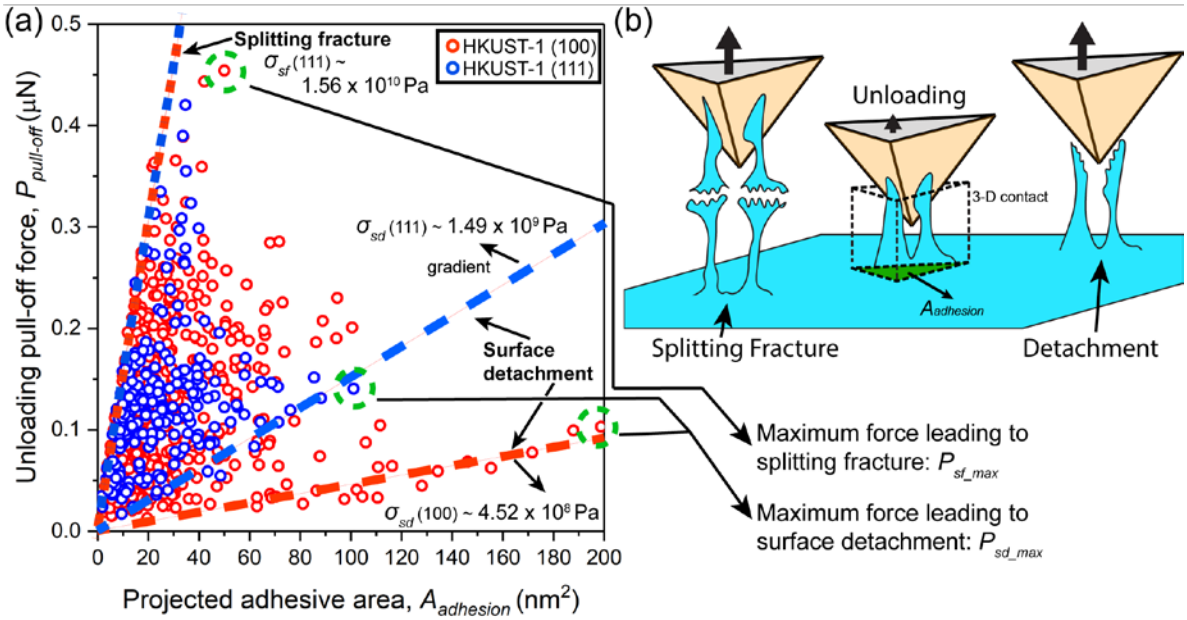

Figure 8.12 (a) Unloading adhesion pull-off force ($P_{\text{pull-off}}$) as a function of the projected adhesive area (A_{adhesion}). (b) Schematic illustrating the two distinctive tensile detachment modes: surface detachment and splitting fracture. Note that in reality, the contact between the stretched portion of the material and the indenter should be in 3-D as the triangular prism enclosed by the dashed lines.

The stretching displacement originates from the point where the resultant force drops down to zero and ends at the point when the most negative force (i.e. the pull-off force) emerges, namely the unloading curve regime #2 in Figure 8.9b. Within this regime, the adhesive forces dominate and they are produced by the composite forces, which are the sum of the van der Waals forces and the forces from stretching part of the sample adhering to the indenter. Therefore, after exceeding the pull-off force, the HKUST-1 framework adhering to the indenter surface starts to detach. Regarding the detachment, two forms of detachment are proposed here: surface detachment and splitting fracture (see Figure 8.12b). The stretch of the material can be treated as the tensile forces of infinite numbers of columns integrated over the projected area (A_{adhesion}) wherein the adhesion takes effect. In Figure 8.12a, two

distinct bounds were detected, which can be regarded as the states of sole surface detachment and sole splitting fracture, respectively. In addition, within the two bounds, the combined effect of both contributes to the detachment, *viz.* the degradation of the adhesion effect. In essence, the pure splitting fracture (at the higher bound) resembles a tensile test at the nanoscale, where the engineering stress resulting from the splitting fracture (σ_{sf}) was determined as $\sim 1.56 \times 10^{10}$ Pa. Similarly, the surface detachment stresses (σ_{sd}) is $\sim 4.52 \times 10^{8}$ Pa for the {100}-oriented facet and $\sim 1.49 \times 10^{9}$ Pa for the {111}-oriented facet (see Figure 8.12a). Furthermore, it was found that the maxima of the stretch displacement ($\Delta\alpha$), which equal to 7.60 nm for the {100}-oriented facet and 6.13 nm for the {111}-oriented facet. In principle, full detachment can occur at any points of $\Delta\alpha \leq \Delta\alpha_{max}$ due to the nanoporous nature of HKUST-1, however, the indenter does not detach from the material if the stretch displacement is too small as shown in Figure 8.11. It is worth noting that the maxima of the stretch displacement may also be unloading rate dependent. Nevertheless, as shown in the equation (3.7) and (3.11) of Chapter 3, even for materials of Tabor parameters (μ) in either the DMT or the JKR zones, the pull-off adhesive force and the stretch displacement are fixed for each of the indenter-to-sample system.

8.8.2 Adhesive Force and Adhesion Energy

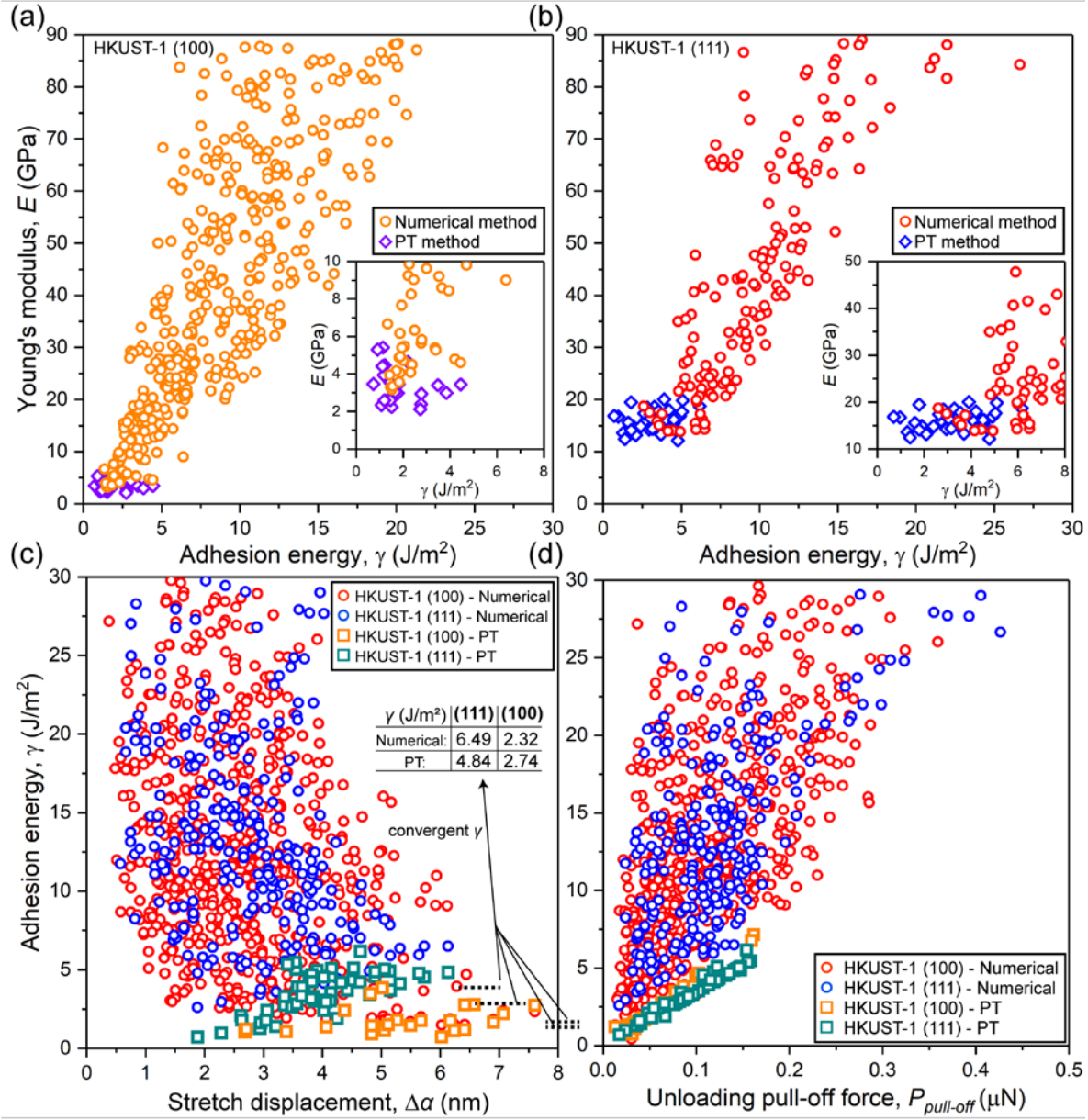

Figure 8.13 The Young's modulus (E) versus the adhesion energy (γ) obtained from AFM nanoindentation on the two crystallographic facets (a) (100) and (b) (111). (c) The adhesion energy declines before converging as the stretch displacement increases. (d) The correlation between the adhesion energy and the adhesive force was acquired using the numerical simulation method and the PT method.

In fact, the adhesion energy (γ) is fundamentally the tensile forces integrated over the projected area (A_{adhesion}) and then over the stretch displacement ($\Delta\alpha$). As shown in the table of Figure 8.13c, the average adhesion energy can be determined.

To gain a better understanding of the adhesion effect on the measurement of the elastic properties, the correlation between the Young's modulus (E) and the adhesion energy (γ) has been investigated (see Figure 8.13a-b). From the standpoints of γ and $P_{\text{pull-off}}$, it was found that almost all accurate measurements of E were taken when γ and $P_{\text{pull-off}}$ were small, namely: $\gamma \lesssim 3.84$ J/m^2 for facet (100); $\gamma \lesssim 6.17$ J/m^2 for facet (111); and $P_{\text{pull-off}} \lesssim 0.16$ μN for both facets. Therefore, small $P_{\text{pull-off}}$ is desired for accurate measurement of E, and this suggests that it requires the unloading process, at which only the surface detachment occurs since the values of $P_{\text{pull-off}}$ leading to the two detachment modes have already been characterised in Figure 8.12 ($P_{\text{sd\_max}} < P_{\text{sf\_max}}$). This conclusion is also well supported by the definition of the Lennard-Jones potential, which is one of the important basis of the numerical simulation.

8.9 Nanoscale Failure Modes

8.9.1 Identification of Failure Modes

The AFM-based nanoindentation has also been extended to characterise the mechanical failure mechanisms of HKUST-1. In this chapter, four distinctive failure modes during the loading stage will be considered, together with the abnormal pop-out phenomenon throughout the unloading stage (see Figure 8.14). The four failure modes are: Mode I – slippage along the aligned pores; Mode II – fracture the crystalline structure; Mode III – accumulated densification; and Mode IV – continuous buckling of bonds along the indentation direction. A schematic of a *P-h* curve distorted by different failure modes are depicted in Figure 8.14a together with a number of representative *P-h* curves from the AFM-based nanoindentation in Figure 8.14b-c. These failure modes could result in the reductions of the Young's modulus and hardness measured by the indentation experiments.

Furthermore, the threshold forces for Mode I and II, and the pop-out have been determined as shown in Figure 8.15a-c, respectively.

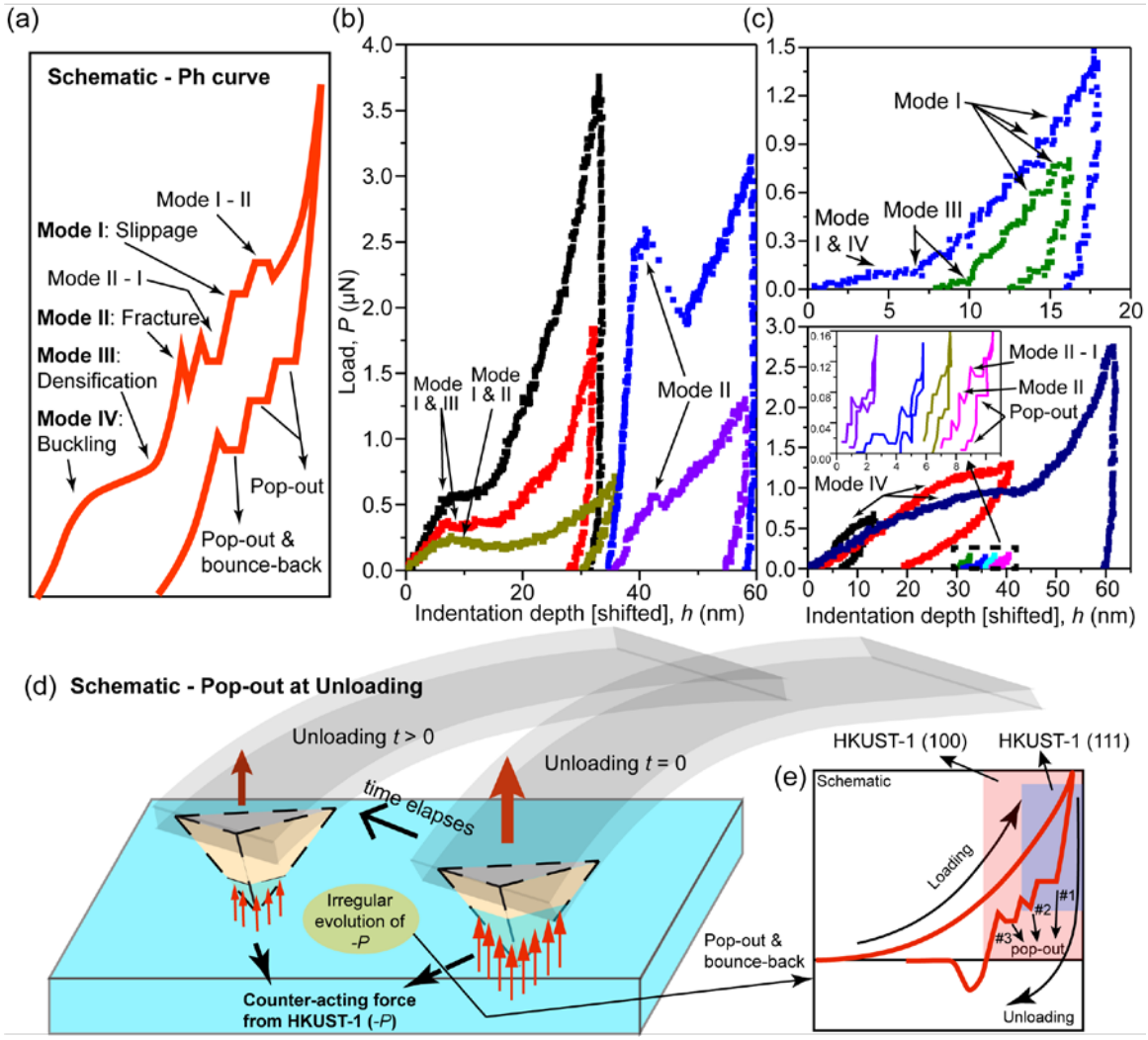

Figure 8.14 (a) Schematic showing the four failure modes incorporating their features in a *P-h* curve. (b-c) AFM-based nanoindentation on HKUST-1 crystals inducing four distinctive failure modes, which are reflected by the abnormal *P-h* curves. Mode I – slippage aligned with the channel of framework porosity; Mode II – structural fracture; Mode III – densification of the framework; Mode IV – continuous buckling of the organic ligament but without complete pore collapse. And the irregular unloading recovery in the form of pop-out detected by AFM nanoindentation. (d) Schematic introducing the force analysis to elucidate the mechanism of pop-out. (e) Schematic of a typical *P-h* curve with the three different pop-out phenomena marked (#1, #2, #3, they were observed in the AFM nanoindentation experiment), and the extent of pop-out detected on the two HKUST-1 facets are highlighted.

8.9.2 Statistical Analysis of the Failure Modes

Statistical analysis was used to examine the occurrence of the failure modes discovered in the AFM-based nanoindentation experiments, the probability of the *P-h* curves showing the failure modes I, II, III, IV, and the pop-out are 12.3%, 11.8%, 4.1%, 20.9%, and 11.6% for the {100}-orientated facet; and 13.3%, 12.0%, 3.0%, 8.6%, and 12.0% for the {111}-oriented facet. Because of the high force and displacement sensitivity of AFM (hence much localised properties were detected), the accurate identification of the contact point on the HKUST-1 porous framework is important to pinpoint the occurrence of every failure mode. In other words, there are certain level of uncertainties associated with the abovementioned probabilities. In light of the above percentages derived from as many as 846 indentations, the following observations and trends can be drawn: the occurrence probabilities of the slippage and fracture (Mode I and II) failures are nearly the same, meanwhile, approximate to the value of the pop-out during the unloading stage. This is in an excellent accordance with the observations made on the layered CuBDC nanosheets in Chapter 7, in which the pop-out is a form of recovery at the opposite direction of the slippage and fracture failures. Moreover, the continuous buckling of bonds (Mode IV) happened much more frequently on the {100}-oriented facet than on the {111}-oriented facet. This is well supported by the plots of failure stress in Figure 8.15d-e wherein it is observed that the Mode IV failure is active throughout the full extent of indentation depth on the {100}-oriented facet, while in contrast, its occurrence was confined to a limited range of stresses and depths while indenting on the {111}-oriented facet.

A force analysis has been conducted to gain a better understanding of the mechanism of the pop-out phenomenon observed during the unloading stage. If the indenter is unloaded smoothly, that is to say, the counter-acting force exerted on the indenter tip is steadily being reduced, there would be no pop-out. As shown in Figure 8.14d, the evolution of the

interaction force between the indenter and the porous HKUST-1 framework may not be coherent due to the randomly triggered framework bounce-back event, which will instantaneously maintain (pop-out #1 in Figure 8.14e) or even increase (pop-out #2) the force acting on the indenter tip. Furthermore, the combination of the pop-out #1 followed by #2, which forms the third pop-out mode #3, has also been observed.

8.9.3 Fracture Strengths and Threshold Forces

The threshold forces leading to Mode I and II during the loading stage as well as the pop-out during the unloading stage have been plotted against the corresponding threshold displacements in Figure 8.15a-c. Figure 8.15a shows that the pop-out distortion only arises at the early part of the unloading curve while indenting on the {111}-oriented facet (also highlighted in Figure 8.14e) but in contrast, the entire unloading process on the {100}-oriented facet can be susceptible to pop-out. In terms of Mode I and II, it was found the unit threshold force (P_{unit}) and the unit indentation depth (i.e. displacement h_{unit}), are responsible for the slippage and fracture failures. By proportionally augmenting P_{unit} and h_{unit}, in other words, the stressed area of the framework that is perpendicular to the indentation direction is assumed to be constant (the extreme condition), the lines in Figure 8.15b-c were drawn and defined the bounds of the relative correlation between $P_{\text{threshold}}$ and $h_{\text{threshold}}$. The unit threshold depths (h_{unit}), unit threshold forces (P_{unit}), and the corresponding unit threshold stress are summarised in Table 8.1. Clearly, with the increasing indentation depth, the area of the framework stressed actually spreads rapidly and this is the reason for the dispersion of the data points in Figure 8.15b-c.

Table 8.1 (left) Unit threshold indentation depths (h_{unit}) and corresponding unit threshold forces (P_{unit}) for the two oriented facets, which results in slippage and fracture failures. The upper and lower bounds together with the intermediate regime are indicated in Figure 8.15b-c. The corresponding stress (σ_{unit}) based on the projected indenter-to-sample area is also presented. (right) The dimensions of a unit cell along different crystallographic axes (corresponding to the vertical markers in Figure 8.1).

		HKUST-1 (100)			HKUST-1 (111)		
		h_{unit} (Å)	P_{unit} (nN)	σ_{unit} (GPa)	h_{unit} (Å)	P_{unit} (nN)	σ_{unit} (GPa)
Mode I - Slippage	Upper bound	1.6	30.9	449.2	0.9	13.6	624.8
	Intermediate regime	4.1	28.4	62.9	6.5	43.6	38.4
	Lower bound	10.7	25.1	8.2	4.9	15.6	24.2
Mode II - Fracture	Upper bound	1.6	21.5	312.5	1.7	23.4	301.3
	Intermediate regime	5.8	33.3	36.8	5.8	35.4	39.2
	Lower bound	18.0	25.0	2.9	14.2	31.9	5.9

	(100) h_{cell} (Å)	(111) h_{cell} (Å)
Top view	13.2	10.6
Side view	13.2	15.3

Reversely, by tracing back to the shallowest indentations, the converged smallest volume (based on which the upper bound Figure 8.15b-c was defined) and the largest volume (lower bound) have been determined. In fact, they are the stressed HKUST-1 framework at the scale of its unit cell but exhibiting two stages of Mode I or Mode II failures under the imposed indentation stress (designated as unit threshold stress, σ_{unit}). The threshold depths at the lower bound are marked as the vertical markers #1 and #2 on the crystallographic images (see Figure 8.1a-b). Note that the failure threshold depth defined by the upper bound scale (see Table 8.1), which accounts for only 5.88%−12.12% of the height of a unit cell (nearly invisible in Figure 8.1), is not marked out accordingly. Hereto, the current analysis suggests that failure at such a small length scale must have initiated from the rupturing of the Cu−BTC−Cu linkages, found at the molecular level.

It can be seen in Table 8.1, the unit cell of HKUST-1 along the [111]-axis is far more resistant to both slippage and fracture failures since it can withstand a higher stress. More intriguing, it was found that a relatively lower stress was needed to incur the fracture failure than the slippage failure. This finding cannot be detected at larger scales since by close

inspection of Figure 8.15d-e, it is evident that the stresses that induce the slippage, as a whole, are very close to the ones triggering the fracture of the HKUST-1 framework. Therefore, for the first time, the effects of anisotropy and propensity to failure of HKUST-1 have been interpreted at the scale of its unit cell.

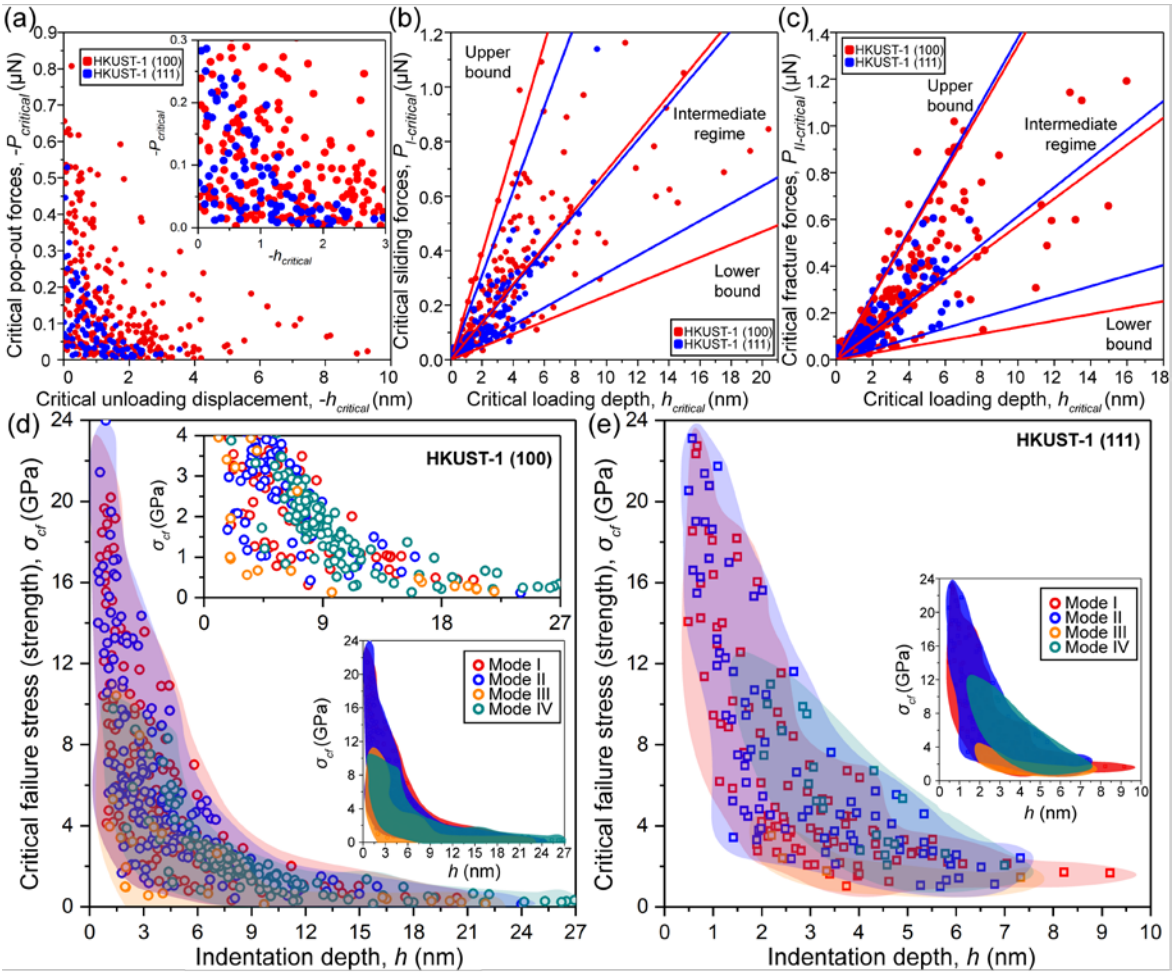

Figure 8.15 (a) Threshold forces that activate the pop-out recovery as a function of the unloading displacement (starting from the maximum indentation load). (b-c) Threshold forces generate the slippage and the fracture failures, respectively. The lines at the upper and lower bounds define the extremes of the loading conditions which produce the two failure modes. The definition of the lines is explained in Table 8.1. (d-e) The corresponding stresses of the four distinct failure modes. The failure maps of the failure modes are plotted accordingly.

Throughout the indentation depth, all of the four failure modes could occur at relatively shallow depth during the indentation on the {100}-oriented facet. Whereas for the indentation on the {111}-oriented facet, the slippage (Mode I) and fracture (Mode II) happened only if the indenter penetrates deeper than 0.50 nm (the corresponding true contact area, A, and project contact area, $A_{projected}$, are 1.15 nm^2 and 0.67 nm^2), which approximate to the span of an unit cell (one pore) shown in the left image of Figure 8.1b and the unit threshold depth is approximately one third of the thickness of the repetitive unit layer marked in the right image of Figure 8.1b. This suggests the indentations which approach the surface aiming at the centre of a pore not only collapse the pore, but also cause the breakage of the benzene ring underneath resulting in the sliding all the way down along the channel where the benzene rings are aligned. Moreover, for the penetration of the indenter along the [111]-axes, the accumulated densification (Mode III) and the continuous buckling of bonds (Mode IV) start to prominently show up after indenting more than 2 nm deep into the framework.

Interestingly, for both {100}- and {111}-oriented facets, it was found that the threshold stresses producing the Mode III and IV failures are limited to 12 GPa, which is the maximum stress that the densified framework can bear during the occurrence of Mode III. One exception is that the maximum threshold stress for {111}-oriented facet is ~66.08% lower than the one for {100}-oriented facet. This is not surprising because, for indentation along the [111]-axis, the maximum stress concentrates below the indenter apex (i.e. align with the indentation direction) which preferentially leads to the Mode I and II, while for indentation along the [100]-axis, the maximum stresses are situated sideways (see the simulated stress fields in the FE model in Figure 8.4a-b). According to Figure 8.15, for Mode IV, once past the maximum stress, the framework starts to collapse following the buckling of bonds.

8.10 Summary of the Chapter

In summary, a reliable and systematic approach has been developed to quantify the anisotropic elastic properties, adhesion properties, and failure modes of HKUST-1 at the nanoscale. A series of important nanomechanical properties have been quantified employing both the instrumented indentation technique (IIT) and the AFM-based nanoindentation experiments. The results are summarised as follows:

- The nanomechanical properties of HKUST-1 quantified in this study include the Young's modulus, hardness, adhesion energy, adhesive force, indenter-to-sample interaction force field, and the failure modes of the HKUST-1 framework bridging multiple length scales (in the range from the unit cell size to 27 nm).

- The failure modes during the indenter loading stage are classified as Modes I-IV: the slippage along the aligned porosity channels, fracture of the porous framework, densification of the porous framework, and buckling of the Cu-BTC-Cu coordination linkages. The threshold stress of each mode has been determined.

- Framework recovery can give rise to the pop-out effect has been characterised.

- The concept of the nanoscale tensile test is proposed to quantify the material adhesive behaviour. In this test, the tensile force can be exerted by the unloading AFM indenter tip withdrawing from the sample surface.

- More importantly, this work sheds light on the influence of the elastic anisotropy along the [100]- and [111]-axes and the directional auxeticity (*viz.* negative Poisson's ratio) on the [110]-axis, on the mechanical behaviour of HKUST-1.

Chapter 9: Conclusions and Future Work

In the chapter, important conclusions have been drawn in the following three aspects: (a) significance of the nanoscale mechanical studies of MOF materials; (b) collection of the nanomechanical properties characterised in my research; (c) future research work. In summary, the main achievement described in the thesis is the establishment of a novel nanoindentation technique based on the atomic force microscopy (AFM) along with the systematic guidance encompassing procedures from the instrument calibration and implementation, synthesis of the porous metal-organic framework (MOF) nanomaterials, to the processing and analysis of the experimental data. In the thesis, three representative MOF materials have been selected because they exhibit distinctive structural features, respectively on behalf of the porous crystalline structures of low elastic anisotropy, crystalline nanosheets, and crystalline structures of high anisotropy and auxeticity. Overall, the nanoscale mechanical properties quantified in this thesis are classified into four categories: elasticity, plasticity, adhesion, and failure modes. For each category, the primary nanoscale properties measured herein are: Young's modulus for elasticity; hardness, yield stress, ultimate strength, and work hardening coefficient for plasticity; adhesive force and energy; and threshold forces, threshold indentation depths, and strengths of the failure modes.

9.1 Significance of the Nanoscale Mechanical Studies of Metal-Organic Framework (MOF) Materials

- Accurately quantifying nanoscale mechanical properties of metal-organic frameworks (MOFs) is challenging because of the complicated deformation of the multidentate inorganic-organic-inorganic linkages. Due to self-similarity nature of MOF structures, mechanical properties at the scale close to the size of unit lattice are important. Robust porosity in MOFs determines their performance and durability in encapsulating guest molecules and maintaining accessible channels or active sites.
- The three model MOF systems studied are: nanocrystals (<500 nm) and micron-sized crystals (~1 to 2 μm) of ZIF-8; nanosheets (thickness of the thinnest one t ~ 2 nm, about two monolayers) and nanosheet stacks (t ~ 4 to 400 nm) of CuBDC; submillimetre-sized crystals of HKUST-1 (≥300 μm).

- Atomic force microscope (AFM) possesses high force (<0.05 nN) and displacement (≲0.05 nm) sensitivities, which make it the optimal candidate to physically stress the MOF nanostructures and then extracting nanoscale mechanical responses.

9.2 Nanoscale Mechanical Properties Characterised

- Elasticity: effective modulus (E_{eff}) and Young's modulus (E)

  By using the Oliver and Pharr method to analyse the force-displacement data from AFM nanoindentation, I have measured the Young's moduli of ZIF-8 crystals (including the polycrystalline thin film of nanocrystals and the individual micron-sized crystals with the {110}-oriented facet indented), CuBDC nanosheets along the $\{\bar{2}01\}$-oriented facet, and HKUST-1 crystals on the {100}- and {111}-oriented facets: E ~3.0–4.0, ~22.9, and ~4.08 and ~14.28 (in GPa), respectively. The Poisson's ratio (v) of ZIF-8 was taken as 0.4 according to Ref. [7]. While for the CuBDC nanosheets, v is also assumed to be 0.4 since its effect on the measurement of E has been demonstrated to be negligible. With regard to the HKUST-1 crystals, v is assumed to be zero to circumvent the effect of compressibility so as to concentrate on the elastic anisotropy.

  For the AFM nanoindentation experiments on the polycrystalline thin film of ZIF-8 nanocrystals and CuBDC nanosheets, high unloading strain rate (>60 s^{-1} for ZIF-8 and >140 s^{-1} for CuBDC) were imposed to minimise the interfering effects of the time-dependent creep and thermal drift as well as the influence of the structural failure and fracture of crystalline framework, which could cause erroneously deviations on the measurement of E. While for the HKUST-1 crystals, whose E was derived from the lower portions of the unloading curves that have little correlation with the unloading strain rate but are highly dependent on the adhesive forces.

- Plasticity: hardness (H), yield stress (σ_y), ultimate strength (σ_u), and work hardening coefficient (n)

  After considering a series of factors (§3.4) that may introduce errors in the mechanical property measurement, the hardness of ZIF-8, CuBDC, and HKUST-1 was measured: ~500 MPa for ZIF-8, ~2000 MPa for CuBDC, and ~463 MPa for the {100}-oriented facet and ~491 MPa for the {111}-oriented facet of HKUST-1. The hardness of ZIF-8 measured by AFM nanoindentation is in a good agreement with the value acquired from the instrumented indentation technique (IIT) in Ref. [45] wherein the loading force (~6 mN) was more than three orders of magnitude times and the indentation depth (~1 μm) was about 100 times of the ones applied by the AFM instrument.

  For ZIF-8 and HKUST-1, the hardness was obtained according to its definition: $H = P_{max}/A_{contact}$. The difference is that the hardness of HKUST-1 was adopted from the IIT result because the relatively blunt Berkovich indenter in the IIT avoided the excessive crystal failures. While for ZIF-8, it was not possible to impose the IIT indentation on such small crystals thus tested by AFM nanoindentation. The exception is the CuBDC nanosheet, whose hardness was calculated according to its yield stress since the contact area characterised in the experiment was not accurate owing to the interfacial movement.

  Furthermore, the work hardening coefficient (n = 0.17275) of CuBDC was obtained based on the pile-up height of the indents from AFM nanoindentation. And the yield stress (σ_y ~448 MPa) and ultimate strength (σ_u ~674 MPa) of CuBDC were estimated using the developed iteration method.

- Adhesion: adhesive force (P_{ad}) and work of adhesion (γ)

  The precise magnitudes of the adhesive force and work of adhesion are normally dependent on the local nature of the indenter-to-surface contact. By using the adhesion model based on the Sneddon method (§4.7.1), it was found the work of adhesion between the cube-corner indenter tip and the micron-sized crystals of ZIF-8 broadly ranging from 0.42 to 3.31 J/m^2 (as a reference, the value calculated by DFT is ~0.28 J/m^2 in Ref. [71]). In comparison with ZIF-8, the adhesion methods (both the analytical method in §4.7.7 and the numerical method in §4.7.6) for deriving the mechanical properties of HKUST-1 were directly involved the adhesive force and work of adhesion. The adhesive forces on the (100) and (111) planes were measured in the range of 47.71 nN to 158.55 nN, in addition, the work of adhesion ranges from 1.65 J/m^2 to 6.17 J/m^2 (more specific values for each crystallographic facet are available in Chapter 8).

- Failure mechanisms: distinctive failure modes, corresponding threshold forces and threshold indentation depths resulting in these failures, as well as strengths to resist the occurrences of these failure modes have been summarise in Table 9.1.

Table 9.1 Failure modes of the ZIF-8 crystals, CuBDC sheets, and HKUST-1 crystals.

	Phase	Size (μm)	Orient-ation	Failure Modes					
				Loading				Unloading	
				I*	II*	III*	IV*		
ZIF-8	Nano-crystal	$l < 0.5$	(100) and (110)	S^1	F^1	D^1	B^1		
	Micron-crystal	$l \in [1\ 2]$	(110)	S^2	F^2	D^2	B^2		
CuBDC	Nano-sheet	$t \in [0.002\ 0.4]$	$(\bar{2}01)$	S^3	F^3	D^3		P^3	R^3
HKUST-1	Submillimetre-crystal	$l \in [300\ 1500]$	(100)	S^4	F^4	D^4	B^4	P^4	P^4
			(111)	S^5	F^5	D^5	B^5	P^5	P^5

* For clarification purpose, failure modes of the ZIF-8 nanocrystals are designated to Mode A, B, C, and D accordingly (§6.3). Note that the letters S, F, D, B, P, and R are the initials of slippage, fracture, delamination, buckling, pop-out, and recovery, respectively. Details of the failure modes in the table are elucidated as follows.

Slippage[1]	Grain boundary (shear-induced) slippage happening at the grain boundary interface of adjacent polycrystals.
Slippage[2]	Sliding of the indenter along the aligned porosity of ZIF-8 crystals, and this is linked to the rupturing of the mIM organic linkages through shearing of the coordinated ZnN_4 clusters.
Slippage[3]	Sideward sliding of the nanosheets.
Slippage[4]	Slippage along the aligned porosity.
Slippage[5]	Breakage of the benzene ring underneath the indenter resulting in the sliding all the way down along the channel where the benzene rings align.
Fracture[1]	Polycrystalline fracture.
Fracture[2]	Buckling of the mIM organic linkages triggering pore collapse.
Fracture[3]	Snap/fracture of the nanosheets.
Fracture[4]	Buckling of the BTC organic linkages triggering pore collapse.
Fracture[5]	Ditto.
Delamination[3]	Detachment of the nanosheets from the layer underneath.
Densification[1]	Accumulated compaction of porous frameworks.
Densification[2]	Associated with the breakage of the ZnN_4−mIM−ZnN_4 coordination linkages, followed by the sequential pore collapse and material densification.
Densification[4]	Associated with the breakage of the Cu−BTC−Cu coordination linkages, followed by the sequential pore collapse and material densification.

Densification[5]	Ditto.
Buckling[1]	Continuous buckling of bonds along the indentation direction but without complete pore collapse.
Buckling[2]	Similar to Slippage[2], this is linked to the rupturing of the mIM organic linkages through shearing of the coordinated ZnN_4 clusters.
Buckling[4]	Related to the rupturing of the BTC organic linkages through shearing of the coordinated Cu nodes.
Buckling[5]	Ditto.
Pop-out[3]	As the indenter starts to unload, the nanosheets that were pushed away by the indenter at the loading stage recover together with the formation of new cohesive layers between the adjacent nanosheets. In the force analysis: the indenter-to-sample contact system is in a quasi-equilibrium state, i.e. increment of the interaction force ≈ decrement of the compressive force exerted by the surrounding material.
Pop-out[4]	Irregular relaxation of the Cu−BTC−Cu linkage since it is echoing the failure at loading, it tends to occur at the same levels of forces.
Pop-out[5]	Resembling Pop-out[4]. It is also called pop-out and bounce-back in the thesis because of the abrupt force uprising in the unloading *P-h* curve.
Recovery[3]	Ditto on Pop-out[3] except for the resultant force on the indenter is not in equilibrium over time, and increment of the interaction force >> decrement of the compressive force exerted by the surrounding material.

9.3 Future Work

- In this work, the AFM-based nanoindentation has primarily been applied to the MOF materials, whose stiffness and hardness are normally in the range of 1–30 GPa and 0.015–2.5 GPa, respectively.[38] Additional AFM-based nanoindentation with the employment of different AFM indenters whose cantilevers have different levels of spring constants will be implemented on a wider scope of materials from the much softer matters such as biological entities to the stiffer materials such as dense hybrids.
- The applicability of the nanoscale tensile test will be further evaluated by applying it to other materials. A more established technique is desired with the promise of its wider usage.
- The approaches herein for the characterisation of adhesion effect, adhesive force, and adhesion energy, will be applied to other nanomaterials, especially the soft ones such as hydrogels. The ultimate goal is to develop an approach which can be widely used in nanostructured materials whose adhesion properties cover the entire range of the Tabor parameter in the adhesion map (see Figure 8.8).
- AFM nanoindentation will be used to study other crystalline materials for the purpose of probing their failure mechanisms and furthermore, broadening the library of the nanoscale failure modes.
- Nanoscratch using the AFM probes will also be explored since the applied force is much lower than the instrumented scratch technique (see §6.4 in Chapter 6) and more importantly, it is envisaged that the MOF systems under lateral stresses would exhibit distinctive failure modes comparing with the ones studied using the AFM-based nanoindentation.

PUBLICATIONS

1. **Zeng, Z.**, Tan, J. C. AFM Nanoindentation to Quantify the Mechanical Properties of Nano- and Micron-Sized Crystals of a Metal-Organic Framework Material, *ACS Applied Materials & Interfaces*, **2017**, *9*, pp. 39839-39854.

2. **Zeng, Z.**, Flyagina, I., Tan, J. C. AFM Nanoindentation to Quantify the Nanoscale Mechanical Properties and Failure Modes of Thin Metal-Organic Framework Nanosheets, Manuscript in Preparation.

3. **Zeng, Z.**, Tan, J. C. AFM Nanoindentation to Quantify the Nanoscale Mechanical Properties, Adhesive Behaviour, and Failure Modes of the Auxetic Metal-Organic Frameworks: HKUST-1, Manuscript in Preparation.

4. Mukherjee, S. (co-first author), **Zeng, Z. (co-first author)**, Shirolkar, M.M., Samanta, P., Chaudhari, A. K., Tan J. C., and Ghosh, S. K. Self-assembled, Fluorine-rich Porous Organic Polymers: A Class of Mechanically Stiff and Hydrophobic Materials, *Chemistry – A European Journal*, **2018**, *24*, pp. 11771-11778.

5. Ehrenreich, M. (co-first author), **Zeng, Z. (co-first author)**, Burger, S., Warren, M., Gaultois, M.W., Tan, J.C., Kieslicha, G. Mechanical Properties of the Ferroelectric Metal-Free Perovskite [MDABCO](NH_4)I_3, *Chemical Communications*, **2019**, In Press.

6. Ryder, M. R., **Zeng, Z.**, Titov, K., Sun, Y., Mahdi, E. M., Flyagina, I., Bennett, T. D., Civalleri, B., Kelley, C. S., Frogley, M.D., Cinque, G., Tan J. C. Dielectric Properties of Zeolitic Imidazolate Frameworks in the Broad-Band Infrared Regime, *The Journal of Physical Chemistry Letters*, **2018**, *9*, pp. 2678-2684.

7. Tian, T., **Zeng, Z.**, Vulpe, D., Casco, M., Divitini, G., Midgley, P., Albero, J. S., Tan, J. C., Moghadam, P., Fairen-Jimenez, D. A Sol-Gel Monolithic Metal-Organic Framework with Enhanced Methane Uptake, *Nature Materials*, **2018**, *17*, pp. 174-179.

8. Titov, K., **Zeng, Z.**, Ryder, M. R., Chaudhari, A. K., Civalleri, B., Kelley, C. S., Frogley, M.D., Cinque, G., Tan J. C. Probing Dielectric Properties of Metal-Organic Frameworks: MIL-53(Al) as a Model System for Theoretical Predictions and Experimental Measurements via Synchrotron Far- and Mid-InfraRed Spectroscopy, *The Journal of Physical Chemistry Letters*, **2017**, *8*, pp. 5035-5040.

9. Mehta, J. P., Tian, T., **Zeng, Z.**, Divitini, G., Connolly, B. M., Midgley, P. A., Tan, J. C., Fairen-Jimenez, D., Wheatley, A. E. H. Sol-Gel Synthesis of Robust Metal-Organic Frameworks for Nanoparticle Encapsulation, *Advanced Functional Materials*, **2018**, *28*, p. 1705588.

REFERENCES

(1) Stock, N.; Biswas, S. Synthesis of Metal-Organic Frameworks (MOFs): Routes to Various MOF Topologies, Morphologies, and Composites. *Chem. Rev.* **2012**, *112*, pp. 933-969.

(2) Furukawa, H.; Cordova, K. E.; O'Keeffe, M.; Yaghi, O. M. The Chemistry and Applications of Metal-Organic Frameworks. *Science* **2013**, *341*, p. 1230444.

(3) Dey, C.; Kundu, T.; Biswal, B. P.; Mallick, A.; Banerjee, R. Crystalline Metal-Organic Frameworks (MOFs): Synthesis, Structure and Function. *Acta Crystallogr. B Struct. Sci. Cryst. Eng. Mater.* **2014**, *70*, pp. 3-10.

(4) Dang, S.; Zhu, Q. L.; Xu, Q. Nanomaterials Derived from Metal-Organic Frameworks. *Nat. Rev. Mater.* **2017**, *3*, p. 17075.

(5) Hu, Y. H.; Zhang, L. Hydrogen Storage in Metal-Organic Frameworks. *Adv. Mater.* **2010**, *22*, pp. 117-130.

(6) Allendorf, M. D.; Stavila, V. Crystal Engineering, Structure-Function Relationships, and the Future of Metal-Organic Frameworks. *CrystEngComm* **2015**, *17*, pp. 229-246.

(7) Tan, J. C.; Civalleri, B.; Lin, C. C.; Valenzano, L.; Galvelis, R.; Chen, P. F.; Bennett, T. D.; Mellot-Draznieks, C.; Zicovich-Wilson, C. M.; Cheetham, A. K. Exceptionally Low Shear Modulus in a Prototypical Imidazole-Based Metal-Organic Framework. *Phys. Rev. Lett.* **2012**, *108*, p. 095502.

(8) Ryder, M. R.; Civalleri, B.; Cinque, G.; Tan, J. C. Discovering Connections between Terahertz Vibrations and Elasticity Underpinning the Collective Dynamics of the HKUST-1 Metal-Organic Framework. *CrystEngComm* **2016**, *18*, pp. 4303-4312.

(9) Tan, J. C.; Civalleri, B. Metal-Organic Frameworks and Hybrid Materials: From Fundamentals to Applications. *CrystEngComm* **2015**, *17*, pp. 197-198.

(10) Zhu, Q. L.; Xu, Q. Metal-Organic Framework Composites. *Chem. Soc. Rev.* **2014**, *43*, pp. 5468-5512.

(11) Yaghi, O. M.; Li, G. M.; Li, H. L. Selective Binding and Removal of Guests in a Microporous Metal-Organic Framework. *Nature* **1995**, *378*, pp. 703-706.

(12) Moghadam, P. Z.; Li, A.; Wiggin, S. B.; Tao, A.; Maloney, A. G. P.; Wood, P. A.; Ward, S. C.; Fairen-Jimenez, D. Development of a Cambridge Structural Database Subset: A Collection of Metal-Organic Frameworks for Past, Present, and Future. *Chem. Mater.* **2017**, *29*, pp. 2618-2625.

(13) Phan, A.; Doonan, C. J.; Uribe-Romo, F. J.; Knobler, C. B.; O'Keeffe, M.; Yaghi, O. M. Synthesis, Structure, and Carbon Dioxide Capture Properties of Zeolitic Imidazolate Frameworks. *Acc. Chem. Res.* **2010**, *43*, pp. 58-67.

(14) Valenzano, L.; Civalleri, B.; Chavan, S.; Bordiga, S.; Nilsen, M. H.; Jakobsen, S.; Lillerud, K. P.; Lamberti, C. Disclosing the Complex Structure of UiO-66 Metal Organic Framework: A Synergic Combination of Experiment and Theory. *Chem. Mater.* **2011**, *23*, pp. 1700-1718.

(15) Ryder, M. R.; Civalleri, B.; Tan, J. C. Isoreticular Zirconium-Based Metal-Organic Frameworks: Discovering Mechanical Trends and Elastic Anomalies Controlling Chemical Structure Stability. *Phys. Chem. Chem. Phys.* **2016**, *18*, pp. 9079-9087.

(16) Díaz-García, M.; Mayoral, Á.; Díaz, I.; Sánchez-Sánchez, M. Nanoscaled M-MOF-74 Materials Prepared at Room Temperature. *Cryst. Growth Des.* **2014**, *14*, pp. 2479-2487.

(17) Janiak, C.; Vieth, J. K. MOFs, Mils and More: Concepts, Properties and Applications for Porous Coordination Networks (PCNs). *New J. Chem.* **2010**, *34*, pp. 2366-2388.

(18) Wang, L. J.; Deng, H.; Furukawa, H.; Gándara, F.; Cordova, K. E.; Peri, D.; Yaghi, O. M. Synthesis and Characterization of Metal-Organic Framework-74 Containing 2, 4, 6, 8, and 10 Different Metals. *Inorg. Chem.* **2014**, *53*, pp. 5881-5883.

(19) Wharmby, M. T.; Mowat, J. P. S.; Thompson, S. P.; Wright, P. A. Extending the Pore Size of Crystalline Metal Phosphonates toward the Mesoporous Regime by Isoreticular Synthesis. *J. Am. Chem. Soc.* **2011**, *133*, pp. 1266-1269.

(20) Sebastian, H.; Rochus, S.; Jan-Dierk, G.; A., F. R. Flexibility and Sorption Selectivity in Rigid Metal-Organic Frameworks: The Impact of Ether-Functionalised Linkers. *Chem. Eur. J.* **2010**, *16*, p. 14296-14306.

(21) Caro, J. Are MOF Membranes Better in Gas Separation Than Those Made of Zeolites? *Curr. Opin. Chem. Eng.* **2011**, *1*, pp. 77-83.

(22) Bao, Z.; Chang, G.; Xing, H.; Krishna, R.; Ren, Q.; Chen, B. Potential of Microporous Metal-Organic Frameworks for Separation of Hydrocarbon Mixtures. *Energy Environ. Sci.* **2016**, *9*, p. 3612-3641.

(23) Qiu, S.; Xue, M.; Zhu, G. Metal-Organic Framework Membranes: From Synthesis to Separation Application. *Chem. Soc. Rev.* **2014**, *43*, pp. 6116-6140.

(24) Li, J. R.; Sculley, J.; Zhou, H. C. Metal-Organic Frameworks for Separations. *Chem. Rev.* **2012**, *112*, pp. 869-932.

(25) Lee, J.; Farha, O. K.; Roberts, J.; Scheidt, K. A.; Nguyen, S. T.; Hupp, J. T. Metal-Organic Framework Materials as Catalysts. *Chem. Soc. Rev.* **2009**, *38*, pp. 1450-1459.

(26) Li, H.; Wang, K.; Sun, Y.; Lollar, C. T.; Li, J.; Zhou, H.-C. Recent Advances in Gas Storage and Separation Using Metal-Organic Frameworks. *Mater. Today* **2018**, *21*, pp. 108-121.

(27) Ryder, M. R.; Tan, J. C. Nanoporous Metal Organic Framework Materials for Smart Applications. *Mater. Sci. Tech.* **2014**, *30*, pp. 1598-1612.

(28) Usman, M.; Mendiratta, S.; Lu, K. L. Metal-Organic Frameworks: New Interlayer Dielectric Materials. *ChemElectroChem* **2015**, *2*, pp. 786-788.

(29) Dolgopolova, E. A.; Shustova, N. B. Metal-Organic Framework Photophysics: Optoelectronic Devices, Photoswitches, Sensors, and Photocatalysts. *MRS Bull.* **2016**, *41*, pp. 890-896.

(30) Zhang, X.; Wang, W.; Hu, Z.; Wang, G.; Uvdal, K. Coordination Polymers for Energy Transfer: Preparations, Properties, Sensing Applications, and Perspectives. *Coord. Chem. Rev.* **2015**, *284*, pp. 206-235.

(31) Li, S. L.; Xu, Q. Metal-Organic Frameworks as Platforms for Clean Energy. *Energy Environ. Sci.* **2013**, *6*, pp. 1656-1683.

(32) Cui, Y. J.; Yue, Y. F.; Qian, G. D.; Chen, B. L. Luminescent Functional Metal-Organic Frameworks. *Chem. Rev.* **2012**, *112*, pp. 1126-1162.

(33) Horcajada, P.; Chalati, T.; Serre, C.; Gillet, B.; Sebrie, C.; Baati, T.; Eubank, J. F.; Heurtaux, D.; Clayette, P.; Kreuz, C.; Chang, J. S.; Hwang, Y. K.; Marsaud, V.; Bories, P. N.; Cynober, L.; Gil, S.; Ferey, G.; Couvreur, P.; Gref, R. Porous Metal-Organic Framework Nanoscale Carriers as a Potential Platform for Drug Delivery and Imaging. *Nat. Mater.* **2010**, *9*, p. 172-178.

(34) Butler, K. T.; Hendon, C. H.; Walsh, A. Electronic Chemical Potentials of Porous Metal-Organic Frameworks. *J. Am. Chem. Soc.* **2014**, *136*, pp. 2703-2706.

(35) Burtch, N. C.; Heinen, J.; Bennett, T. D.; Dubbeldam, D.; Allendorf, M. D. Mechanical Properties in Metal-Organic Frameworks: Emerging Opportunities and Challenges for Device Functionality and Technological Applications. *Adv. Mater.* **2017**, p. 1704124.

(36) Allendorf, M. D.; Foster, M. E.; Léonard, F.; Stavila, V.; Feng, P. L.; Doty, F. P.; Leong, K.; Ma, E. Y.; Johnston, S. R.; Talin, A. A. Guest-Induced Emergent Properties in Metal-Organic Frameworks. *J. Phys. Chem. Lett.* **2015**, p. 1182-1195.

(37) Jiang, J.; Zhao, Y.; Yaghi, O. M. Covalent Chemistry Beyond Molecules. *J. Am. Chem. Soc.* **2016**, *138*, pp. 3255-3265.

(38) Tan, J. C.; Cheetham, A. K. Mechanical Properties of Hybrid Inorganic-Organic Framework Materials: Establishing Fundamental Structure-Property Relationships. *Chem. Soc. Rev.* **2011**, *40*, pp. 1059-1080.

(39) Li, W.; Henke, S.; Cheetham, A. K. Research Update: Mechanical Properties of Metal-Organic Frameworks – Influence of Structure and Chemical Bonding. *APL Mater.* **2014**, *2*, p. 123902.

(40) Park, K. S.; Ni, Z.; Cote, A. P.; Choi, J. Y.; Huang, R. D.; Uribe-Romo, F. J.; Chae, H. K.; O'Keeffe, M.; Yaghi, O. M. Exceptional Chemical and Thermal Stability of Zeolitic Imidazolate Frameworks. *Proc. Natl. Acad. Sci. USA* **2006**, *103*, pp. 10186-10191.

(41) Evans, J. D.; Coudert, F. X. Predicting the Mechanical Properties of Zeolite Frameworks by Machine Learning. *Chem. Mater.* **2017**, *29*, pp. 7833-7839.

(42) Coudert, F. X. Systematic Investigation of the Mechanical Properties of Pure Silica Zeolites: Stiffness, Anisotropy, and Negative Linear Compressibility. *Phys. Chem. Chem. Phys.* **2013**, *15*, pp. 16012-16018.

(43) Zhang, K.; Lively, R. P.; Dose, M. E.; Brown, A. J.; Zhang, C.; Chung, J.; Nair, S.; Koros, W. J.; Chance, R. R. Alcohol and Water Adsorption in Zeolitic Imidazolate Frameworks. *Chem. Commun.* **2013**, *49*, pp. 3245-3247.

(44) Lu, G.; Li, S.; Guo, Z.; Farha, O. K.; Hauser, B. G.; Qi, X.; Wang, Y.; Wang, X.; Han, S.; Liu, X.; DuChene, J. S.; Zhang, H.; Zhang, Q.; Chen, X.; Ma, J.; Loo, S. C. J.; Wei, W. D.; Yang, Y.; Hupp, J. T.; Huo, F. Imparting Functionality to a Metal-Organic Framework Material by Controlled Nanoparticle Encapsulation. *Nat. Chem.* **2012**, *4*, p. 310.

(45) Tan, J. C.; Bennett, T. D.; Cheetham, A. K. Chemical Structure, Network Topology, and Porosity Effects on the Mechanical Properties of Zeolitic Imidazolate Frameworks. *Proc. Natl. Acad. Sci.* **2010**, *107*, pp. 9938-9943.

(46) Schejn, A.; Balan, L.; Falk, V.; Aranda, L.; Medjahdi, G.; Schneider, R. Controlling ZIF-8 Nano- and Microcrystal Formation and Reactivity through Zinc Salt Variations. *CrystEngComm* **2014**, *16*, pp. 4493-4500.

(47) Lee, Y. R.; Jang, M. S.; Cho, H. Y.; Kwon, H. J.; Kim, S.; Ahn, W. S. ZIF-8: A Comparison of Synthesis Methods. *Chem. Eng. J.* **2015**, *271*, pp. 276-280.

(48) Wasuke, M.; Fumie, I.; Keiko, Y.; Hirokazu, N.; Satoshi, T.; Michihiko, K. Synthesis of New Adsorbent Copper(II) Terephthalate. *Chem. Lett.* **1997**, *26*, pp. 1219-1220.

(49) Rodenas, T.; Luz, I.; Prieto, G.; Seoane, B.; Miro, H.; Corma, A.; Kapteijn, F.; Xamena, F. X. L. I.; Gascon, J. Metal-Organic Framework Nanosheets in Polymer Composite Materials for Gas Separation. *Nat. Mater.* **2015**, *14*, pp. 48-55.

(50) Chui, S. S. Y.; Lo, S. M. F.; Charmant, J. P. H.; Orpen, A. G.; Williams, I. D. A Chemically Functionalizable Nanoporous Material [Cu3(TMA)2(H2O)3]n. *Science* **1999**, *283*, pp. 1148-1150.

(51) Wu, Y.; Kobayashi, A.; Halder, G. J..; Peterson, V. K..; Chapman, K. W.; Lock, N.; Southon, P. D., Kepert, C. J.. Negative Thermal Expansion in the Metal-Organic Framework Material Cu_3(1,3,5-Benzenetricarboxylate)$_2$. *Angew. Chem. Int. Ed.* **2008**, *47*, pp. 8929-8932.

(52) Min Wang, Q.; Shen, D.; Bülow, M.; Ling Lau, M.; Deng, S.; Fitch, F. R.; Lemcoff, N. O.; Semanscin, J. Metallo-Organic Molecular Sieve for Gas Separation and Purification. *Microporous Mesoporous Mat.* **2002**, *55*, pp. 217-230.

(53) Liang, Z.; Marshall, M.; Chaffee, A. L. CO_2 Adsorption-Based Separation by Metal-Organic Framework (Cu-BTC) Versus Zeolite (13x). *Energy Fuels* **2009**, *23*, p. 2785-2789.

(54) Hartmann, M.; Kunz, S.; Himsl, D.; Tangermann, O.; Ernst, S.; Wagener, A. Adsorptive Separation of Isobutene and Isobutane on Cu3(BTC)2. *Langmuir* **2008**, *24*, pp. 8634-8642.

(55) Tian, T.; Zeng, Z.; Vulpe, D.; Casco, M. E.; Divitini, G.; Midgley, P. A.; Silvestre-Albero, J.; Tan, J. C.; Moghadam, P. Z.; Fairen-Jimenez, D. A Sol-Gel Monolithic Metal-Organic Framework with Enhanced Methane Uptake. *Nat. Mater.* **2017**, *17*, p. 174.

(56) Talin, A. A.; Centrone, A.; Ford, A. C.; Foster, M. E.; Stavila, V.; Haney, P.; Kinney, R. A.; Szalai, V.; El Gabaly, F.; Yoon, H. P.; Léonard, F.; Allendorf, M. D. Tunable Electrical Conductivity in Metal-Organic Framework Thin-Film Devices. *Science* **2014**, *343*, p. 66-69.

(57) Li, L.; Sun, F.; Jia, J.; Borjigin, T.; Zhu, G. Growth of Large Single MOF Crystals and Effective Separation of Organic Dyes. *CrystEngComm* **2013**, *15*, pp. 4094-4098.

(58) Tovar, T. M.; Zhao, J.; Nunn, W. T.; Barton, H. F.; Peterson, G. W.; Parsons, G. N.; LeVan, M. D. Diffusion of CO_2 in Large Crystals of Cu-BTC MOF. *J. Am. Chem. Soc.* **2016**, *138*, pp. 11449-11452.

(59) Umemura, A.; Diring, S.; Furukawa, S.; Uehara, H.; Tsuruoka, T.; Kitagawa, S. Morphology Design of Porous Coordination Polymer Crystals by Coordination Modulation. *J. Am. Chem. Soc.* **2011**, *133*, pp. 15506-15513.

(60) Macrae, C. F.; Bruno, I. J.; Chisholm, J. A.; Edgington, P. R.; McCabe, P.; Pidcock, E.; Rodriguez-Monge, L.; Taylor, R.; van de Streek, J.; Wood, P. A. Mercury CSD 2.0 - New Features for the Visualization and Investigation of Crystal Structures. *J. Appl. Crystallogr.* **2008**, *41*, pp. 466-470.

(61) Silva, P.; Vilela, S. M. F.; Tome, J. P. C.; Almeida Paz, F. A. Multifunctional Metal-Organic Frameworks: From Academia to Industrial Applications. *Chem. Soc. Rev.* **2015**, *44*, p. 6774-6803.

(62) Howarth, A. J.; Liu, Y. Y.; Li, P.; Li, Z. Y.; Wang, T. C.; Hupp, J.; Farha, O. K. Chemical, Thermal and Mechanical Stabilities of Metal-Organic Frameworks. *Nat. Rev. Mater.* **2016**, *1*, pp. 15018-15032.

(63) Li, W.; Henke, S.; Cheetham, A. K. Research Update: Mechanical Properties of Metal-Organic Frameworks – Influence of Structure and Chemical Bonding. *APL Mater.* **2014**, *2*, p. 123902.

(64) Ryder, M. R.; Tan, J. C. Explaining the Mechanical Mechanisms of Zeolitic Metal-Organic Frameworks: Revealing Auxeticity and Anomalous Elasticity. *Dalton Trans.* **2016**, *45*, pp. 4154-4161.

(65) Wu, H.; Yildirim, T.; Zhou, W. Exceptional Mechanical Stability of Highly Porous Zirconium Metal-Organic Framework UiO-66 and Its Important Implications. *J. Phys. Chem. Lett.* **2013**, *4*, pp. 925-930.

(66) Ortiz, A. U.; Boutin, A.; Fuchs, A. H.; Coudert, F. X. Anisotropic Elastic Properties of Flexible Metal-Organic Frameworks: How Soft Are Soft Porous Crystals? *Phys. Rev. Lett.* **2012**, *109*, p. 195502.

(67) Tan, J. C.; Civalleri, B.; Erba, A.; Albanese, E. Quantum Mechanical Predictions to Elucidate the Anisotropic Elastic Properties of Zeolitic Imidazolate Frameworks: ZIF-4 vs. ZIF-zni. *CrystEngComm* **2015**, *17*, pp. 375-382.

(68) Marmier, A.; Evans, K. E. Flexibility in MOFs: Do Scalar and Group-Theoretical Counting Rules Work? *Dalton Trans.* **2016**, *45*, pp. 4360-4369.

(69) Banlusan, K.; Antillon, E.; Strachan, A. Mechanisms of Plastic Deformation of Metal-Organic Framework-5. *J. Phys. Chem. C* **2015**, *119*, pp. 25845-25852.

(70) Ortiz, A. U.; Boutin, A.; Fuchs, A. H.; Coudert, F. X. Investigating the Pressure-Induced Amorphization of Zeolitic Imidazolate Framework ZIF-8: Mechanical Instability Due to Shear Mode Softening. *J. Phys. Chem. Lett.* **2013**, *4*, pp. 1861-1865.

(71) Hegde, V. I.; Tan, J. C.; Waghmare, U. V.; Cheetham, A. K. Stacking Faults and Mechanical Behavior Beyond the Elastic Limit of an Imidazole-Based Metal-Organic Framework: ZIF-8. *J. Phys. Chem. Lett.* **2013**, *4*, p. 3377-3381.

(72) Bahr, D. F.; Reid, J. A.; Mook, W. M.; Bauer, C. A.; Stumpf, R.; Skulan, A. J.; Moody, N. R.; Simmons, B. A.; Shindel, M. M.; Allendorf, M. D. Mechanical Properties of Cubic Zinc Carboxylate IRMOF-1 Metal-Organic Framework Crystals. *Phys. Rev. B* **2007**, *76*, p. 184106.

(73) Henke, S.; Li, W.; Cheetham, A. K. Guest-Dependent Mechanical Anisotropy in Pillared-Layered Soft Porous Crystals – a Nanoindentation Study. *Chem. Sci.* **2014**, *5*, pp. 2392-2397.

(74) Reddy, C. M.; Rama Krishna, G.; Ghosh, S. Mechanical Properties of Molecular Crystals-Applications to Crystal Engineering. *CrystEngComm* **2010**, *12*, pp. 2296-2314.

(75) Kiran, M. S. R. N.; Varughese, S.; Reddy, C. M.; Ramamurty, U.; Desiraju, G. R. Mechanical Anisotropy in Crystalline Saccharin: Nanoindentation Studies. *Cryst. Growth Des.* **2010**, *10*, pp. 4650-4655.

(76) Ramamurty, U.; Jang, J. I. Nanoindentation for Probing the Mechanical Behavior of Molecular Crystals – a Review of the Technique and How to Use It. *CrystEngComm* **2014**, *16*, pp. 12-23.

(77) Stock, N.; Biswas, S. Synthesis of Metal-Organic Frameworks (MOFs): Routes to Various MOF Topologies, Morphologies, and Composites. *Chem. Rev.* **2012**, *112*, p. 933-969.

(78) Eslava, S.; Zhang, L. P.; Esconjauregui, S.; Yang, J. W.; Vanstreels, K.; Baklanov, M. R.; Saiz, E. Metal-Organic Framework ZIF-8 Films as Low-Kappa Dielectrics in Microelectronics. *Chem. Mater.* **2013**, *25*, pp. 27-33.

(79) Van de Voorde, B.; Ameloot, R.; Stassen, I.; Everaert, M.; De Vos, D.; Tan, J. C. Mechanical Properties of Electrochemically Synthesised Metal-Organic Framework Thin Films. *J. Mater. Chem. B* **2013**, *1*, pp. 7716-7724.

(80) Bundschuh, S.; Kraft, O.; Arslan, H. K.; Gliemann, H.; Weidler, P. G.; Woll, C. Mechanical Properties of Metal-Organic Frameworks: An Indentation Study on Epitaxial Thin Films. *Appl. Phys. Lett.* **2012**, *101*, p. 101910.

(81) Stassen, I.; Styles, M.; Van Assche, T.; Campagnol, N.; Fransaer, J.; Denayer, J.; Tan, J. C.; Falcaro, P.; De Vos, D.; Ameloot, R. Electrochemical Film Deposition of the Zirconium Metal-Organic Framework UiO-66 and Application in a Miniaturized Sorbent Trap. *Chem. Mater.* **2015**, *27*, pp. 1801-1807.

(82) Buchan, I.; Ryder, M. R.; Tan, J. C. Micromechanical Behavior of Polycrystalline Metal-Organic Framework Thin Films Synthesized by Electrochemical Reaction. *Cryst. Growth Des.* **2015**, *15*, pp. 1991-1999.

(83) Furukawa, H.; Ko, N.; Go, Y. B.; Aratani, N.; Choi, S. B.; Choi, E.; Yazaydin, A. Ö.; Snurr, R. Q.; O'Keeffe, M.; Kim, J.; Yaghi, O. M. Ultrahigh Porosity in Metal-Organic Frameworks. *Science* **2010**, *329*, pp. 424-428.

(84) Bohan, S.; Jiuhao, Y.; R., A. M.; Dingke, W.; Bin, M.; Zhenfei, C.; Jichang, L. A Cobalt Metal-Organic Framework with Small Pore Size for Adsorptive Separation of CO_2 over N_2 and CH_4. *AIChE J.* **2017**, *63*, pp. 4532-4540.

(85) Hay, J.; Herbert, E. Measuring the Complex Modulus of Polymers by Instrumented Indentation Testing. *Exp. Techniques* **2013**, *37*, pp. 55-61.

(86) Cao, Y.; Yang, D.; Soboyejoy, W. Nanoindentation Method for Determining the Initial Contact and Adhesion Characteristics of Soft Polydimethylsiloxane. *J. Mater. Res.* **2005**, *20*, pp. 2004-2011.

(87) Kaufman, J. D.; Klapperich, C. M. Surface Detection Errors Cause Overestimation of the Modulus in Nanoindentation on Soft Materials. *J. Mech. Behav. Biomed. Mater.* **2009**, *2*, pp. 312-317.

(88) Oliver, W. C.; Pharr, G. M. An Improved Technique for Determining Hardness and Elastic-Modulus Using Load and Displacement Sensing Indentation Experiments. *J. Mater. Res.* **1992**, *7*, pp. 1564-1583.

(89) Tan, J. C.; Furman, J. D.; Cheetham, A. K. Relating Mechanical Properties and Chemical Bonding in an Inorganic-Organic Framework Material: A Single-Crystal Nanoindentation Study. *J. Am. Chem. Soc.* **2009**, *131*, pp. 14252-14254.

(90) Tan, J. C.; Merrill, C. A.; Orton, J. B.; Cheetham, A. K. Anisotropic Mechanical Properties of Polymorphic Hybrid Inorganic-Organic Framework Materials with Different Dimensionalities. *Acta. Mater.* **2009**, *57*, pp. 3481-3496.

(91) Tan, J. C.; Saines, P. J.; Bithell, E. G.; Cheetham, A. K. Hybrid Nanosheets of an Inorganic-Organic Framework Material: Facile Synthesis, Structure, and Elastic Properties. *ACS Nano* **2012**, *6*, pp. 615-621.

(92) Chaudhari, A. K.; Han, I.; Tan, J. C. Multifunctional Supramolecular Hybrid Materials Constructed from Hierarchical Self-Ordering of In Situ Generated Metal-Organic Framework (MOF) Nanoparticles. *Adv. Mater.* **2015**, *27*, pp. 4438-4446.

(93) Hu, Z.; Sun, Y.; Zeng, K.; Zhao, D. Structural-Failure Resistance of Metal-Organic Frameworks toward Multiple-Cycle CO_2 Sorption. *Chem. Commun.* **2017**, *53*, pp. 8653-8656.

(94) Young, T. J.; Monclus, M. A.; Burnett, T. L.; Broughton, W. R.; Ogin, S. L.; Smith, P. A. The Use of the PeakForce TM Quantitative Nanomechanical Mapping AFM-Based Method for High-Resolution Young's Modulus Measurement of Polymers. *Meas. Sci. Technol.* **2011**, *22*, p. 125703.

(95) Smolyakov, G.; Pruvost, S.; Cardoso, L.; Alonso, B.; Belamie, E.; Duchet-Rumeau, J. AFM PeakForce QNM Mode: Evidencing Nanometre-Scale Mechanical Properties of Chitin-Silica Hybrid Nanocomposites. *Carbohydr. Polym.* **2016**, *151*, pp. 373-380.

(96) Tan, J. C.; Jain, P.; Cheetham, A. K. Influence of Ligand Field Stabilization Energy on the Elastic Properties of Multiferroic MOFs with the Perovskite Architecture. *Dalton Trans.* **2012**, *41*, pp. 3949-3952.

(97) Li, W.; Thirumurugan, A.; Barton, P. T.; Lin, Z.; Henke, S.; Yeung, H. H. M.; Wharmby, M. T.; Bithell, E. G.; Howard, C. J.; Cheetham, A. K. Mechanical Tunability via Hydrogen Bonding in Metal-Organic Frameworks with the Perovskite Architecture. *J. Am. Chem. Soc.* **2014**, *136*, pp. 7801-7804.

(98) Mukherjee, S.; Zeng, Z.; Shirolkar, M. M.; Samanta, P.; Chaudhari, A. K.; Tan, J. C.; Ghosh, S. K. Self-Assembled, Fluorine-Rich Porous Organic Polymers: A Class of Mechanically Stiff and Hydrophobic Materials. *Chem. Eur. J.*

(99) Arslanoglu, Z.; Altan, H.; Kale, E.; Bilgic, F.; Sahin, O. Nanomechanical Behaviour and Surface Roughness of New Generation Dental Fissure Sealants. *Acta Phys. Pol. A* **2016**, *130*, pp. 388-393.

(100) Altan, A.; Damlar, İ.; Şahin, O. Can Resorbable Fixation Screws Replace Titanium Fixation Screws? A nano-Indentation Study. *J. Oral Maxillofac. Surg.* **2016**, *74*, pp. 1421-1421.

(101) Juday, R.; Silva, E. M.; Huang, J. Y.; Caldas, P. G.; Prioli, R.; Ponce, F. A. Strain-Related Optical Properties of ZnO Crystals Due to Nanoindentation on Various Surface Orientations. *J. Appl. Phys.* **2013**, *113*, p. 183511.

(102) Zelenak, M.; Valicek, J.; Hloch, S.; Kozak, D.; Samardzic, I.; Harnicarova, M.; Klich, J.; Hlavacek, P.; Cincio, R. Comparison of Mechanical Properties of Surface Layers with Use of Nanoindentation and Microindentation Tests. *Metalurgija* **2012**, *51*, pp. 309-312.

(103) Dimitriadis, E. K.; Horkay, F.; Maresca, J.; Kachar, B.; Chadwick, R. S. Determination of Elastic Moduli of Thin Layers of Soft Material Using the Atomic Force Microscope. *Biophys. J.* **2002**, *82*, pp. 2798-2810.

(104) Lin, D. C.; Dimitriadis, E. K.; Horkay, F. Robust Strategies for Automated AFM Force Curve Analysis-I. Non-Adhesive Indentation of Soft, Inhomogeneous Materials. *J. Biomech. Eng.* **2007**, *129*, pp. 430-440.

(105) Lin, D. C.; Dmitriadis, E. K.; Horkay, F. Robust Strategies for Automated AFM Force Curve Analysis-II: Adhesion-Influenced Indentation of Soft, Elastic Materials. *J. Biomech. Eng-T. Asme* **2007**, *129*, pp. 904-912.

(106) Tranchida, D. K., Z.; Piccarolo, S. Atomic Force Microscope Nanoindentations to Reliably Measure the Young's Modulus of Soft Matter. *Modern Research and Educational Topics on Microscopy* **2007**, pp. 737-746.

(107) Costa, K. D.; Yin, F. C. Analysis of Indentation: Implications for Measuring Mechanical Properties with Atomic Force Microscopy. *J. Biomech. Eng.* **1999**, *121*, pp. 462-471.

(108) Galluzzi, M.; Biswas, C. S.; Wu, Y.; Wang, Q.; Du, B.; Stadler, F. J. Space-Resolved Quantitative Mechanical Measurements of Soft and Supersoft Materials by Atomic Force Microscopy. *NPG Asia Mater.* **2016**, *8*, p. e327.

(109) Ganser, C.; Czibula, C.; Tscharnuter, D.; Schoberl, T.; Teichert, C.; Hirn, U. Combining Adhesive Contact Mechanics with a Viscoelastic Material Model to Probe Local Material Properties by AFM. *Soft Matter* **2018**, *14*, pp. 140-150.

(110) Speziale, S.; Marquardt, H.; Duffy, T. S. Brillouin Scattering and its Application in Geosciences. *Rev. Mineral. Geochem.* **2014**, *78*, pp. 543-603.

(111) Liu, L. G.; Chen, C. C.; Lin, C. C.; Yang, Y. J. Elasticity of Single-Crystal Aragonite by Brillouin Spectroscopy. *Phys. Chem. Miner.* **2005**, *32*, pp. 97-102.

(112) Li, Z.; Nevitt, M. V.; Ghose, S. Elastic Constants of Sodalite Na4Al3Si3O12Cl. *Appl. Phys. Lett.* **1989**, *55*, pp. 1730-1731.

(113) Yeganeh-Haeri, A.; Weidner, D. J.; Parise, J. B. Elasticity of A-Cristobalite: A Silicon Dioxide with a Negative Poisson's Ratio. *Science* **1992**, *257*, pp. 650-652.

(114) Nye, J. F., *Physical Properties of Crystals*. Clarendon Press: 1985; p 352

(115) Hayes, W.; Loudon, R., *Scattering of Light by Crystals*. Courier Corporation: 2012; p 368.

(116) Radhakrishnan, D.; Narayana, C. Guest Dependent Brillouin and Raman Scattering Studies of Zeolitic Imidazolate Framework-8 (ZIF-8) under External Pressure. *J. Chem. Phys.* **2016**, *144*, p. 134704.

(117) Dovesi, R.; Orlando, R.; Erba, A.; Zicovich-Wilson, C. M.; Civalleri, B.; Casassa, S.; Maschio, L.; Ferrabone, M.; Pierre, D. L. M.; D'Arco, P.; Noël, Y.; Causà, M.; Rérat, M.; Kirtman, B. Crystal14: A Program for the Ab Initio Investigation of Crystalline Solids. *Int. J. Quantum Chem.* **2014**, *114*, pp. 1287-1317.

(118) Clark, S. J.; Segall, M. D.; Pickard, C. J.; Hasnip, P. J.; Probert, M. J.; Refson, K.; Payne, M. C. First Principles Methods Using Castep. *Z. Kristall.* **2005**, *220*, pp. 567-570.

(119) Evans, J. D.; Fraux, G.; Gaillac, R.; Kohen, D.; Trousselet, F.; Vanson, J. M.; Coudert, F. X. Computational Chemistry Methods for Nanoporous Materials. *Chem. Mater.* **2017**, *29*, pp. 199-212.

(120) Mattesini, M.; Soler, J. M.; Ynduráin, F. Ab Initio Study of Metal-Organic Framework-5 Zn4O(1,4-benzenedicarboxylate)3: An Assessment of Mechanical and Spectroscopic Properties. *Phys. Rev. B* **2006**, *73*, p. 094111.

(121) Perdew, J. P.; Burke, K.; Ernzerhof, M. Generalized Gradient Approximation Made Simple. *Phys. Rev. Lett.* **1996**, *77*, pp. 3865-3868.

(122) Kuc, A.; Enyashin, A.; Seifert, G. Metal-Organic Frameworks: Structural, Energetic, Electronic, and Mechanical Properties. *J. Phys. Chem. B* **2007**, *111*, pp. 8179-8186.

(123) Becke, A. D. Density-Functional Thermochemistry. III. The Role of Exact Exchange. *J. Chem. Phys.* **1993**, *98*, pp. 5648-5652.

(124) Hobday, C. L.; Marshall, R. J.; Murphie, C. F.; Sotelo, J.; Richards, T.; Allan, D. R.; Düren, T.; Coudert, F. X.; Forgan, R. S.; Morrison, C. A.; Moggach, S. A.; Bennett, T. D. A Computational and Experimental Approach Linking Disorder, High-Pressure Behavior, and Mechanical Properties in UiO Frameworks. *Angew. Chem. Int. Ed.* **2016**, *55*, pp. 2401-2405.

(125) Banlusan, K.; Strachan, A. First-Principles Study of Elastic Mechanical Responses to Applied Deformation of Metal-Organic Frameworks. *J. Chem. Phys.* **2017**, *146*, p. 184705.

(126) Greathouse, J. A.; Allendorf, M. D. Force Field Validation for Molecular Dynamics Simulations of IRMOF-1 and Other Isoreticular Zinc Carboxylate Coordination Polymers. *J. Phys. Chem. C* **2008**, *112*, pp. 5795-5802.

(127) Basdogan, Y.; Keskin, S. Simulation and Modelling of MOFs for Hydrogen Storage. *CrystEngComm* **2015**, *17*, pp. 261-275.

(128) Jurn, H.; David, D. On Flexible Force Fields for Metal-Organic Frameworks: Recent Developments and Future Prospects. *Wiley Interdiscip. Rev. Comput. Mol. Sci.* **2018**, *8*, p. e1363.

(129) Rogge, S. M. J.; Waroquier, M.; Van Speybroeck, V. Reliably Modeling the Mechanical Stability of Rigid and Flexible Metal-Organic Frameworks. *Acc. Chem. Res.* **2018**, *51*, pp. 138-148.

(130) Hu, Z.; Zhang, L.; Jiang, J. Development of a Force Field for Zeolitic Imidazolate Framework-8 with Structural Flexibility. *J. Chem. Phys.* **2012**, *136*, p. 244703.

(131) Pharr, G. M.; Oliver, W. C.; Clarke, D. R. Hysteresis and Discontinuity in the Indentation Load-Displacement Behavior of Silicon. *Scr. Mater.* **1989**, *23*, pp. 1949-1952.

(132) Pharr, G. M.; Oliver, W. C.; Clarke, D. R. The Mechanical Behavior Indentation of Silicon During Small-Scale *J. Elec. Mater.* **1990**, *19*, pp. 881-887.

(133) Pharr, G. M.; Oliver, W. C.; Harding, D. S. New Evidence for a Pressure-Induced Phase Transformation During the Indentation of Silicon. *J. Mater. Res.* **1991**, *6*, pp. 1129-1130.

(134) Banlusan, K.; Strachan, A. Shockwave Energy Dissipation in Metal-Organic Framework MOF-5. *J. Phys. Chem. C* **2016**, *120*, pp. 12463-12471.

(135) Jiang, Z.; Li, Z.; Qin, Z.; Sun, H.; Jiao, X.; Chen, D. LDH Nanocages Synthesized with MOF Templates and Their High Performance as Supercapacitors. *Nanoscale* **2013**, *5*, pp. 11770-11775.

(136) Cao, F.; Zhao, M.; Yu, Y.; Chen, B.; Huang, Y.; Yang, J.; Cao, X.; Lu, Q.; Zhang, X.; Zhang, Z.; Tan, C.; Zhang, H. Synthesis of Two-Dimensional CoS1.097/Nitrogen-Doped Carbon Nanocomposites Using Metal-Organic Framework Nanosheets as Precursors for Supercapacitor Application. *J. Am. Chem. Soc.* **2016**, *138*, pp. 6924-6927.

(137) Chhowalla, M.; Shin, H. S.; Eda, G.; Li, L. J.; Loh, K. P.; Zhang, H. The Chemistry of Two-Dimensional Layered Transition Metal Dichalcogenide Nanosheets. *Nat. Chem.* **2013**, *5*, pp. 263-275.

(138) Zhao, S.; Wang, Y.; Dong, J.; He, C. T.; Yin, H.; An, P.; Zhao, K.; Zhang, X.; Gao, C.; Zhang, L.; Lv, J.; Wang, J.; Zhang, J.; Khattak, A. M.; Khan, N. A.; Wei, Z.; Zhang, J.; Liu, S.; Zhao, H.; Tang, Z. Ultrathin Metal-Organic Framework Nanosheets for Electrocatalytic Oxygen Evolution. *Nat. Energy.* **2016**, *1*, pp. 16184-16193.

(139) Chaudhari, A. K.; Kim, H. J.; Han, I.; Tan, J. C. Optochemically Responsive 2D Nanosheets of a 3D Metal-Organic Framework Material. *Adv. Mater.* **2017**, *29*, p. 1701463-1701471.

(140) Meiting, Z.; Qipeng, L.; Qinglang, M.; Hua, Z. Two-Dimensional Metal-Organic Framework Nanosheets. *Small Methods* **2017**, *1*, p. 1600030.

(141) Huang, P.; Guo, D.; Xie, G.; Li, J. Softened Mechanical Properties of Graphene Induced by Electric Field. *Nano Lett.* **2017**, *17*, pp. 6280-6286.

(142) Hu, Z.; Mahdi, E. M.; Peng, Y.; Qian, Y.; Zhang, B.; Yan, N.; Yuan, D.; Tan, J. C.; Zhao, D. Kinetically Controlled Synthesis of Two-Dimensional Zr/Hf Metal-Organic Framework Nanosheets via a Modulated Hydrothermal Approach. *J. Mater. Chem. A* **2017**, *5*, pp. 8954-8963.

(143) Penkov, O. V.; Pukha, V. E.; Devizenko, A. Y.; Kim, H. J.; Kim, D. E. Self-Healing Phenomenon and Dynamic Hardness of C60-Based Nanocomposite Coatings. *Nano Lett.* **2014**, *14*, pp. 2536-2540.

(144) Ozden, S.; Yang, Y.; Tiwary, C. S.; Bhowmick, S.; Asif, S.; Penev, E. S.; Yakobson, B. I.; Ajayan, P. M. Indentation Tests Reveal Geometry-Regulated Stiffening of Nanotube Junctions. *Nano Lett.* **2016**, *16*, pp. 232-236.

(145) Lee, C.; Wei, X. D.; Kysar, J. W.; Hone, J. Measurement of the Elastic Properties and Intrinsic Strength of Monolayer Graphene. *Science* **2008**, *321*, pp. 385-388.

(146) Payamyar, P.; Kaja, K.; Ruiz-Vargas, C.; Stemmer, A.; Murray, D. J.; Johnson, C. J.; King, B. T.; Schiffmann, F.; VandeVondele, J.; Renn, A.; Gotzinger, S.; Ceroni, P.; Schutz, A.; Lee, L. T.; Zheng, Z. K.; Sakamoto, J.; Schluter, A. D. Synthesis of a Covalent Monolayer Sheet by Photochemical Anthracene Dimerization at the Air/Water Interface and Its Mechanical Characterization by AFM Indentation. *Adv. Mater.* **2014**, *26*, pp. 2052-2058.

(147) Zeng, Z.; Tan, J. C. AFM Nanoindentation to Quantify Mechanical Properties of Nano- and Micron-Sized Crystals of a Metal-Organic Framework Material. *ACS Appl. Mater. Interfaces* **2017**, *9*, pp. 39839-39854.

(148) Cohen, S. R.; Kalfon-Cohen, E. Dynamic Nanoindentation by Instrumented Nanoindentation and Force Microscopy: A Comparative Review. *Beilstein J. Nanotechnol.* **2013**, *4*, pp. 815-833.

(149) Ferencz, R.; Sanchez, J.; Blümich, B.; Herrmann, W. AFM Nanoindentation to Determine Young's Modulus for Different EPDM Elastomers. *Polymer Test.* **2012**, *31*, pp. 425-432.

(150) Kontomaris, S. V.; Stylianou, A. Atomic Force Microscopy for University Students: Applications in Biomaterials. *Eur. J. Phys.* **2017**, *38*, p. 033003.

(151) Pratt, J. R.; Smith, D. T.; Newell, D. B.; Kramar, J. A.; Whitenton, E. Progress toward Système International D'unités Traceable Force Metrology for Nanomechanics. *J. Mater. Res.* **2004**, *19*, pp. 366-379.

(152) Ebenstein, D. M.; Pruitt, L. A. Nanoindentation of Biological Materials. *Nano Today* **2006**, *1*, pp. 26-33.

(153) Roos, W. H.; Bruinsma, R.; Wuite, G. J. L. Physical Virology. *Nat. Phys.* **2010**, *6*, pp. 733-743.

(154) Kasas, S.; Dietler, G. Probing Nanomechanical Properties from Biomolecules to Living Cells. *Pflugers Arch.* **2008**, *456*, pp. 13-27.

(155) Radmacher, M.; Fritz, M.; Kacher, C. M.; Cleveland, J. P.; Hansma, P. K. Measuring the Viscoelastic Properties of Human Platelets with the Atomic Force Microscope. *Biophys. J.* **1996**, *70*, pp. 556-567.

(156) Raman, A.; Trigueros, S.; Cartagena, A.; Stevenson, A. P. Z.; Susilo, M.; Nauman, E.; Contera, S. A. Mapping Nanomechanical Properties of Live Cells Using Multi-Harmonic Atomic Force Microscopy. *Nat. Nanotech.* **2011**, *6*, pp. 809-814.

(157) Gavara, N.; Chadwick, R. S. Determination of the Elastic Moduli of Thin Samples and Adherent Cells Using Conical Atomic Force Microscope Tips. *Nat. Nanotech.* **2012**, *7*, pp. 733-736.

(158) Lekka, M.; Laidler, P.; Gil, D.; Lekki, J.; Stachura, Z.; Hrynkiewicz, A. Z. Elasticity of Normal and Cancerous Human Bladder Cells Studied by Scanning Force Microscopy. *Eur. Biophys. J.* **1999**, *28*, pp. 312-316.

(159) Sen, S.; Subramanian, S.; Discher, D. E. Indentation and Adhesive Probing of a Cell Membrane with AFM: Theoretical Model and Experiments. *Biophys. J.* **2005**, *89*, pp. 3203-3213.

(160) Hermanowicz, P.; Sarna, M.; Burda, K.; Gabrys, H. AtomicJ: An Open Source Software for Analysis of Force Curves. *Rev. Sci. Instrum.* **2014**, *85*, p. 063703.

(161) Haase, K.; Pelling, A. E. Investigating Cell Mechanics with Atomic Force Microscopy. *J. Royal Soc. Interface* **2015**, *12*.

(162) Lal, R.; John, S. A. Biological Applications of Atomic-Force Microscopy. *Am. J. Physiol.* **1994**, *266*, pp. 1-21.

(163) Hofmann, U. G.; Rotsch, C.; Parak, W. J.; Radmacher, M. Investigating the Cytoskeleton of Chicken Cardiocytes with the Atomic Force Microscope. *J. Struct. Biol.* **1997**, *119*, pp. 84-91.

(164) Wu, H. W.; Kuhn, T.; Moy, V. T. Mechanical Properties of L929 Cells Measured by Atomic Force Microscopy: Effects of Anticytoskeletal Drugs and Membrane Crosslinking. *Scanning* **1998**, *20*, pp. 389-397.

(165) Sato, M.; Nagayama, K.; Kataoka, N.; Sasaki, M.; Hane, K. Local Mechanical Properties Measured by Atomic Force Microscopy for Cultured Bovine Endothelial Cells Exposed to Shear Stress. *J. Biomech.* **2000**, *33*, pp. 127-135.

(166) Tao, N. J.; Lindsay, S. M.; Lees, S. Measuring the Microelastic Properties of Biological-Material. *Biophys. J.* **1992**, *63*, pp. 1165-1169.

(167) Burnham, N. A.; Colton, R. J. Measuring the Nanomechanical Properties and Surface Forces of Materials Using an Atomic Force Microscope. *J. Vac. Sci. Technol. A.* **1989**, *7*, pp. 2906-2913.

(168) Bowen, W. R.; Lovitt, R. W.; Wright, C. J. Application of Atomic Force Microscopy to the Study of Micromechanical Properties of Biological Materials. *Biotechnol. Lett.* **2000**, *22*, pp. 893-903.

(169) Heinz, W. F.; Hoh, J. H. Spatially Resolved Force Spectroscopy of Biological Surfaces Using the Atomic Force Microscope. *Trends Biotechnol.* **1999**, *17*, pp. 143-150.

(170) Radmacher, M. Measuring the Elastic Properties of Biological Samples with the AFM. *IEEE Eng. Med. Biol. Mag.* **1997**, *16*, pp. 47-57.

(171) Mathur, A. B.; Collinsworth, A. M.; Reichert, W. M.; Kraus, W. E.; Truskey, G. A. Endothelial, Cardiac Muscle and Skeletal Muscle Exhibit Different Viscous and Elastic Properties as Determined by Atomic Force Microscopy. *J. Biomech.* **2001**, *34*, pp. 1545-1553.

(172) Shroff, S. G.; Saner, D. R.; Lal, R. Dynamic Micromechanical Properties of Cultured Rat Atrial Myocytes Measured by Atomic-Force Microscopy. *Am. J. Physiol., Cell Physiol.* **1995**, *269*, pp. 286-292.

(173) Crick, S. L.; Yin, F. C. P. Assessing Micromechanical Properties of Cells with Atomic Force Microscopy: Importance of the Contact Point. *Biomech. Model. Mechanobiol.* **2007**, *6*, pp. 199-210.

(174) Almqvist, N.; Bhatia, R.; Primbs, G.; Desai, N.; Banerjee, S.; Lal, R. Elasticity and Adhesion Force Mapping Reveals Real-Time Clustering of Growth Factor Receptors and Associated Changes in Local Cellular Rheological Properties. *Biophys. J.* **2004**, *86*, pp. 1753-1762.

(175) Hutter, J. L.; Chen, J.; Wan, W. K.; Uniyal, S.; Leabu, M.; Chan, B. M. C. Atomic Force Microscopy Investigation of the Dependence of Cellular Elastic Moduli on Glutaraldehyde Fixation. *J. Microsc-Oxford.* **2005**, *219*, pp. 61-68.

(176) Radmacher, M. Measuring the Elastic Properties of Living Cells by the Atomic Force Microscope. *Methods Cell Biol.* **2002**, *68*, pp. 67-90.

(177) Jaasma, M. J.; Jackson, W. M.; Keaveny, T. M. Measurement and Characterization of Whole-Cell Mechanical Behavior. *Ann. Biomed. Eng.* **2006**, *34*, pp. 748-758.

(178) Kolambkar, Y. M. Extracting Mechanical Properties of Cells/Biomaterials Using the Atomic Force Microscope. University of Cincinnati, 2004.

(179) Jee, A. Y.; Lee, M. Comparative Analysis on the Nanoindentation of Polymers Using Atomic Force Microscopy. *Polymer Test.* **2010**, *29*, pp. 95-99.

(180) Moeller, G. AFM Nanoindentation of Viscoelastic Materials with Large End-Radius Probes. *J. Polym. Sci., Part B: Polym. Phys.* **2009**, *47*, pp. 1573-1587.

(181) Cappella, B.; Stark, W. Adhesion of Amorphous Polymers as a Function of Temperature Probed with AFM Force-Distance Curves. *J. Colloid Interface Sci.* **2006**, *296*, pp. 507-514.

(182) Sirghi, L.; Rossi, F. Adhesion and Elasticity in Nanoscale Indentation. *Appl. Phys. Lett.* **2006**, *89*, p. 243118.

(183) Notbohm, J.; Poon, B.; Ravichandran, G. Analysis of Nanoindentation of Soft Materials with an Atomic Force Microscope. *J. Mater. Res.* **2012**, *27*, pp. 229-237.

(184) Bielinski, D. Application of Microindentation to Study Ageing of Rubber. *KGK* **2009**, *62*, pp. 50-54.

(185) Gavara, N. Combined Strategies for Optimal Detection of the Contact Point in AFM Force-Indentation Curves Obtained on Thin Samples and Adherent Cells. *Sci. Rep.* **2016**, *6*, p. 21267.

(186) Nyland, L. R.; Maughan, D. W. Morphology and Transverse Stiffness of Drosophila Myofibrils Measured by Atomic Force Microscopy. *Biophys. J.* **2000**, *78*, pp. 1490-1497.

(187) Domke, J.; Radmacher, M. Measuring the Elastic Properties of Thin Polymer Films with the Atomic Force Microscope. *Langmuir* **1998**, *14*, pp. 3320-3325.

(188) Carlisle, C. R.; Coulais, C.; Guthold, M. The Mechanical Stress-Strain Properties of Single Electrospun Collagen Type I Nanofibers. *Acta Biomater.* **2010**, *6*, pp. 2997-3003.

(189) Nakajima, K.; Watabe, H.; Nishi, T. Single Polymer Chain Rubber Elasticity Investigated by Atomic Force Microscopy. *Polymer* **2006**, *47*, pp. 2505-2510.

(190) Malina, E., W. Mechanical Behavior of Atomically Thin Graphene Sheets Using Atomic Force Microscopy Nanoindentation. University of Vermont, 2011.

(191) Nemes-Incze, P.; Kukucska, G.; Koltai, J.; Kurti, J.; Hwang, C.; Tapaszto, L.; Biro, L. P. Preparing Local Strain Patterns in Graphene by Atomic Force Microscope Based Indentation. *Sci. Rep.* **2017**, *7*, p. 3035.

(192) Vandamme, M.; Ulm, F. J. Viscoelastic Solutions for Conical Indentation. *Int. J. Solids. Struct.* **2006**, *43*, pp. 3142-3165.

(193) Rundlöf, M.; Karlsson, M.; Wågberg, L.; Poptoshev, E.; Rutland, M.; Claesson, P. Application of the JKR Method to the Measurement of Adhesion to Langmuir-Blodgett Cellulose Surfaces. *J. Colloid Interface Sci.* **2000**, *230*, pp. 441-447.

(194) Gillies, G.; Prestidge, C. A. Interaction Forces, Deformation and Nano-Rheology of Emulsion Droplets as Determined by Colloid Probe AFM. *Adv. Colloid. Interface Sci.* **2004**, *108-109*, pp. 197-205.

(195) Mermut, O.; Lefebvre, J.; Gray, D. G.; Barrett, C. J. Structural and Mechanical Properties of Polyelectrolyte Multilayer Films Studied by AFM. *Macromolecules* **2003**, *36*, pp. 8819-8824.

(196) VanLandingham, M. R.; Dagastine, R. R.; Eduljee, R. F.; McCullough, R. L.; Gillespie, J. W. Characterization of Nanoscale Property Variations in Polymer Composite Systems: 1. Experimental Results. *Compos. Part A Appl. Sci. Manuf.* **1999**, *30*, pp. 75-83.

(197) Johnson, K. L.; Kendall, K.; Roberts, A. D. Surface Energy and the Contact of Elastic Solids. *Proc. Royal Soc. A* **1971**, *324*, pp. 301-313.

(198) Vinckier, A.; Dumortier, C.; Engelborghs, Y.; Hellemans, L. Dynamical and Mechanical Study of Immobilized Microtubules with Atomic Force Microscopy. *J. Vac. Sci. Technol. B* **1996**, *14*, pp. 1427-1431.

(199) de Pablo, P. J.; Schaap, I. A. T.; MacKintosh, F. C.; Schmidt, C. F. Deformation and Collapse of Microtubules on the Nanometer Scale. *Phys. Rev. Lett.* **2003**, *91*, p. 098101.

(200) Ivanovska, I. L.; de Pablo, P. J.; Ibarra, B.; Sgalari, G.; MacKintosh, F. C.; Carrascosa, J. L.; Schmidt, C. F.; Wuite, G. J. L. Bacteriophage Capsids: Tough Nanoshells with Complex Elastic Properties. *Proc. Natl. Acad. Sci. USA* **2004**, *101*, pp. 7600-7605.

(201) Roos, W. H.; Wuite, G. L. Nanoindentation Studies Reveal Material Properties of Viruses. *Adv. Mater.* **2009**, *21*, pp. 1187-1192.

(202) Schaer-Zammaretti, P.; Ubbink, J. Imaging of Lactic Acid Bacteria with AFM – Elasticity and Adhesion Maps and Their Relationship to Biological and Structural Data. *Ultramicroscopy* **2003**, *97*, pp. 199-208.

(203) Stolz, M.; Raiteri, R.; Daniels, A. U.; VanLandingham, M. R.; Baschong, W.; Aebi, U. Dynamic Elastic Modulus of Porcine Articular Cartilage Determined at Two Different Levels of Tissue Organization by Indentation-Type Atomic Force Microscopy. *Biophys. J.* **2004**, *86*, pp. 3269-3283.

(204) Radhakrishnan, P.; Lewis, N. T.; Mao, J. J. Zone-Specific Micromechanical Properties of the Extracellular Matrices of Growth Plate Cartilage. *Ann. Biomed. Eng.* **2004**, *32*, pp. 284-291.

(205) Tomkoria, S.; Patel, R. V.; Mao, J. J. Heterogeneous Nanomechanical Properties of Superficial and Zonal Regions of Articular Cartilage of the Rabbit Proximal Radius Condyle by Atomic Force Microscopy. *Med. Eng. Phys.* **2004**, *26*, pp. 815-822.

(206) Fan, Z.; Swadener, J. G.; Rho, J. Y.; Roy, M. E.; Pharr, G. M. Anisotropic Properties of Human Tibial Cortical Bone as Measured by Nanoindentation. *J. Orthop. Res.* **2002**, *20*, pp. 806-810.

(207) T.S., G.; N., T.; I.I., T.; R., P.; B., R. On the Ability of Nanoindentation to Measure Anisotropic Elastic Constants of Pyrolytic Carbon. *ZAMM - Journal of Applied Mathematics and Mechanics / Zeitschrift für Angewandte Mathematik und Mechanik* **2013**, *93*, pp. 301-312.

(208) Delafargue, A.; Ulm, F.-J. Explicit Approximations of the Indentation Modulus of Elastically Orthotropic Solids for Conical Indenters. *Int. J. Solids. Struct.* **2004**, *41*, pp. 7351-7360.

(209) Swadener, J. G.; Pharr, G. M. Indentation of Elastically Anisotropic Half-Spaces by Cones and Parabolae of Revolution. *Philos. Mag. A* **2001**, *81*, pp. 447-466.

(210) G., S. J.; Jae-Young, R.; M., P. G. Effects of Anisotropy on Elastic Moduli Measured by Nanoindentation in Human Tibial Cortical Bone. *Journal of Biomedical Materials Research* **2001**, *57*, pp. 108-112.

(211) Cao, C.; Sun, Y.; Filleter, T. Characterizing Mechanical Behavior of Atomically Thin Films: A Review. *J. Mater. Res.* **2014**, *29*, pp. 338-347.

(212) Lee, J. U.; Yoon, D.; Cheong, H. Estimation of Young's Modulus of Graphene by Raman Spectroscopy. *Nano Lett.* **2012**, *12*, pp. 4444-4448.

(213) Lee, G. H.; Cooper, R. C.; An, S. J.; Lee, S.; van der Zande, A.; Petrone, N.; Hammerberg, A. G.; Lee, C.; Crawford, B.; Oliver, W.; Kysar, J. W.; Hone, J. High-Strength Chemical-Vapor-Deposited Graphene and Grain Boundaries. *Science* **2013**, *340*, pp. 1073-1076.

(214) Senden, T.; Ducker, W. Experimental Determination of Spring Constants in Atomic Force Microscopy. *Langmuir* **1994**, *10*, pp. 1003-1004.

(215) Cleveland, J. P.; Manne, S.; Bocek, D.; Hansma, P. K. A Nondestructive Method for Determining the Spring Constant of Cantilevers for Scanning Force Microscopy. *Rev. Sci. Instrum.* **1993**, *64*, pp. 403-405.

(216) Green, C. P.; Lioe, H.; Cleveland, J. P.; Proksch, R.; Mulvaney, P.; Sader, J. E. Normal and Torsional Spring Constants of Atomic Force Microscope Cantilevers. *Rev. Sci. Instrum.* **2004**, *75*, pp. 1988-1996.

(217) Hazel, J. L.; Tsukruk, V. V. Spring Constants of Composite Ceramic/Gold Cantilevers for Scanning Probe Microscopy. *Thin Solid Films* **1999**, *339*, pp. 249-257.

(218) Sader, J. E.; Chon, J. W. M.; Mulvaney, P. Calibration of Rectangular Atomic Force Microscope Cantilevers. *Rev. Sci. Instrum.* **1999**, *70*, pp. 3967-3969.

(219) Hutter, J. L.; Bechhoefer, J. Calibration of Atomic-Force Microscope Tips. *Rev. Sci. Instrum.* **1993**, *64*, pp. 1868-1873.

(220) Burnham, N. A.; Chen, X.; Hodges, C. S.; Matei, G. A.; Thoreson, E. J.; Roberts, C. J.; Davies, M. C.; Tendler, S. J. B. Comparison of Calibration Methods for Atomic-Force Microscopy Cantilevers. *Nanotechnology* **2003**, *14*, p. 1.

(221) King, R. B. Elastic Analysis of Some Punch Problems for a Layered Medium. *Int. J. Solids. Struct.* **1987**, *23*, pp. 1657-1664.

(222) Hutter, J. L.; Bechhoefer, J. Calibration of Atomic-Force Microscope Tips (Thermal Tune Method to Determine the Spring Constant of Cantilever). *Rev. Sci. Instrum.* **1993**, *64*, pp. 1868-1873.

(223) Briscoe, B. J.; Sebastian, K. S.; Adams, M. J. The Effect of Indenter Geometry on the Elastic Response to Indentation. *J. Phys. D: Appl. Phys.* **1994**, *27*, p. 1156-1162.

(224) Giannakopoulos, A. E.; Larsson, P. L.; Vestergaard, R. Analysis of Vickers Indentation. *Int. J. Solids. Struct.* **1994**, *31*, pp. 2679-2708.

(225) Bolshakov, A.; Oliver, W. C.; Pharr, G. M. An Explanation for the Shape of Nanoindentation Unloading Curves Based on Finite Element Simulation. *Thin Films: Stresses and Mechanical Properties V* **1995**, *356*, pp. 675-680.

(226) Villarrubia, J. S. Algorithms for Scanned Probe Microscope Image Simulation, Surface Reconstruction, and Tip Estimation. *J. Res. Natl. Inst. Stand. Technol.* **1997**, *102*, pp. 425-454.

(227) Pharr, G. M.; Bolshakov, A. Understanding Nanoindentation Unloading Curves. *J. Mater. Res.* **2002**, *17*, pp. 2660-2671.

(228) Oliver, W. C.; Pharr, G. M. Measurement of Hardness and Elastic Modulus by Instrumented Indentation: Advances in Understanding and Refinements to Methodology. *J. Mater. Res.* **2004**, *19*, pp. 3-20.

(229) Tranchida, D.; Piccarolo, S.; Deblieck, R. A. C. Some Experimental Issues of AFM Tip Blind Estimation: the Effect of Noise and Resolution. *Meas. Sci. Technol.* **2006**, *17*, p. 2630-2636.

(230) Calabri, L.; Pugno, N.; Menozzi, C.; Valeri, S. AFM Nanoindentation: Tip Shape and Tip Radius of Curvature Effect on the Hardness Measurement. *J. Phys.: Condens. Matter* **2008**, *20*, p. 474208.

(231) Monclus, M. A.; Young, T. J.; Di Maio, D. AFM Indentation Method Used for Elastic Modulus Characterization of Interfaces and Thin Layers. *J. Mater. Sci.* **2010**, *45*, pp. 3190-3197.

(232) Roa, J. J.; Oncins, G.; Diaz, J.; Sanz, F.; Segarra, M. Calculation of Young's Modulus Value by Means of AFM. *Recent Pat. Nanotechnol.* **2011**, *5*, pp. 27-36.

(233) Cannara, R. J.; Brukman, M. J.; Carpick, R. W. Cantilever Tilt Compensation for Variable-Load Atomic Force Microscopy. *Rev. Sci. Instrum.* **2005**, *76*, p. 053706.

(234) Johnson, K. L. Adhesion and Friction between a Smooth Elastic Spherical Asperity and a Plane Surface. *Proc. Royal Soc. Lond. A: Math. Phys. Eng. Sci.* **1997**, *453*, pp. 163-179.

(235) Hues, S. M.; Draper, C. F.; Lee, K. P.; Colton, R. J. Effect of PZT and PMN Actuator Hysteresis and Creep on Nanoindentation Measurements Using Force Microscopy. *Rev. Sci. Instrum.* **1994**, *65*, pp. 1561-1565.

(236) Gołek, F.; Mazur, P.; Ryszka, Z.; Zuber, S. AFM Image Artifacts. *Appl. Surf. Sci.* **2014**, *304*, pp. 11-19.

(237) Pethicai, J. B.; Hutchings, R.; Oliver, W. C. Hardness Measurement at Penetration Depths as Small as 20 nm. *Philos. Mag. A* **1983**, *48*, pp. 593-606.

(238) Bolshakov, A.; Pharr, G. M. Influences of Pileup on the Measurement of Mechanical Properties by Load and Depth Sensing Indentation Techniques. *J. Mater. Res.* **1998**, *13*, pp. 1049-1058.

(239) Carpick, R. W.; Ogletree, D. F.; Salmeron, M. A General Equation for Fitting Contact Area and Friction vs Load Measurements. *J. Colloid Interface Sci.* **1999**, *211*, pp. 395-400.

(240) Wai, S. W.; Spinks, G. M.; Brown, H. R.; Swain, M. Surface Roughness: Its Implications and Inference with Regards to Ultra Microindentation Measurements of Polymer Mechanical Properties. *Polymer Test.* **2004**, *23*, pp. 501-507.

(241) Kim, J. Y.; Lee, J. J.; Lee, Y. H.; Jang, J. I.; Kwon, D. Surface Roughness Effect in Instrumented Indentation: A Simple Contact Depth Model and its Verification. *J. Mater. Res.* **2006**, *21*, pp. 2975-2978.

(242) Kim, J. Y.; Kang, S. K.; Lee, J. J.; Jang, J. I.; Lee, Y. H.; Kwon, D. Influence of Surface-Roughness on Indentation Size Effect. *Acta. Mater.* **2007**, *55*, pp. 3555-3562.

(243) Xia, Y.; Bigerelle, M.; Marteau, J.; Mazeran, P. E.; Bouvier, S.; Iost, A. Effect of Surface Roughness in the Determination of the Mechanical Properties of Material Using Nanoindentation Test. *Scanning* **2014**, *36*, pp. 134-149.

(244) Maslenikov, I.; Useinov, A.; Birykov, A.; Reshetov, V. Reducing the Influence of the Surface Roughness on the Hardness Measurement Using Instrumented Indentation Test. *IOP Conf. Ser.: Mater. Sci. Eng.* **2017**, *256*, p. 012003.

(245) Lucas, B. N.; Oliver, W. C.; Swindeman, J. E. The Dynamics of Frequency-Specific, Depth-Sensing Indentation Testing. *Mater. Res. Soc. Symp. Proc.* **1998**, *522*, pp. 3-14.

(246) Rotsch, C.; Jacobson, K.; Radmacher, M. Dimensional and Mechanical Dynamics of Active and Stable Edges in Motile Fibroblasts Investigated by Using Atomic Force Microscopy. *Proc. Natl. Acad. Sci. USA* **1999**, *96*, pp. 921-926.

(247) Cappella, B.; Dietler, G. Force-Distance Curves by Atomic Force Microscopy. *Surf. Sci. Rep.* **1999**, *34*, pp. 1-104.

(248) Ullner, C. Requirement of a Robust Method for the Precise Determination of the Contact Point in the Depth Sensing Hardness Test. *Measurement* **2000**, *27*, pp. 43-51.

(249) Li, X. D.; Bhushan, B. A Review of Nanoindentation Continuous Stiffness Measurement Technique and Its Applications. *Mater. Charact.* **2002**, *48*, pp. 11-36.

(250) Chudoba, T.; Griepentrog, M.; Dück, A.; Schneider, D.; Richter, F. Young's Modulus Measurements on Ultra-Thin Coatings. *J. Mater. Res.* **2004**, *19*, pp. 301-314.

(251) Ebenstein, D. M.; Wahl, K. J. A Comparison of JKR-Based Methods to Analyze Quasi-Static and Dynamic Indentation Force Curves. *J. Colloid Interface Sci.* **2006**, *298*, pp. 652-662.

(252) Fischer-Cripps, A. C., *Critical Review of Analysis and Interpretation of Nanoindentation Test Data*. 2006; Vol. 200, pp. 4153-4165.

(253) Lim, Y. Y.; Chaudhri, M. M. Indentation of Elastic Solids with a Rigid Vickers Pyramidal Indenter. *Mech. Mater.* **2006**, *38*, pp. 1213-1228.

(254) Moseson, A. J.; Basu, S.; Barsoum, M. W. Determination of the Effective Zero Point of Contact for Spherical Nanoindentation. *J. Mater. Res.* **2008**, *23*, pp. 204-209.

(255) Kalidindi, S. R.; Pathak, S. Determination of the Effective Zero-Point and the Extraction of Spherical Nanoindentation Stress-Strain Curves. *Acta. Mater.* **2008**, *56*, pp. 3523-3532.

(256) Johnson, K. L., *Contact Mechanics*. Cambridge University Press: Cambridge, 1985.

(257) Joslin, D. L.; Oliver, W. C. A New Method for Analyzing Data from Continuous Depth-Sensing Microindentation Tests. *J. Mater. Res.* **1990**, *5*, pp. 123-126.

(258) Larsson, P. L.; Giannakopoulos, A. E.; SÖderlund, E.; Rowcliffe, D. J.; Vestergaard, R. Analysis of Berkovich Indentation. *Int. J. Solids. Struct.* **1996**, *33*, pp. 221-248.

(259) Giannakopoulos, A. E.; Larsson, P. L. Analysis of Pyramid Indentation of Pressure-Sensitive Hard Metals and Ceramics. *Mech. Mater.* **1997**, *25*, pp. 1-35.

(260) Cheng, Y. T.; Cheng, C. M. Relationships between Hardness, Elastic Modulus, and the Work of Indentation. *Appl. Phys. Lett.* **1998**, *73*, pp. 614-616.

(261) Cheng, Y. T.; Cheng, C. M. Scaling Relationships in Conical Indentation of Elastic-Perfectly Plastic Solids. *Int. J. Solids. Struct.* **1999**, *36*, pp. 1231-1243.

(262) Cheng, Y. T.; Cheng, C. M. Scaling Approach to Conical Indentation in Elastic-Plastic Solids with Work Hardening. *J. Appl. Phys.* **1998**, *84*, pp. 1284-1291.

(263) Saha, R.; Nix, W. D. Effects of the Substrate on the Determination of Thin Film Mechanical Properties by Nanoindentation. *Acta. Mater.* **2002**, *50*, pp. 23-38.

(264) Bédoui, F.; Sansoz, F.; Murthy, N. S. Incidence of Nanoscale Heterogeneity on the Nanoindentation of a Semicrystalline Polymer: Experiments and Modeling. *Acta. Mater.* **2008**, *56*, pp. 2296-2306.

(265) Tranchida, D.; Piccarolo, S.; Soliman, M. Nanoscale Mechanical Characterization of Polymers by AFM Nanoindentations: Critical Approach to the Elastic Characterization. *Macromolecules* **2006**, *39*, pp. 4547-4556.

(266) Chizhik, S. A.; Huang, Z.; Gorbunov, V. V.; Myshkin, N. K.; Tsukruk, V. V. Micromechanical Properties of Elastic Polymeric Materials as Probed by Scanning Force Microscopy. *Langmuir* **1998**, *14*, pp. 2606-2609.

(267) Silberzan, P.; Perutz, S.; Kramer, E. J.; Chaudhury, M. K. Study of the Self-Adhesion Hysteresis of a Siloxane Elastomer Using the JKR Method. *Langmuir* **1994**, *10*, pp. 2466-2470.

(268) Maugis, D., *Contact, Adhesion and Rupture of Elastic Solids* Springer: 2000; Vol. 130, pp. 264-272.

(269) Meitl, M. A.; Zhu, Z. T.; Kumar, V.; Lee, K. J.; Feng, X.; Huang, Y. Y.; Adesida, I.; Nuzzo, R. G.; Rogers, J. A. Transfer Printing by Kinetic Control of Adhesion to an Elastomeric Stamp. *Nat. Mater.* **2005**, *5*, p. 33.

(270) Jin, C.; Ebenstein, D. M. Nanoindentation of Compliant Materials Using Berkovich Tips and Flat Tips. *J. Mater. Res.* **2017**, *32*, pp. 435-450.

(271) Yang, F. Indentation of an Incompressible Elastic Film. *Mech. Mater.* **1998**, *30*, pp. 275-286.

(272) Chadwick, R. Axisymmetric Indentation of a Thin Incompressible Elastic Layer. *SIAM J. Appl. Math.* **2002**, *62*, pp. 1520-1530.

(273) Williams, M. L.; Landel, R. F.; Ferry, J. D. The Temperature Dependence of Relaxation Mechanisms in Amorphous Polymers and Other Glass-Forming Liquids. *J. Am. Chem. Soc.* **1955**, *77*, pp. 3701-3707.

(274) Tsui, O. K. C.; Wang, X. P.; Ho, J. Y. L.; Ng, T. K.; Xiao, X. D. Studying Surface Glass-to-Rubber Transition Using Atomic Force Microscopic Adhesion Measurements. *Macromolecules* **2000**, *33*, pp. 4198-4204.

(275) Thomas, J.; Gomes, K.; Lowman, A.; Marcolongo, M. The Effect of Dehydration History on PVA/PVP Hydrogels for Nucleus Pulposus Replacement. *J. Biomed. Mater. Res. Part B Appl. Biomater.* **2004**, *69*, pp. 135-140.

(276) Ho, S. P.; Goodis, H.; Balooch, M.; Nonomura, G.; Marshall, S. J.; Marshall, G. The Effect of Sample Preparation Technique on Determination of Structure and Nanomechanical Properties of Human Cementum Hard Tissue. *Biomaterials* **2004**, *25*, pp. 4847-4857.

(277) Carrillo, F.; Gupta, S.; Balooch, M.; Marshall, S. J.; Marshall, G. W.; Pruitt, L.; Puttlitz, C. M. Nanoindentation of Polydimethylsiloxane Elastomers: Effect of Crosslinking, Work of Adhesion, and Fluid Environment on Elastic Modulus. *J. Mater. Res.* **2006**, *21*, pp. 535-537.

(278) Bembey, A. K.; Oyen, M. L.; Bushby, A. J.; Boyde, A. Viscoelastic Properties of Bone as a Function of Hydration State Determined by Nanoindentation. *Philos. Mag.* **2006**, *86*, pp. 5691-5703.

(279) Chapman, K. W.; Halder, G. J.; Chupas, P. J. Guest-Dependent High Pressure Phenomena in a Nanoporous Metal-Organic Framework Material. *J. Am. Chem. Soc.* **2008**, *130*, pp. 10524-10526.

(280) Ma, Q. T.; Yang, Q. Y.; Ghoufi, A.; Yang, K.; Lei, M.; Ferey, G.; Zhong, C. L.; Maurin, G. Guest-Modulation of the Mechanical Properties of Flexible Porous Metal-Organic Frameworks. *J. Mater. Chem. A* **2014**, *2*, pp. 9691-9698.

(281) Méndez-Méndez, J. V.; Alonso-Rasgado, M. T.; Correia Faria, E.; Flores-Johnson, E. A.; Snook, R. D. Numerical Study of the Hydrodynamic Drag Force in Atomic Force Microscopy Measurements Undertaken in Fluids. *Micron* **2014**, *66*, pp. 37-46.

(282) Dürholt, J. P.; Keupp, J.; Schmid, R. The Impact of Mesopores on the Mechanical Stability of HKUST-1: A Multiscale Investigation. *Eur. J. Inorg. Chem.* **2016**, *2016*, pp. 4517-4523.

(283) Yang, K.; Zhou, G. L.; Xu, Q. The Elasticity of MOFs under Mechanical Pressure. *RSC Adv.* **2016**, *6*, pp. 37506-37514.

(284) Berthold, T.; Benstetter, G.; Frammelsberger, W.; Rodríguez, R.; Nafría, M. Numerical Study of Hydrodynamic Forces for AFM Operations in Liquid. *Scanning* **2017**, *2017*, p. 12.

(285) Sneddon, I. N. The Relation between Load and Penetration in the Axisymmetric Boussinesq Problem for a Punch of Arbitrary Profile. *Int. J. Eng. Sci.* **1965**, *3*, pp. 47-57.

(286) Borodich, F. M.; Keer, L. M.; Korach, C. S. Analytical Study of Fundamental Nanoindentation Test Relations for Indenters of Non-Ideal Shapes. *Nanotechnology* **2003**, *14*, pp. 803-808.

(287) McElhaney, K. W.; Vlassak, J. J.; Nix, W. D. Determination of Indenter Tip Geometry and Indentation Contact Area for Depth-Sensing Indentation Experiments. *J. Mater. Res.* **1998**, *13*, pp. 1300-1306.

(288) Pugno, N. M. A General Shape/Size-Effect Law for Nanoindentation. *Acta. Mater.* **2007**, *55*, pp. 1947-1953.

(289) Touhami, A.; Nysten, B.; Dufrêne, Y. F. Nanoscale Mapping of the Elasticity of Microbial Cells by Atomic Force Microscopy. *Langmuir* **2003**, *19*, pp. 4539-4543.

(290) A-Hassan, E.; Heinz, W. F.; Antonik, M. D.; D'Costa, N. P.; Nageswaran, S.; Schoenenberger, C. A.; Hoh, J. H. Relative Microelastic Mapping of Living Cells by Atomic Force Microscopy. *Biophys. J.* **1998**, *74*, pp. 1564-1578.

(291) Hertz, H. Üeber Die Berührung Fester Elastischer Körper. *Journal für die reine und angewandte Mathematik* **1882**, *92*, pp. 156-171.

(292) Boussinesq, J. Applications Des Potentiels a I'etude De Equilibre Et Dumouvement Des Solides Elastiques. *Gauthier-Villars: Paris* **1885**.

(293) Akhremitchev, B. B.; Walker, G. C. Finite Sample Thickness Effects on Elasticity Determination Using Atomic Force Microscopy. *Langmuir* **1999**, *15*, pp. 5630-5634.

(294) Bilodeau, G. G. Regular Pyramid Punch Problem. *J. Appl. Mech.* **1992**, *59*, pp. 519-523.

(295) Na, S.; Sun, Z.; Meininger, G. A.; Humphrey, J. D. On Atomic Force Microscopy and the Constitutive Behavior of Living Cells. *Biomech. Model. Mechanobiol.* **2004**, *3*, pp. 75-84.

(296) Rico, F.; Roca-Cusachs, P.; Gavara, N.; Farre, R.; Rotger, M.; Navajas, D. Probing Mechanical Properties of Living Cells by Atomic Force Microscopy with Blunted Pyramidal Cantilever Tips. *Phys. Rev. E* **2005**, *72*, p. 021914.

(297) Maugis, D.; Barquins, M. Adhesive Contact of Sectionally Smooth-Ended Punches on Elastic Half-Spaces: Theory and Experiment. *J. Phys. D: Appl. Phys.* **1983**, *16*, p. 1843.

(298) Derjaguin, B. V.; Muller, V. M.; Toporov, Y. P. Effect of Contact Deformations on the Adhesion of Particles. *J. Colloid Interface Sci.* **1975**, *53*, pp. 314-326.

(299) Lennard-Jones, J. E. Perturbation Problems in Quantum Mechanics. *Proc. Royal Soc. Lond. A* **1930**, *129*, pp. 598-615.

(300) Tabor, D. Surface Forces and Surface Interactions. *J. Colloid Interface Sci.* **1977**, *58*, pp. 2-13.

(301) Maugis, D. Adhesion of Spheres: The JKR-DMT Transition Using a Dugdale Model. *J. Colloid Interface Sci.* **1992**, *150*, pp. 243-269.

(302) Johnson, K. L.; Greenwood, J. A. An Adhesion Map for the Contact of Elastic Spheres. *J. Colloid Interface Sci.* **1997**, *192*, pp. 326-333.

(303) Piétrement, O.; Troyon, M. General Equations Describing Elastic Indentation Depth and Normal Contact Stiffness Versus Load. *J. Colloid Interface Sci.* **2000**, *226*, pp. 166-171.

(304) Carson, C. G.; Hardcastle, K.; Schwartz, J.; Liu, X. T.; Hoffmann, C.; Gerhardt, R. A.; Tannenbaum, R. Synthesis and Structure Characterization of Copper Terephthalate Metal-Organic Frameworks. *Eur. J. Inorg. Chem.* **2009**, p. 2338-2343.

(305) Markiewicz, P.; Goh, M. C. Atomic Force Microscope Tip Deconvolution Using Calibration Arrays. *Rev. Sci. Instrum.* **1995**, *66*, pp. 3186-3190.

(306) Dongmo, L. S.; Villarrubia, J. S.; Jones, S. N.; Renegar, T. B.; Postek, M. T.; Song, J. F. Experimental Test of Blind Tip Reconstruction for Scanning Probe Microscopy. *Ultramicroscopy* **2000**, *85*, pp. 141-153.

(307) Necas, D.; Klapetek, P. Gwyddion: An Open-Source Software for Spm Data Analysis. *Cent. Eur. J. Phys.* **2012**, *10*, pp. 181-188.

(308) Bragg, W. H.; Bragg, W. L. The Reflection of X-Rays by Crystals. *Proc. Royal Soc. Lond. A* **1913**, *88*, pp. 428-438.

(309) Briscoe, B. J.; Fiori, L.; Pelillo, E. Nano-Indentation of Polymeric Surfaces. *J. Phys. D: Appl. Phys.* **1998**, *31*, pp. 2395-2405.

(310) Derjaguin, B. Untersuchungen Über Die Reibung Und Adhäsion, IV. *Kolloid-Zeitschrift* **1934**, *69*, pp. 155-164.

(311) Doerner, M. F.; Nix, W. D. A Method for Interpreting the Data from Depth-Sensing Indentation Instruments. *J. Mater. Res.* **1986**, *1*, pp. 601-609.

(312) Hay, J. C.; Bolshakov, A.; Pharr, G. M. A Critical Examination of the Fundamental Relations Used in the Analysis of Nanoindentation Data. *J. Mater. Res.* **1999**, *14*, pp. 2296-2305.

(313) Tranchida, D.; Piccarolo, S. Relating Morphology to Nanoscale Mechanical Properties: From Crystalline to Mesomorphic iPP. *Polymer* **2005**, *46*, pp. 4032-4040.

(314) Tranchida, D.; Piccarolo, S. On the Use of the Nanoindentation Unloading Curve to Measure the Young's Modulus of Polymers on a Nanometer Scale. *Macromol. Rapid Commun.* **2005**, *26*, pp. 1800-1804.

(315) Cheng, Y. T.; Cheng, C. M. Relationships between Initial Unloading Slope, Contact Depth, and Mechanical Properties for Spherical Indentation in Linear Viscoelastic Solids. *Mater. Sci. Eng. A* **2005**, *409*, pp. 93-99.

(316) Coates, C. S.; Ryder, M. R.; Hill, J. A.; Tan, J. C.; Goodwin, A. L. Large Elastic Recovery of Zinc Dicyanoaurate. *APL Mater.* **2017**, *5*, p. 066107.

(317) Jones, J. E. On the Determination of Molecular Fields. —II. From the Equation of State of a Gas. *Proc. Royal Soc. Lond. A* **1924**, *106*, pp. 463-477.

(318) Greenwood, J. A. Adhesion of Elastic Spheres. *Proc. Royal Soc. Lond. A: Math. Phys. Eng. Sci.* **1997**, *453*, pp. 1277-1297.

(319) Jin, C.; Jagota, A.; Hui, C. Y. An Easy-to-Implement Numerical Simulation Method for Adhesive Contact Problems Involving Asymmetric Adhesive Contact. *J. Phys. D: Appl. Phys.* **2011**, *44*, p. 405303.

(320) Johnson, K. L. Mechanics of Adhesion. *Tribol. Int.* **1998**, *31*, pp. 413-418.

(321) Hrennikoff, A. Solution of Problems of Elasticity by the Framework Method. *J. Appl. Mech.* **1941**, pp. 169–175.

(322) Courant, R. Variational Methods for the Solution of Problems of Equilibrium and Vibrations. *Bull. Amer. Math. Soc.* **1943**, *49*, pp. 1-23.

(323) ABAQUS Analysis User's Guide. *Hibbitt, Karlsson & Sorensen, Inc.* **2016**.

(324) Johnson, G. R.; Cook, W. H. Fracture Characteristics of Three Metals Subjected to Various Strains, Strain Rates, Temperatures and Pressures. *Eng. Fract. Mech.* **1985**, *21*, pp. 31-48.

(325) MathWorks, Matlab Documentation. **2018**.

(326) OriginLab, Origin User Guide. **2017**.

(327) Seifert, E. Originpro 9.1: Scientific Data Analysis and Graphing Software—Software Review. *J. Chem. Inf. Model.* **2014**, *54*, pp. 1552-1552.

(328) Python, Python Documentation. **2017**.

(329) Sweers, K. K. M.; Bennink, M. L.; Subramaniam, V. Nanomechanical Properties of Single Amyloid Fibrils. *J. Phys.: Condens. Matter* **2012**, *24*, p. 243101.

(330) Fischer-Cripps, A. C., *Nanoindentation, 2nd Ed.* 2004.

(331) Tranchida, D.; Kiflie, Z.; Acierno, S.; Piccarolo, S. Nanoscale Mechanical Characterization of Polymers by Atomic Force Microscopy (AFM) Nanoindentations: Viscoelastic Characterization of a Model Material. *Meas. Sci. Technol.* **2009**, *20*, p. 095702.

(332) Feng, G.; Ngan, A. H. W. Effects of Creep and Thermal Drift on Modulus Measurement Using Depth-Sensing Indentation. *J. Mater. Res.* **2002**, *17*, pp. 660-668.

(333) Lucas, M.; Gall, K.; Riedo, E. Tip Size Effects on Atomic Force Microscopy Nanoindentation of a Gold Single Crystal. *J. Appl. Phys.* **2008**, *104*, p. 113515.

(334) Karsten, D.; Mathias, G.; George, M. P. Indentation Size Effect in Spherical and Pyramidal Indentations. *J. Phys. D: Appl. Phys.* **2008**, *41*, p. 074005.

(335) Williamson, D. M.; Hamilton, N. R.; Palmer, S. J. P.; Jardine, A. P.; Leppard, C. Thermodynamic Work of Adhesion Measurements of Polymer Bonded Explosive Constituents via the Wilhelmy Plate Technique and their Application to AFM Pull-Off Experiments. *J. Phys. Conf. Ser.* **2014**, *500*, p. 112068.

(336) Okamatsu, T.; Yasuda, Y.; Ochi, M. Thermodynamic Work of Adhesion and Peel Adhesion Energy of Dimethoxysilyl-Terminated Polypropylene Oxide/Epoxy Resin System Jointed with Polymeric Substrates. *J. Appl. Polym. Sci.* **2001**, *80*, pp. 1920-1930.

(337) Chen, Y.; Bakshi, S. R.; Agarwal, A. Intersplat Friction Force and Splat Sliding in a Plasma-Sprayed Aluminum Alloy Coating During Nanoindentation and Microindentation. *ACS Appl. Mater. Interfaces* **2009**, *1*, pp. 235-238.

(338) Maschmann, M. R.; Zhang, Q. H.; Wheeler, R.; Du, F.; Dai, L. M.; Baur, J. In Situ SEM Observation of Column-Like and Foam-Like CNT Array Nanoindentation. *ACS Appl. Mater. Interfaces* **2011**, *3*, pp. 648-653.

(339) Steinmann, P. A.; Tardy, Y.; Hintermann, H. E. Adhesion Testing by the Scratch Test Method: The Influence of Intrinsic and Extrinsic Parameters on the Critical Load. *Thin Solid Films* **1987**, *154*, pp. 333-349.

(340) Beake, B. D.; Davies, M. I.; Liskiewicz, T. W.; Vishnyakov, V. M.; Goodes, S. R. Nano-Scratch, Nanoindentation and Fretting Tests of 5–80 nm Ta-C Films on Si(100). *Wear* **2013**, *301*, pp. 575-582.

(341) Beake, B. D.; Harris, A. J.; Liskiewicz, T. W. Review of Recent Progress in Nanoscratch Testing. *Tribology* **2013**, *7*, pp. 87-96.

(342) Marx, J.; Rabiei, A. Overview of Composite Metal Foams and Their Properties and Performance. *Adv. Eng. Mater.* **2017**, *19*, p. 1600776.

(343) Coleman, J. N.; Lotya, M.; O'Neill, A.; Bergin, S. D.; King, P. J.; Khan, U.; Young, K.; Gaucher, A.; De, S.; Smith, R. J.; Shvets, I. V.; Arora, S. K.; Stanton, G.; Kim, H. Y.; Lee, K.; Kim, G. T.; Duesberg, G. S.; Hallam, T.; Boland, J. J.; Wang, J. J.; Donegan, J. F.; Grunlan, J. C.; Moriarty, G.; Shmeliov, A.; Nicholls, R. J.; Perkins, J. M.; Grieveson, E. M.; Theuwissen, K.; McComb, D. W.; Nellist, P. D.; Nicolosi, V. Two-Dimensional Nanosheets Produced by Liquid Exfoliation of Layered Materials. *Science* **2011**, *331*, pp. 568-571.

(344) He, J. B.; Kanjanaboos, P.; Frazer, N. L.; Weis, A.; Lin, X. M.; Jaeger, H. M. Fabrication and Mechanical Properties of Large-Scale Freestanding Nanoparticle Membranes. *Small* **2010**, *6*, pp. 1449-1456.

(345) Evans, J. D.; Coudert, F. X. Macroscopic Simulation of Deformation in Soft Microporous Composites. *J. Phys. Chem. Lett.* **2017**, *8*, pp. 1578-1584.

(346) Bocciarelli, M.; Bolzon, G.; Maier, G. Parameter Identification in Anisotropic Elastoplasticity by Indentation and Imprint Mapping. *Mech. Mater.* **2005**, *37*, pp. 855-868.

(347) Chen, Z.; Wang, X.; Atkinson, A.; Brandon, N. Spherical Indentation of Porous Ceramics: Elasticity and Hardness. *J. Eur. Ceram. Soc* **2016**, *36*, pp. 1435-1445.

(348) Louche, H.; Piette-Coudol, F.; Arrieux, R.; Issartel, J. An Experimental and Modeling Study of the Thermomechanical Behavior of an Abs Polymer Structural Component During an Impact Test. *Int. J. Impact Eng.* **2009**, *36*, pp. 847-861.

(349) Majzoobi, G. H.; Dehgolan, F. R. Determination of the Constants of Damage Models. *Procedia. Eng.* **2011**, *10*, pp. 764-773.

(350) Taljat, B.; Pharr, G. M. Development of Pile-up During Spherical Indentation of Elastic-Plastic Solids. *Int. J. Solids. Struct.* **2004**, *41*, pp. 3891-3904.

(351) Hollomon, J. H. Tensile Deformation. *Min. Eng.* **1945**, *162*, pp. 268-290.

(352) Matthews, J. R. Indentation Hardness and Hot Pressing. *Acta. Mater.* **1980**, *28*, pp. 311-318.

(353) Cahoon, J. R.; Broughton, W. H.; Kutzak, A. R. The Determination of Yield Strength from Hardness Measurements. *Metall. Trans.* **1971**, *2*, pp. 1979-1983.

(354) Tabor, D. The Hardness and Strength of Metals. *J. Inst. Metals* **1951**, *79*, pp. 1-18.

(355) Garcia, E.; Nistal, A.; Khalifa, A.; Essa, Y.; Martín de la Escalera, F.; Osendi, M. I.; Miranzo, P. Highly Electrically Conducting Glass-Graphene Nanoplatelets Hybrid Coatings. *ACS Appl. Mater. Interfaces* **2015**, *7*, pp. 17656-17662.

(356) Qin, J. S.; Du, D. Y.; Guan, W.; Bo, X. J.; Li, Y. F.; Guo, L. P.; Su, Z. M.; Wang, Y. Y.; Lan, Y. Q.; Zhou, H. C. Ultrastable Polymolybdate-Based Metal-Organic Frameworks as Highly Active Electrocatalysts for Hydrogen Generation from Water. *J. Am. Chem. Soc.* **2015**, *137*, pp. 7169-7177.

(357) Maiti, S.; Pramanik, A.; Manju, U.; Mahanty, S. Cu_3(1,3,5-Benzenetricarboxylate)$_2$ Metal-Organic Framework: A Promising Anode Material for Lithium-Ion Battery. *Microporous Mesoporous Mat.* **2016**, *226*, pp. 353-359.

(358) Hendon, C. H.; Walsh, A. Chemical Principles Underpinning the Performance of the Metal-Organic Framework HKUST-1. *Chem. Sci.* **2015**, *6*, pp. 3674-3683.

(359) Talin, A. A.; Centrone, A.; Ford, A. C.; Foster, M. E.; Stavila, V.; Haney, P.; Kinney, R. A.; Szalai, V.; El Gabaly, F.; Yoon, H. P.; Leonard, F.; Allendorf, M. D. Tunable Electrical Conductivity in Metal-Organic Framework Thin-Film Devices. *Science* **2014**, *343*, p. 66-69.

(360) Heinen, J.; Ready, A. D.; Bennett, T. D.; Dubbeldam, D.; Friddle, R. W.; Burtch, N. C. Elucidating the Variable-Temperature Mechanical Properties of a Negative Thermal Expansion Metal-Organic Framework. *ACS Appl. Mater. Interfaces* **2018**, *10*, pp. 21079-21083.

(361) Wu, H.; Yildirim, T.; Zhou, W. Exceptional Mechanical Stability of Highly Porous Zirconium Metal–Organic Framework UiO-66 and Its Important Implications. *J. Phys. Chem. Lett.* **2013**, *4*, pp. 925-930.

(362) Lu, H.; Wang, B.; Ma, J.; Huang, G.; Viswanathan, H. Measurement of Creep Compliance of Solid Polymers by Nanoindentation. *Mech. Time-Depend. Mat.* **2003**, *7*, pp. 189-207.